

Universität
Rostock



Traditio et Innovatio

Investigating the effect of the compression rate on
the kinetic response of diamond anvil cell
experiments

Dissertation

zur

Erlangung des akademischen Grades

doctor rerum naturalium (Dr. rer. nat)

der Mathematisch-Naturwissenschaftlichen Fakultät

der Universität Rostock

vorgelegt von

Christian Plückthun, geb. am 21.07.1990 in Essen
aus Hamburg

Rostock, 18.07.2021

https://doi.org/10.18453/rosdok_id00003440

1. Gutachter: Prof. Dr. Ronald Redmer, University of Rostock

2. Gutachter: Prof. Dr. Carmen Sanchez-Valle, University of Münster

Einreichung: 18.07.2021

Verteidigung: 19.11.2021

Universität Rostock

Institut für Physik

18051 Rostock

Tel: +49 381 498-6916

Fax: +49 381 498-6912

Internet: <http://www.physik.uni-rostock.de>

Email des Autors: christian.plueckthun@xfel.eu

Abstract

High pressure and high temperature experiments using either dynamic (shock, ramp) or static compression techniques play a fundamental role in improving our understanding of the behaviour of matter under extreme conditions relevant to (exo-) planetary interiors. The main difference between the two techniques is the strain rates that can be achieved during the experiments, which are orders of magnitude apart. However, the strain rates between the two technologies have hardly been studied due to the lack of technical means. Only recently have new pressure and temperature paths opened up to investigate kinetic phenomena in the microsecond-millisecond time range, as new technologies such as the piezo actuator-driven diamond anvil cell (dDAC) or adaptations to the membrane diamond anvil cell (mDAC) became available. Nevertheless, difficulties to interpret experimental results may be encountered in those experiments where the sample is compressed under non-hydrostatic conditions and differential stresses, the properties of the gasket material, the pressure calibrant and the pressure transmitting medium have to be considered.

The present thesis examines the high-pressure behavior of cubic (fcc, bcc) and hexagonal (hcp) symmetric sample material that was generated by dynamic compression in mDAC, dDAC and laser heated mDAC experiments. Those experiments have been performed at both the general purpose and laser heating station of ECB P02.2, PETRA III, DESY, Hamburg and reached compression rates from 0.1 GPa/s- 38 TPa/s, which corresponds here to a strain rate range of seven orders of magnitude, covering 10^{-4} s^{-1} - 10^2 s^{-1} . To shed light on the sample response, the events were meticulously tracked with resolutions of 1 s - 500 μs . Different sample materials were selected to perform investigation of the micro-stress, differential stress, lattice parameter and/or spin/phase transition evolution: 1. Due to their common usage in DAC experiments (Au, Pt, Re); 2: Their dependence on hydrostatic conditions (Zn, Re) and 3. Their complex phase diagram and importance to the composition of the Earth interior ([Fe,Mg]O, MgO, FeO).

From micro-strain analysis of Au and Pt a grain size dependence of the micro-stress evolution was determined but an indifference to strain rates of the order of 10^{-4} s^{-1} - 10^0 s^{-1} , whereas the differential stress recorded a clear dependence to the utilization of a pressure transmitting medium and to increasing strain rates. This made adjustment of α , the parameter determining the ratio of isostress and isostrain, from 0.5 \rightarrow 0.75 necessary. Furthermore, hcp metals such as Zn observed the change of the main deformation mechanism within the lattice para-

meter evolution at strain rates of 10^0 s^{-1} - 10^2 s^{-1} , whilst Re revealed a time dependence of the onset of texture in runs with soft Ss gasket and at strain rates of 10^{-4} s^{-1} - 10^{-3} s^{-1} . But, if enclosed by a Re gasket indifference to strain rates up to 10^0 s^{-1} . Besides those findings, a strain rate dependence of both spin crossover and rB1 \rightarrow B1 phase transition onset and pressure interval are revealed in [Fe,Mg]O, showing direct correlation where increasing compression rates result in lower onset pressures and broad transition intervals. In contrast the α -Fe \rightarrow ε -Fe transition is indifferent to any changes based on strain rates of the order of 10^{-2} s^{-1} - 10^0 s^{-1} . Last but not least, laser heating runs using [Fe,Mg]O and above 1400K found inconsistencies in the pressure trend of Pt and in comparison the trends observed in the KCl insulator or literature data. Thus, showing a dependence of the thermal pressure evolution of Pt upon the developments in the [Fe,Mg]O and KCl matrix. Finally, first commissioning experiments of the X-ray and laser heating DAC setup at the HED instrument, European XFEL, were performed and showed 2.25-4.5 MHz repetition, pulse-to-pulse resolved X-ray diffraction image collection capabilities and a time dependence of the rB1 \rightarrow B1 phase transition in [Fe,Mg]O at elevated temperatures (450-650 K).

Zusammenfassung

Hochdruck- und Hochtemperaturexperimente, die entweder auf dynamischer (Shock, Ramp) oder statischer Kompression basieren, spielen eine fundamentale Rolle in der Erweiterung unseres Verständnisses vom Verhalten von geologischen Materialien unter extremen Bedingungen, die etwas für das (Exo-) Planeteninnere relevant sind. Der Hauptunterschied zwischen den beiden Methoden liegt in der erreichbaren Deformationsrate und der Dauer des extremen Zustand, die im Zeitraum eines Experimentes erzielt werden kann und der Unterschied beläuft sich auf mehrere Größenordnungen. Dabei sind jedoch die Deformationsraten zwischen den beiden Methoden (10^{-2} - 10^4 s $^{-1}$) aufgrund fehlender technischer Mittel kaum untersucht worden. Erst in jüngster Zeit haben sich, mit der Verfügbarkeit von neuen Technologien wie der dynamischen Diamantstempelzelle (dDAC) oder Anpassungen der Membran-Diamantstempelzelle (mDAC), neue Druck und Temperaturpfade zur Untersuchung von kinetischen Phänomenen im Zeitbereich von Mikrosekunden bis Millisekunden eröffnet. Hierbei kann es jedoch zu Schwierigkeiten bei der Interpretation der experimentellen Ergebnisse kommen, da die Probe unter nicht-hydrostatischen Bedingungen komprimiert wird und somit Differenzspannungen berücksichtigt werden müssen sowie die Eigenschaften vom Dichtungsmaterial, des Druck-Kalibriermediums und des druckübertragenden Mediums. Die vorliegende Arbeit untersucht das Hochdruckverhalten von kubischen (fcc, bcc) und hexagonal (hcp) symmetrischen Proben, das durch dynamische Kompression in der mDAC und dDAC als auch laserbeheizten mDAC Experimenten erzeugt wurde. Die Experimente wurden sowohl an der Universal- als auch an der Laserheizstation von ECB P02.2, PETRA III, DESY, Hamburg durchgeführt und erzielten Kompressionsraten von 0.1 GPa/s - 38 TPa/s, was in den verwendeten Materialien einer Deformationsrate über sieben Größenordnungen entspricht, die 10^{-4} s $^{-1}$ - 10^2 s $^{-1}$ umfasst. Um die Reaktion der Probe zu erfassen, wurden die Ereignisse mit einer Auflösung von 1 s - 500 μ s akribisch nachverfolgt. Verschiedene Proben wurden ausgewählt, um die Entwicklung anhand der Mikrospannung, der differentiellen Spannung, der Gitterparameter und/oder des Spin/Phasenüberganges zu untersuchen und den Einfluss zu quantifizieren: 1. Aufgrund ihrer häufigen Verwendung in DAC-Experimenten (Au, Pt, Re); 2. Ihrer Abhängigkeit von hydrostatischen Bedingungen (Zn, Re) und 3. Ihres komplexen Phasendiagrammes und der Relevanz für das Erd- und Planeteninnere ([Fe,Mg]O, MgO, FeO).

Dabei wurde mit Hilfe der Mikrospannungsanalyse in Au und Pt eine Körnergrößenabhängigkeit

der Spannungsentwicklung festgestellt, jedoch eine Indifferenz zu Deformationsraten von 10^{-4} s^{-1} - 10^0 s^{-1} . Dem entgegen wies die Differenzspannung eine deutliche Abhängigkeit zur Nutzung eines druckübertragenden Mediums auf, so wie zur zunehmenden Deformationsrate. Dabei eine Anpassung von α von $0.5 \rightarrow 0.75$ notwendig wurde. Des Weiteren wurde bei Deformationsraten von 10^0 s^{-1} - 10^2 s^{-1} im hcp-Metall: Zink, die Änderung des Hauptdeformationsmechanismus anhand der Gitterparameterentwicklung beobachtet, während Re in einer weichen Ss-Dichtung und bei Deformationsraten von 10^{-4} s^{-1} - 10^{-3} s^{-1} eine zeitliche Abhängigkeit der Ausbildung einer bevorzugten Orientierung zeigte, aber eine Indifferenz gegenüber Deformationsraten bis zu 10^0 s^{-1} sobald sie von einer Re-Dichtung eingeschlossen war. Neben diesen Erkenntnissen fand sich eine Abhängigkeit bei Spin- und rB1 \rightarrow B1-Phasenübergangs zur Deformationsrate. Diese weist eine direkte Korrelation auf, bei der steigende Kompressionsraten niedrigere Drücke für den Beginn des Überganges fanden, aber dieser Übergang über ein größeren Druckbereich stattfand. Im Gegensatz dazu war der α -Fe \rightarrow ϵ -Fe-Übergang unabhängig von der Deformationsrate im Bereich von 10^{-2} s^{-1} - 10^0 s^{-1} . Zudem wurde bei den mit Laser geheizten Experimenten in [Fe,Mg]O eine Abhängigkeit des thermischen Drucks von Pt in der Matrix aus [Fe,Mg]O und KCl festgestellt, wobei sich nicht nur Unstimmigkeiten in der Druckentwicklung im Vergleich zur Literatur, sondern auch zur Druckentwicklung in KCl-isolator oberhalb von 1400 K deutlich zeigten. Zu guter Letzt wurden erste Experimente zur Inbetriebnahme des Röntgen- und Laserheizungsaufbaus für DAC-Experimente am HED-Instrument, European XFEL, durchgeführt. Sie zeigen eine pulsaufgelöste Aufnahmefähigkeit von Röntgendiffraktionsbildern bei einer 2.25 - 4.5 MHz hohen Wiederholungsrate und fanden eine zeitliche Abhängigkeit des rB1 \rightarrow B1-Phasenüberganges in [Fe,Mg]O bei erhöhter Temperatur (450 - 650 K).

Contents

1	Introduction	1
1.1	High-pressure as a dynamic system	1
2	High P-T: The properties of material	4
2.1	Definition of solids	5
2.2	Introduction to rheology	6
2.2.1	Elasticity	7
2.2.2	Defects: Plasticity and ductility	9
2.3	Equation of State	12
2.4	The 'gap' between static and shock compression experiments	15
3	The diamond anvil cell (DAC) and X-ray diffraction	17
3.1	Introducing the DAC	17
3.2	Pressure determination	18
3.3	Non-hydrostatic conditions and lattice preferred orientation	20
3.4	Differential Stress	21
3.5	Pressure transmitting media	25
3.6	Diamond cupping	26
3.7	High temperatures	27
3.8	Dynamic compression in DAC	28
3.8.1	Membrane diamond anvil cell (mDAC)	28
3.8.2	Piezo-driven dynamic diamond anvil cell (dDAC)	29
3.9	X-ray diffraction	30
3.9.1	X-ray diffraction at ECB P02.2, PETRA III, DESY	31
3.9.2	The European XFEL, a new tool for high pressure experiments	32
4	Sample material and synthesis	34
4.1	Synthesis of [Mg,Fe]O	36
4.1.1	Introduction	36
4.1.2	The wet chemistry approach	38
4.1.3	Gas-mixing experiments	39
4.1.4	Mössbauer spectroscopy and XRD	43

5	Results	46
5.1	X-ray diffraction at the ECB P02.2	47
5.1.1	Platinum	50
5.1.2	Rhenium	53
5.1.3	Gold	57
5.1.4	Zinc	60
5.1.5	Iron	62
5.1.6	Wüstite, periclase and ferropericlase solid solutions	64
5.2	[Fe,Mg]O LH-mDAC at the ECB P02.2	68
5.3	Combining the diamond anvil cell and European XFEL,	71
6	Discussion	74
6.1	P02.2tool vs. Dioplas	74
6.2	Stress and strain in cubic metals: Pt, Au	76
6.3	The effect of high strain rates on hcp metals and [Fe,Mg]O	81
6.3.1	Zinc	81
6.3.2	Rhenium	83
6.3.3	Iron	88
6.3.4	Wüstite, Periclase solid solutions	90
6.4	Laser heating	92
7	Summary and implications	95
8	Outlook	99
	Bibliography	101
	Appendix	119
	Register of abbreviation	123
	Curriculum vitae	125
	Acknowledgements	129
	Statement of authorship	131

List of Figures

1.1	The Earth interior	1
2.1	The structure of a crystal	5
2.2	The correlation of plastic and elastic deformation	6
2.3	The stress tensor	7
2.4	Independent elastic constants	8
2.5	The elastic modulus surface	8
2.6	Overview of point defect types in a crystal structure	9
2.7	Principles of linear creep mechanism	10
2.8	Screw and edge dislocation	10
2.9	Mechanism of grain boundary sliding	11
2.10	The effect of stacking faults and twinning	11
3.1	The diamond anvil cell (DAC)	17
3.2	The different diamond anvils	18
3.3	Pressure determination using Ruby or Raman shift	19
3.4	Schematic of the development of texture (LPO)	21
3.5	Principles of radial diffraction in DAC	22
3.6	Line-shift analysis: The gamma plot	23
3.7	Line-shift analysis: d -spacing under hydrostatic conditions	24
3.8	Line-width analysis	25
3.9	Schematic of the effect of pressure transmitting media	25
3.10	The effect of high load on the diamond anvils: Diamond cupping	27
3.11	Schematic drawing of the original mDAC setup	28
3.12	Schematic drawing of the original design of the dDAC	29
3.13	Current dDAC design	30
3.14	The basic theory of X-ray diffraction	30
3.15	The reason of the synchrotron ring	31
3.16	Schematic drawing of the on-axis laser heating setup at ECB P02.2	32
3.17	The SASE process	33
4.1	The Wüstite (FeO) phase diagram	35

4.2	The Large volume pressure assembly (LVP)	36
4.3	Photographs of the SEM sample observation	38
4.4	The Rotary evaporator setup	39
4.5	Schematic drawing of the random ionic volume diffusion of particles	40
4.6	Speeding up the diffusion: The effect of grain boundaries	41
4.7	Schematic overview of the gas-mixing furnaces at BGI	43
4.8	Representative results from Mössbauer spectroscopy	44
4.9	Powder diffraction pattern of synthesized (Fe,Mg)O solid solutions	45
5.1	X-ray diffraction raw data images of the Perkin Elmer XRD 1621	48
5.2	Contour plot of Re and Pt in mDAC	48
5.3	X-ray diffraction raw data images of the LAMBDA GaAs 2M detectors	49
5.4	Contour plots of Fe ₁₀ Mg ₉₀ O in dDAC	49
5.5	Micro-strain and pressure development of Pt in mDAC	51
5.6	Micro-strain and pressure development of Pt in dDAC	51
5.7	Micro-strain and grain size evolution in Pt	52
5.8	Differential stress evolution in Pt	52
5.9	Lattice parameter development of Re as a function of relative volume	54
5.10	Micro-strain and pressure development of Re in mDAC and dDAC	54
5.11	Micro-strain and compression rate development of Re	55
5.12	Grain size evolution in Re	55
5.13	Texture development in Re	56
5.14	Au dDAC fast compression raw X-ray diffraction images	58
5.15	Pressure and compression rate development during 0.5 ms Au exposures	58
5.16	Pressure and micro-strain evolution of Au during dDAC compression	59
5.17	Grain size and micro-strain evolution in Au	59
5.18	Au micro-stress and differential stress evolution as a function of pressure	60
5.19	Lattice parameter evolution of Zn as a function of relative volume	61
5.20	Micro-strain and pressure evolution during Zn compression experiments	62
5.21	Lattice parameter development of hcp Fe as a function of relative volume	63
5.22	The micro-strain and pressure evolution of Fe during dDAC compression	64
5.23	The pressure and compression rate development of MgO	64
5.24	Volume development of Fe ₁₀ Mg ₉₀ O and Fe ₄₀ Mg ₆₀ O	65
5.25	Bulk modulus evolution of Fe ₁₀ Mg ₉₀ O and Fe ₄₀ Mg ₆₀ O	66
5.26	The c and a-axis evolution of FeO during the B1 to rB1 transition.	66
5.27	Pressure, micro-strain and compression rate evolution in ferroperricite and wüstite	67
5.28	Raw XRD and azimuthal integration of (Fe ₂₀ ,Mg ₈₀)O during high PT	68
5.29	Volume evolution of (Fe ₂₀ ,Mg ₈₀)O as a function of pressure	69
5.30	Bulk modulus development of (Fe ₂₀ ,Mg ₈₀)O during High-PT	70

5.31	Raw XRD image of LaB_6 , calibrating the AGIPD detector	71
5.32	Volume development of Pt and $\text{Mg}_{10}\text{Fe}_{90}\text{O} + \text{Pt}$ at 2.25 MHz repetition	72
5.33	Streak camera observation of the black body radiation at HED	72
5.34	Pulse resolved volume development of Pt at 2.25 MHz	73
5.35	Melting of Pt and Magnesiowüstite during laser heating	73
6.1	Micro-strain evolution of Re based on the azimuthal integration with Dioptas and P02.2tool	75
6.2	FWHM evolution of Re based on the azimuthal integration with Dioptas and P02.2tool	75
6.3	Strength of Pt during mDAC and dDAC compression	77
6.4	Strength of Au during dDAC compression	79
6.5	Strength of Pt and Au in Neon	80
6.6	Evolution of the Zn axial ratio across the initial compression intervals	82
6.7	The c/a axial ratio of Re in mDAC and dDAC experiments	84
6.8	Texture development during Re compression in Ss gasket	85
6.9	The micro-stress evolution in Re	87
6.10	Development of the iron bcc-hcp phase transition	88
6.11	The c/a axial ratio of all Fe during dDAC compression	89
6.12	Representative X-ray diffraction image series of iron	89
6.13	Volume development of $\text{Fe}_{10}\text{Mg}_{90}\text{O}$ and $\text{Fe}_{40}\text{Mg}_{60}\text{O}$	90
6.14	The compression rate dependence of bulk modulus evolution in ferropentlandite	91
6.15	The B1-rB1 transition of wüstite	92
6.16	$\text{Fe}_{20}\text{Mg}_{80}\text{O}$ volume evolution as a function of pressure using KCl and Pt EoS	93
8.1	rB1 \rightarrow B1 transition during Laser heating of $(\text{Fe}_{90},\text{Mg}_{10})\text{O}$	99
2	Lattice parameter evolution of consecutive ramps of Zn as a function of relative volume	121
3	The temperature development during the laser heated mDAC experiments	121
4	The c/a axial ratio in consecutive Re compression cycles	121
5	The thermal stress distribution and displacement-induced deformation of Pt	122

List of Tables

4.1	Overview of the ferropericlasite synthesis in literature	36
4.2	Experimental parameters of the LVP experiment	37
4.3	SEM mass spectrum	37
5.1	Run summary	46
5.2	Summary of the EoS and other parameter	47
5.3	Overview of the Pt runs at ECB P02.2	50
5.4	Overview of the Re runs at ECB P02.2	53
5.5	Overview of the Au runs at ECB P02.2	57
5.6	Overview of the Zn runs at ECB P02.2	61
5.7	Overview of the Fe runs at ECB P02.2	63
5.8	Overview of the (Fe,Mg)O and endmember runs at ECB P02.2	65
5.9	Overview of the laser heated (Fe,Mg)O runs at ECB P02.2	68
1	Summary of all the gas-mixing runs performed at BGI	120

A distributed system is one where the failure of some
computer I've never heard of can keep me from getting my work done.
– *Leslie Lamport*

Chapter 1

Introduction

1.1 High-pressure as a dynamic system

Direct samples of the conditions in the Earth's interior are limited to the shallow region of the Earth interior, by diamond inclusions, melt- or volcanic activities, mantle orogens and peridotites. Further knowledge of the composition at greater depth has been obtained by meteorite/asteroid samples [1], or the recovered material at the lunar landing sites. Nevertheless, they resulted in robust numerical models and theoretical calculations directly comparing to seismic wave measurements.

In 1992, the first planetary body orbiting another host star was discovered [4]. Since then, 4375 exoplanets have been confirmed, their masses smaller, or far exceeding our Earth's [5] (as of the 07.04.2021). These discoveries have given rise to the question of the structures, dynamic processes and terrestrial evolution at a variety of conditions expected in their interiors, with our only reference being our Earth's interior [Fig. 1.1]. The last century has given a rise to a rapid evolution in both static and dynamic high-pressure and high-temperature experimental techniques. Those developments occurred more or less in parallel to the increasing X-ray brightness and brilliance at Synchrotrons and, recently, X-ray

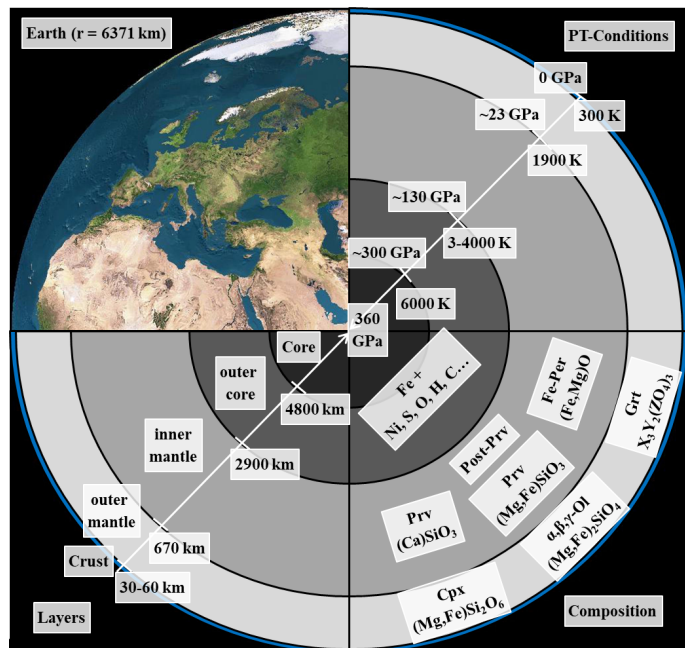


Figure 1.1: Schematic representation of the Earth interior. Abbreviations: Per = periclase; Prv = perovskite; Grt = garnet; Cpx = clinopyroxene; α, β, γ -Ol = olivine, wadsleyite and ringwoodite; modified after [2, 3].

Free-Electron Laser facilities [6, 7]. The evolution enabled profound, direct and simple "windows" to perform measurements at conditions in the Earth's deep interior and thus the possibility to verify models, seismic observations and predictions: For example, the 410, 530 and 660 km discontinuity as the most likely transition zone of *olivine* \rightleftharpoons *wadsleyite* \rightleftharpoons *ringwoodite* \rightleftharpoons *perovskite* + *periclase* [8].

However, due to the available compression/strain rates and the observed timescales, common dynamic and static compression techniques represent two extremes of the material behaviour. Dynamic, respectively, shock compression experiments act on ns-ps time scales (simulating e.g. asteroid impacts) with compression/strain rates of $> 10^5 s^{-1} - 10^8 s^{-1}$, whilst static techniques, like anvil compression, create long lasting, hydrostatic conditions (e.g. Earth's and planetary interior) with strain rates $< 10^{-3} s^{-1}$. Both techniques complement each other, yet the behaviour at intermediate compression rates [9], $10^{-3} s^{-1} - 10^5 s^{-1}$, (simulating e.g. large body impacts, planetesimal collisions, or earthquakes) are unreachable by established techniques. Because of the different behaviour of material at given compression rates a direct comparison of static and dynamic data was not possible and restricted the analysis and interpretation.

In 2007, the piezo-driven dynamic diamond anvil cell approach of *Evans et al.*, [10] was presented, followed in 2014 by a modification of the membrane diamond anvil cell [11]. Both techniques enable experiments at these intermediate compression rates. At first they were limited to optical methods such as rapid microphotography [12, 13, 14], but nowadays it is possible to use X-ray structural resolved analysis by means of new fast detectors (e.g. LAMBDA GaAs 2M, PILATUS 1M-F, or EIGER 1M) [15, 16] at third generation synchrotron sources (e.g. APS, or PETRA III). Due to those developments, it is possible to investigate strain rate dependent phenomena such as growth rate, morphology formation, deformation mechanism, transition onset and metastable or intermediate phases at compression rates between those of common static and dynamic/shock experiments. In recent experiments, compression rates were found to: 1. affect the amorphization pressure of plagioclase [17]; 2. lead to the formation of high dense amorphous ice [13]; 3. change the crystal growth mechanism which results in a new morphology in ice VI phase [12, 18]; 4. enables a selective phase transition path in L-Serine [19] or 5. stabilizes metastable hcp-krypton or methane hydrates [14, 20]. Furthermore, first experiments investigate the effect of the compression rate on the phase diagram of Bismuth [21] or the formation of coesite and stishovite of α -quartz [22] were performed. Their observations correlate with the recent findings in dynamic/shock compression experiments by *Schoelmerich et al.*, 2020 [23], which report hindered complex structural changes and the persistent stability of stishovite to pressures exceeding 300 GPa. Moreover, a martensitic phase transition of B1 to B2 KCl was studied in terms of (effective) activation energy [16] as a function of compression rate and it shows a linear relationship between compression rate and prominence/sharpness of the transition. The increased time resolution of the detectors

and the possibility to create conditions representative to seismic wave propagation have also been used [24, 25, 26]. Thereby, *Mendez et al., 2021* [26] reports the development of the H₂O bulk modulus up to 180 GPa and across three phase transitions, while *Marquardt et al., 2018 and Marquardt et al., 2021* [24, 25] investigated the bulk modulus softening in ferropericlase (Fe,Mg)O, which is associated with the iron spin crossover as well as the dependence of its onset to the imposed compression rates.

Nevertheless, dynamic compression, either by piezo-actuator, or rapid mDAC drivers, are novel tools/techniques and interpretation of the obtained data requires an understanding of the deformation mechanism, elastic and plastic, and their changes during the various compression rate. Furthermore, observable compression rates are still limited by 1: the amount of photons of a given wavelength and direction that can be concentrated onto the sample per unit of time (source brilliance); 2: the diffraction intensity across the short exposures and 3: the required exposure times of the detectors.

This work is a benchmark study investigating the effect of various compression rates in diamond anvil cell experiments. The following chapters describe the methods, tools, samples and results of the fast compression studies in DACs performed at the ECB P02.2 beamline PETRA III and the first commissioning results at the HED instrument, European XFEL, enabling an increased source brilliance compared to synchrotron facilities and detectors capable of 4.5 MHz image acquisition rates [27]. Chapter 2 presents the fundamentals of high-pressure and high-temperature conditions, whilst chapter 3 introduces the diamond anvil cell, the instrumental setups and methods used in the course of this study. Chapter 4 describes the choice of samples, their quality, origin and the synthesis of ferropericlase (Fe,Mg)O solid solutions. Followed by the experimental results in chapter 5 and the discussion of the effect of compression rates on the kinetic response of materials in chapter 6. Finally, the results and implications of the technique and the advancement of XFEL facilities are drawn in the last section with an outlook and suggestions for a possible future research on the topic.

Chapter 2

High P-T: The properties of material

In general, high-pressure and high-temperature experiments are trying to reproduce conditions where direct samples are missing (e.g Earth's mantle, exo-planets, asteroid impacts). Theories and models are depending on the quality of experimental data and their uncertainties. Thus, results of high P-T experiments can be associated with a modification of the nominal definitions of the language, e.g. pure iron Earth's core = uncertain mixture of all the elements, or certain = dubious [28]. High P-T experiments try to simulate not only the pressure and temperature conditions of Earth's interior, exoplanets, or large scale impacts, but also try to match time scales of compression, temperature uniformity/gradient, hydrostaticity, the phase- and the chemical equilibrium associated with the PT conditions [6]. A remarkable progress in the development of high P-T techniques has been achieved within the last decades accompanying the enormous rise in available source brilliance by Synchrotron and more recently soft and hard X-ray Free-electron Laser Facilities [7]. The progress enables accurate *in-situ* measurements for a variety of chemical and physical properties such as crystal structure, element partitioning, radiative heat transfer, spin state, solubility, amorphization and melting, equation of state, oxidation state, density, wave velocity or thermal conductivity [6]. Two complementary experimental types (quasi-static and dynamic/shock) are commonly used to access a variety of high-pressure, high-and-low temperature conditions. On the one hand, the quasi-static compression confines the sample between anvils and even though the maximum pressure range is limited by the strength and the design of the anvil, its conditions can be kept for hours and even years. Different techniques are available for specific conditions [6], enabling sample sizes of centimeters in LVP down to some small number of single grains in the DAC. On the other hand, dynamic/shock compression experiments study the propagation of a shock-wave through a sample and they have to be compatible with the nanosecond duration of the shock-wave and enable the investigation of very high-P at simultaneously high-T conditions, but not high-P and low-T.

In this chapter the fundamentals of solid state physics and the dependence of physical para-

meters will be introduced: stress, deformation, temperature, pressure and time, which are required to understand the rheological behaviour of material properties exposed to various environmental conditions.

2.1 Definition of solids

A solid, respectively, crystal is build up by a regular, periodic and quasi-infinite crystal lattice based on three translation vectors \mathbf{a} , \mathbf{b} and \mathbf{c} which are also called basic vectors. Any point, representing an atom, in the crystal lattice can be defined by:

$$point = n_1 \mathbf{a} + n_2 \mathbf{b} + n_3 \mathbf{c} \quad (2.1)$$

where n_1 to n_3 ranges through all integral values (negative, zero, positive). Each of those points is identical with the others and will show the same structure, orientation and composition. The direction of a vector in the crystal lattice is designated as $[uvw]$ and further provides the distance between two identical point. Therefore, all equivalent directions (e.g. $[100]$, $[010]$, $[001]$, $[\bar{1}00]$, $[0\bar{1}0]$ and $[00\bar{1}]$ in a cubic crystal) can be written as a collective and are referred to as $\langle 100 \rangle$ directions in case of the cubic crystal example. In similar convention, individual but equivalent (100) , (010) and (001) planes in a cubic crystal can be written as $\{100\}$ planes. Those plane indices are designated as *Miller indices* (hkl) , representing the shortest vector normal to the plane, albeit in reciprocal space giving the equation:

$$h : k : l = \frac{1}{x_1} : \frac{1}{x_2} : \frac{1}{x_3} \quad (2.2)$$

where x_1 to x_3 are the intercept's integers of the crystal plane along the crystal axes [29] [Fig.2.1].

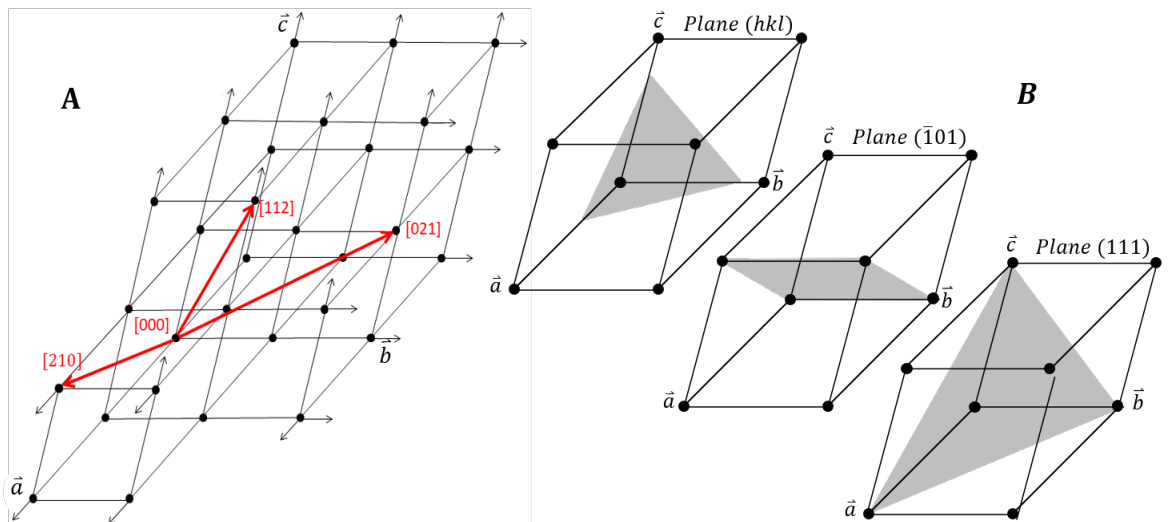


Figure 2.1: The structure of a crystal. A: All positions in the atom structure can be reached by the multiple of integers with the lattice spacing a , b and c . B: Miller indices and some examples of the resulting naming convention.

2.2 Introduction to rheology

The deformation behaviour of a solid body subjected to external forces is directly linked to its various solid state properties given by the periodic arrangement of atoms and can either be described by elasticity or plasticity (Fig 2.2). Elasticity determines the range of accumulable strain where recovery to its original state is still possible, whilst plasticity determines the stress range where strain leads to permanent deformations in the solid material. Both ranges are thermodynamically dependent on the specific heat capacity, thermal expansion, Debye temperature, Grüneisen parameter and melting temperatures of the solid. In addition, plasticity further depends on the shear modulus along active dislocations [30].

Within the Earth's interior the stress induced by the mass of the overlaying material results in a strain field that is assumed to be truly continuous. This strain field leads plastic deformation to become ductile deformation, meaning that although the material can maintain its coherence, it will undergo changes in size, shape and internal structure. In crystalline materials, the ductile deformation is controlled by motion of defects and local disruptions in the periodic arrangement of atoms, characteristic for every grain of crystalline substances [32]. A constitutive equation of strain ε [33, 34] can be used to express the ductile deformation of a crystalline material in terms of other parameters [32]:

$$\varepsilon = f(\sigma, T, P, S_i, M_j) \quad (2.3)$$

where σ is stress, T is temperature, P is pressure, S_i the microstructural parameters of the material (grain size, density of defects etc.) and M_j the material properties (lattice parameter, bond strengths, activation energy, etc.). As a result, the total strain ε will consist of several components combining the sum of all different deformation mechanism (e.g. [33, 34, 35]). Depending on the conditions Power-Law Creep, Linear Creep and Low-Temperature Plasticity and Power-Law Breakdown are considered to be the most relevant deformation mechanism in the Earth's interior [32].

At low stress levels and small grain sizes, Linear Creep dominates deformation due to its insensitivity to stress and sensitivity to grain size changes. At intermediate stress levels and medium to very high temperatures Power-Law Creep takes over [32] and the accumulated strain can be described by:

$$\dot{\varepsilon} = A\sigma^n d^{-m} \exp(-Q/RT) \quad (2.4)$$

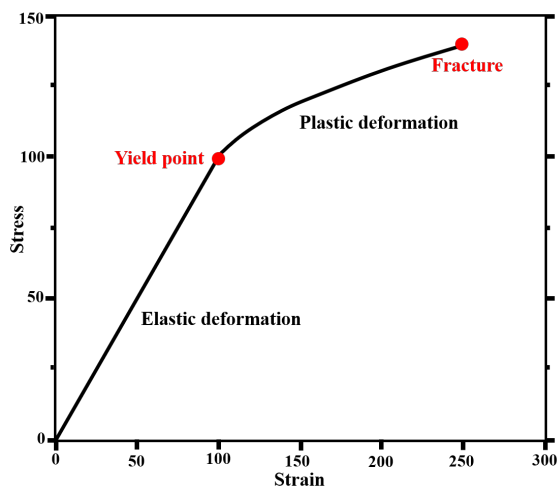


Figure 2.2: Deformation path of a crystal exposed to increasing external forces. Linear and recoverable elastic deformation at low stress level is replaced by non-linear plastic deformation. “Yield point” marks the stress conditions of first imminent deformation and “Fracture” the point of crystal breakdown (modified after [31]).

where A is a constant, n is a stress exponent, d is the grain size, m is the grain-size exponent, Q is the activation enthalpy ($Q = E^* + PV^*$), R is the ideal gas constant and T is the temperature. It is usually grain-size independent ($m = 0$), yet very sensitive to stress [35]. If the stress is increased further and at low temperature conditions, Low-Temperature Plasticity and Power-Law Breakdown become dominant [32].

2.2.1 Elasticity

A 2^{nd} -order tensor can be used to describe Stress, the reaction of a face exposed to an external force. The amount of stress induced to the face can be measured as strain within the crystallographic planes.

$$\sigma = \begin{bmatrix} \sigma_{11} & \sigma_{12} & \sigma_{13} \\ \sigma_{21} & \sigma_{22} & \sigma_{23} \\ \sigma_{31} & \sigma_{32} & \sigma_{33} \end{bmatrix}$$

The orientation of the stress tensor (Fig 2.3) and the amount of strain accumulated within the planes can be described by Hooke's Law [36] and is proportional to the magnitude of stress,

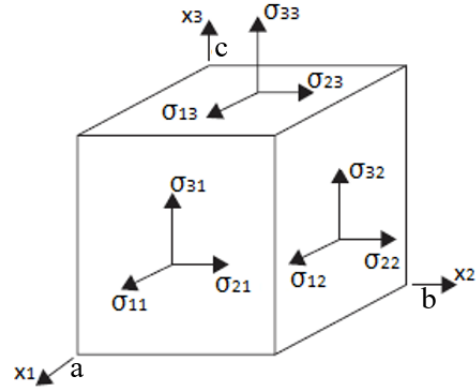
$$\varepsilon = s\sigma \quad (2.5)$$

or

$$\sigma = c\varepsilon \quad (2.6)$$

where s is the elastic compliance and c is the elastic stiffness of the solid. The elastic stiffness can be written as the inversion of the elastic compliance $c = \frac{1}{s}$.

Figure 2.3: Stress tensor components applied to a crystal (modified after [37]).



The elastic stiffness of a crystalline material is described by a 4th-rank tensor of single-crystal elastic constants (c_{ij} GPa) and can be expressed as a 6x6 matrix in correlation with stress and strain [38].

$$\begin{pmatrix} \sigma_1 \\ \sigma_2 \\ \sigma_3 \\ \sigma_4 \\ \sigma_5 \\ \sigma_6 \end{pmatrix} = \begin{pmatrix} c_{11} & c_{12} & c_{13} & c_{14} & c_{15} & c_{16} \\ c_{12} & c_{22} & c_{23} & c_{24} & c_{25} & c_{26} \\ c_{13} & c_{23} & c_{33} & c_{34} & c_{35} & c_{36} \\ c_{14} & c_{24} & c_{34} & c_{44} & c_{45} & c_{46} \\ c_{15} & c_{25} & c_{35} & c_{45} & c_{55} & c_{56} \\ c_{16} & c_{26} & c_{36} & c_{46} & c_{56} & c_{66} \end{pmatrix} \begin{pmatrix} \varepsilon_1 \\ \varepsilon_2 \\ \varepsilon_3 \\ \varepsilon_4 \\ \varepsilon_5 \\ \varepsilon_6 \end{pmatrix}$$

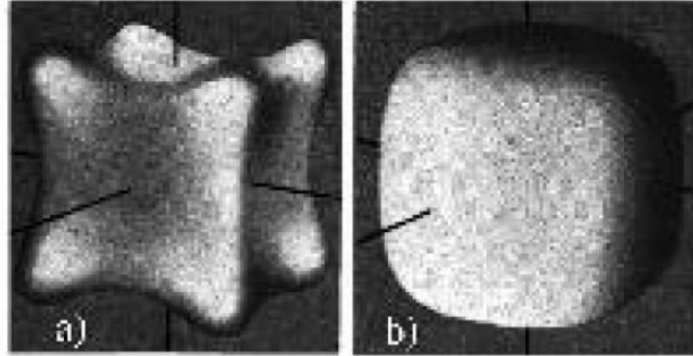
where, σ is the stress tensor, ε the strain tensor and c_{ij} individual single-crystal elastic constants. The single-crystal elastic constants are the most important parameter of elasticity and plasticity. They specify the directional deformation dependencies in a crystal [30] and are retrieved either by empirical or first-principle methods. The crystal symmetry restricts the number of independent elastic constants, allowing three at the highest – cubic – and 21 at the lowest – triclinic – symmetry [39]. The independent single-crystal elastic constants of the two extremes are shown as an example (Fig. 2.4).

Figure 2.4: Independent elastic constants within the highest (cubic) and lowest (triclinic) crystal symmetry [38].

Cubic 23, $m\bar{3}$, 432, $\bar{4}3m$, $m\bar{3}m$	Triclinic 1, $\bar{1}$
$\begin{pmatrix} c_{11} & c_{12} & c_{12} & 0 & 0 & 0 \\ & c_{11} & c_{12} & 0 & 0 & 0 \\ & & c_{11} & 0 & 0 & 0 \\ & & & c_{44} & 0 & 0 \\ & & & & c_{44} & 0 \\ & & & & & c_{44} \end{pmatrix}$	$\begin{pmatrix} c_{11} & c_{12} & c_{13} & c_{14} & c_{15} & c_{16} \\ & c_{22} & c_{23} & c_{24} & c_{25} & c_{26} \\ & & c_{33} & c_{34} & c_{35} & c_{36} \\ & & & c_{44} & c_{45} & c_{46} \\ & & & & c_{55} & c_{56} \\ & & & & & c_{66} \end{pmatrix}$

However, even within materials with similar crystal symmetry and structure, individual determination of the c_{ij} is necessary due to a large degree of freedom in the resulting elastic modulus shapes (i.e. Fig 2.5),

Figure 2.5: Difference of the ‘elastic modulus surface’ of gold (a) and aluminum (b), resulting from the single elastic constants. Both are cubic and have the space group $m\bar{3}m$ [40].



The single-crystal elastic constants provide the basis for different elastic moduli such as bulk modulus ($K_T =$ isothermal, or $K_S =$ adiabatic) and shear modulus. Those moduli are commonly used to describe the average elastic behaviour of a crystal, or of an aggregate [41]. The bulk modulus is defined as the tendency of an object to deform in all directions when subjected to a uniformly load, whereas, the shear modulus describes the object’s tendency to deform in shape whilst keeping a constant volume.

The moduli are expressed either as:

$$K_R = \left[\left(\frac{s_{11} + s_{22} + s_{33}}{3} + 2 \frac{s_{12} + s_{13} + s_{23}}{3} \right) / 3 \right]^{-1} \quad (2.7)$$

and

$$G_R = \left[\left(4 \frac{s_{11} + s_{22} + s_{33}}{3} - 4 \frac{s_{12} + s_{13} + s_{23}}{3} + (s_{44} + s_{55} + s_{66}) \right) / 5 \right]^{-1} \quad (2.8)$$

if the strain is assumed to be implied by uniform stress [42]

or as:

$$K_V = \left(\frac{c_{11} + c_{22} + c_{33}}{3} + 2 \frac{c_{12} + c_{13} + c_{23}}{3} \right) / 3 \quad (2.9)$$

and

$$G_V = \left(\frac{c_{11} + c_{22} + c_{33}}{3} - \frac{c_{12} + c_{13} + c_{23}}{3} + (c_{44} + c_{55} + c_{66}) \right) / 5 \quad (2.10)$$

if the stress is assumed to result in uniform strain [43].

In the conducted experiments neither the stress nor the strain are truly uniform and the measured moduli invariantly lay between both predictions of Voigt and Reuss. Thus, determining them as the upper and lower boundary conditions is only viable if either strain or stress are truly uniform. In order to address the difference in predictions and measurements, both equations have been brought into relation,

$$K_{VRH} = (K_V + K_R) / 2 \quad (2.11)$$

$$G_{VRH} = (G_V + G_R) / 2 \quad (2.12)$$

by calculations using nine of all independent 21 single-crystal elastic constants. Despite the resulting uncertainty for lower symmetry materials the results of the measurements and the predictions are in good approximation [41].

2.2.2 Defects: Plasticity and ductility

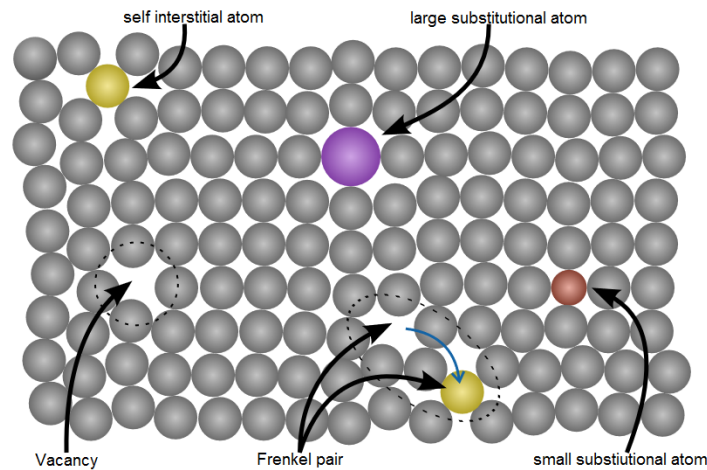


Figure 2.6: Overview of point defect types in a crystal structure: Vacancy, interstitial atoms (self-interstitial, Frenkel pair) and impurities (substitutional large, small atoms) [modified after DeniFeri – commons.wikipedia.org]

Plastic deformation, the cracking and fracturing of materials, becomes ductile deformation at the conditions of Earth’s interior, where the strain field is assumed to be truly continuous [32]. Furthermore, the impact deformation processes to some extent resembles ductile deformation, as time scales during the experiment are too short and the plastic deformation, meaning destruction of the sample, only happens after the experimental data have been collected. Plastic, respectively, ductile deformation is a macroscopic scale deformation based on the abundance of microscale defects, which raises the total energy state of the system. Thus, the systems strives to re-establish the lowest energy state by relocalizing or changing the abundance of defects, trying to maintain crystallinity in micro-scale regions and macroscopic coherence of the crystal. Those microscale defects can be assigned to three categories: point

defects, line defects or dislocations and planar defects [32].

The first category: point defects contain all types of lattice vacancies, atoms interstitial to the lattice plane, impurities and element substitutes (Fig 2.6). Point defects lead to diffusion creep, incorporating Linear creep to transport matter, or relocate stresses through the crystal. Dependent on the environmental conditions, either Nabarro-Herring-Creep [44] or Coble-Creep [45] dominate the transport through the crystal lattice (Fig 2.7). Nabarro-Herring-Creep dominates at high temperatures whilst Coble-Creep dominates at low temperatures, where intergrain transport is limited by higher lattice frictions [32].

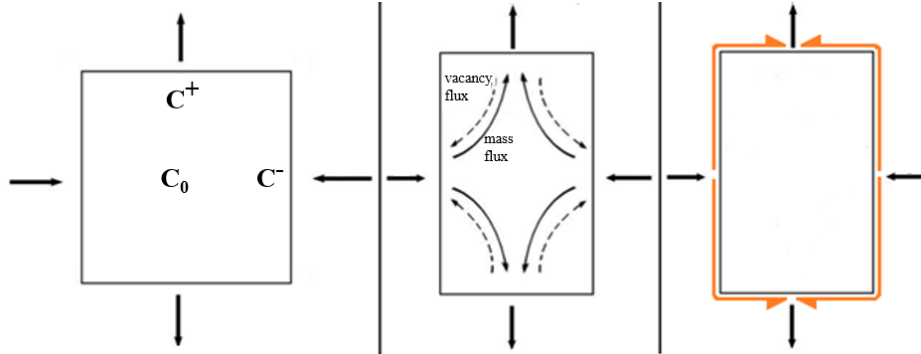


Figure 2.7: Principles of linear creep mechanisms in a cube shape crystal subjected to tensile stress on a pair of faces. (Left) Flow directions of matter, C^+ increase of matter and C^- decrease of matter; (Center) Nabarro-Herring-Creep, tensile stress on two faces leads to generation of defects allowing creep transport towards these faces [46]; (Right) Coble-Creep, transport through the crystal is limited due to lattice friction, thus matter is transported alongside the grain boundaries (modified after [32]).

The second category: Line defects or dislocations are the most common cause for plastic deformation associated to Power-Law-Creep (Eq. 2.4) [47]. It is the most energetically economic way to deform under an applied stress σ and each of the dislocations is associated with a crystallographic slip vector, called Burgers vector \vec{b} , indicating the interatomic distance of a slip motion [46]. Two defined types of dislocations exist as a result of their orientation to the Burgers vector (Fig. 2.8): Screw dislocations, running parallel to \vec{b} , and edge dislocations, running perpendicular to \vec{b} .

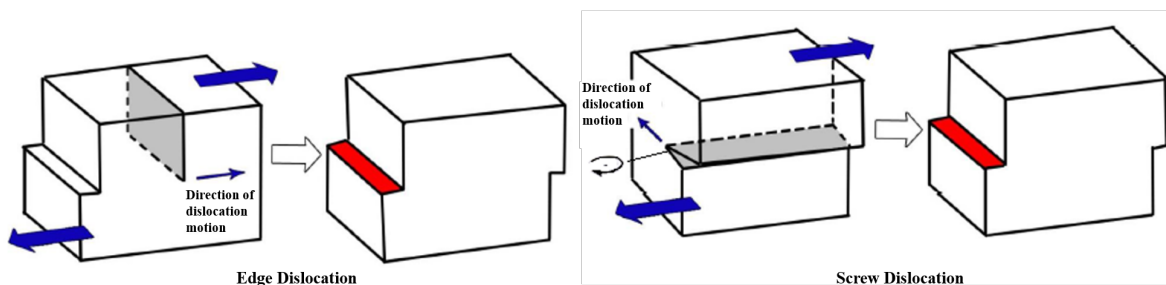


Figure 2.8: Edge (Left) and screw (Right) dislocation leading to a slip of the crystal lattice plane. The dislocation sweeps through the crystal creating a step of length \vec{b} (red) in the structure (modified after [46]).

Those represent the extremes. More common dislocations containing both components are referred to as mixed dislocation. Screw dislocations move by slip, breaking the atomic bonds ahead of their path and restoring the periodic arrangement behind themselves. It is the most simple and mass conservative motion, whereas edge dislocations and "mixed dislocations"

further entail non-conservative climbing movements "out of" its glide plane, requiring the diffusion of neighbour atoms towards or away from the dislocation. However, all of those motions lead to an extension of slipped areas generating new surfaces with length \vec{b} once the dislocation steps out of the crystal [32].

The third and last category: Planar defects involve both mechanism, Linear-Creep and Power-Law-Creep. The most abundant planar defects are grain boundaries, thin layers of point defects and dislocations, allowing not only mass transport in a crystalline material but also grain boundary sliding [2.9] and grain relocation. They enable the fast distribution and take an account of most of the accumulated strain [32]

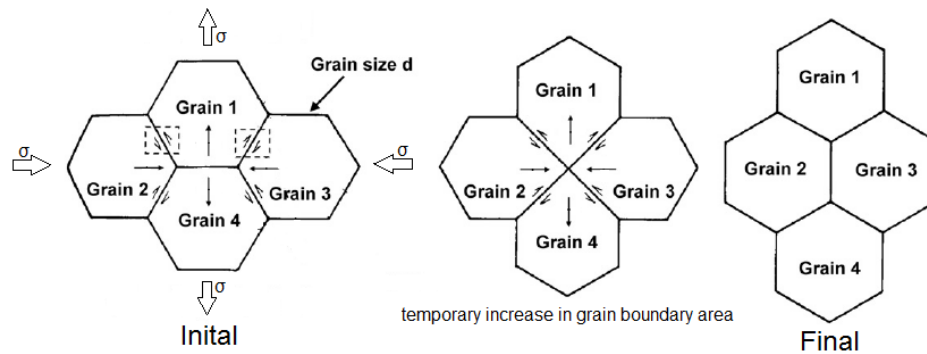


Figure 2.9: Grain boundary sliding during uniaxial compression. Initial state (Left), activating grain boundary sliding due to uniaxial stress; Temporary grain boundary area increase due to deformation along the grains (Center); Final state (Right), stress has been removed of the crystal by reordering of grains (modified after [48]).

Further planar defects are stacking faults and twin-growths (Fig 2.10). Stacking faults are interruptions of the periodic stacking sequence of atom planes, where twins are generated by accumulation of those stacking faults, or dislocations leading to lateral displacement along the glide planes of the crystal. Thus, the total displacement is taken up by small increments at each of the lattice rows [49].

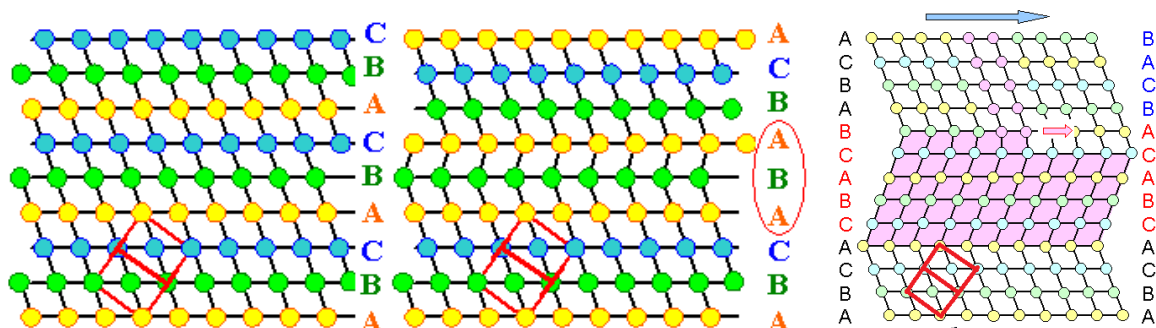


Figure 2.10: Stacking fault and twinning in cubic face centered (fcc) layered system. (Left) Initial periodic ABCABC... stacking sequence; (Centre) Stacking fault leading to a hexagonal close packed (hcp) stacking sequence within the fcc sequence: ABCABABC; (Right) Deformation twinning based on small displacements of many lattice planes leading to a large displacement along the glide plane (modified after tf.uni-kiel.de)

2.3 Equation of State

Equations of state (EoS) are semi-empirical equations used to account for the functional relationship of material properties. These functions usually link the thermodynamic state of a system, defined by pressure, temperature and sample properties (volume or density), allowing interpolation and extrapolation of the systems behaviour [46, 50]. Thereby, EoS provide an excellent tool to link the macroscopic observations (e.g. shock wave propagation after an earthquake, or impact) and the microscopic world of atomic structures.

As we are trying to understand high-pressure and high-temperature influences on solid material the total free Helmholtz energy $F_{V,T}$ consists of three independent compounds:

$$F_{V,T} = F_s(V) + F_{vib}(V, T) + F_{el}(V, T) \quad (2.13)$$

where F_s is cold compression, meaning static lattice energy, F_{vib} the atomic vibration energy and F_{el} the thermodynamic excitation energy of the electrons. Unless very high compression of metals has to be considered (e.g. shock compression experiments [51]) the electronic component can be neglected, resulting in an isothermal and a temperature dependent free energy component. Pressure is obtained by the derivative of the free Energy:

$$P = - \left(\frac{\delta F}{\delta V} \right)_T \quad (2.14)$$

and results in

$$P_{V,T} = P_{298K}(V) + P_{th}(V, T) \quad (2.15)$$

At ambient temperatures the Birch–Murnaghan EoS [52] is the most common formulation of EoS and is accurate at low to moderate strain rates of up to 30 % [50]. Its formulation varies with the relation between the experimental pressure condition and resulting strain. A Linear relation can be explained using 2nd-order Birch-Murnaghan EoS:

$$P = \frac{3}{2} K_0 \left[\left(\frac{V_0}{V} \right)^{\frac{7}{3}} - \left(\frac{V_0}{V} \right)^{\frac{5}{3}} \right] \quad (2.16)$$

whereas non-linear relations require either 3rd-order 4th-order Birch Murnaghan EoS:

$$P = 3K_0 f_E (1 + 2f_E)^{\frac{5}{2}} [1 + a_1 f_E + a_2 f_E^2] \quad (2.17)$$

$$a_1 = \frac{3}{2} [K_0' - 4] \quad (2.18)$$

$$a_2 = \frac{3}{2} \left[K_0 K_0'' + K_0' (K_0' - 7) + \frac{143}{9} \right] \quad (2.19)$$

and

$$f_E = \frac{1}{2} \left[\left(\frac{V_0}{V} \right)^{\frac{2}{3}} - 1 \right] \quad (2.20)$$

where P represents the pressure in GPa, f_E the Eulerian strain, K_0 , K_0' , K_0'' , V_0 , and V the bulk modulus (GPa), its first and second derivatives, ambient pressure volume (\AA^3) and

volume (\AA^3) under compression.

Other common equation of state are the Vinet EoS [53, 54] and Holzapfel EoS [55], which are base on the approximation of internal energy (binding energy and electron bond length).

$$P = 3K_0 \left(\frac{1-x}{x^2} \right) \exp \left[\frac{3}{2} (K_0' - 1)(1-x) \right] \quad (2.21)$$

and

$$P = 3K_0 x^{-5} (1-x) \exp [(cx + c_0)(1-x)] \quad (2.22)$$

where $x = (V/V_0)^{\frac{1}{3}}$, c and c_0 are determined by K_0' and the Fermi gas behaviour for $x \rightarrow 0$. The Vinet EoS allows determination of the sample properties up to high strain rates whilst the Holzapfel EoS is only recommended at extreme compression [50].

Changing temperature within an experiment, e.g in this study by means of laser heating, has a large impact on the EoS. EoS are specific and reliable only at the P-T conditions they were acquired and the largest amount of literature EoS has been obtained at ambient temperature. Temperature increase changes the total free Helmholtz energy $F_{V,T}$ in the system by the factors $F_{vib}(V,T)$, respectively, $P_{th}(V,T)$ and $F_{el}(V,T)$, respectively, $P_{el}(V,T)$. Therefore, those parameter have to be taken into account when using EoS to determine the pressure across high-T experiments.

The thermal pressure $P_{th}(V,T)$ [Pa] can be determined by the Mie-Grüneisen-Debye (MGD) approach using the Mie-Grüneisen equation [56, 57, 58, 59, 60]]:

$$P_{th} = \frac{\gamma}{V \times 10^{-30} \times N_A} (E(T, \Theta_D) - E(T_{ambient}, \Theta_D)) \quad (2.23)$$

where γ is the Grüneisen parameter is only a function of the volume:

$$\gamma = \gamma_0 \left(\frac{V}{V_0} \right)^q \quad (2.24)$$

Furthermore, V is the observed volume within the unit cell in \AA^3 , N_A the Avogadro constant, $E(T, \Theta_D) - E(T_{ambient}, \Theta_D)$ the increase in thermal energy and q the development of γ/V [61]. The thermal energy can be written with the help of the Debye model:

$$E(T, \Theta_D) = 9nRT \left(\frac{T}{\Theta_D} \right)^3 \int_0^{\Theta_D/T} \frac{z^3 dz}{e^z - 1} = 3nRTD(x) \quad (2.25)$$

where n is the number of atoms per unit cell, R the gas constant and $D(x)$ the Debye integral:

$$D(x) = 3/x^3 \int_0^x \frac{z^3 dz}{e^z - 1} \quad (2.26)$$

with $x = \Theta_D/T$ and Θ_D dependent on the Grüneisen parameter and volume variation:

$$\Theta_D = \Theta_{D_0} \left(\frac{V}{V_0} \right)^{-\gamma} \quad (2.27)$$

However, $D(x)$ can not be solved without knowing the heat capacity, acoustic velocities, or Debye temperature at the observed P-T condition. Furthermore, those information are scarce

even at conditions in the Earth's mantle and linear approximations of the Debye function are needed to obtain fits, with an uncertainty of a few percentages [58], even without the exact heat capacity knowledge [57]. Following the approximation by *Jue Wang, 1989* [62] and using the obtained $x = \Theta_D/T$ ratios from our *in-situ* observations results in the $D(x)$ relation:

$$D(x) = \frac{(((0.0946173x - 4.432582)x + 85.07724)x + 800.6087)x + 3953.632}{(((x + 15.121491)x + 143.155337)x + 682.0012)x + 3953.632} \quad (2.28)$$

and allows for a direct calculation of P_{th} .

The electronic thermal pressure $P_{el}(V,T)$ is given by [63, 64]:

$$P_{el}(V,T) = - \left(\frac{\delta \Delta f_{el}(V,T)}{\delta V} \right)_T \quad (2.29)$$

Here, Δf_{el} is the temperature dependent contribution to the electronic free energy density $f_{el}(V,T)$, written as:

$$\Delta f_{el} = (u_{el}(V,T) - Ts_{el}(V,T)) - (u_{el}(V,T=0) - Ts_{el}(V,T=0)) \quad (2.30)$$

where u_{el} and s_{el} are the total electronic energy density, respectively, entropy density of the material. However, those quantities need to be calculated based on the electron density of a state $n(\epsilon, V)$ and depend on the electronic specific heat capacity and the Fermi-Dirac distribution function:

$$c_{vel} = \left(\frac{\delta u_{el}}{\delta T} \right)_V \text{ and } f(\epsilon, V) = \left(\frac{1}{\exp^{(\epsilon-\mu)/k_B T} + 1} \right) \quad (2.31)$$

with k_B the Boltzmann constant. Compared to the contributions of $P_{298K}(V)$, P_{th} the electronic component is very small, nevertheless, it can compensate slight pressure differences observed at higher T [64] and should be included/added to the final pressure estimation if known.

Nonetheless, this thermal EoS requires knowledge of the achieved temperatures across the experiment and general tools to observe *in-situ* temperature are based on the thermal radiation of any object emitted by the random motion of their constituent atoms, or by calibrated direct reading of thermocouples. The calculations of thermal radiation depend on the corrected emission spectra using either Planck's radiation law [29] for black bodies, absorbing all radiant energy falling upon them without reflection:

$$I_s(\lambda) = \frac{2\pi hc^2}{\lambda^5} \times \left(\frac{1}{\exp\left(\frac{hc}{\lambda k_B T}\right) - 1} \right) \quad (2.32)$$

or Wien's displacement law, determining the wavelength, or frequency of the maximum spectral intensity of the Planck's law at a specific temperature [65]:

$$\lambda_{max} = \frac{0.002897 \text{ m K}}{T}; f_{max} = 5.879 \times 10^{10} \frac{\text{Hz}}{\text{K}} T \quad (2.33)$$

where λ is the wavelength, c the speed of light, h the Planck's constant, k_B the Boltzmann constant and f the frequency.

Planck's law refers to an ideal blackbody, yet real objects do not radiate with the ideal properties but with a lower emissivity expressed as $\varepsilon < 1$, where $\varepsilon = 1$ equals the ideal blackbody state. Fortunately, most of those objects, e.g. rocks, wood and most non-metallic surfaces, have a high emissivity around > 0.85 and a simple adjustment can be made:

$$I_s(\lambda) = \varepsilon(\lambda, T) \times I_s(\lambda)_{Ideal} \quad (2.34)$$

2.4 The 'gap' between static and shock compression experiments

Experimental pathways to reach high-pressure are either dynamic or static approaches. On the one hand, dynamic, or shock compression experiments use the likes of gas guns, lasers and magnets to accelerate a projectile onto the sample and probe the properties of material by the resulting shock wave propagation and particle velocity [10]. They are very rapid, lasting only a fraction of a microsecond and reach in unison high-pressure and high-temperature conditions of up to several hundreds of GPa and several thousands of Kelvin (i.e. [66, 67]). Thereby, enabling for example density, pressure and enthalpy determination by following the Rankine-Hugoniot equations [68]:

$$\rho_0 U_S = \rho_1 (U_S - u_p) \quad (2.35)$$

$$P_1 - P_0 = \rho_0 (U_S - u_0)(u_p - u_0) \quad (2.36)$$

and

$$e_1 - e_0 = \frac{1}{2}(P_1 + P_0)(V_1 - V_0) \quad (2.37)$$

where P, e, V, ρ describe pressure, energy, volume and density of the sample. Thereby, the subscripts $_0$ refers to the ambient, respectively starting and $_1$ to shocked state conditions, $V = \frac{1}{\rho}$ is the specific volume and U_S, u_p are the shock and particle velocity. Those relations assume no heat conduction, due to the very short time interval of impact and shock events and are referred to as the Rankine-Hugoniot-relations. If the starting conditions are assumed to be at atmospheric pressure, P_0 becomes negligible and its particle velocity u_0 will also become ≈ 0 resulting in (Eq. 2.36) which can be expressed as:

$$P_1 = \rho_0 U_S u_p \quad (2.38)$$

where $\rho_0 U_S$ is called the shock impedance at given pressure [68]. To be able to describe all parameters (P, e, V, U_S, u_p) as a function of one of them an additional equation has to be

included that assumes for example a linear relation of the Hugoniot EoS for most materials [69]:

$$U_S = C_0 + Su_p \quad (2.39)$$

where C_0 and S are predetermined the constant related to the bulk wave speed and the entropy in the system.

However, shock experiments are destructive, resulting in a single shot requirement of the sample material. Additionally, the short experimental time interval limits the diagnostic possibilities [10]. Furthermore, shock experiments result in a pressure and temperature dependence leading to relatively high-temperatures compared to those suggested for the geothermal gradient in the Earth, or in terrestrial exoplanets (i.e. [66]).

Whilst on the other hand, static experiments are using anvils to apply a given force onto the sample material, enabling nearly infinite data collection time and extensive analysis with a variety of non-destructive techniques (i.e. X-ray emission spectroscopy, Brillouin spectroscopy, X-ray diffraction), keeping the pressure conditions constant for days to weeks. The maximum pressure achievable is again up to several hundreds of GPa [70], routinely ≈ 300 GPa [71], where temperature possibilities are < 1 to a few thousands of Kelvin [72, 73, 74].

Both techniques have developed into powerful complimentary tools enhancing the knowledge of material properties under extreme conditions. Nevertheless, the extreme variety in timescales and the missing possibility to explore slow and intermediate compression rates (between 10^{-2} s^{-1} to 10^5 s^{-1} [9]), prevent direct comparison of their experimental results. Recent developments of the membrane diamond anvil cell (mDAC), the piezo-driven dynamic diamond anvil cell (dDAC) [10], or the rapid compression mDAC [11] are the first tools to explore those intermediate compression rates and are opening up the conditions between static and dynamic experiments, via microphotography, or direct X-ray structural probing, using novel fast detectors and high brilliance X-ray source facilities.

Chapter 3

The diamond anvil cell (DAC) and X-ray diffraction

3.1 Introducing the DAC

The diamond anvil cell (DAC) has been established as one of the primary tools to investigate materials under high-static pressure and at over 100 GPa, since its development in the early 60s [75], reaching from Earth and planetary science [23], over material science [76], physics [77] and chemistry [78] to biology [79]. Generating these conditions routinely and in combination with the needs of e.g. spectroscopy or diffraction has lead to the development of different types of cells: Mao-Bell-type [80]; Merrill-Bassett-type [81] and Boehler-type DAC [82]. These days, standard DAC assemblies (Fig, 3.1) fit easily in one hand and reach ≈ 300 GPa routinely, generating up to a maximum 400 GPa [71]. Thus, enabling exploration across the whole pressure range of the Earth's interior, up to 360 GPa at the inner core, either using standard or beveled diamonds (Fig. 3.2).

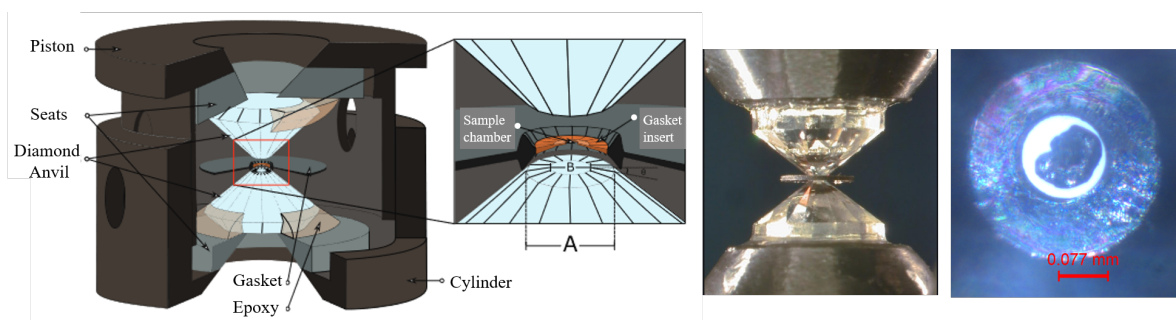


Figure 3.1: Overview of a symmetric diamond anvil cell (DAC) assembly and its basic compounds: Piston, Cylinder, Seats, Diamond anvils, Gasket and Epoxy. From left to right: Basic setup (modified after [83]), aligned diamonds and supporting Gasket (courtesy S. Merkel), loaded sample.

The main principle of the DAC is based on two flat topped diamonds precisely aligned to face each other with their culets (Fig 3.1). Measurement methods using their transparency over the ultraviolet, visible, infrared and X-ray spectral range allow to *in-situ* observe a sample contained between both anvils. The diamond anvils are glued to seats, here we are using a mixture of (Brand: Catalyst and resin), to ensure proper pre-orientation, which likewise are

tightened to a larger cell body (Fig 3.1)). Those alignment steps are crucial for the later experiment, because an eventual inaccuracy of the diamond alignment will result in diamond failure at low pressure, due to the strong anisotropy of diamonds, hence its instability under high shear stresses [i.e.[84, 85, 86, 87, 88]]. A metal gasket is placed between the parallel anvil culets in order to prevent them from bumping against each other, in order to support the anvils and to obtain a container for the sample. Commonly used gasket materials are rhenium (Re), tungsten (W), beryllium (Be) or stainless steel (SS). In more specific cases, like radial X-ray diffraction, amorphous boron and epoxy gaskets are required. The incoming radiation has to travel through the gasket material, hence the requirement for X-ray transparency. The gasket is either pre-pressurized roughly to half of the expected pressure in the experiment, or pre-determined to a certain thickness corresponding to the chosen sample chamber height. This process leaves imprints of the diamond culets in the gasket material, here after called indentation. The indentation depth, or pre-pressure implied can be roughly followed by a ruby chip placed on one of the diamond culets before pressurization.

In the center of the indentation a hole, as a rule of thumb between $\frac{1}{3}$ to $\frac{1}{2}$ of its diameter, is drilled to form a chamber for sample loading, either by use of an electron-discharge machine (EDM; e.g. by Betsa or Thorlabs), or an infrared laser (e.g. check Brand used by DESY). Afterwards, the gasket is placed back, to the same position, between the two diamonds and the sample can be loaded into the cavity originating from one diamond culet and the gasket hole. Following the loading process, the cell is closed and pressure can be increased either manually with the help of 4 lever screws bringing the diamonds closer together, or automated by using different drivers pushing the diamonds towards each other.

In this work, a comparison of time dependent compression experiments using different automated drivers (mDAC and dDAC) requires the use of symmetric piston-cylinder DAC (Fig 3.1). Those symmetric DAC are widely spread in the high-pressure community, hence experimental stations have been adjusted to fit its dimensions and various measurement techniques are available.

3.2 Pressure determination

Once the sample is loaded into the DAC, it becomes crucial to determine the starting pressure and to keep track of its development during the experiment. A pressure standard is required to determine the pressure and the most common secondary pressure standard at ambient temperatures is ruby, $\text{Al}_2\text{O}_3:\text{Cr}^{3+}$, already mentioned in the gasket indentation process. A laser induces fluorescence in a ruby and originates from the Cr^{3+} ion. It shows a strong

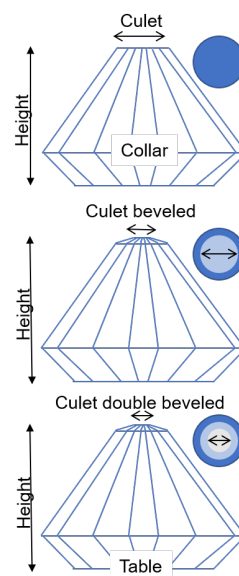


Figure 3.2: From top to bottom: standard, single beveled and double beveled diamond anvil.

peak doublet R_1 and R_2 at 6942 Å and 6928 Å under hydrostatic conditions, only showing an approximate 2% uncertainty due to line broadening [89]. Non-hydrostatic conditions lead to a broadening and overlap of the R_1 and R_2 peaks, tending to result in larger uncertainties of the pressure [90]. The shift of the R_1 peak position (Fig. 3.3) can be correlated to the pressure during compression by the following equation:

$$P [\text{GPa}] = \frac{A}{B} \left[\left(1 + \frac{\Delta\lambda [\text{nm}]}{\lambda_0} \right)^B - 1 \right] \quad (3.1)$$

where P is pressure, λ_0 the wavelength at ambient P-T conditions (6942 Å) and $\Delta\lambda$ the shift of the R_1 peak. A and B are refined parameters obtained during calibration experiments (e.g [89, 91, 92, 93]) in the last years. For example $A = 1905$ [GPa] and $B = 7.665 - 5.0$ based on *Mao et al., (1986)*, where $B = 7.665$ represents hydrostatic and $B = 5.0$ non-hydrostatic conditions. Hence, results are bound to the chosen calibration parameter and mentioning those becomes necessary to avoid inconsistencies or misinterpretation.

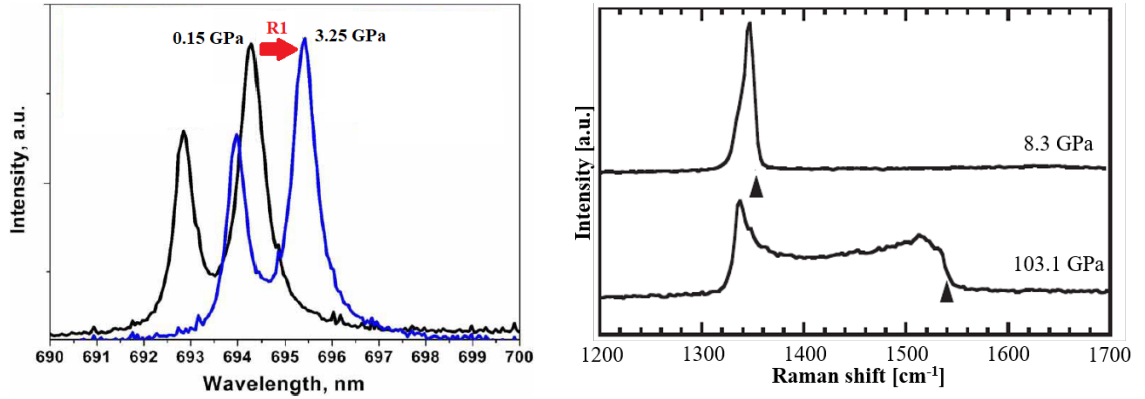


Figure 3.3: Pressure dependent Ruby and Raman shift. (Left) Observed R_1 and R_2 shift of Ruby, $\text{Al}_2\text{O}_3:\text{Cr}^{3+}$, during compression (modified after [94]) and (Right) Raman band shift of diamond at the center of the culet, showing the P gradient in the anvil (modified after [95])

An alternative method, mostly used to determine high-pressures above 100 GPa, is laser-induced diamond fluorescence [96, 97]. It uses the high-frequency edge shift of the diamond Raman band ν as a linear dependent parameter [98] of the pressure, respectively, normal stress at the diamond culet (Fig. 3.3). It is described by the equation:

$$P [\text{GPa}] = K_0 \frac{\Delta\nu}{\nu_0} \left[1 + \frac{1}{2}(K_0' - 1) \frac{\Delta\nu}{\nu_0} \right] \quad (3.2)$$

where K_0 547(± 11) GPa is the bulk modulus of a quasi-hydrostatic compressed elastic body at ambient pressure, K_0' 3.75(± 20) its first derivative, ν_0 the wavelength of the high-frequency edge at ambient conditions and $\Delta\nu$ the observed wavelength shift. Thereby, ν_0 is defined as the minimum of the first derivative of the whole Raman spectrum. Another advantage resulting from the method is that no compound other than the sample has to be loaded into the cell, preventing additional parasitic features in the experimental data. If those features do not compromise the analysis, micro-diamonds can be used and directly embedded in the sample volume, enabling pressure measurements up to 270 GPa [99]. Applying not only high-pressure but also high-temperature conditions into the pressure calculation requires additional

optical sensors like the $\text{Sr}_4\text{BO}_7:\text{Sm}^{+2}$, or Sm:YAG (yttrium-aluminum-garnet) fluorescence. The former shows much lower line broadening and wavelength shift at elevated temperatures ($< 900\text{ K}$) compared to ruby fluorescence and has the advantage of only one peak ${}^7\text{D}_0$ - ${}^5\text{F}_0$, thus removing uncertainties due to the overlapping of ruby R_1 and R_2 peaks [100, 101, 102, 103, 104]. The second sensor is independent of temperature ($< 850\text{ K}$) in contrast to ruby fluorescence, thus allowing for accurate pressure and temperature determination if collaboratively used [105, 106, 107]. Determination of the conditions beyond 900 K , however, needs further corrections and the use of cross correlation only is no longer feasible. With the accessibility of X-ray or neutron sources, direct measurement of the samples unit cell parameter can be performed. Hereby, pressure information can be obtained *in-situ* during the experiment from the sample, if the P - V - T equation of state (EoS) are well known. In general, a small amount of a well characterized substances is mixed with the sample material, resulting in an accurate, internal pressure standard. Common pressure standards are metals, like Au, or Pt, which have been used for a long time in technical applications and industrial processes. Due to their frequent use, their high-pressure and high-temperature properties have been accurately determined. Special efforts have been made to obtain very precise EoS and their uncertainties are eliminated by cross-correlating the results of various metals in the pressure scales itself [59, 108]. Internal pressure calibrants have the advantage of obtaining Bulk modulus properties of the sample material directly from the diffraction images following the thermodynamic definition [109]:

$$K = -V \times \frac{dP}{dV} \quad (3.3)$$

where V is the volume of the sample material and P the pressure observed by the internal pressure calibrant. However, their Bragg reflections show on the diffraction image and can complicate the analysis of the sample material, due to an overlap of their peaks across the compression intervals. Nevertheless, even for Au and Pt mentioning the EoS parameters used in the experiment remains unavoidable, more so at simultaneous very high-pressures and high-temperature where the amount of accessible data is restricted by the complexity and difficulty of the experiment.

3.3 Non-hydrostatic conditions and lattice preferred orientation

Because of the much higher toughness and strength of the diamonds in comparison to most of the sample materials and common for anvil experiment, the stress imposed on the sample is not uniform. Instead both anvils imply a strong uniaxial stress component σ_{33} (parallel to the diamond anvil axis), which can only partially be evened out by the surrounding, containing force along σ_{11} of the gasket material. The discrepancy results in the following expressions to characterize the stress state and stress components [110]:

$$\sigma_{ij} = \sigma_p + D_{ij} \quad (3.4)$$

and

$$D_{ij} = \begin{bmatrix} -t/3 & 0 & 0 \\ 0 & -t/3 & 0 \\ 0 & 0 & 2t/3 \end{bmatrix}$$

where, σ_p describes the hydrostatic (normal) and D_{ij} the deviatoric stress component in the sample.

The non-homogeneous distribution of stress results in texture, respectively, lattice preferred orientation (LPO) of the sample. Thereby, the whole sample material and individual grains are deformed plastically and tend to rotate into the direction of lower stress σ_{11} . LPO was first studied by *D'Halloy, (1833)* who pointed out its special significance for the alignment of crystals and as an indicator of the processes resulting in their formation. Yet, analyses of preferred orientations have only recently become widely used in Earth Science, through the emergence of quantitative analytical methods [111]. Thus, our understanding of the conditions and deformation mechanisms leading to preferred orientation is limited and results obtained at non-hydrostatic conditions are difficult to analyse and should be treated with caution. Two types of preferred orientation are distinguishable and can be correlated to a certain extend (Fig. 3.4): The lattice preferred orientation (LPO), or texture [113] describes the crystallographically preferred orientation (CPO), whereas shape preferred orientation (SPO) describes morphologically preferred orientation [111].

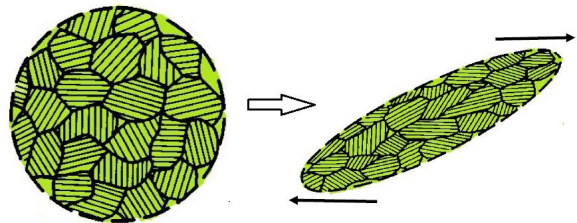


Figure 3.4: Change of shape preferred orientation during plastic deformation (left: circle \rightarrow right: ellipsoid) and the generation of lattice preferred orientation due to crystal rotation (left: crystals with random crystallographic orientation \rightarrow right: rotation of crystals and forced alignment of crystallographic planes) [112].

3.4 Differential Stress

The difference in the axial σ_{33} and radial σ_{11} stress component is called differential, or uniaxial stress [110] and different approaches can be used to obtain information about stress and strain (η) in the sample material.

The first approach: Line shift analysis can be performed by direct measurements in a radial geometry setup of DAC experiments (Fig. 3.5), observing the divergence of the stress axis of the diamonds and the normal of the diffraction plane as a function of the ψ angle.

This can be expressed by [114]:

$$d_m(hkl) = d_p(hkl) \times [1 + (1 - 3 \cos^2 \psi) \times Q(hkl)] \quad (3.5)$$

where $d_m(hkl)$ describes the measured lattice spacing at deviatoric stresses (D_{ij}), d_p lattice spacing under hydrostatic pressure σ_p , ψ angle between diffraction plane and load direction and $Q(hkl)$ the strain on individual lattice planes. As a consequence (Eq. 3.5), it is evident

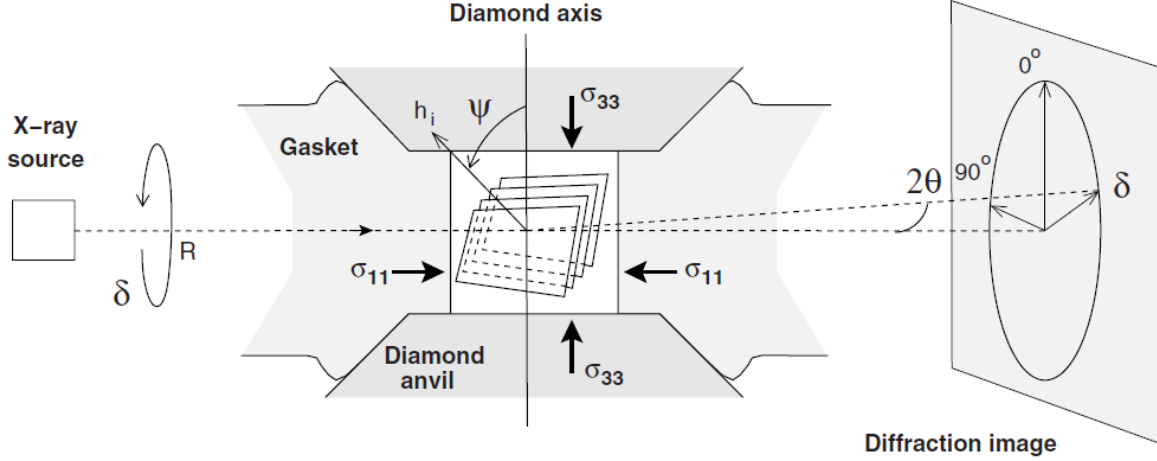


Figure 3.5: Synchrotron sourced angle dispersive radial diffraction setup for diamond anvil cells. The incoming monochromatic beam travels through the sample and gasket, thus allows the collection of diffraction images perpendicular to the compression axis. σ_{33} and σ_{11} are the axial and radial stress compound applied by either diamond anvils or the containing gasket. Here, the azimuthal angle δ is used to analyse the position and intensity of Bragg reflections, whilst ψ is calculated in regards of the maximum stress direction and diffraction plane normal [115].

that the deviatoric stress compound (D_{ij}) vanishes - $(1 - 3 \cos^2 \psi) \times Q(hkl) = 0$ - at an angle $\psi = \cos^{-1}(1/\sqrt{3})$. Hence at the "magic angle" of $\psi = \cos^{-1}(1/\sqrt{3}) \approx 54.74^\circ$ both measured and supposed hydrostatic lattice spacing are equal and result in the following condition [116]:

$$d_m(hkl) = d_p \quad (3.6)$$

The average micro-strain can be used to estimate the differential stress (t) in relation to its single crystal elastic constants or compliance:

$$t = 6G \langle Q(hkl) \rangle f(x, \alpha) \quad (3.7)$$

where G is the shear modulus - Voigt-Reuss-Hill (VRH) average - of the sample, $\langle Q(hkl) \rangle$ the average lattice strain and $f(x, \alpha)$ a function of α , determining the relative weights of isostrain or isostress conditions and the elastic anisotropy parameter $x = 2(s_{11} - s_{12})/s_{44}$ [116, 117, 118]. Thereby, $f(x) \approx 1$ for isotropic and a large degree of anisotropic aggregates.

The second approach: Gamma-plots, are a variation of the line shift analysis based on d -spacing analysis in combination with lattice strain equations. The assumption is that the actual stress condition in the sample is a mixture of isostress and isostrain and it can be used for cubic materials without the limitation to a radial diffraction setup as it results from Eq. 3.4. The relation can be expressed as [116]:

$$a_m(hkl) = M_0 + M_1 [3 (1 - 3 \cos^2 \psi) \Gamma(hkl)] \quad (3.8)$$

where

$$\Gamma(hkl) = (h^2k^2 + k^2l^2 + l^2h^2)/(h^2 + k^2 + l^2)^2 \quad (3.9)$$

is a value in range 0-1/3, $a_m(hkl)$ the measured lattice parameter, M_0 is the intercept of the gamma-plots, M_1 is the slope and ψ is the angle between diffraction plane and load direction. Thereby, gamma-plots ($a_m(hkl)$ vs $3(1 - 3 \cos^2 \psi)\Gamma(hkl)$) (Fig. 3.6) are in general straight lines for conventional DAC experiment geometries ($\psi = 90^\circ - \theta$) with an error of 1/10 % and even less in case of energy dispersive X-ray diffraction (EDXD) setups, where ψ becomes independent from (hkl) [116]. Both parameters, the intercept (M_0) and slope (M_1), are functions dependent on t:

$$M_0 = a_p \{1 + (\alpha t/3)(1 - 3 \cos^2 \psi)[(s_{11} - s_{12}) - (1 - \alpha^{-1})(2G_V)^{-1}]\} \quad (3.10)$$

and

$$M_1 = -a_p(\alpha t s/3) \quad (3.11)$$

and knowing the single crystal compliance s of the sample at a given pressure, enable direct computation of t based on the relation:

$$t \approx \left(\frac{-3M_1/M_0}{s} \right) / \alpha \quad (3.12)$$

where

$$s = (s_{11} - s_{12} - s_{44}/2) \quad (3.13)$$

is the single crystal compliance, α , determining the relative weights of isostrain and isostress conditions, a value in range 0.5-1 and a_p the lattice parameter under hydrostatic stress [119]. Furthermore, G_V is the shear modulus by *Voigt, (1928)* [43] and here written in the expression [116]:

$$(2G_V)^{-1} = 5(s_{11} - s_{12})s_{44}/2[3(s_{11} - s_{12}) + s_{44}] \quad (3.14)$$

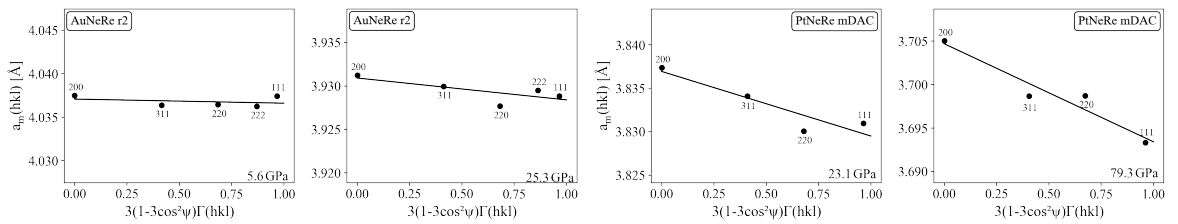


Figure 3.6: Gamma plots obtained during the analysis of our experiments. Right two: Au + Ne in dDAC and Left two: Pt + Ne in mDAC. Error in a_m is smaller than the marker.

In addition, the gamma-plot calculations enable another way to investigate the hydrostaticity during the experiment by means of:

$$std^2(a_m) = std^2(a_p) + std_D^2. \quad (3.15)$$

where, $std(a_m)$ describes the standard deviation of measured lattice parameter and is the linear result of two compounds $std(a_p)$ and std_D . Thereby,

$$std_D = (\alpha t s) a_p \left[\langle \zeta^2 \rangle - \langle \zeta \rangle^2 \right]^{\frac{1}{2}} \quad (3.16)$$

with

$$\zeta = (1 - 3 \cos^2 \psi) \Gamma(hkl) \quad (3.17)$$

describes the d -spacing variations independent of the trend given in Eq. 3.4. and $std^2(a_p)$ the variation of d -spacing under hydrostatic condition.

A range of $std(a_p)$ values has been commonly observed and proposed for standard DAC experiments to represent hydrostatic conditions ($std(a_p) < 0.0004$) and non hydrostatic conditions ($std(a_p) \geq 0.0004$). An example of a std^2_D and $std^2(a_m)$ plot obtained from lattice parameter during the compression interval of AuNe[Ss] is shown in (Fig. 3.7). Finally, an important note has to be made that all gamma plot equations above are limited to non-isotropic samples, otherwise the single crystal compliance s becomes 0 [116].

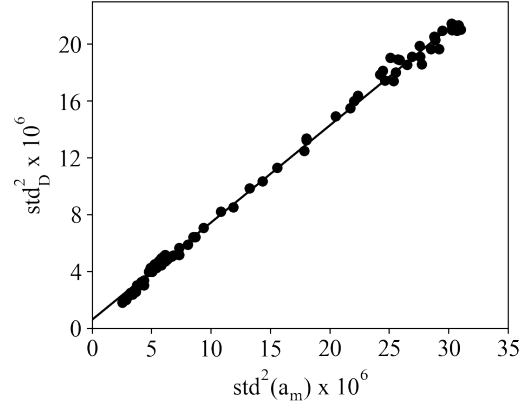


Figure 3.7: Acquisition of $std(a_p)$ based on std^2_D and $std^2(a_m)$ of the lattice parameter of AuNe[Ss] during compression. The intercept of the linear regression determines $std(a_p)^2$.

Third: Line-width analysis observes the broadening of diffraction lines as a result of non-hydrostatic conditions during an experiment. Thereby, it is affected by grain size variation -reduction due to increasing pressure- and micro-strain variations on the lattice planes of the individual crystallites. Their relation can be expressed as [114, 120]:

$$(2w_{hkl} \cos(\theta_{hkl}))^2 = \left(\frac{\lambda}{d}\right)^2 + \eta_{hkl}^2 \sin^2(\theta_{hkl}) \quad (3.18)$$

where, $2w_{hkl}$ is the full-width at half-maximum (FWHM) of the diffraction line on the 2θ -scale [121], d the grain size, λ the wavelength and η_{hkl} the micro-strain. The equation can be transformed into:

$$\eta_{hkl}^2 = \left[(2w_{hkl} \cos(\theta_{hkl}))^2 - \left(\frac{\lambda}{d}\right)^2 \right] / \sin^2(\theta_{hkl}) \quad (3.19)$$

enabling micro-strain determination of each diffraction line. Both the grain size and micro-strain can be obtained from a $2w \cos(\theta)^2$ vs $\sin^2(\theta)$ plot (Fig. 3.8), where the grain size is lattice independent and given by the intercept of the plot and micro-strain is given by the slope. The equation is based on a (hkl) -dependence of η relating to an equal probability in the crystallites of having planes with stress conditions between 0 and p_{max} (maximum stress), hence, it is dependent on the Young's modulus of the sample material [122] and the following relation can be used to compute p_{max} [114]:

$$2p_{max} = \langle \eta_{hkl} \rangle E/2, \quad (3.20)$$

At the same time, $2 \times p_{max} \cong t$, hence it can be taken as another measure of the differential stress during the experiment [114].

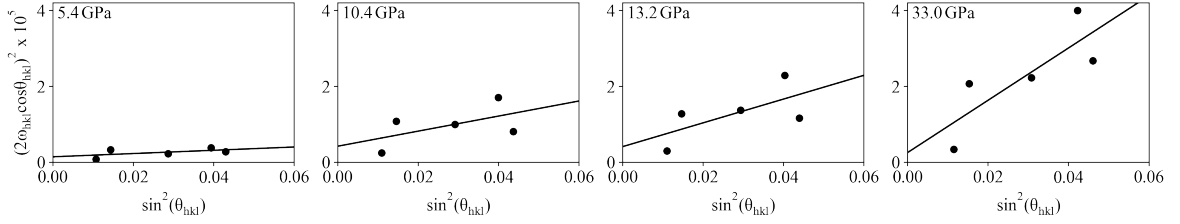


Figure 3.8: Evolution of the FWHM and peak position correlation of AuNe[Re] during dDAC compression. Micro-strain information is obtained from the slope of the linear regression and the intercept beholds information of the samples grain size. Error in the data is less then the size of the marker.

Within this study the second, line-width, and third, line-shift, approach are used to evaluate the experimental conditions in the samples. There are two main reasons for this: First the dDAC is a novel device and access to the current radial diffraction setups are very limited as they are still in development; and second the Radial diffraction analysis has a lot of constrains assumed based on results of common DAC experiments, i.e. assumed common $Q(hkl)$ value rang and those may not represent the fast compression environment.

3.5 Pressure transmitting media

To reduce the affect of non-homogeneous stress distribution in the sample material, pressure transmitting media (PTM) can be loaded simultaneously into the DAC. They insulate the sample from the surrounding gasket material and prevent direct contact with the opposing diamond culet. They provide quasi-hydrostatic conditions for the sample, distributing the uniaxial applied force of the diamonds as homogeneously as possible onto the sample material (Fig 3.9).

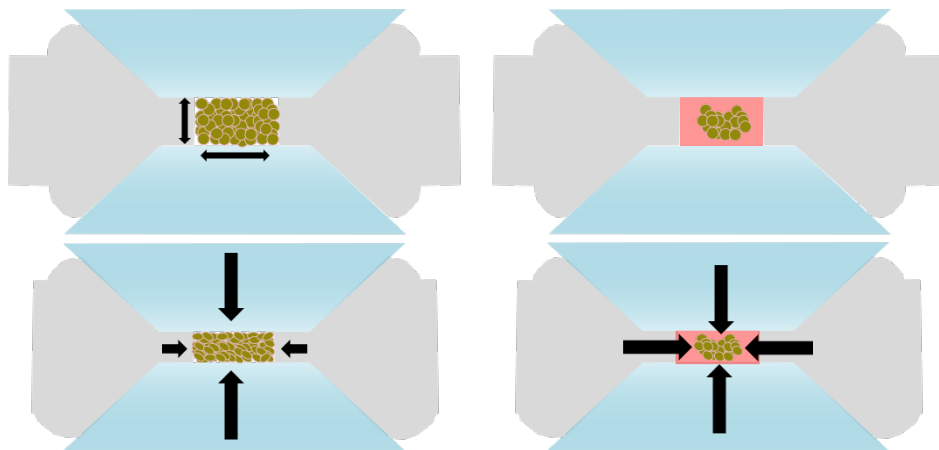


Figure 3.9: Diamond anvil compression. (Left) Effect of the applied pressure on powder sample without PTM. Randomly orientated crystals are forced to rotate and start to align along preferred orientation axis. (Right) Powder sample is surrounded by PTM (reddish color). During the compression the PTM distributes the uniaxial stress homogeneously onto the sample and prevents alignment along preferred orientation axis.

The choice of the PTM is crucial for the preparation and conduction of the experiments.

It needs to be inert in regard of sample, diamond and gasket material, to have a low shear strength and to interfere only insignificantly with the measurements (e.g. intensity and position of its diffraction peaks). As heating is involved in the experiment the PTM further needs to be a good thermal insulator, because diamonds have a very high thermal conductivity (up to $33 \frac{W}{cmK}$ at ambient temperature) [123] and their culets function as effective evacuation systems. A large variety of PTM can be chosen from: soft solids (alkali halides, KBr, NaCl, LiF), hard solids (Al_2O_3 , MgO), liquids (alcohol, alcohol mixtures (e.g. methanol-ethanol-water in 16 : 4 : 1), silicon oil) and gases (H, Ar, He, Ne, N_2 , Xe). The most recommended ones are the noble gases argon, helium and neon, whilst they start to crystallize at high-pressures, they still homogeneously distribute the pressure due to their very low shear strength [124].

Solid and liquid PTM are commonly loaded with the sample and successful loading can be visually observed with a microscope. In contrast, gaseous PTM require a more complex approach to allow the loading and to verify successful gas containment. Whilst cryogenic cooling and liquid loading is practicable in case of Ar and N_2 and Xe, the other gases H, He and Ne require dedicated gas loading chambers, having condensation temperatures below 73 K (N_2) at atmospheric pressure. Within the gas loading chamber the DAC needs to be operational from the outside and to enable automatic opening and closing of the DAC by tightening or loosening the lever screws. Once loosened a gap appears between the sample hole and the anvil-sided diamond allowing infiltration of the gas PTM into the sample chamber. Afterwards, the gas is sealed within the sample hole hermetically by closing the gap, thereby, preserving pre-pressurised gas within. The now loaded cell is recovered from the gas loading chamber and the presence or lack of success has to be determined by means of ruby or diamond band shift, originating from the pressurised gas within the DAC [125].

In the current work, neon was used as pressure transmitting medium and the symmetric piston-cylinder DAC were loaded at the ECB P02.2 of PETRA III, DESY, Germany.

3.6 Diamond cupping

Using the diamond anvil cell technique is dependent on the properties of diamonds, thus, the maximum pressure achievable is coupled with the limits of the diamond anvils. As mentioned in chapter 3.1, diamond shows a strong anisotropy in its shear resistivity and a process called diamond cupping seems to be the main reason for diamond failure, even if both diamond culets are perfectly aligned to each other. Diamond cupping describes the elastic stretching of the diamond edges, meaning an increase in shoulder height during the experiment and with increasing pressure load (Fig. 3.10). Cupping has been described in all standard, beveled and double beveled anvil cells (e.g [126]). While its effect is mostly negative on the experiment, leading to diamond failure once both diamonds touch, it enables increased precision of pressure determination during the shoulders rise, by flat-

tening out the pressure gradient on the tip of the diamonds [127]. The most imminent effect of cupping is a loss in pressure distribution efficiency onto the sample [128, 129, 130], whilst the diamond itself starts to accumulate strain. Here, the gasket material can help to prevent, respectively, stall out the diamond cupping depending on its yield stress. With high yield stress, the tensile stress and stress gradient in the diamonds can be reduced, making metallic glasses most likely a good candidate for gasket materials [131, 132], whilst the onset of diamond cupping in return increases the stability of the gasket material at higher pressures and supports the enclosure of the sample material [133]. Nevertheless, once the cupping reaches its critical limit, transmission intensity at the rim equals half of that at the central culet [134] and diamond failure is imminent and most likely to happen. An additional factor is the thickness of the gasket. It can help to support the anvils reducing the stress on the culet edges if chosen correctly. Yet, if chosen wrongly, it leads to a faster diamond failure, preventing sample support, thus resulting in non-symmetrical enlarging of the sample hole [133]. Recent investigations of first results in toroidal DAC [135] and dsDAC [136] experimental setups most likely record a reason of the increased pressure range available with those types of DAC experiments. They report either the absence of cupping at much higher pressures compared to standard beveled diamonds [135] or much higher resistivity to pressure variations compared with the yield strength of single crystal diamonds, due to the absence of distinct cleavage directions in the nanocrystalline anvils [136].

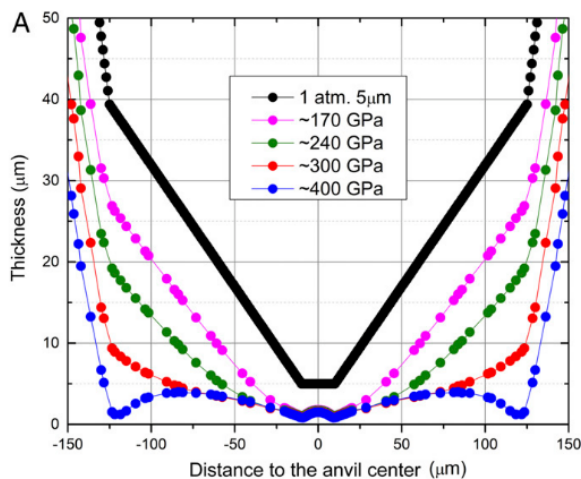


Figure 3.10: Gasket thickness across a compression event up to 400 GPa. With increasing pressure the shoulders/sides of the anvil start to rise and at last cup with the shoulders of the opposing anvil, Figure obtained from [126].

3.7 High temperatures

Static compression experiments, such as diamond anvil cell setups, do not have an intrinsic access to high temperature like shock experiments and they require additional support and setup to enable closer experimental correlation with the environmental conditions in exoplanets and in the Earth's interior. One of those supporting techniques is laser (Light Amplification by Stimulated Emission of Radiation) heating and it has become a major tool to generate high-temperatures in the diamond anvil cell within the last decades. Their setups range from dedicated stationary systems at research facilities (e.g. Carnegie), Synchrotron facilities (e.g. APS, ESRF, PETRA III) [137, 138, 139], and Universities (e.g. Uppsala), to multi-purpose portable systems available at institutes like BGI [140], or the universities of

Potsdam and Dortmund [74].

3.8 Dynamic compression in DAC

Manual adjustment and increase of the pressure in the DAC, by tightening the screws to push the diamond anvils together is the simplest and to some extent fastest way to perform an experiment. However, the manual interaction with the setup limits the pressure control and requires repetitive interruption of the experiment, hence restricting observations to quasi-static conditions. The efforts to overcome the need to interrupt the experiment combined with the demand for a finer pressure control and a wider range of observable conditions led to the development of two drivers in the last three-and-a-half decades: membrane driven DAC (mDAC) [141] and piezo-electric driven DAC (dDAC) [10].

3.8.1 Membrane diamond anvil cell (mDAC)

The membrane DAC combines the standard DAC assembly with an annular metal membrane attached either to the up- or down-stream anvil [3.11]. It is the first device enabling remote, fine control and continuous compression or decompression cycles in DAC experiments [141].

Current common mDAC designs use a gas compressor to control the extension and contraction of the annular membrane by regulating the membranes internal gas-pressure and the speed of gas-pressure increase and decrease. Thus, being attached to the diamond anvil it either applies force onto or releases force from the sample material enabling continuous tracking of diffraction images subjected to compression and decompression rates of up to some few GPa/s. Nevertheless, the applied force allows only relative low compression rates, yet already shows the pressure dependence of crystal growth mechanism and stable phases [19, 22, 142].

Since its development in 1988, mDAC experiments have become a fundamental part of high-pressure research and custom mDAC assemblies have become available in university laboratories, research institutes and synchrotron facilities. Recent attempts investigated the possibilities to increase the range of available compression rates [11]. They combined the standard mDAC setups at ECB P02.2, PETRA III, DESY and HPCAT, APS with an extra intermediate buffer volume and a solenoid valve in close proximity of the mDAC. This setup enables compression rates up to 620 GPa/s, dependent on the pre-compression of gas within the buffer as well as the trigger time of the

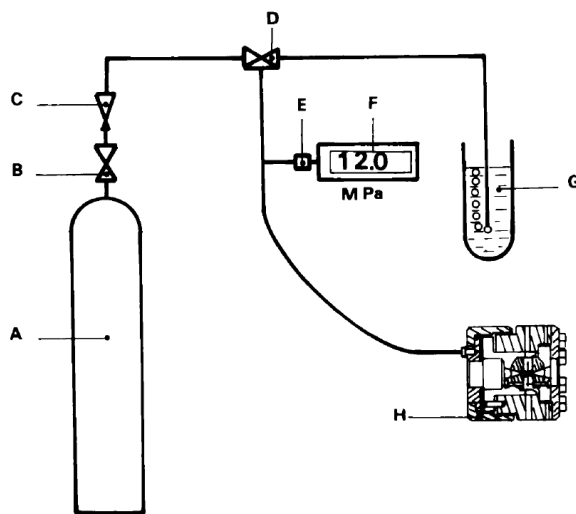


Figure 3.11: Schematic drawing of the original mDAC setup, showing gas-container [A], gas transport [B-E], Membrane pressure readout [F], membrane pressure [H] and He leakage control [G] [141].

solenoid valve.

3.8.2 Piezo-driven dynamic diamond anvil cell (dDAC)

Piezoelectric-actuators are reversible converter of electrical energy into mechanical extension or contraction, creating small displacements at high speed and with large force. Recently, they have been technically implemented as an enhancement of the standard DAC resulting in the piezo-driven dynamic diamond anvil cell (dDAC; Fig. 3.12)[10]. Also, a wave form generator

was used in combination with a power supply amplifier to send an electrical signal to the piezoelectric-actuators, converting the arriving wave profile into extension and reducing the load on the sample by counteracting the load applied by the pressure screws. During the first experiments compression

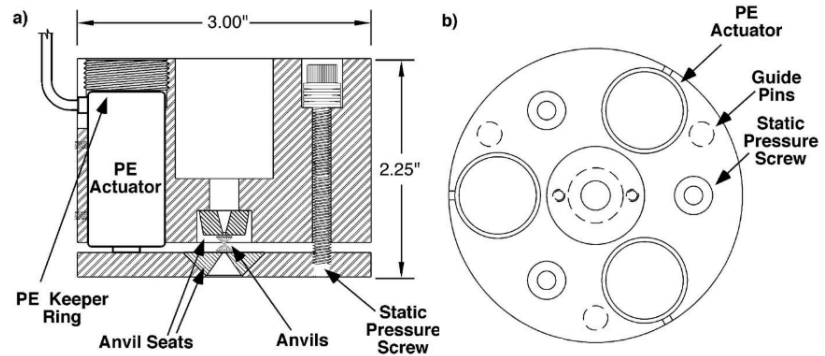


Figure 3.12: Cross sectional and end-on view of the original design schematic of the dDAC [10], showing the location of the diamond anvil, piezo-actuators (PE), static pressure screws and diamond anvil guide pins

rates of up to 500 GPa/s (strain rates of $\approx 0.16 \text{ s}^{-1}$ for metals) were reached, already surpassing compression rates of mDAC experiments by the factor of 100 [10].

Since 2007 a number of groups and collaborations have been formed to use and further develop the dDAC for different technical applications. First, the groups of *Geun Woo Lee* and *Choong-Shik Yoo* (e.g. [18, 20, 143]) investigated the crystal growth mechanism affected by different compression rates at pressures up to some couple of GPa. Recently, they implemented a Michelson interferometer to the setup enabling *in-situ* determination of sample volume changes based on the movement of the upper anvil [144]. Second, a fast X-ray diffraction setup was developed at the ECB P02.2, PETRA III, DESY, Germany in collaboration with the Lawrence Livermore National Laboratory (LLNL) and the Crystallography/Mineralogy group at University Frankfurt. This setup combines the brilliant X-ray source at Petra III with dDAC capabilities of 10^2 TPa/s compression rates [145] and fast data collection capabilities - continuous 4 kHz repetition - using two parallel GaAs LAMBDA detectors [15]. Third, a setup by the High Pressure Collaborative Access Team (HPCAT) at the Advanced Photon Source (APS), enabling compression rates of 10^1 TPa/s [146] and fast data collection at 1 kHz repetition. Fourth, a collaboration of ECB P02.2, PETRA III, DESY and the Los Alamos National Laboratory (LANL) using the setup described by *Jenei et al., (2019)* [145] tries to adapt and characterize a specialized dDAC design for radial diffraction experiments. An overview of the recently developed and reported dDAC configurations of the ECB/LLNL and

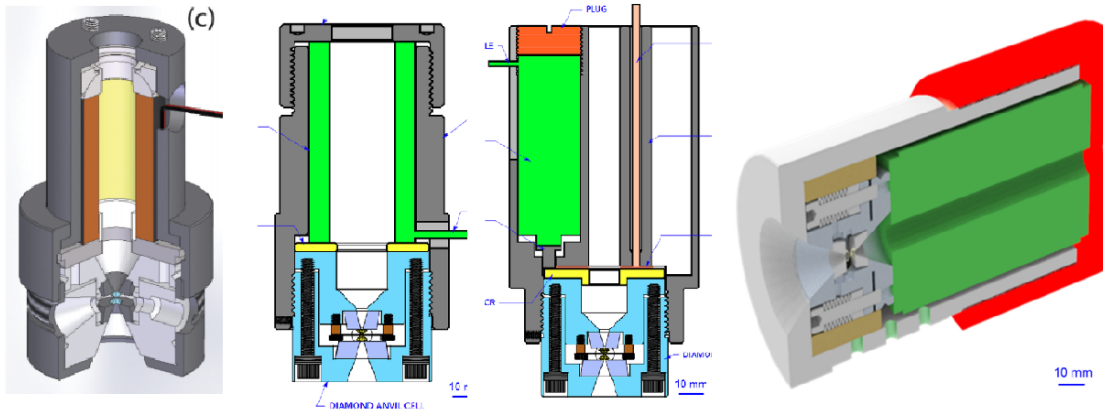


Figure 3.13: Overview of the dDAC designs available at either ECB, LLNL or HPCAT. From left to right: HPCAT assembly in compression mode [147], LLNL hollow cylinder and three piezo configuration, ECB large (90 mm) hollow piezo configuration [145].

HPCAT groups is given in (Fig. 3.13) and first results are summarized in (Chapter 1).

3.9 X-ray diffraction

X-ray diffraction (XRD) in combination with the common DAC, mDAC and dDAC design has become one of the major tools to investigate the characteristics and properties of a material. It relies on Bragg's law [148]:

$$n\lambda = 2d\sin(\theta) \quad (3.21)$$

describing the constructive interference of an incident X-ray with the crystallographic planes of the material (Fig. 3.14). Thereby, n is an integer of the wavelength, λ is the wavelength of the incident ray, d is the lattice spacing of constructive reflections, θ the angle between the impinging incident X-ray. As a result of Bragg's Law, X-ray diffraction can be performed either as angle dispersive X-ray diffraction (ADX) or energy dispersive X-ray diffraction (EDXD). On the one hand, ADXD is using a specific, monochromatic, wavelength λ to enable high resolution diffraction images. However the collection can be time consuming and the sample intensity on the diffraction images varies due to the orientation of lattice planes in the sample. On the other hand, EDXD uses polychromatic or 'white', 'pink' beam, containing a wide range of wavelength λ and the diffracted X-ray is orientation dependent. Whilst its resolution is lower compared to ADXD, experiments can be performed faster and a constant sample volume is observed. Within this study, two large scale, high X-ray source brilliance facility instruments - ECB P02.2, PETRA III, DESY and HED, European XFEL - have been used

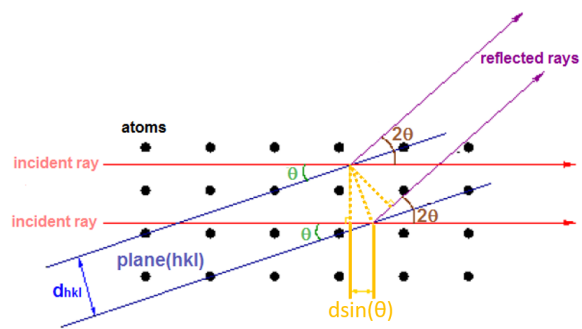


Figure 3.14: Basic theory of X-ray diffraction, showing the constructive interference of X-rays with atoms in crystallographic lattice planes.

with ADXD in diamond anvil cells.

3.9.1 X-ray diffraction at ECB P02.2, PETRA III, DESY

The Extreme Conditions Beamline (ECB) P02.2 at PETRA III is dedicated to powder and single-crystal X-ray diffraction in diamond anvil cell experiments at extreme conditions, where the sample volume is very small and the access angle is restricted by the arrangement of the diamond anvil cell. The ECB beamline is located at PETRA III a third generation synchrotron facility providing a high-brilliance photon flux. It operates with 6 GeV electrons, stored in its 2304 m storage ring and with a maximum beam current of 100 mA [138]. As the fast electrons are forced to follow the circular orbit of the storage ring they emit radiation in the direction of the original straight flight path (Fig. 3.15), where the beamlines and experimental stations are located.

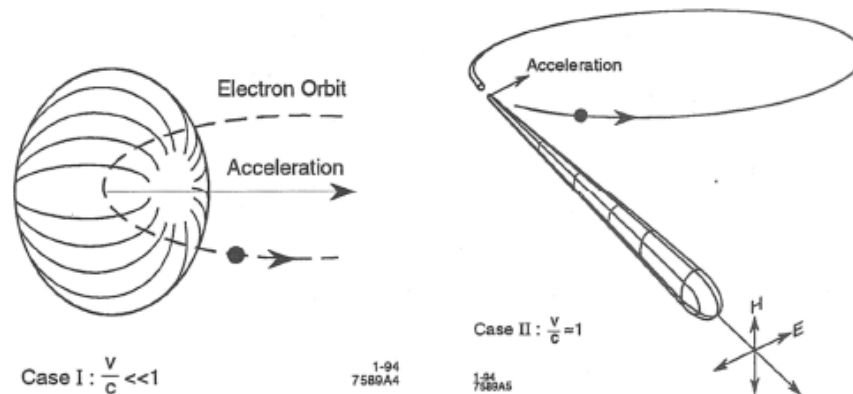


Figure 3.15: Difference in radiation based on the velocity of the electron, respectively photon. Left: slow particle emits radiation in all directions and Right: directed radiation based on fast particle with relativistic velocity [149]

The following information are mainly obtained from [138], where a schematic drawing of the most relevant compounds in the ECB can be found, too. The U23 undulator feeding the ECB endstation provides a high-brilliant polychromatic beam tuned to its seventh harmonic (60 keV), at the minimum gap distance of ≈ 10 mm. The undulator is followed by two pairs of high-heat-load slits to shape the beam profile, cutting down halos and tails, and reduce the heat load on subsequent critical devices. Hereafter, a filter system is setup in combination with a diamond (111) Laue monochromator crystal, enabling simultaneous operation of both side branches: high resolution powder diffraction beamline (HRPD) P02.1 and ECB P02.2. Thereby, it fixes experiments at ECB to the third, fifth and seventh harmonic at 25.6, 42.7 or 60 keV. Standard double crystal monochromator of Si(111) and Si(311) pairs are used to provide energy resolutions of $\Delta e/e = \approx 2 \times 10^{-4}$ Si(111) or $\Delta e/e = \approx 5 \times 10^{-5}$ Si(311) and either compound refractive lenses (CRL) or Kirkpatrick–Baez (KB) mirrors are used as the main focusing optics. The Be, or Al CRLs enable a focus of $8 \mu\text{m}$ (H) \times $2 \mu\text{m}$ (V) FWHM and the Kirkpatrick–Baez (KB) mirrors of $< 2 \mu\text{m}$ (H) \times $2 \mu\text{m}$ (V) FWHM, albeit the KB mirrors cannot maintain an equally small divergence as the CRLs. At the end of all

optical and focusing devices there are two separate experimental stations: general purpose (GP) and laser heating (LH). The GP, is designed to be very versatile, enabling normal DAC staging setups as well as more bulky setups when needed i.e. during cryogenic cooling, or resistive heating. Whereas the LH is a specialized station for off-axis and on-axis laser heating with either Yb-fiber, or CO₂ laser. At the LH, the available staging setup is more restricted to keep the focusing and heating configurations in close alignment and prevent time-consuming setup changes. The data acquisition is accomplished by area detectors (Perkin Elmer XRD 1621, PILATUS 300K or 1M [138], or GaAs LAMBDA [145]) selectable by means of the experimental requirements. Those detectors are mounted on translation stages, enabling not only fine tuning of the sample detector distance (SDD), but also access to defined reciprocal space by centering or off-centering the detectors in relation to the beam. In this study, experiments with the mDAC and dDAC setup were performed at 25.6 keV at the GP-station and at 42.7 keV at the LH-station. At the GP-station a CRL focused beam of 8 μm (H) \times 2 μm (V) was used to enable high intensity diffraction images across a variety of short exposure times from 0.5 μs to 0.266 s, whilst a KB focused beam of < 2 μm (H) \times 2 μm (V) was used in the LH experiments at exposure times of 2 - 5 s and in combination with continues on-axis laser heating, the LH setup is illustrated [Fig. 3.16].

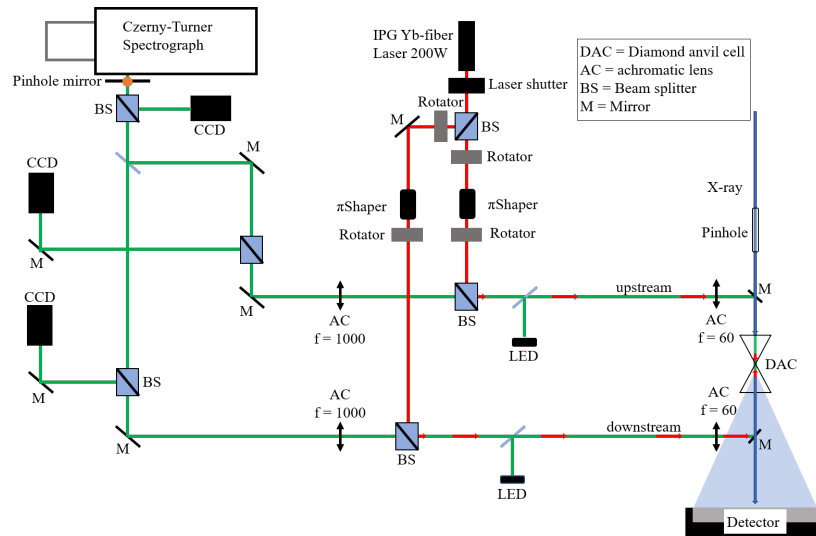


Figure 3.16: Schematic drawing of the on-axis laser heating setup at ECB P02.2, PETRA III, DESY (modified after Morgenroth, 2014 [150]). The green solid line represents the path of observation and temperature measurement, red and red arrows the path of the laser beam and blue the X-ray path.

3.9.2 The European XFEL, a new tool for high pressure experiments

The High Energy Density (HED) scientific Instrument at European XFEL is dedicated to enable Hard X-ray free-electron laser (FEL) radiation in combination with placing material under certain extreme conditions, like temperature, pressure or electric and magnetic fields. The HED instrument is located at the SASE 2 beamline of the European XFEL, representing the first XFEL facility capable of providing a high brilliant photon flux up to energies of 25 KeV. Within the first 1.7 km, electron bunches produced in the injector photon cathode are

accelerated to relativistic velocities by oscillating microwaves in cryo-cooled and superconducting niobium cavities (-271°C). The electron bunches can be directed into three SASE beamlines (five in the future), where they pass through undulators (The SASE 2 undulators have a total length of 205 m), a periodic arrangement of magnets (10-20 mm distance) forcing the electrons into a well defined slalom course (Fig. 3.17) [151]. During each turn the electrons emit directed X-ray radiation (Fig. 3.15), which emitted back in the electron bunches overtakes the leading electrons. The overtaken electrons obtain momentum of, or lose momentum to the radiation and as a consequence organize themselves into groups. Those groups emit their light "in sync" (self-amplified spontaneous emission (SASE) process), thus generating X-ray flashes, up to 27,000 pulses/s at the European XFEL, with the properties of laser light [152].

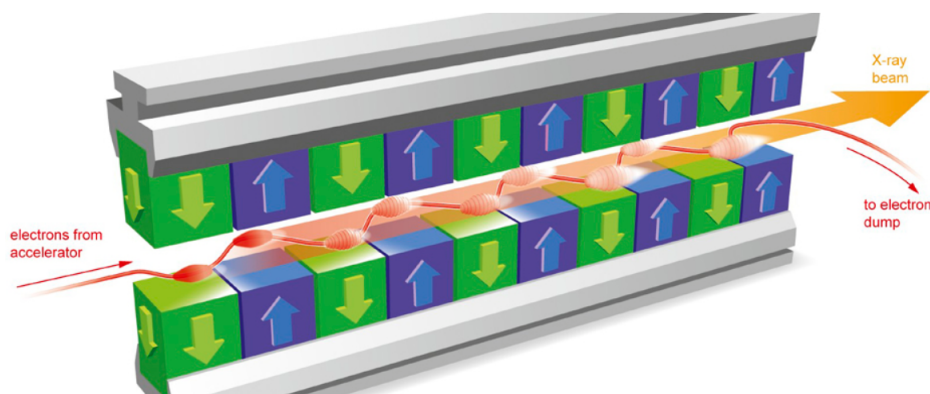


Figure 3.17: Enforced slalom course of the electrons due to a changing magnetic orientation in the undulator segments [153].

Subsequent to the undulators and up to the end of the experimental stations, a large variety of photon diagnostics and optics are installed to enable the measurement, manipulation and characterization of the X-ray photons at 4.5 MHz repetition (e.g. [154, 155, 156, 157, 158, 159]). The HED instrument consists of two main interaction chambers, IC1 and IC2 [27]. IC1 is designed as a large multi-purpose station with interchangeable target and detector setup configurations. In contrast, IC2 is a smaller and dedicated interaction chamber for diffraction experiments on diamond anvil cells, or shock targets incorporating HE-OL transport into the chamber and the capabilities of off-axis, or on-axis laser heating and temperature measurements [160]. Our study was performed at IC2, during the commissioning beamtime of both the laser heating setup, combining SPI 100 W Laser, Shimadzu high speed streak camera and the first half of the novel 4.5 MHz AGIPD detector modules [161].

Chapter 4

Sample material and synthesis

Geological samples of the Earth's interior and the exoplanets are much less accessible than samples related to the Earth's crust and surface. In fact there is only a very limited amount of material, obtained either from meteorites, volcanic eruptions or meteorite impacts, which allow us to take a direct look at conditions of high-pressure, high-temperature, variant oxygen fugacity, volatile interactions and very high stresses. However, those conditions are crucial for the stability of certain phases and their corresponding phase equilibria. Therefore, samples associated with extreme pressure and temperatures can seldom be obtained, or only in limited quantity and at high price. Instead, those need to be synthesized by matching and recreating their environmental requirements in the laboratory. It is necessary to quantify the experimental conditions during research at high-pressure and high-temperature and the new drivers, fast mDAC and piezo-driven DAC, introduce a new critical parameter to the conditions, which needs to be matched, respectively taken into account during the experiment analysis. This parameter is called kinetics and describes the available compression rate variations, meaning timescale and magnitude of the compression event. This makes inevitable to re-investigation even materials considered "well characterized" until now.

In this study, several materials were selected to investigate their kinetic response in fast membrane and piezo-driven DAC compression experiments. To estimate and define the kinetic effect calibrant materials, Au, Pt and Re were chosen as well as two common materials for gaskets, Re and stainless steel. Furthermore, common hcp phase samples were chosen, Zinc (Zn) and Iron (Fe), because they show a lattice parameter development based on the conditions (hydrostatic vs. non-hydrostatic) reached in the experiment [162, 163, 164], making them excellent tools to observe the possible effects of compression rate variations. In addition, Fe shows remnant bcc reflections within the stability field of hcp, whilst the conditions are non-hydrostatic [164], which could again help to determine the changes in the kinetic response of the material.

Last but not least, MgO (periclase), FeO (wüstite) and their solid solutions [Fe,Mg]O (fer-

ropericlaste) were chosen. $[\text{Fe,Mg}]\text{O}$ is a "simple" single oxide and the second most abundant mineral in Earth's interior ($\sim 20\%$), thus considered to strongly affect the Earth's interiors bulk properties. Therefore, extensive research has been performed on ferropericlaste, which revealed a complex phase diagram despite its simple composition. On the one hand, the phase diagram shows multiple phase transitions in pure FeO and high iron content solid solutions, within the pressure range of the Earth's mantle [Fig. 4.1] and electronic transitions (spin crossover). On the other hand, increasing MgO content moves the phase transitions towards higher onset pressures, corresponding to the pressure range predicted in the Earth's core or larger exoplanets and the lower iron content results in a spin crossover onset at lower pressures. Despite the extensive observations, large variations on the onset of structural and electronic transitions prevail even at ambient temperature, static compression and without taking into account the variation based on the composition of the solid solutions.

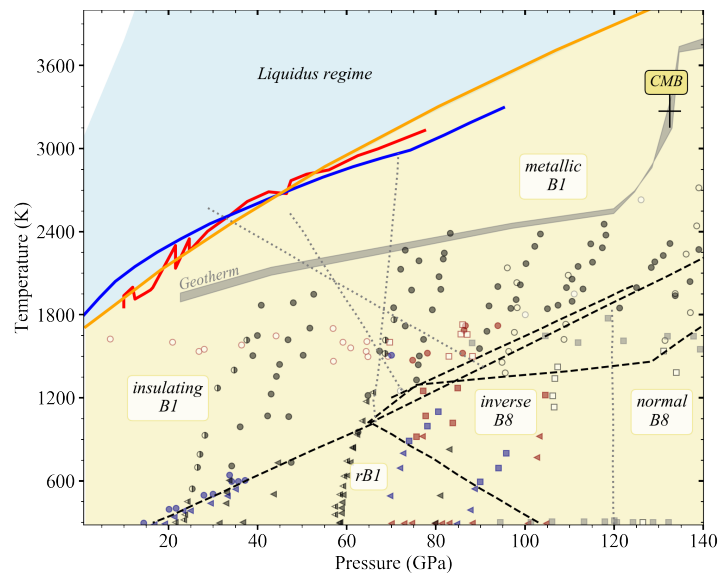


Figure 4.1: Wüstite (FeO) phase diagram across the Earth's mantle pressure range, modified after [165, 166, 167]. This phase diagram is based only on pure FeO experiments, albeit with a variety of cation deficiency (3-6%). Indicated are the different equilibrium phase stability fields, dashed black lines [165, 166, 167, 168, 169], the Earth's geotherm, gray shadowed [170] and the core mantle boundary (CMB). Shown is data on B1 (circles), rB1 (left triangles), B8 (squares) and B2 (stars). The color coding is as follows: black [171], half black [172], dark blue [165], dark red [168], open dark red [173], white [169], open black [174] and gray [166, 167]. In addition, dotted gray lines represent electronic transitions, insulator to metallic [165, 169, 171] and the inverse B8 – normal B8 [166, 167] transitions. Colored lines, solid blue [165], red [166, 167], orange [169] show melting curves.

The stable phase of FeO at Earth's crust and surface conditions are fully oxidized minerals, such as magnetite (Fe_3O_4), or hematite (Fe_2O_3), hence the metastable samples of $[\text{Fe,Mg}]\text{O}$ have to be synthesized in the laboratory. The other sample materials, Au, Pt, Re, Fe, Zn, and gaskets, stainless steel and Re, are purchasable with high purity. The following sections report the path of synthesis and characterization of the $[\text{Fe,Mg}]\text{O}$ solid solutions as well as the problems and the ideas related to them, which I researched at the chemistry laboratory at European XFEL and at the Bavarian Research Institute (BGI).

Table 4.1: Overview of the ferropericlase $[Fe,Mg]O$ synthesis in literature.

Ref.	material _{starting}	Methods
[168]	$Fe_2O_3 + MgO$	Furnace (1473 K; 24 h) + powder XRD + EMP
[175]	$Fe_2O_3 + MgO$	Furnace (1473 K; 100 h), Anvil press (2073 K; 25 GPa; 24 h) + XRD + Mössbauer
[176]	$FeC_2O_4 + MgO$	Furnace + Mössbauer
[177]	$^{57}FeO + MgO$	Furnace (1378-1478 K; 3x8 h) + EMP Mössbauer
[178]	$^{57}Fe_2O_3 + MgO$	Furnace (1473 K, -11 fO ₂) + Anvil press (1873 K; 14 GPa) + EMP + Mössbauer
[14]	$^{57}Fe_2O_3 + MgO$	Furnace (1673 K; -9 fO ₂ , 2x20 h)
[179]	$^{57}Fe_2O_3 + MgO$	Furnace (1673 K; -9 fO ₂ ; 2x20 h) + EMP
[180]	$^{57}FeO + MgO$	Furnace (1673 K; -9 fO ₂ ; 2x20 h) + EMP + Mössbauer
[181]		Piston cylinder apparatus
[182]	$^{57}Fe_2O_3 + MgO$	Furnace (1473 K; -11 fO ₂ , 24 h) + Anvil press (1673 K; 14 GPa) + EMP + Mössbauer
[183]	$FeO + MgO$	Furnace (1350 K; 12 h) + powder XRD + EMP
[184]	$^{57}Fe + MgO$	dissolve and precipitation + Furnace (1573 K; -7 → -11 fO ₂) + powder XRD

4.1 Synthesis of $[Mg,Fe]O$

4.1.1 Introduction

Synthesizing solid solutions is a common task needed to obtain samples for the analysis of Earth's interior properties. However, comparing the temperature, pressure, oxygen fugacity and the required timescales at those conditions vary drastically in the literature (Tab. 4.1). Even more concerning is that the variation is not only restricted to the conditions, but also affects fundamental choice of the starting material (FeO , Fe_2O_3 , Fe) and the initial preparation of the starting mixture, either via grinding or dissolving and precipitation.

The first approach of synthesis was by using the Large Volume Press (LVP) of ECB P61B at PETRA III and was performed to identify the possibility of higher pressure to compensate a shorter synthesis time. The 6/6 cube assembly configuration for the second stage anvils was chosen and the sample - a 20 mm³ stoichiometric mixture of in ethanol ground 80% MgO and 20% FeO powder - was embedded into a Pt-graphite capsule and further prepared for heating and compression [Fig. 4.2]. A temperature ramp profile of 14 hours [Tab 4.2] was chosen, using a maximum of 5 GPa and 1200 °C. The temperature was kept at 1200 °C for 6 hours during maximum compression. Afterwards the sample was quenched to ambient temperature in 6 seconds. The duration of heating was restricted by regulations due to the build

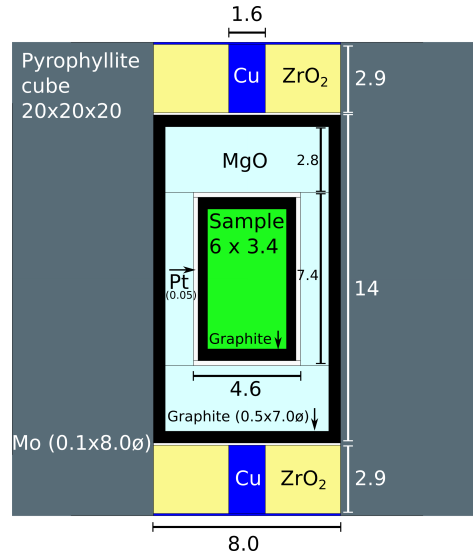


Figure 4.2: Cross section of the large volume press cell assembly with various components and $FeO + MgO$ sample

up phase of the ECB P21B, prohibiting high temperatures on the LVP without beamline scientists at the facility during the night. *Post-mortem* analysis was performed with a Zeiss Ultra55 Scanning Electron Microscope (SEM) at the IMPCM Sorbonne University. The SEM is equipped with a Schottky SEM-Field Emission Gun (FEG) and measurements were performed with an Energy Dispersive Spectroscopy Detector (X-EDS, Bruker Quantax) using 15 kV and a beam current of 10 nA. A map of the resulting material [Fig. 4.3] shows the elemental distribution. It is far from a homogeneous mixture and the diffusion of Mg/Fe seems to have barely started. In addition, a contamination with silica (SiO₂) was observed, originating most likely from grinding and mixing FeO and MgO in an agate mortar [Tab. 4.3].

Table 4.2: LVP setup parameters. 220 bar oil pressure and 800 watts corresponds to 5.1 GPa and ~1200° C at the sample.

Time (min)	Oil Pressure (bar)	Power /time (watts)/(min)
20	15	0 / 20
20	50	0 / 20
60	220	0 / 60
600	220	0 - 800 / 30 800 / 360 10 / 0.1 0 / 0.1
720	0	0

Table 4.3: SEM mass spectrum. All elements are given in mass percent (%).

Spectrum	O	Mg	Si	Fe
40	45.82	33.87	0.23	20.08
41	46.27	29.32	16.88	7.53
42	33.29	25.21	0.14	41.36
43	33.91	26.55	0.18	39.36
Mean value:	39.82	28.74	4.36	27.08
Sigma:	7.19	3.83	8.35	16.19
Sigma mean	3.60	1.91	4.17	8.09

Despite this failure, the approach provided information and insights into the synthesis as well as into the arising problems related to it. Most obvious is the contamination with Si in the sample material. Si is one of the most abundant elements in the Earth’s mantle, yet it is preserved as bridgmanite (Mg,Fe)SiO₃ or, at greater depth, as post-perovskite [REF]. Its incorporation in the sample would drastically alter the properties of our starting material as it would diminish our chance to explain the observations. Another insight is the state of diffusion and the homogeneity of the sample material after the process. It shows that the grain size in combination with the time period at high temperature are much more important for spreading the diffusion process than the imposed pressure, which can be used to improve the grain size and the sample purity.

A Different approach was chosen as described by *Longo et al., 2011* [184]. This approach uses gas-mixing furnaces to keep steady temperature and oxygen fugacity conditions for long timescales (days to weeks), allowing the diffusion process to spread through the whole sample material. In addition, it is using a wet chemistry approach as a basis to obtain fine grained mixtures of MgO and FeO through dissolution and precipitation. This approach reduces

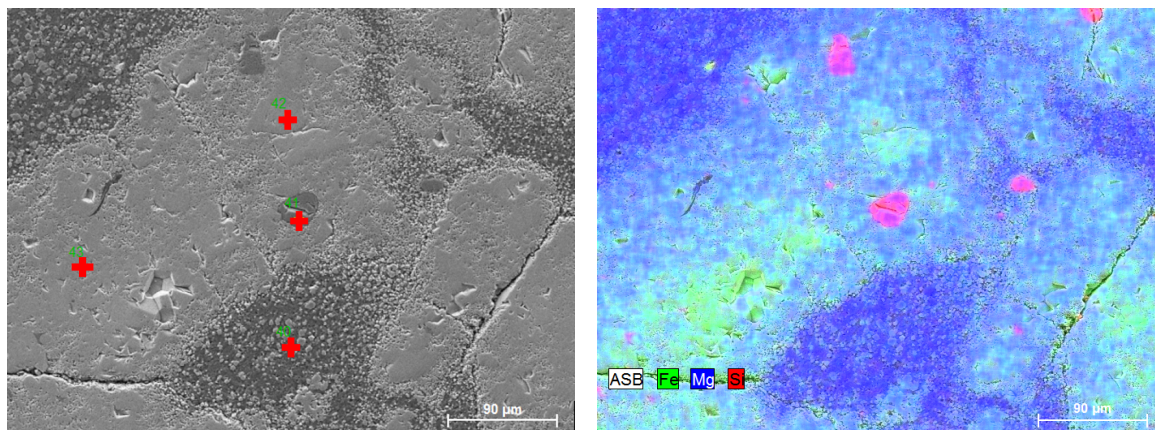


Figure 4.3: Sample composition after the initial test with the LVP. (Left) High resolution image of the sample and markers of the SEM spectrum measurements [4.3] and (Right) resulting SEM map showing non-homogeneous composition of MgO, FeO and SiO contamination.

the possibility for contamination during the grinding and the fine grain size and larger grain boundary area decrease the required time in the gas-mixing furnaces [185]. Here, decreasing the time spent in gas-mixing furnaces was the main reason for choosing this approach, as there is a lack of gas-mixing furnaces available at European XFEL and DESY.

4.1.2 The wet chemistry approach

The wet chemistry approach by *Longo et al., 2011* [184] can be divided into several steps: 1. Dissolve a stoichiometric mixture of Fe and Mg metals in HNO₃; 2. Slowly evaporate the HNO₃ at 50 °C using a hot plate; 3. Add NH₄OH for oxide precipitation; 4. Remove excess HNO₃ and NH₄OH with the help of a Bunsen Burner (1200 - 1500 °C); 5. Use the Gas-mixing furnaces at 1300 °C and controlled oxygen fugacity of 10⁻⁷ - 10⁻¹¹ for solid state diffusion and homogeneous samples; 6. Use of multianvil apparatus to obtain coarse grains for electron microprobe analysis.

Following this approach, different concentrations of HNO₃ were prepared and tested to dissolve the starting material (Fe, or FeO). Unfortunately, concentrations above 20 % resulted in direct Fe²⁺ oxidation independent of the feed rate. In addition, the use of a hotplate in combination with concentrations below 20 % resulted in oxidation, even with a slight temperature increase up to 40 °C. Full evaporation of the solution took between 1-2 days, as reported by *Longo et al., 2011* [184].

A discussion with collaborators of Dr. Longo and her prior supervisor lead us to change our setup. Now it consisted of a water cooled rotary evaporator (Hei-Vap, Heidolph Instruments) in combination with a Schlenk line and vacuum pump to allow for a constant flux of nitrogen and cooling that prevents oxidation [Fig. 4.4]. This setup enabled Fe²⁺ dissolution of both FeO and Fe with HNO₃ concentrations of 20, 25 or 30 %, resulting in a light greenish Fe²⁺ solvent. Thereafter, MgO was slowly added into the mixture and the vacuum

pump was activated to remove the solvent and start precipitation of fine grained FeO, Fe and MgO powder. Nevertheless, despite variations of the evaporation rate, nitrogen flow rate and amount of NH_4OH the sample material exhibited some amount of reduction, resulting in a green-yellow gel-like mixture of MgO, FeO and an amount of Fe_2O_3 , whereupon the excess amount of HNO_3 and NH_4OH was removed with the help of a Bunsen burner.



Figure 4.4: Setup of the Rotary Evaporator connected to the Schlenk line and vacuum pump. The Schlenk line provides nitrogen flow into the system and the ice cold water bath prevents oxidation of the precipitating mixture.

4.1.3 Gas-mixing experiments

Solid state diffusion

Solid state diffusion is quite similar to the creep mechanism, albeit it is the thermally activated random motion of particles (atoms, ions, molecules) in the material at atomic scales (Fig 4.5). Especially in solids, this is the only mechanism of particles that changes their location within the mineral, based on concentration inhomogeneities.

The process of mass transport by diffusion has been described by Fick's first law [29] as the mass flux of a compound diffusing through the material in the opposite direction of a concentration gradient and depends on the distance it has to cover before homogeneity is achieved within the material:

$$J = -D \frac{\Delta C}{\Delta x} \quad (4.1)$$

where J is the diffusion mass flux, D the diffusion coefficient, or diffusivity, C describes the concentration difference and x is the distance related to a concentration gradient [186]. This means that the diffusion mass flux is an ever changing variable during the homogenisation process, where the concentration gradient decreases and the diffusion front progresses through

the material.

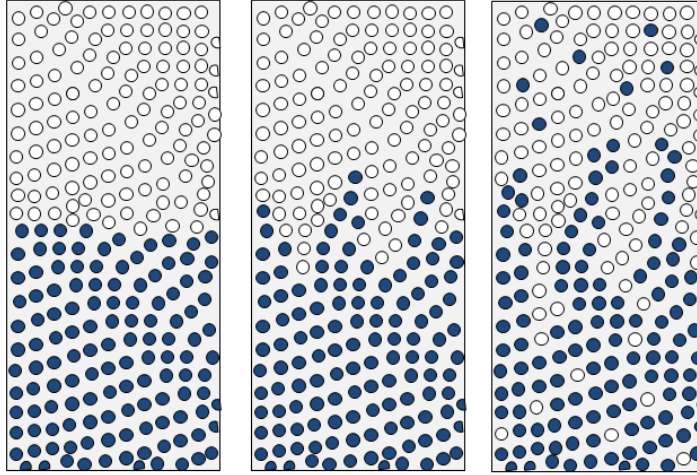


Figure 4.5: Random ionic volume diffusion of particles. Initial state (Left) with particles of species one, in blue (i.e. Fe^{2+}) and particles of species two, in white (i.e. Mg^{2+}). The concentration gradient between both species leads to a net flux of species one intruding into species two and species two intruding into species one (Center). As time passes (Right) both species will intermix with each other and start to homogenize (modified after [186]).

The diffusion coefficient is not a constant. Instead it needs to be determined depending on the properties (i.e composition, structure, bond strength, valency and ionic radius) of the compound/materials and the environmental conditions (i.e temperature, pressure and oxygen fugacity). The diffusion coefficient is mostly affected by the amount of vacancies (defects) in the periodic arrangement of atoms accepting the relocated particles. [186, 187].

Based on the Arrhenius relation and taking into account experimental diffusivity uncertainties (very good data $\leq 10\%$, normal experiments 30%) the temperature and pressure dependence of the diffusivity can be expressed by:

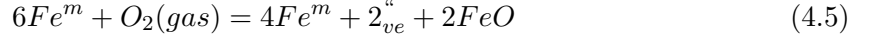
$$D = D_0 \exp \left[-\frac{E}{RT} \right] \quad (4.2)$$

$$D = D_0 \exp \left[-\frac{E + P\Delta V}{RT} \right] \quad (4.3)$$

where T is the temperature (K), D_0 is a positive pre-exponential factor of D for $T = \infty$, E is the activation energy, R is the universal gas constant and $E + P\Delta V$ is the activation volume at a given pressure P [186, 188]. Whilst the temperature dependence results in a linear positive diffusivity trend, with higher temperature, the pressure dependence is non-linear and can increase or decrease the resulting diffusivity [186, 187] dependent on the compound/material investigated. Oxygen fugacity can change the valence state of multivalent systems affecting the diffusivity in opposing directions. On the one hand, higher valency results in higher bond strength, but increasing numbers of vacancies and on the other hand decreasing valency results in lower bond strength, but less vacancies. The diffusivity of a multivalent element can be written as:

$$D_{\text{element}} = X_x D_x + X_y D_y \quad (4.4)$$

where $X_i = \frac{Element^i}{Element^i + Element^j}$ and x, respectively, y are valence states of the element within the material [189]. The effect of oxidation on the amount of vacancies can be demonstrated by the example of iron oxidation [186]:



where Fe^m describes metallic iron and $2_{ve}''$ the number of resulting vacancies in the periodic ordering by oxidation. As mentioned before, vacancies (defects; see chapter 2.2.3) accept moving ions and are the main pathways through a material/compound enabling higher diffusion rates.

Here we are using gas-mixing furnaces to control temperature and oxygen fugacity in compressed pellets of fine grained powder. Diffusion types utilized during the synthesis in gas-mixing experiments are ionic volume diffusion (Fig 4.5), intergrain exchange of Fe^{2+} and Mg^{2+} , and grain boundary diffusion (Fig 4.6)[186, 190]. Based on the two compound system MgO and Fe, FeO or Fe_2O_3 the intergrain diffusivity depends on the exchange coefficient of magnesium and iron resulting in:

$$D_{i-j} = \frac{D_i^* D_j^*}{X_i D_i^* + X_j D_j^*} \left(1 + \frac{\Delta \ln \gamma_i}{\Delta X_i} \right) \quad (4.6)$$

where D_{i-j} is the diffusion exchange coefficient of the two atomic species (Mg, Fe) in the compound, X is the mole fraction of the species, D^* is the individual diffusion coefficients, including all above mentioned dependencies, and γ the thermodynamic activity of the species [191]. However, even at elevated temperatures and controlled oxygen fugacity, the ionic volume diffusion rate for solid materials is low [192]. The main process utilized in the gas-mixing furnaces is grain boundary diffusion, reaching diffusion rates several magnitudes higher than ionic volume diffusion. Grain boundaries can be referred to as few atoms thick interruptions of the periodic arrangement of atoms existing along the boundary front. Those interruptions result in extended defect sides, enabling fast diffusion pathways, and are distinguishable by lower coordination numbers and variant bounding length between the atoms [185].

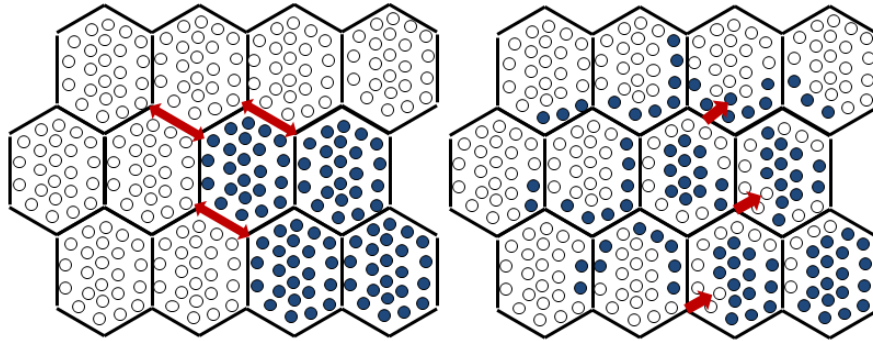


Figure 4.6: Interruptions of the periodic arrangement of atoms along grain boundaries represent preferred diffusion paths (left) and enable fast re-localization of ions. The diffusion rate is many orders of magnitude higher than volume diffusion transporting the arriving ions into the grain (right).

Experiments

The gas-mixing experiments and sample characterization have been carried out at the Bavarian Research Institute (BGI), Bayreuth, Germany and with funding of the DFG Core Facility project. A total of 3 weeks had been approved, the first one for testing and learning the procedure and the other two weeks to carry out preparation, loading of the gas-mixing furnaces and preparation for characterization.

Various stoichiometric mixtures of Fe, FeO or Fe₂O₃ and MgO were discussed and prepared, due to the problems in the reproduction of the wet chemistry approach. FeO based starting materials were the first idea, however it shows a non-stoichiometry in Fe²⁺ and Fe³⁺ [193], which would introduce uncertainties in the weighted amount. It was replaced by Fe₂O₃ and Fe (99.995 %). Furthermore, ⁵⁷Fe₂O₃ was induced into solid solutions with low iron content in order to increase Fe signal in the characterization measurements and to enable a more universal usage of small sample amounts in e.g. synchrotron studies using Mössbauer or X-ray emission approaches.

During the first week only manually ground mixtures could be used due to the lack of results from the wet chemistry process. Precipitated mixtures were available in the later two weeks. This time, zirconium mortars (94.7% ZrO₂ + 5.2% Yr₂O₃) were used in the grinding and mixing process to prevent reoccurrence of Si contamination. The stoichiometric mixtures were prepared for the gas-mixing furnace, pressing them into multiple pellets of ≈ 200 mg with the size of ∅ 5 mm by 3-5 mm using a pellet press with 20 kN force. The compaction of the fine grained powder into pellets enlarges the grain boundary front and enables higher diffusion rates in the furnaces.

Platinum wire was used to create a holder for the pellets inside the gas-mixing furnaces. The holder was attached to a ceramic rod with platinum hooks, keeping the sample well centered in the furnaces hot spot. This setup is designed to drop-quench the sample after the synthesis. It keeps the controlled oxygen fugacity atmosphere in a recovery vessel and thus prevents the fast oxidation of the hot sample material while cooling down.

The gas-mixing furnace [Fig 4.7] was set to 1573 K and CO/CO₂ gas-flow conditions were calculated in respect of temperature, iron concentration and the iron/wüstite oxygen fugacity buffer equilibrium after *Eugster and Wones (1962)*:

$$\log(f_{O_2})[IW] = -27215 \times T^{-1} + 6.57 \quad (4.7)$$

$$\mu_{O_2}[IW] = \log(f_{O_2})[IW] \times R \frac{J}{mol} \times T \times \ln(10) \quad (4.8)$$

$$\mu_{O_2}[Mg_{(x)}Fe_{(1-x)}] \frac{kJ}{mol} = \mu_{O_2}[IW] + 2(xMgO)^2 \times [(5.76 + 3.47 \times 10^{-3} \times T) + 0.41(3 - 4(xMgO))] \quad (4.9)$$

where R is the ideal gas constant, T the temperature (K) selected for the experiment and $xMgO$ the concentration of Mg in the solid solution (e.g. 10 % or 90 %).

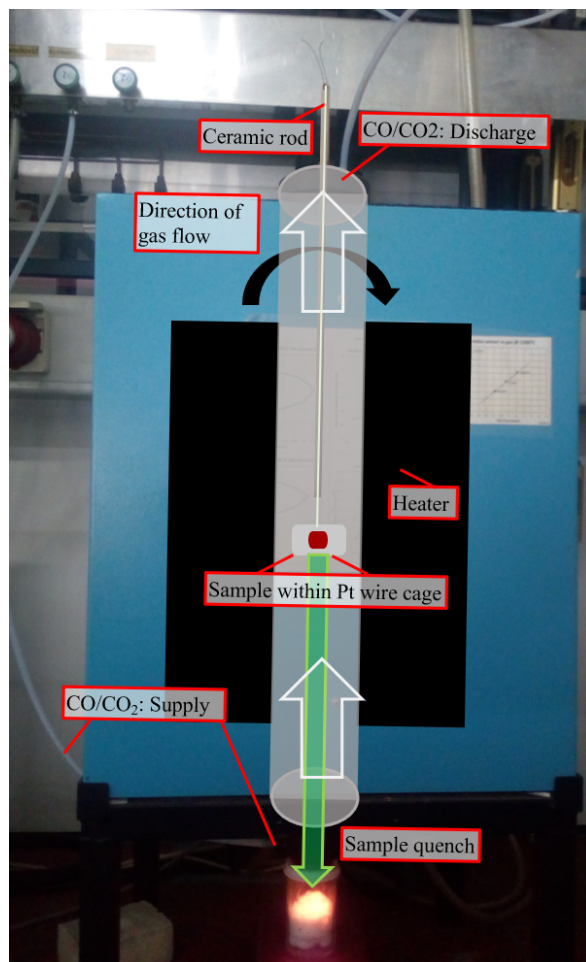


Figure 4.7: Schematic overview of the gas-mixing furnaces at BGI. The sample is inserted attached to platinum hooks on a ceramic rod, keeping the sample in the center of the furnace. Once the furnace is closed, the gas-flow, from bottom to top, is regulated and the sample is kept in pre-determined CO_2/CO atmosphere. Afterwards, the platinum wires can be shaken to release the sample and sample container of the hooks whilst still keeping the sample in oxygen free atmosphere during quench.

A variety of durations of keeping the sample within the furnace was tested during the three weeks at BGI ranging from 12 h to 48 h for the manually ground samples and 24 h for the samples obtained by precipitation. An overview of all runs conducted during the three weeks can be found in [Supp.Tab. 1].

4.1.4 Mössbauer spectroscopy and XRD

Sample characterization was performed with Mössbauer spectroscopy and X-ray powder diffraction after the recovery from the gas-mixing furnaces. Mössbauer spectroscopy was chosen to identify the amount of remnant Fe^{3+} and magnetic components in the mixture, whereas

X-ray powder diffraction (XRD) was chosen in order to identify the structure of possible magnetic or remnant phases. The results of the X-ray and Mössbauer analysis were implemented in the following gas-mixing runs adjusting oxygen fugacity, or duration of the synthesis, if necessary.

Mössbauer spectroscopy relies on the Mössbauer effect [194, 195], describing a zero-phonon translation gamma-ray emission of solid samples as their response to resonant absorption. The effective mass of a nuclei in a solid sample becomes the effective mass of the whole rigid crystal structure. The incident and emitted gamma rays have the same energy, thus prevent nuclei recoil and crystal lattice vibrations to a degree of zero-phonon translation and enable the direct observation of the sample valence state and the atom coordination [196].

Mössbauer spectra were collected for velocities of ± 12 mm/s at room temperature, using a constant acceleration Mössbauer spectrometer with a 50 mCi ^{57}Co radiation source in a $6\ \mu\text{m}$ Re matrix [Fig. 4.8]. Calibrations were performed using a pure ^{57}Fe -foil and the fine ground powder sample, in quantities between 18-66 mg, which were mounted in 12 mm X-ray spectroscopy sample holders. The sample quantities were calculated to provide an actual Mössbauer thickness of 10, enabling reasonable data resolution and acquisition times based on the amount of ^{57}Fe and Fe in the sample material. The first results obtained during the initial week of testing showed that timescales of 24 h are insufficient for the grounded mixtures, which still contained hyperfine (Zeeman) splitting as a result of remnant magnetic phases in the sample. Those samples needed an additional 24 h in the gas-mixing furnaces, or could be kept in the furnaces for 48 h straight, removing all magnetic properties and further decreasing the amount of Fe^{3+} . In contrast, the samples obtained by dissolving and precipitation (the wet chemistry approach) resulted in non-magnetic samples with low Fe^{3+} contribution in the Mössbauer spectra after a single 24 h run in the gas-mixing furnace.

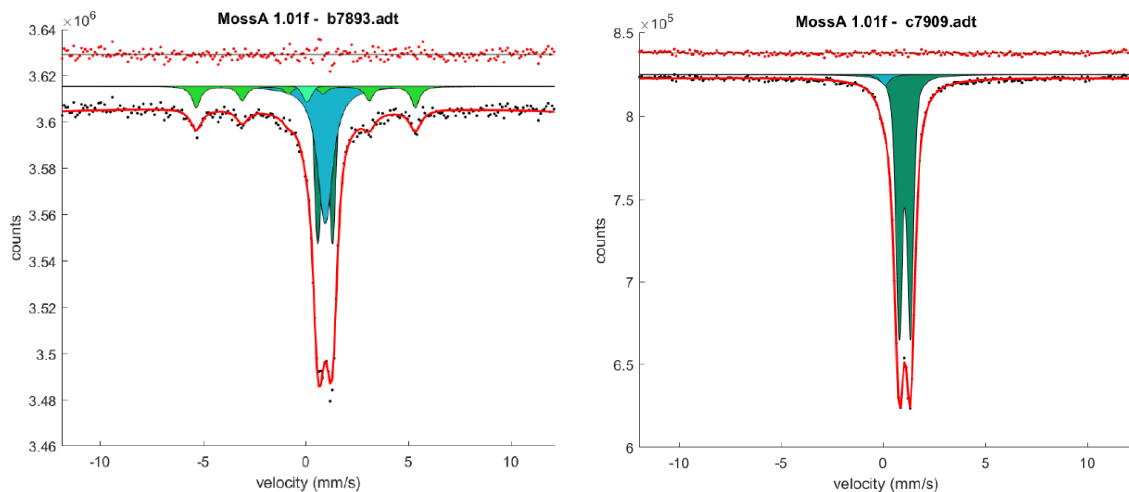


Figure 4.8: Representative Mössbauer spectra of FeO (left) and $\text{Fe}_{10}\text{Mg}_{90}\text{O}$ (right). FeO shows the full range of magnetic ordering (Zeeman splitting, light green sixlet), Fe^{3+} and Fe^{2+} , whereas $\text{Fe}_{10}\text{Mg}_{90}\text{O}$ shows almost pure Fe^{2+} with 3 wt% Fe^{3+} after 48 h in the gas-mixing furnace.

X-ray powder diffraction images [Fig. 4.9] were collected using a Philips X'Pert Pro X-ray diffraction system equipped with a Philips X'celerator detector. Operation was performed at 40 kV and 40 mA with monochromated $\text{CoK}\alpha_1$ ($\lambda = 1.78897 \text{ \AA}$) radiation in reflection mode with a symmetrically cut, curved Johansson Ge(111) crystal. The diffraction pattern show remnant, parasitic spinel type phases in manually ground starting material recovered from the gas-mixing furnace after ≤ 24 h and the samples had to be reintroduced into the furnaces for an additional 24 h cycle. Afterwards, they showed only fcc phase reflections. Complete reduction and synthesis of fcc phase $[\text{Fe,Mg}]\text{O}$ solid solutions could also be achieved by keeping the manually ground starting material inside the gas-mixing furnaces for 48 h straight. In contrast, the precipitated starting material showed pure fcc diffraction images after 24 h, reducing the time in the gas-mixing furnaces to a half.

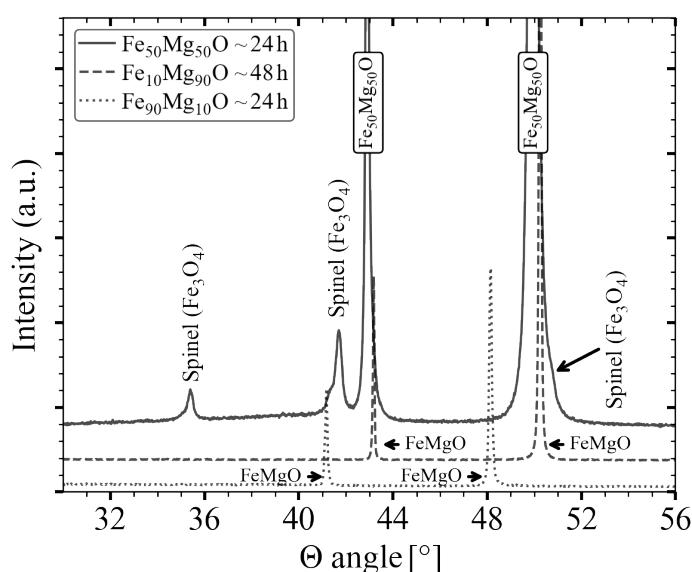


Figure 4.9: Powder diffraction pattern of $[\text{Fe,Mg}]\text{O}$ solid solutions after 24 h (solid and dotted line) or 48 h (dashed line) in the gas mixing furnace. The grounded sample (solid dashed line) shows remnant spinel-type diffraction peaks, whilst longer heating (dashed line) or dissolution and precipitation (dotted line) created $[\text{Fe,Mg}]\text{O}$ with pure fcc structure.

Chapter 5

Results

X-ray diffraction experiment have been performed on common pressure calibration materials (gold (Au), Platinum (Pt)), gasket materials (stainless steel (SS), Rhenium (Re)), simple hexagonal closed packed metals (Re, zinc (Zn), iron (Fe)) as well as simple oxides: wüstite (FeO), periclase (MgO) and the ferropericlase solid solution (Fe,Mg)O at the Extreme Conditions Beamline (ECB) P02.2, at PETRA III, DESY, Hamburg, Germany.

Either membrane or piezo-actuator drivers were used to enable a variety of compression rates, slow (≤ 0.1 GPa/s) to fast (tens of TPa/s). All experiments were conducted in symmetric piston-cylinder-type DACs, equipped with 0.04-0.3 mm culet diamonds and the samples, either pure powder, or powder in combination with Ne (PTM), were loaded into Re, or SS gaskets indented to 0.2-0.3 μm thickness. The samples were probed by a 8 (horizontal) x 3 (vertical) μm^2 X-ray beam with a wavelength of 0.4847 Å (25.6 keV) and the sample-detector distance (SDD) as well as

Table 5.1: Overview of all performed loadings and runs at the ECB P02.2 beamline, PETRA III, DESY.

Sample	Loadings	mDAC	dDAC	Runs
Rhenium (Re)	9	5	4	18
Gold (Au)	5		5	12
Platinum (Pt)	7	3	4	9
Zinc (Zn)	4		4	8
Iron (Fe)	7		7	7
Periclase (MgO)	1		1	7
Ferropericlase (Fe ₁₀)	3		3	4
Ferropericlase (Fe ₂₀)	5	5 LH ^{*1}		5
Ferropericlase (Fe ₄₀)	1		1	1
Magnesiowüstite (Fe ₈₀)	2		2	2
Wüstite (FeO)	2		2	2
Total	46	13	33	75

^{*1} Laser heating experiments at 42.7 keV

instrumental peak broadening correction was calibrated either from NIST SRM 674a (CeO₂, mDAC) or NIST SRM 647b (Cr₂O₃, dDAC). In addition, first continuous LH experiments on Fe₂₀Mg₈₀O were performed at 42.7 keV with a beam size of 2 (horizontal) x 2 (vertical) μm^2 , focused by KB-mirrors. These experiments extend the spin crossover observations, at high resolution, to the conditions occurring in the Earth's interior. A general overview of the performed loadings and the resulting number of runs is given [Tab. 5.1].

Table 5.2: Summary of EoS parameters, single-crystal elastic constants (C_{ij}), Debye-temperature, Grüneisen parameter and structure factor used in the analysis.

Sample	Symmetry	V_0 (Å)	K (GPa)	K'	Θ_{D_0} (K)	γ	q	Ref.
Re	hcp	29.4056	359	5.43				[197]
Pt	fcc	60.38	277.0	4.95	230	2.72	0.5	[59]
Au	fcc	67.8474	166.65	5.4823				[198]
Zn	hcp	30.424* ¹	56.0	5.0				[199]
Fe	bcc	23.5511	165.0	5.33				[200]
	hcp	22.3332	165.0	5.33				[200]
FeO	B1	79.617	149.4	3.6				[201]
MgO	B1	74.185	168.80	4.2516				[202]
[Fe,Mg]O	B1* ²	75.62	161.4	3.98				[175]
	rB1* ³	60.0767	150.0	4				courtesy Speziale
KCl	B2	53.53	23.7	4.4	235* ⁴	2.3* ⁵	0.8* ⁵	[203]

Sample	c_{11} (GPa)	c_{12} (GPa)	c_{13} (GPa)	c_{33} (GPa)	c_{44} (GPa)	c_{66} (GPa)		
Re	612.5	270	206	682.7	162.5	$\frac{c_{11}-c_{12}}{2}$		[204]
	$+5 \times P$	$+2.9 \times P$	$+5.8 \times P$	$+2.3 \times P$	$+6.1 \times P$	$+1.1 \times P$		[205]
Pt	351.2	257.5			73.07			[206]
	$+6.782 \times P$	$+5.51 \times P$			$+1.927 \times P$			[206]
Au	192.2	163.4			41.8			[207]
	$+6.71 \times P$	$+5.85 \times P$			$+1.83 \times P$			[208]

*¹[209]; *² [Fe₁₀, Mg₉₀]O; *³ [Fe₉₀, Mg₁₀]O; *⁴[210]; *⁵[211]

In this chapter, I present the results of the individual sample materials, with a focus on the development of stresses, onset and timescales of phase transitions and spin crossovers, as well as the general lattice parameter, hence volume, development at different compression rates, using established EoS, single-crystal elastic constants (c_{ij}), elastic compliance, Young's modulus, Shear modulus, structure factor, Grüneisen parameter and Debye temperature from literature [Tab. 5.2]. Moreover, I present first pulse-to-pulse resolved benchmark results on Pt and Mg₁₀Fe₉₀O at 2.25 MHz repetition rate X-ray diffraction experiments performed at the HED instrument, European XFEL.

5.1 X-ray diffraction at the ECB P02.2

X-ray diffraction images were obtained across both mDAC and dDAC experiments. In the mDAC experiments the XRD images were collected on the large area Perkin Elmer XRD 1621 detector using the general-purpose setup station at the ECB P02.2, at SDD of about 350 mm. A total of 1100 - 5600 raw images taken with the exposure time of 266 ms were recorded as a function of pressure during each experiment. Representative raw images of Pt

and Re are illustrated [Fig. 5.1] and show the recorded azimuthal range (360°) and usable Bragg reflections during the compression events.

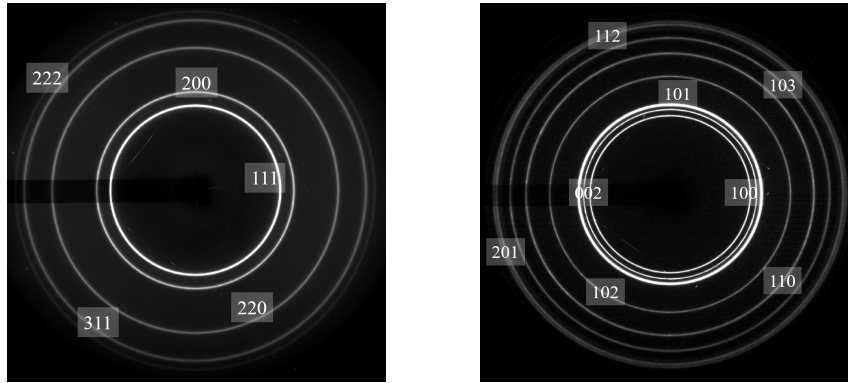


Figure 5.1: Raw X-ray diffraction images of Pt (left) and Re (right) obtained via Perkin Elmer XRD 1621 during mDAC compression experiments. Bragg reflection lines usable during the analysis are indexed and could be obtained for the whole 360° azimuthal range.

The compression ramps are presented as contour plots of stacked, azimuthal integrated diffraction patterns as a function of time, starting from the bottom coinciding with the start of the compression ramp [Fig. 5.2]. In this representation, the pressure oscillation (pressure increase and decrease) can be observed as a 2θ shift of the diffraction lines as well as their intensity variations due to the development of lattice preferred orientation (LPO).

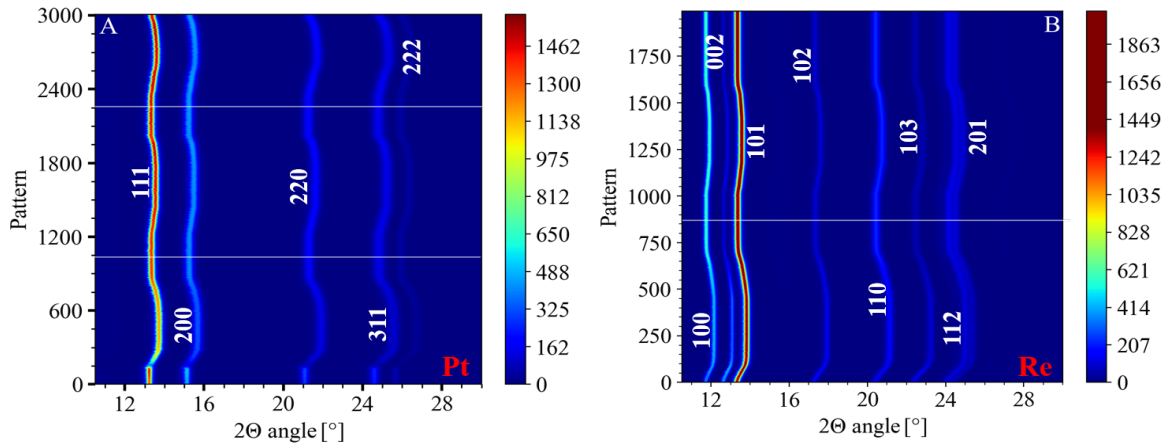


Figure 5.2: Contour plots of integrated diffraction patterns of A) Pt in Re gasket at a compression rate of 0.2 GPa/s and B) Re in stainless steel gasket at 2.6 GPa/s depicting pressure variations during the experimental runs. The colorbar corresponds to diffraction intensity.

dDAC experiments have been performed using two LAMBDA GaAs 2M detectors, at SDD 311-314mm and in off-centered detector geometry enabling an approximate 2θ coverage for LAMBDA 2 (L2) of $10-25^\circ$ and for LAMBDA 1 (L1) of $15-30^\circ$ with an azimuthal range of 70° . Off-centering of the Lambda detectors with respect of the X-ray axis allowed for higher 2θ range to be covered compared to the centered geometry. Raw XRD images are illustrated [Fig. 5.3] showing the observable Bragg reflections and azimuthal coverage on both detector arrays, whereby the off-centered geometry results in a different number and range of Bragg reflections.

A total of 8 to 420 diffraction images were recorded with exposures ranging from 0.5- 100 ms. An example of contour plots based on the azimuthal integrated XRD pattern are depicted [Fig. 5.4] and show the 2Θ shift of the diffraction lines and the variation in diffraction peak intensity during the compression runs.

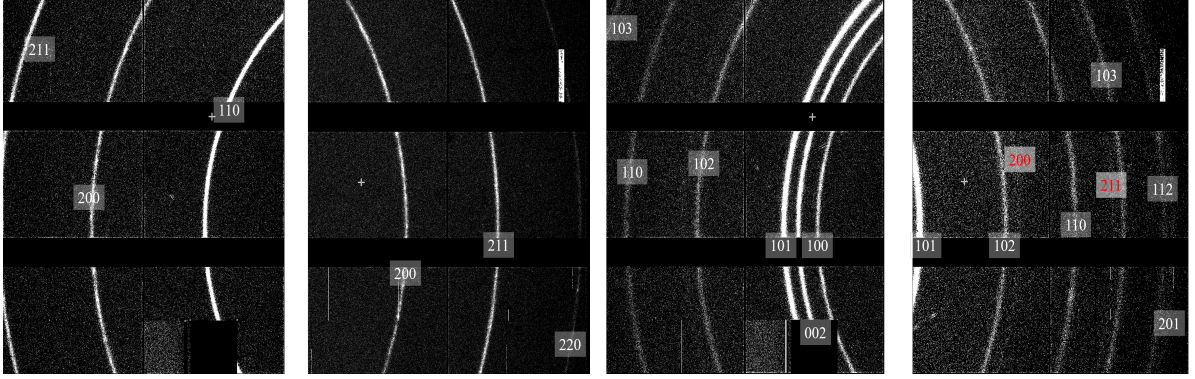


Figure 5.3: Raw X-ray diffraction images of (left) α -Fe (bcc) and (right) ϵ -Fe (hcp) obtained via LAMBDA GaAs 2M detectors during dDAC compression, showing the variance in refinable Bragg reflections and azimuthal coverage of the LAMBDA detector arrays.

Only diffraction lines with sufficient intensities were selected and used to obtain peak position and full width at half maximum (FWHM) information. Larger quantity of diffraction lines was available during mDAC runs compared to the dDAC runs, because of the higher peak intensity by longer exposure times as well as the coverage of the whole 360° azimuthal range. In fact, in some dDAC runs the abundance and/or intensity of diffraction lines was insufficient to refine lattice parameter and unit cell volumes.

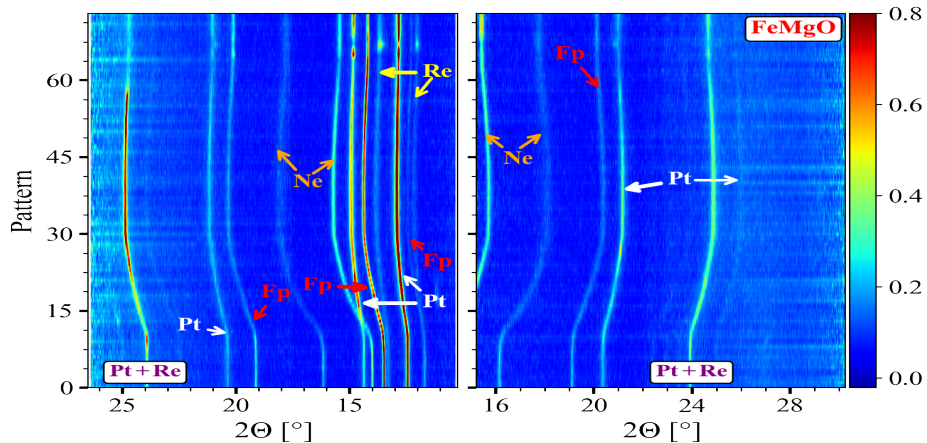


Figure 5.4: Example of contour plots of integrated diffraction patterns of a $\text{Fe}_{10}\text{Mg}_{90}\text{O} + \text{PtNe}[\text{Re}]$ run at 76 GPa/s in a dDAC, depicting the variation in observable Bragg reflections and reflection intensity on the detectors, due to the off-centered setup. Furthermore, it shows the good resolution of the diffraction lines despite the low diffraction intensity from short exposure times and low azimuthal coverage.

In all experiments with sufficient refinable lattice parameter the differential stress and micro-strain evolution was investigated following the line-width [206] and/or line-shift [212] approach [Chapter 3.4]

5.1.1 Platinum

Platinum (Pt) is a well studied pressure calibrant and a total of 7 runs were performed [Tab. 5.3], three loadings using mDAC and two dDAC. Maximum pressures between 36-91 GPa were reached. Pressure were determined using EoS of Fei et al., 2007 [59].

Table 5.3: *Experimental run conditions of Pt*

Run mDAC	Sample	Gasket	culet	P_{start}	Exposure	Membrane	comp. rate $_{\emptyset}$	strain rate	PTM
			(mm)	(GPa)	(ms)	$\frac{bar}{min}$	GPa/s	s^{-1}	
Pt no4	Pt	Re	0.3	4	266	40	0.85	2×10^{-3}	-
Pt no17	Pt	Re	0.3	8	266	40	0.85	2×10^{-3}	Ne
Pt no172	Pt	Re	0.3	2	266	1	0.23	4×10^{-4}	-
Run dDAC	Sample	Gasket	culet	P_{start}	Exposure	Piezo	comp. rate $_{\emptyset}$	strain rate	PTM
			(mm)	(GPa)	(ms)	(Volt)		s^{-1}	
Pt r1	Pt	Re	0.3	0.5	10	1000	36	9×10^{-2}	Ne
Pt r2	Pt	Re	0.3	15	10	1000	38	8×10^{-2}	Ne
Pt r3	Pt	Re	0.3	23	10	1000	27	5×10^{-2}	Ne
Pt*1	Pt	Re	0.3	20	10	1000	394	8×10^{-1}	-

*1 diamonds failed during compression

The membrane driven pressure ramps of Pt in Re gasket are summarized in [Fig. 5.5]. The average compression rates vary from slow (~ 0.23 GPa/s) to most rapid (5.6 GPa/s). The micro-strain derived from [Eq. 3.18] is shown as a function of pressure and compression rate, which is given as (apparent) pressure derivative with time. In the slow Pt[Re] run ($4 \times 10^{-4} s^{-1}$) an initial fast increase of the micro-strain can be observed with onset of compression and within the pressure range of 5-8 GPa. Upon further compression, the micro-strain is relatively independent of pressure and starts decreasing on decompression. The initial increase of micro-strain precedes the maximum pressure conditions and the fastest compression rates are observed at ~ 35 GPa.

The faster run ($2 \times 10^{-3} s^{-1}$) shows also the initial fast increase at the initiation of the compression, but here the micro-strain development correlates with the compression rate maximum. Upon several further pressure decrease-increase cycles, micro-strain becomes relatively independent of the pressure exhibiting only minor maxima or minima during compression or decompression periods.

In the run with Ne PTM ($2 \times 10^{-3} s^{-1}$) the micro-strain in the sample increases step-wise correlating with two peaks in the compression rate, however the maximum is reached at much higher absolute pressures (>75 GPa) compared to the runs without PTM. In this case, the micro-strain most likely reflects the hardening of the PTM which induces plasticity in the sample.

At somewhat higher compression rates achieved using the dDAC with Ne PTM (strain rate one order of magnitude higher) [Fig. 5.6], micro-strain in the sample steadily increases with pressure, reaching the maximum at the pressure plateau. Here, the three pressure cycles

were performed on the same sample loading.

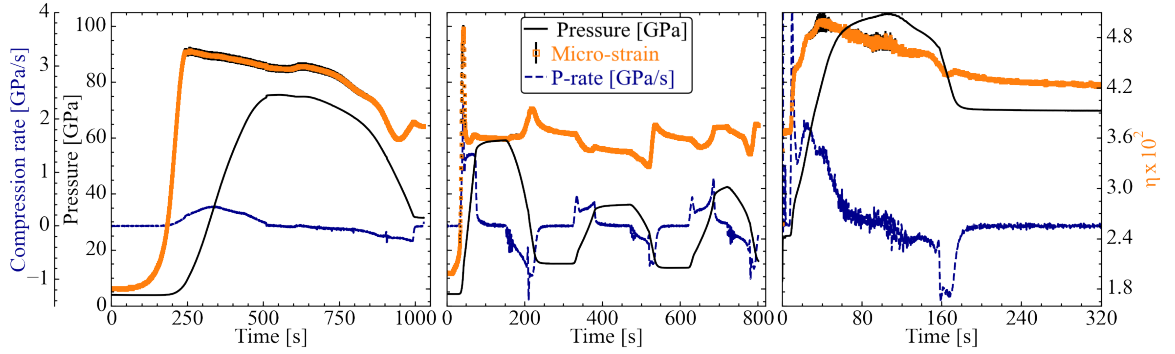


Figure 5.5: Pressure, micro-strain and compression rate in the mDAC runs. Form left to right: Pt[Re] ($4 \times 10^{-4} \text{s}^{-1}$); Pt[Re] ($2 \times 10^{-3} \text{s}^{-1}$) and PtNe[Re] ($2 \times 10^{-3} \text{s}^{-1}$) strain rate.

An additional run was performed with Pt without any PTM in the dDAC. Unfortunately, it ended in a failure of the diamonds during the compression event and a comparison with the non-hydrostatic slower runs in mDAC is possible only based on a very low amount of XRD images. Nevertheless, the micro-strain vs P trend of both runs with Ne in mDAC or dDAC data are very similar and an overview of the development during the initial compression events is depicted [Fig. 5.7], comparing the micro-strain as a function of pressure for all the Pt runs. The compression starts from 20 GPa, where it closely matches with the observations in the slow mDAC run ($4 \times 10^{-4} \text{s}^{-1}$), yet the following trend shows a further micro-strain increase, hence a pressure dependence in contrast to the slower run.

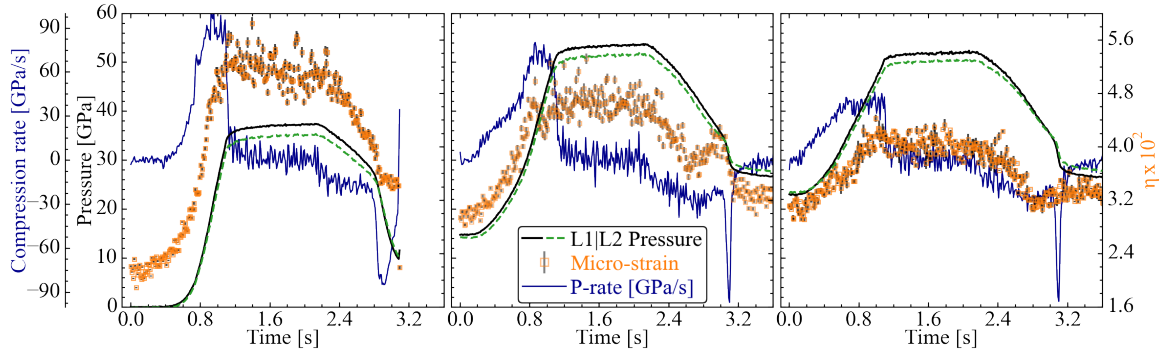


Figure 5.6: Pressure, micro-strain and compression rate in the dDAC runs. Form left to right the three consecutive ramp cycles of: PtNe[Re] ($9 \times 10^{-2} \text{s}^{-1}$); PtNe[Re] ($8 \times 10^{-2} \text{s}^{-1}$) and PtNe[Re] ($5 \times 10^{-2} \text{s}^{-1}$) strain rate.

From the line-width analysis the effective grain size can be obtained from the intercepts as described in chapter 3.4. In the runs the initial grain size [Fig. 5.7] is found to be 320 ± 40 nm, even in consecutive compression events in the dDAC. With the onset of compression both non-hydrostatic mDAC and dDAC runs observe a rapid grain-size decrease to ≈ 150 nm. Both the fast dDAC ($8 \times 10^{-1} \text{s}^{-1}$) and slow mDAC ($4 \times 10^{-4} \text{s}^{-1}$) run record an quasi steady state after the decrease, whereas the fast mDAC ($2 \times 10^{-3} \text{s}^{-1}$) run reaches a plateau only after the apparent grain-size return to 320 ± 40 nm. In contrast, both mDAC and dDAC runs with Ne PTM record different developments. The dDAC run ($9 \times 10^{-2} \text{s}^{-1}$) shows a slow grain-size decrease to ≈ 150 nm across the whole compression event, whilst the mDAC ($2 \times 10^{-3} \text{s}^{-1}$) run shows larger grain-sizes in the range of 10-25 GPa and 70-80 GPa, but reaches also with the

end of the compression ≈ 150 nm.

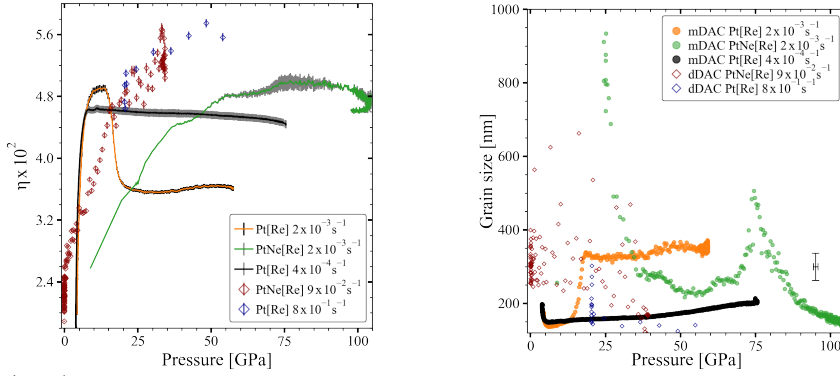


Figure 5.7: (Left) Micro-strain evolution across the initial compression event of each loading. (Right) Effective grain size development in both Pt[Re] mDAC and dDAC runs. The black marker depicts the error range on the grain-size data.

In addition to the line-width analysis [Eq. 3.20], the line-shift analysis [Eq. 3.8] was used to obtain information of the Strength (uniaxial stress) development across the compression events [Fig. 5.8]. A large difference in their resulting strength can be observed in the direct comparison. The observed micro-stress yields much larger strength of the material compared to the differential stress and independent of hydrostatic or non-ydrostatic condition, if $2p_{max}$ is used in the comparison and alpha, the ratio of isostress and isostrain conditions in the differential stress calculation of the sample material, is assumed even ($\alpha = 0.5$). However, those assumptions were made following the example of previous studie [206, 213]. Thereby, the general developments in the slow mDAC run ($4 \times 10^{-4} \text{s}^{-1}$) that reached 20 GPa and at the starting conditions in the fast dDAC run ($8 \times 10^{-1} \text{s}^{-1}$) are coinciding, whereas the fast mDAC run ($2 \times 10^{-3} \text{s}^{-1}$) records a sudden and strong increase in the differential stress parameter between 15-20 GPa, but the micro-stress records a slight decrease. The hydrostatic runs mDAC and dDAC show a continues increase during compression and the dDAC runs record higher differential stress and strength compared to the mDAC runs.

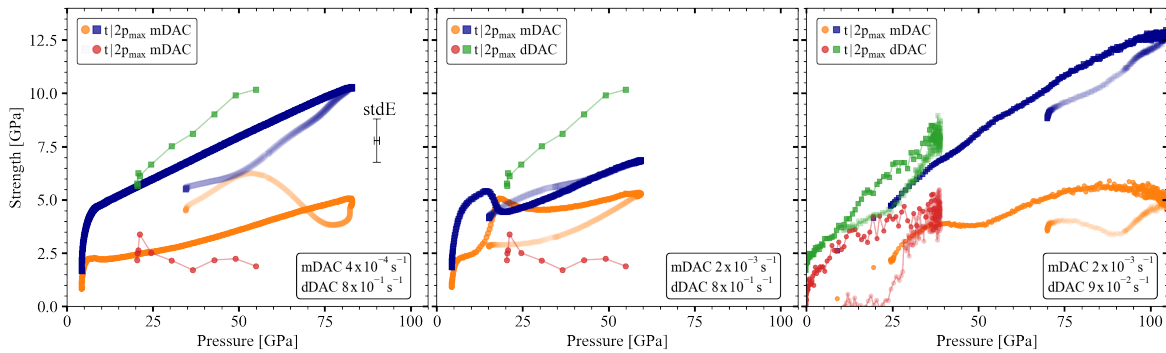


Figure 5.8: The evolution of strength of Pt during mDAC and dDAC compression. From left to right: slow Pt[Re], fast Pt[Re], and fast PtNe[Re] results by mDAC compared to their counterpart in the dDAC. Differential stress $[t]$ of the line-shift analysis is given by the orange and red circles, whilst the micro-stress $[2p_{max}]$ of the line-width analysis is shown as dark blue and green squares

5.1.2 Rhenium

Rhenium (Re) is one of the main used gasket materials and five mDAC and four dDAC loadings were assembled and prepared [Tab. 5.4]. These loadings resulted in a total of 13 mDAC and five dDAC experiments reaching peak pressures between 38 GPa and 100 GPa, where the pressure development was obtained using EoS by [197].

Table 5.4: Experimental run conditions of Re at the ECB P02.2 beamline, PETRA III, DESY.

Run mDAC	Sample	Gasket	culet (mm)	P_{start} (GPa)	Exposure (ms)	Membrane $\frac{bar}{min}$	comp. rate \varnothing	strain rate s^{-1}	PTM
Re no4 1	Re	Re	0.3	0	266	1	0.2 GPa/s	2×10^{-4}	-
Re no4 2* ¹	Re	Re	0.3	16	266	1	0.5 GPa/s	1×10^{-4}	-
Re no4r2 1	Re	Re	0.3	11.5	266	40	5.5 GPa/s	2.5×10^{-3}	-
Re no4r2 2* ¹	Re	Re	0.3	12	266	40	1.8 GPa/s	3×10^{-4}	-
Re no4r2 3* ¹	Re	Re	0.3	18	266	40	1.4 GPa/s	4×10^{-4}	-
Re no4 s 1	Re	SS	0.3	10	266	40	2.6 GPa/s	2.5×10^{-3}	-
Re no4 s 2	Re	SS	0.3	14.5	266	40	1.1 GPa/s	8×10^{-4}	-
SYN7* ¹	Re	Re	0.3	4	266	40	3.6 GPa/s	2×10^{-3}	-
SYN9 1	Re	SS	0.3	0	266	1	0.3 GPa/s	2×10^{-4}	-
SYN9 2* ²	Re	SS	0.3	10	266	1	0.1 GPa/s	1×10^{-4}	-
SYN9 3	Re	SS	0.3	2.5	266	1	0.2 GPa/s	2×10^{-4}	-
SYN9 4	Re	SS	0.3	4.5	266	1	0.2 GPa/s	1×10^{-4}	-
SYN9 5	Re	SS	0.3	7.5	266	1	0.3 GPa/s	1×10^{-4}	-
Run dDAC	Sample	Gasket	culet (mm)	P_{start} (GPa)	Exposure (ms)	Piezo V	comp. rate \varnothing	strain rate s^{-1}	PTM
Load9	Re	Re	0.2	0	2	550	1.3 TPa/s	2.3×10^0	-
Load11	Re	Re	0.2	0	10	650	202 GPa/s	3×10^{-1}	-
Load12	Re	Re	0.3	2	10	550	85 GPa/s	1.5×10^{-1}	Ne
Load12r2	Re	Re	0.3	23	10	600	42 GPa/s	7×10^{-2}	Ne
Re_Gasket* ³	Re	Re	0.1	2	100	1000	16.5 GPa/s	2×10^{-2}	Ne

*¹ diamond broke during compression, *² stopped recording: problems during the experiment, *³ FeO100culetne90feo: Gasket condition, sample moved before the compression ramp and only Re visible.

The lattice parameter and unit cell volume development was investigated in regards of the different compression rates using refined d-spacing information in combination with the diffraction line Miller indices and a representative overview is given [Fig. 5.9]. The a-axis displays a decreasing linear trend during compression indifferent to the gasket material, whilst the c-axis shows a linear decrease in runs with Re gasket, but a delayed, respectively slower decrease in the range of $V/V_0 = 0.94 - 0.915$ when Ss-gasket is used. Furthermore, a general slight variation of the axis parameters of both Re[Re] and Re[Ss] runs is recorded in comparison with runs using Ne PTM. The variation onset can be found during the first few GPa (5-8 GPa) of compression, whereupon pure Re samples show lower c-axis and higher a-axis parameter in

comparison to the ReNe counterpart and indifferent to a run performed with mDAC or dDAC.

From those lattice parameters the pressure development is obtained and an overview of the micro-strain evolution across a representative set of mDAC and dDAC compression and decompression events is shown [Fig. 5.10]. Slow mDAC runs (10^{-4} s^{-1}) on Re[Re] and Re[Ss] observe a sudden increase in micro-strain within the first 5–8 GPa of compression and become pressure independent afterwards. This independence persists even across the decompression period. The same trend is also observed for the Re[Re] dDAC runs performed at strain rates of $1.5 \times 10^{-1} \text{ s}^{-1}$ to $2.3 \times 10^0 \text{ s}^{-1}$ and starting from ambient pressures, whilst the ReNe[Re] run ($1.5 \times 10^{-1} \text{ s}^{-1}$) records a continuous correlation of the pressure and micro-strain evolution.

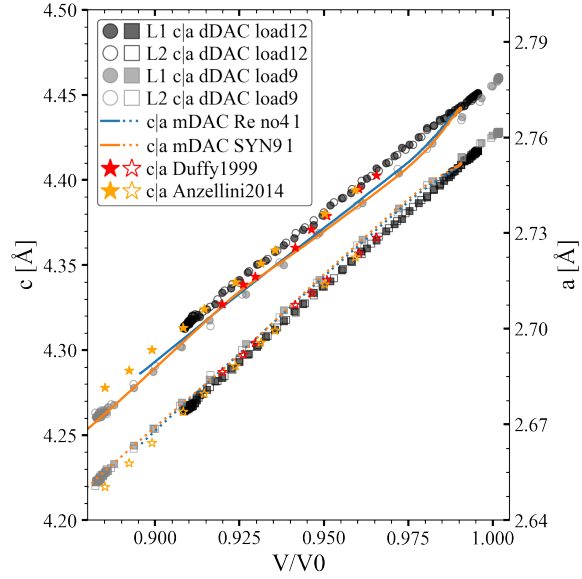


Figure 5.9: Lattice parameter development of Re as a function of relative volume. The solid (L1) and open (L2) circles and squares give Re + Ne[Re] (black) and 50 ms dDAC compression of Re[Re] (gray). The blue or orange solid and dashed line gives Re[Re] and Re[Ss] mDAC, whilst solid and open, red and orange stars are [205, 214].

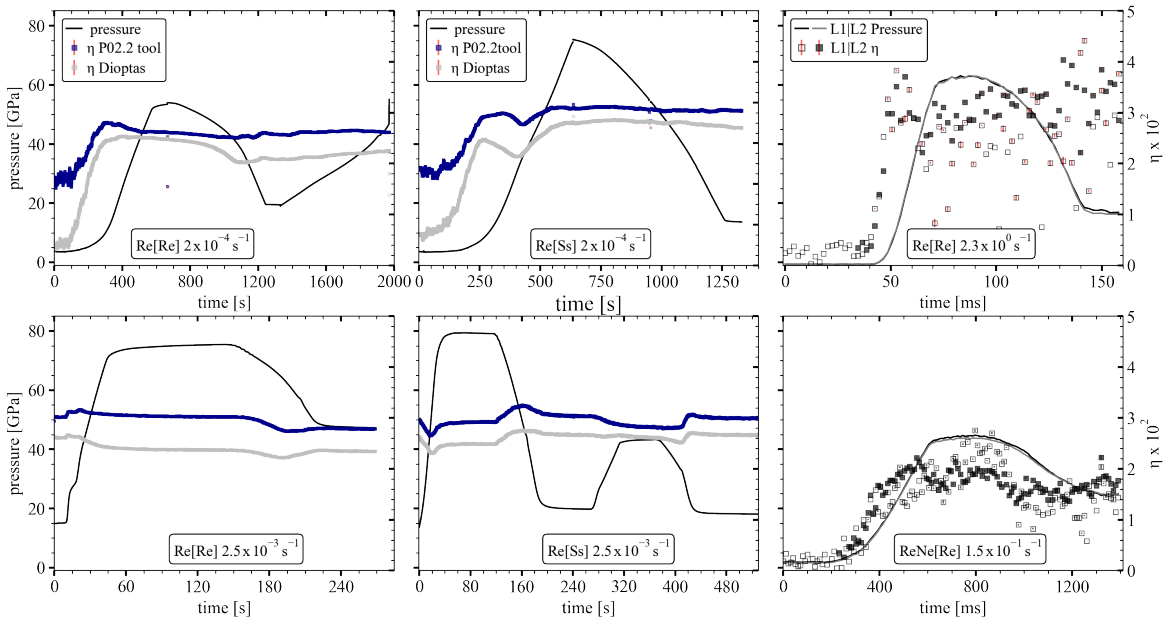


Figure 5.10: Overview of the micro-strain and pressure evolution across initial compression and decompression events of rhenium in mDAC and dDAC runs.

In contrast, the faster mDAC experiments record starting pressure of ~ 15 GPa and with the onset of the compression event only a slight variation of the micro-strain is found. Re[Re] records slightly increasing micro-strain values and a similar pressure independent development comparable to the slow mDAC runs, yet a slight decrease precedes the initial increase.

While, Re[Ss] records decreasing micro-strain values with the onset of the compression event and accumulation during the first decompression period. The exception in the fast Re[Ss] run becomes even more prominent in the comparison of micro-strain and the compression rate changes [Fig. 5.11].

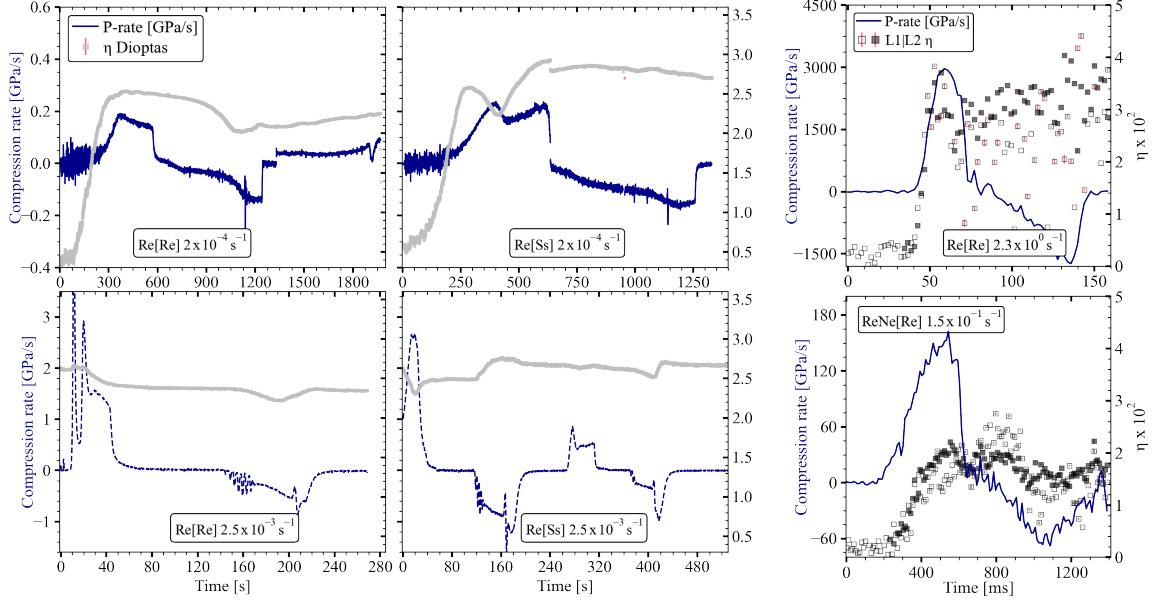


Figure 5.11: The micro-strain and compression rate dependence across initial compression and decompression events of rhenium in mDAC (strain rates of $2 \times 10^{-4} \text{ s}^{-1}$ - $2.5 \times 10^{-3} \text{ s}^{-1}$) and dDAC (strain rates of $1.5 \times 10^{-1} \text{ s}^{-1}$ - $2.3 \times 10^0 \text{ s}^{-1}$).

In these data, the fast Re[Ss] run observes lower micro-strain values at the fastest compression rates and highest values during decompression. All other experiments and independent of a PTM, observe high micro-strain in close proximity to high compression rates. Slow mDAC runs observe their maxima and minima in advance of the maximum compression rates, whilst the dDAC and fast mDAC runs display a coinciding evolution and Re + Ne PTM and even a delayed micro-strain response.

Moreover, the effective grain size evolution was investigated using the line-width analysis, and despite the lower pressure resolution on the dDAC runs, as well as the loss of information due to a negative intercept after the subtraction of the instrumental broadening, a full overview of all initial compression event can be illustrated [Fig. 5.12].

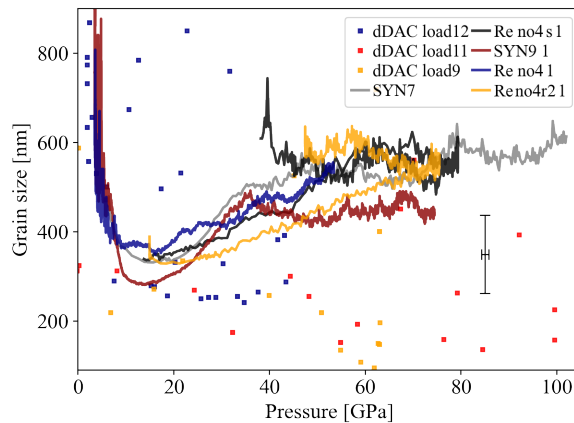


Figure 5.12: Grain size evolution of Re during compression in mDAC and dDAC

The development of the effective grain size is strongly dependent on the compression rate. The dDAC runs record an initial decrease from $\sim 800 \pm 100$ nm to 200 ± 50 nm, during compression to ~ 20 GPa and the small grain size is inherited across further compression. While, all mDAC runs show a decrease from $\sim 700 \pm 100$ nm to 350 ± 50 nm during compression to ~ 20 GPa, at that point the decrease is replaced by a slow recovery across further compression and a plateau at 500-600 nm. One exception can be found in the slow Re[Ss] mDAC run that reaches 500 nm at ~ 40 GPa but shows a steady state at around 400-450 nm.

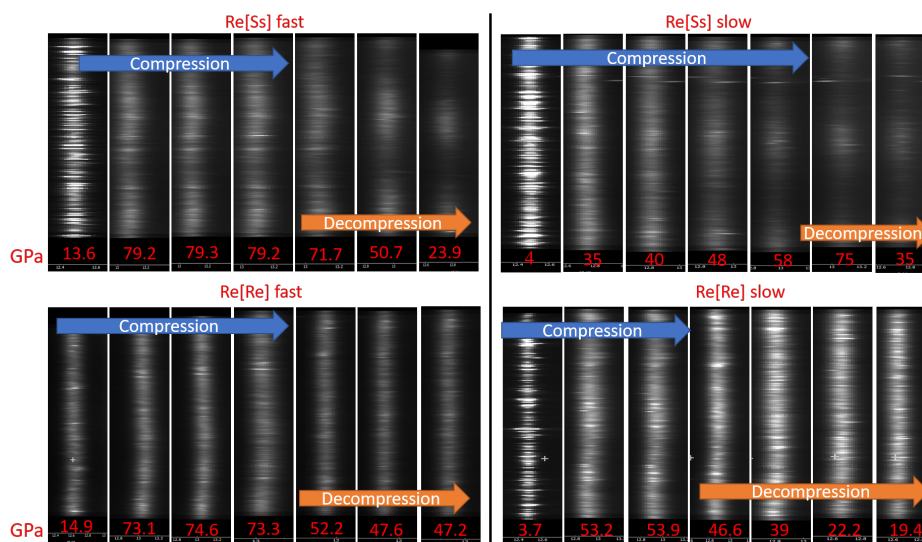


Figure 5.13: The development of the (002) Bragg reflection of Re during mDAC runs performed with Re[Ss] (0.3 and 2.6 GPa/s) and Re[Re] (0.2 and 5.5 GPa/s).

Finally, the evolution of the (002) reflection as a function of pressure during the initial compression events in four of the mDAC loadings in Re and Ss gasket is presented [Fig. 5.13], where different developments in runs with Re and Ss gasket are observed. With the onset of compression all runs record a decrease in intensity, but a more homogeneous diffraction line compared to the relative spotty observations within the initial XRD image. Yet, at a low compression rate, 0.3 GPa/s, the run in Ss gasket observes the onset of azimuthal dependent intensity variations during the compression interval whilst at higher compression rates 2.6 GPa/s the variation is observed only during decompression. In contrast, no azimuthal dependent variation is shown, within neither the slow 0.2 GPa/s nor the fast 5.5 GPa/s run in Re gasket.

5.1.3 Gold

Gold (Au) is a well known pressure calibrant and a total of 12 runs were performed with it [Tab. 5.5], correlating to five dDAC loadings, reaching peak pressures between 35 GPa and 230 GPa. The pressure development during the experiment was obtained using EoS by [198].

Table 5.5: Experimental run conditions of Au at the ECB P02.2 beamline, PETRA III, DESY.

Run dDAC	Sample	Gasket	culet (mm)	P_{start} (GPa)	Exposure (ms)	Piezo Volt	comp. rate \varnothing	strain rate s^{-1}	PTM
Au0.5 1	Au	Re	0.05	≈ 80	0.5		38 TPa/s	4×10^1	-
Au0.5 2	Au	Re	0.05	≈ 150	0.5		14.1 TPa/s	1×10^1	-
Au0.5 3	Au	Re	0.05	≈ 157	0.5		23 TPa/s	2×10^1	-
Au0.5 4	Au	Re	0.05	≈ 172	0.5		24.5 TPa/s	2×10^1	-
Au0.5 51	Au	Re	0.05	≈ 180	0.5		24.5 TPa/s	1×10^1	-
AuNeRe 1* ¹	Au	Re	0.3	1.5	10	1000	5 GPa/s	2×10^{-2}	Ne
AuNeRe 2	Au	Re	0.3	5.5	10	1000	38 GPa/s	1.2×10^{-1}	Ne
AuNeRe 3* ²	Au	Re	0.3	22.4	10	1000	2 GPa/s	6×10^{-3}	Ne
AuRe 1	Au	Re	0.3	3.5	5	1000	345 GPa/s	1×10^0	-
AuRe 2	Au	Re	0.3	9	5	1000	300 GPa/s	1×10^0	-
AuRe r2	Au	Re	0.3	10	10	1000	48 GPa/s	1.3×10^{-1}	-
AuNeSS* ³	Au	SS	0.3	11	10	1000	34 GPa/s	8×10^{-2}	Ne

*¹ almost no pressure increase detected, either cell was not completely closed or applied voltage to the piezo-actuator was low, *² again almost no pressure increase detected, *³ diamond broke during compression,

The first loading was used as a test to evaluate the diffraction image intensity and compression rates achievable with the available dDAC setup. A representative azimuthal integrated single image obtained during the run is shown [Fig. 5.14] to visualize the data quality at the fastest 0.5 ms exposure rate of the LAMBDA GaAs 2M detectors and a sample volume confined on 50 μ m diamond culets. 40 diffraction images were collected in each ramp, where every image shows a very faint signal of the sample and only the (111) Bragg reflection could be used to obtain lattice parameter information, preventing micro-strain calculation on the data. Nevertheless, it proved to enable refinement of the diffraction images with an intensity ≤ 0.04 , due to the detector's very low background.

Five consecutive ramps were performed during the experiment, without diamond failure, reaching a maximum of 175 \rightarrow 230 GPa and compression rates up to 38 TPa/s [Fig. 5.15]. During the first compression event the sample seems to have moved out of the X-ray path and the (111) reflection is only visible at the interval at pressures and after decompression. The data shows a variation of the pressure observed on the two detectors, which slowly diminishes across the next two compression events. During the fourth event both detectors record the same sample pressure evolution across the whole event.

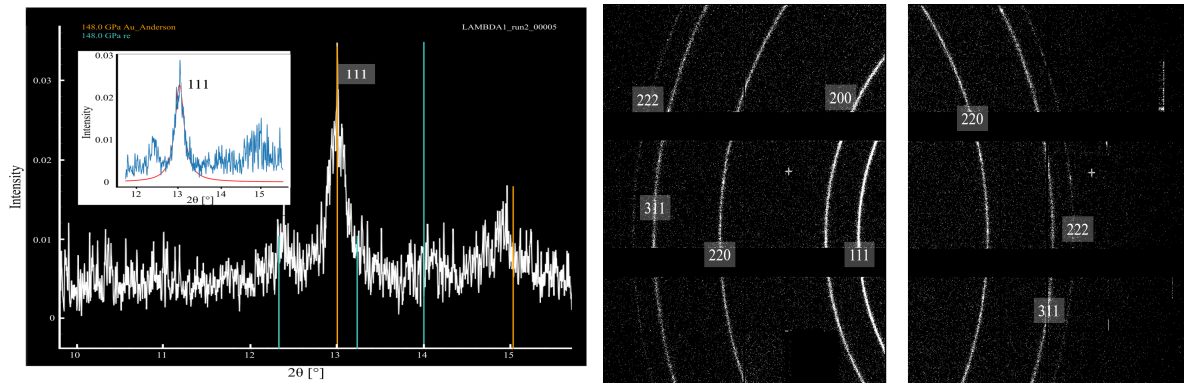


Figure 5.14: Representative raw X-ray diffraction images of Au dDAC experiments: (Left) an azimuthal integrated 0.5 ms exposures and (Right) a slower 5-10 ms exposures in 2D. Refinable Bragg reflection lines are indexed and parasitic Re is visible only during the 0.5 ms exposures using a 50 μm culet.

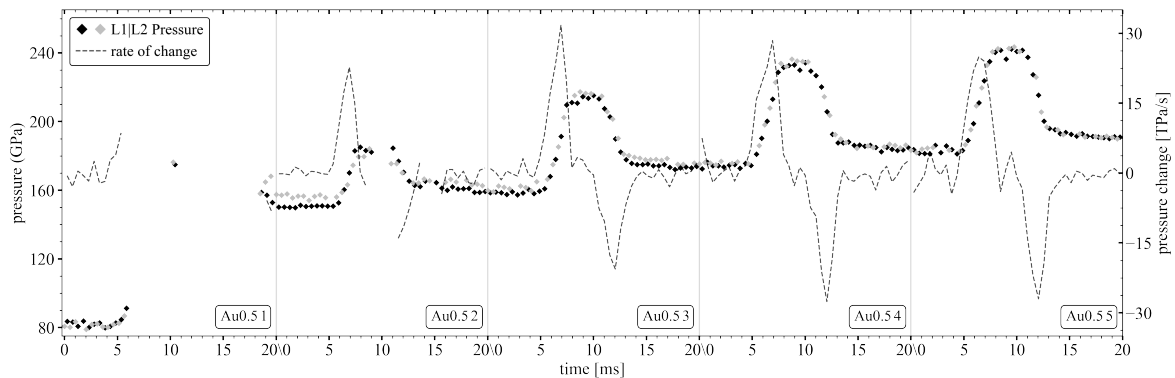


Figure 5.15: The pressure and compression rate of Au[re] recorded during 0.5 ms exposures with the LAMBDA GaAs M2 detectors. The black and gray diamonds depict the pressure development and the dashed line shows the compression rate. Please note that the sample moved out of the X-ray path during the first compression cycle, but was observed through out the consecutive ramps where missing data is due to very low diffraction intensity.

Based on this information, the exposure times and sample volume were adjusted and further runs were performed investigating the micro-strain evolution at compression rates between 34 GPa/s and 350 GPa/s. Within this runs strain rates of $8 \times 10^{-2} \text{ s}^{-1}$ to 10^0 s^{-1} are observed and peak pressures of $\sim 35 \text{ GPa}$ - 65 GPa [Fig. 5.16]. Thereby, two main trends, dependent in the compression rate and hydrostaticity can be observed : 1. A close correlation between the pressure and micro-strain development on both detectors; 2. Deviating peak pressures on the detectors and non-correlating micro-strain evolution. The first trend can be observed in both the slow AuNe[Re] run ($1.2 \times 10^{-1} \text{ s}^{-1}$) and the first ramp of fast Au[Re] run 10^0 s^{-1} , whereas the second trend is observed in the slow Au[Re] run ($1.3 \times 10^{-1} \text{ s}^{-1}$) and in the second ramp with the fast Au[Re] run (10^0 s^{-1}). Runs with Au[ss] were aborted after diamond failure during the initial compression event of AuNe[ss] due to limited experimental time.

Until now only the common peaks of both detectors were used to obtain the micro-strain and pressure information. The micro-strain and effective grain size evolution as a function of pressure during the initial compression events are shown [Fig. 5.17], using all available lattice

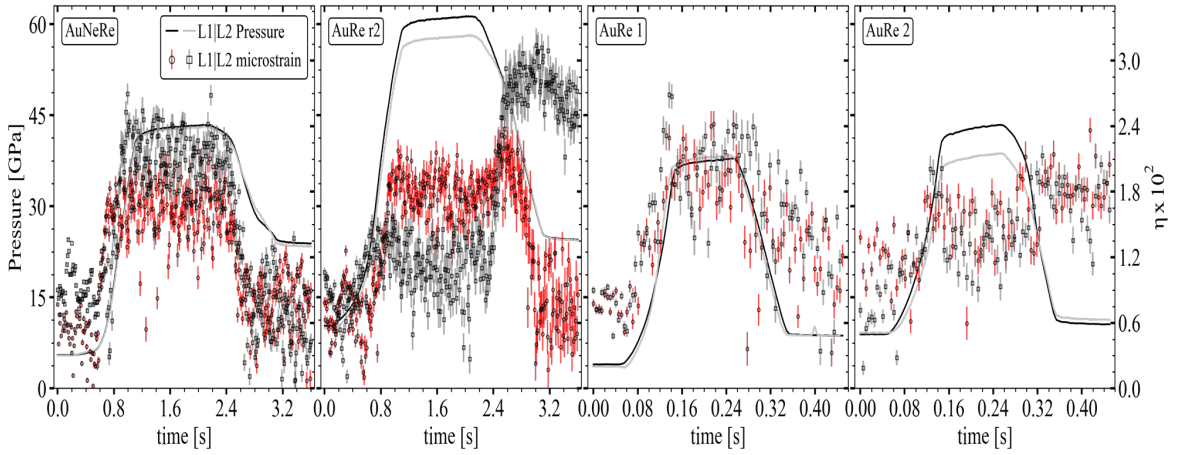


Figure 5.16: Pressure and micro-strain evolution during the experiments on Au and based on the common peaks of both LAMBDA 1 and LAMBDA 2. From left to right: AuNe[Re], $1.2 \times 10^{-1} \text{ s}^{-1}$; Au[Re], $1.3 \times 10^{-1} \text{ s}^{-1}$ and the two consecutive ramps of Au[Re], 10^0 s^{-1} . The pressure is shown as solid black (L1) or gray (L2) lines, whereas micro-strain is given by the black open circle (L1) and square (L2) with red or gray errorbars respectively.

parameters on LAMBDA 2. All runs observe a strong increase in micro-strain across the first 5-8 GPa of the compression event independently of the compression rate. Thereafter, the fast increase turns into a quasi pressure independent steady state in the slow Au[Re] run ($1.3 \times 10^{-1} \text{ s}^{-1}$). In contrast, the fast Au[Re] run (10^0 s^{-1}) as well as both the slow AuNe[Re] and AuNe[SS] runs show further accumulation of micro-strain across the whole compression event. Correlating with the strong micro-strain increase all runs record a decrease of the effective grain size to $240 \pm 50 \text{ nm}$ across the initial 5-8 GPa compression. At this point, the evolution in the slow Au[Re] run ($1.3 \times 10^{-1} \text{ s}^{-1}$) turns into a monotonous very slight decreasing trend, whilst the other runs become quasi pressure independent. The only exception is the AuNe[Re], recording slightly larger grain size 320 nm within the pressure interval of 20-40 GPa.

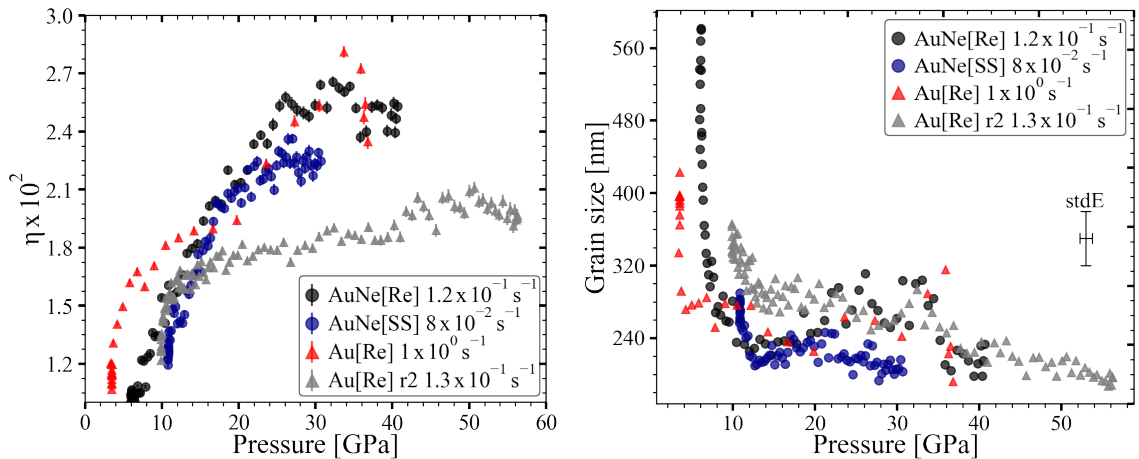


Figure 5.17: Overview of the results of the line-width analysis for all first compression events of Au. (Left) Micro-strain and (Right) effective grain size as a function of pressure.

As said, not only line-width analysis but also line-shift analysis was used to investigate the evolution of differential stress over the compression and decompression events. A comparison

of the results is illustrated [Fig. 5.18]. A large variance in the resulting development of both differential stress and micro-stress is recorded comparing $2p_{max}$ and t , whereas literature [213, 215] shows and [119] claims a close correlation. With the onset of compression all non-hydrostatic runs record an initial fast increase of differential stress and micro-stress ($2p_{max}$), whereas the hydrostatic runs record the initial increase only in the micro-stress development. All runs independent of the compression rate record a much higher micro-stress ($2p_{max}$) accumulation compared to differential stress. Thereby, the micro-stress always shows a linear increase during the compression interval, which precedes the initial fast increase. In contrast, the development of the differential stress seems to be dependent on the compression rate and gasket material. At low strain rates ($1.3 \times 10^0 \text{ s}^{-1}$) a sudden change in the magnitude of the stress increase can be observed between 35-45 GPa, whereas a linear increase can be observed at strain rates of 10^0 s^{-1} . At hydrostatic conditions, Ne PTM, an accumulation of stress is observed at higher pressures, whereby the trend in AuNe[Re] is matching with previous observations [205, 216] at 15 GPa, whilst the trend in AuNe[Ss] shows an accumulation onset at 26 GPa.

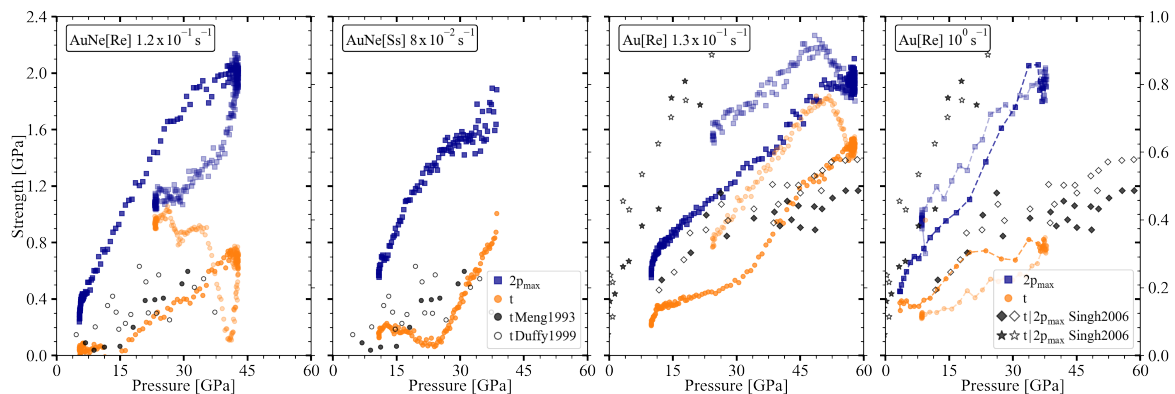


Figure 5.18: Micro-stress ($2p_{max}$) and differential stress (t) evolution as a function of pressure and compared to [119, 205, 216]. From left to right: AuNe[Re], AuNe[Ss], Au[Re] r2, AuRe. The current error on the data is about $\sim 30\%$.

5.1.4 Zinc

Zinc (Zn) has been reported to show a dependence of the lattice parameter development to the degree of hydrostaticity across the compression event and four dDAC loadings were assembled and prepared [Tab. 5.6]. These loadings resulted in a total of eight runs reaching peak pressures between 18 GPa and 38 GPa, where the pressure development was obtained using EoS by [199]. No pressure calibrant (Pt or Au) was used, to prevent overlap of peaks during compression and it would have reduced the amount of sample, thus the total diffracted intensity. The lattice parameter and unit cell volume evolution was investigated with regard to the different compression rates using refined d-spacing information in combination with three to six observable Bragg diffraction lines.

Table 5.6: Experimental run conditions of Zn at the ECB P02.2 beamline, PETRA III, DESY.

Run	Sample	Gasket	culet (mm)	P_{start} (GPa)	Exposure (ms)	Piezo V	comp. rate $_{\varnothing}$	strain rate s^{-1}	PTM
Zn load3	Zn	Re	0.3	1	100	400	3.6 GPa/s	3×10^{-2}	Ne
Zn load7	Zn	Re	0.3	1	100	400	2.7 GPa/s	2×10^{-2}	-
Zn load7 r2	Zn	Re	0.3	2.5	4	500	390 GPa/s	2×10^0	-
Zn load7 r3*1	Zn	Re	0.3	4	4	500	320 GPa/s	2×10^0	-
Zn load10	Zn	Re	0.3	1	20	400	40 GPa/s	3×10^{-1}	Ne
Zn load10 r2	Zn	Re	0.3	11.5	20	550	60 GPa/s	3×10^{-1}	Ne
Zn load10 r3	Zn	Re	0.3	12	20	600	60 GPa/s	3×10^{-1}	Ne
Zn load16	Zn	Re	0.3	2	1000	400	31 TPa/s	2.7×10^2	-

*1 low diffraction intensity, only LAMBDA 2 refinable.

A overview of the lattice parameters as a function of relative volume (V/V_0) of the initial ramp of each loading is shown [Fig. 5.19]. Despite the difference in 2Θ angle observed by the two LAMBDA detectors, their calculated lattice parameters are in excellent agreement with each other. The a-axis shows a monotonous decreasing trend up to $V/V_0 = 0.89$ independent of a pure sample loading or the inclusion of neon (PTM), whereas both slow (load3 and load7) runs record a change in the regression slope that results in larger lattice parameter compared to the observations in both fast (load16 and load10) runs. The c-axis is compressed stronger than the a-axis, by a factor of ten and shows a monotonous decreasing trend across the whole compression interval to $V/V_0 = 0.8$. It has to be noted, that during the 0.5 ms jump compression experiment, XRD images were collected only before and after the compression event, thus leaving the development from ambient to high pressure parameters open for speculations. The other four ramping cycles contain information about the effect of consecutive compression and decompression events [Supp.Fig. 2], albeit a direct comparison is not possible since persistent changes obtained over the course of the previous events cannot be ruled out and their starting conditions are unknown.

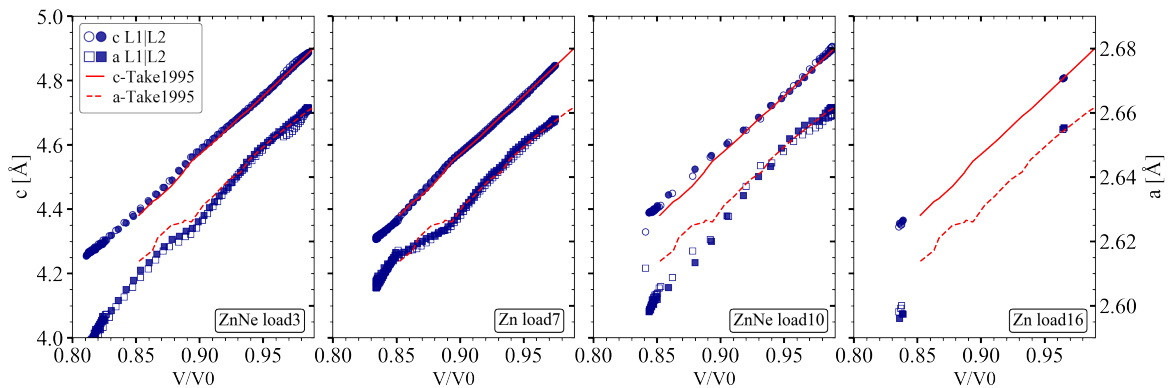


Figure 5.19: Lattice parameter evolution of Zn as a function of relative volume. The current results of either LAMBDA 1 or LAMBDA 2 are represented by open and solid squares and circles. The solid and dashed red line represents literature by Takemura 1995. Notice the scaling difference between c axis and a axis.

The close correlation between the lattice parameters obtained by the two LAMBDA GaAs 2M detectors results in a good match of their pressure evolution. An overview of the micro-strain development across the initial compression and decompression intervals is depicted in [Fig 5.20].

The micro-strain evolution of both LAMBDA detectors is mostly coinciding with each other, except for the 0.5 ms jump compression run. The jump compression run shows a larger variation dependent on the recording detector and especially during decompression. During decompression a variation in the recorded pressure development can be observed, too. Nevertheless, two main trends can be determined dependent on the loading conditions and also applying to the consecutive compression and decompression events of load7 and load10. The first trend is a more or less slow gradual accumulation of micro-strain across the events PTM in runs performed on sample + PTM, whereas the second trend depicts a direct dependence of the micro-strain evolution in pure samples in comparison to the pressure evolution. Pure sample loaded runs record much larger magnitudes of micro-strain during the event compared to the total accumulation in runs with PTM.

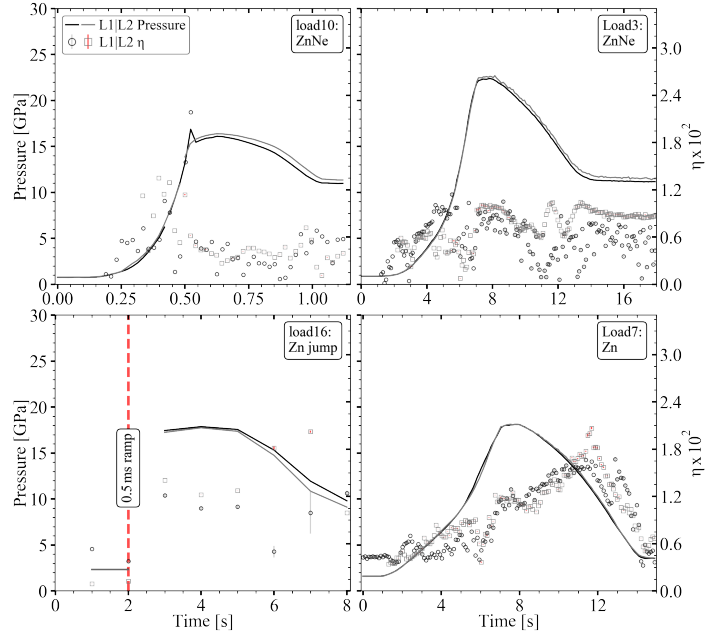


Figure 5.20: Micro-strain (η) and pressure evolution of the initial ramps of Zn + Ne PTM (top) and pure Zn samples (bottom). Top - left to right: 400 ms ramp at 20 ms exposures and 6 s ramp at 100 ms exposures. Bottom - left to right: 0.5 ms jump compression ramp at 1 s exposures and 6 s ramp at 100 ms exposures. The black + gray solid lines show the pressure evolution of the two detectors and black + gray open circles/ squares the correlating micro-strain evolution.

5.1.5 Iron

Iron (Fe) is another material reported to show a lattice parameter development dependent on the degree of hydrostaticity across the compression event and seven dDAC loadings were prepared [Tab. 5.7], resulting in seven distinct runs with peak pressures of 38 GPa - 65 GPa. Here, the pressure developments across the compression and decompression events were obtained either of the bcc-Fe and hcp-Fe EoS by [200] or indirectly by using an internal platinum pressure calibrant [206].

The lattice parameter and unit cell volume evolution of both bcc and hcp Fe was investigated in regards to the different compression rates using refined d-spacing information in combin-

ation with the diffraction lines Miller indices.

Table 5.7: Experimental run conditions of Fe at the ECB P02.2 beamline, PETRA III, DESY.

Run mDAC	Sample	Gasket	culet (mm)	P_{start} (GPa)	Exposure (ms)	Piezo Volt	comp. rate $_{\emptyset}$	strain rate s^{-1}	PTM
Fer1	Fe	Re	0.3	5	10	550	160 GPa/s	6×10^{-1}	-
Fer2	Fe	Re	0.3	6	1	650	1.03 TPa/s	4×10^0	-
Fer3	Fe	Re	0.3	0.5	100	500	10 GPa/s	4×10^{-2}	-
load2	Fe + Pt	Re	0.2	6	10	550	287 GPa/s	1×10^0	Ne
load8	Fe + Pt	Re	0.2	0	10	550	262 GPa/s	1×10^0	-
load15	Fe	Re	0.2	0	10	550	260 GPa/s	1×10^0	-
load18* ¹	Fe	Re	0.2	0.5	100	550	10 GPa/s	4×10^{-2}	-

*¹ Very low intensity on the diffraction images, after the fcc-hcp phase transition. L1 records only one peak, thus the hcp pressure evolution was no longer refinable.

A representative overview of the hcp Fe lattice parameter development is shown [Fig. 5.21] based on three to six persisting reflections after the compression event. Both axes display a monotonous decreasing trend showing only a slight variation in the development of pure Fe[Re] and FeNe[Re] runs, which is independent of the compression rate. At V/V_0 ratios below 0.86 FeNe[Re] shows slightly higher c-axis and lower a-axis parameter on L2 compared to the other runs.

The close correlation between the lattice parameters of both LAMBDA GaAs 2M detectors results in a good match of their pressure evolution and a representative overview of the micro-strain and pressure development as a function of time is depicted in [Fig. 5.22]. The micro-strain evolution shows two distinct trends that are independent of the achieved strain rates, $10^{-2} s^{-1}$ to $4 \times 10^0 s^{-1}$. Pure Fe[Re] or FePt[Re] runs shows the accumulation of micro-strain with the onset of the bcc to hcp phase transition, preceded by either a stable plateau or monotonous slow increase during compression and even across the decompression. Whereas, FePtNe[Re] records accumulation of micro-strain across the whole compression event and relaxation during decompression.

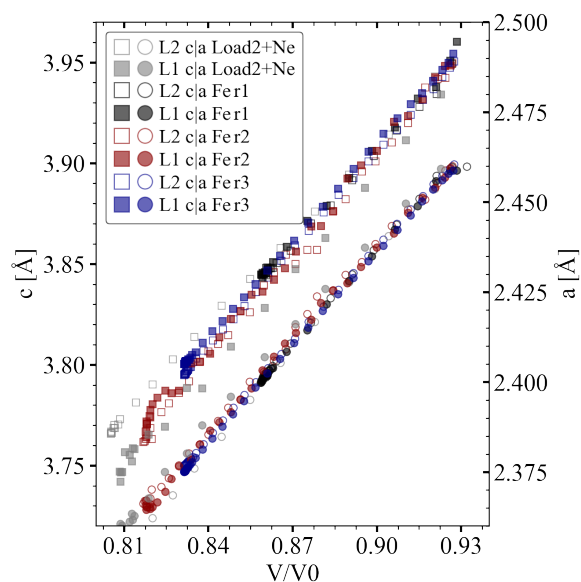


Figure 5.21: Lattice parameter development of hcp Fe as a function of relative volume. The solid (L1) and open (L2) circles and squares show the a-axis and c-axis lattice parameter evolution.

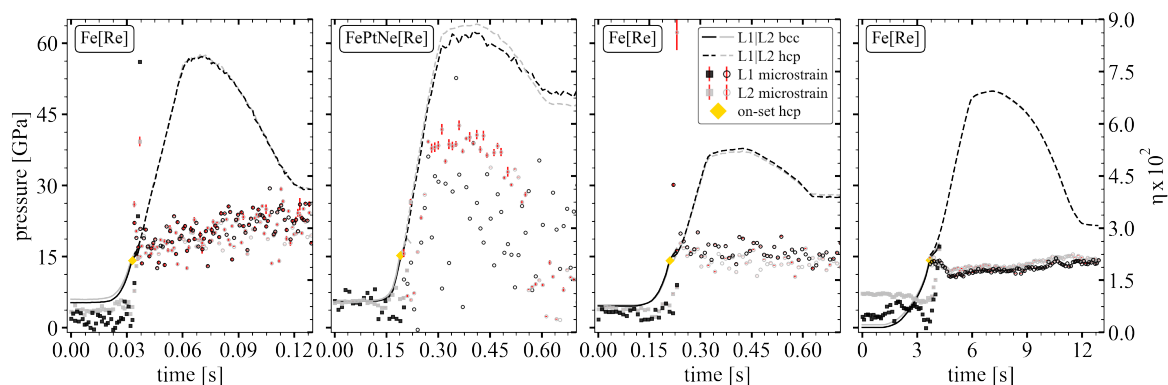


Figure 5.22: The micro-strain and pressure evolution during experiments on Fe. Showing for left to right four experimental runs performed over 50 ms, 200 ms, 200 ms and 5 s compression intervals. The black (L1) and silver (L2) dashed lines show pressure, whilst the micro-strain is given by black (L1) and gray (L2) solid squares (bcc), respectively open circles (hcp) with red errorbars.

5.1.6 Wüstite, periclase and ferropericlase solid solutions

Ferropericlase (Fe,Mg)O is the second most abundant mineral within the Earth's mantle and a product of the endmember periclase (MgO) and wüstite (FeO). Ferropericlase shows a very variant phase diagram within the pressure interval up to 100 GPa and dependent on the iron content [Fig. 4.1]. Initial experiments have been performed on MgO, the lowest Z sample within the (Fe,Mg)O solid solutions, investigating the limits of the diffraction intensity at short exposures times ≤ 20 ms and small amounts of sample in 0.04 mm culet diamonds. Those runs reached peak pressures of 220-270 GPa over the course of seven consecutive compression cycles with compression rates exceeding 1.4 TPa/s [Fig. 5.23].

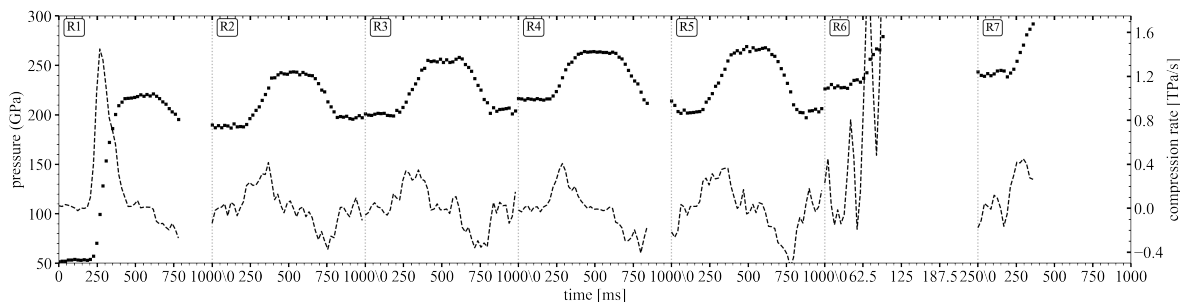


Figure 5.23: Pressure and compression rate development within MgO runs, testing the diffraction line intensity limits for the lowest Z endmember in [Fe,Mg]O solid solutions and the available compression rates using the 60 mm piezo actuator.

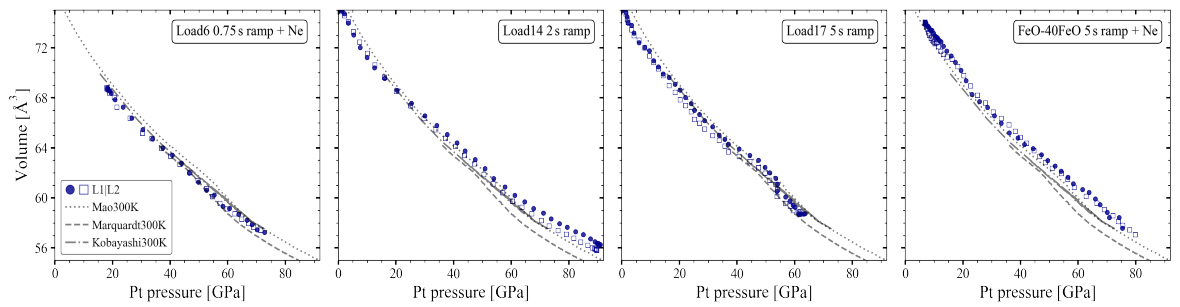
The reflection intensity of the sample material is faint and parasitic Re reflections are recorded during all runs, most likely from the tail of the X-ray beam. The calculations had to be performed on the basis of the MgO (200) peak only, resulting in missing coverage of the events during run1 and run6 where the peaks intensity was low. Based on the information the exposure times and the sample volume were adjusted in preparation for a total of nine loadings. Those resulted in 2. GPa/s to 76 GPa/s compression rates at a resolution of 100 ms to 30 ms. A general overview of all the run conditions is given [Tab. 5.8] and pressure information of the compression events was obtained using Pt EoS by [206].

Table 5.8: Experimental run conditions of $[\text{Fe},\text{Mg}]\text{O}$ and endmember at the ECB P02.2 beamline, PETRA III, DESY.

Run dDAC	Sample	Gasket	culet (mm)	P_{start} (GPa)	Exposure (ms)	piezo Volt	comp. rate \varnothing	strain rate s^{-1}	PTM
MgO_r1	MgO	Re	0.04	53	20	1000	820 GPa/s	1×10^0	-
MgO_r2	MgO	Re	0.04	188	20	1000	270 GPa/s	2×10^{-1}	-
MgO_r3	MgO	Re	0.04	200	20	1000	265 GPa/s	2×10^{-1}	-
MgO_r4	MgO	Re	0.04	216	20	1000	240 GPa/s	2×10^{-1}	-
MgO_r5	MgO	Re	0.04	215	20	1000	320 GPa/s	3×10^{-1}	-
MgO_r6	MgO	Re	0.04	229	5	1000	1.44 TPa/s	8×10^{-1}	-
MgO_r7	MgO	Re	0.04	241	20	1000	360 GPa/s	2×10^{-1}	-
Load6	$\text{Fe}_{10}\text{Mg}_{90}\text{O}^{*1}$	Re	0.2	17.5	30	550	76 GPa/s	2×10^{-1}	Ne
Load14	$\text{Fe}_{10}\text{Mg}_{90}\text{O}^{*1}$	Re	0.2	0	50	650	45 GPa/s	1×10^{-1}	-
Load17	$\text{Fe}_{10}\text{Mg}_{90}\text{O}^{*1}$	Re	0.2	0	100	550	18 GPa/s	5×10^{-2}	-
$\text{FeO}-10\text{FeO}^{*3}$	$\text{Fe}_{10}\text{Mg}_{90}\text{O}^{*2}$	Re	0.2	3.5	100	1000	11.6 GPa/s	6×10^{-2}	Ne
$\text{FeO}-40\text{FeO}^{*3}$	$\text{Fe}_{40}\text{Mg}_{60}\text{O}^{*2}$	Re	0.2	7	100	1000	16.5 GPa/s	5×10^{-2}	Ne
FeO fast	FeO^{*2}	Re	0.3	4	50	1000	7 GPa/s	2×10^{-2}	-
FeO slow	FeO^{*2}	Re	0.3	0	50	1000	2.2 GPa/s	1×10^{-2}	-

*1 sample + 30 wt% Pt, *2 sample + 10 wt% Pt and performed with the short 60 mm piezo actuator, *3 Pt reflections lost during compression, overlap with Re.

Within the covered pressure interval, ambient to ~ 90 GPa, high iron content solid solutions and the wüstite endmember undergo several phase transitions, whereas low iron content solid solutions change from high spin to low spin Fe configuration [Fig. 4.1].

**Figure 5.24:** Volume development of representative low iron content $[\text{Fe},\text{Mg}]\text{O}$ solid solutions, $B1\text{-Fe}_{10}\text{Mg}_{90}\text{O}$ and $B1\text{-Fe}_{40}\text{Mg}_{60}\text{O}$, during the compression event.

Here [Fig. 5.24], runs performed on $\text{Fe}_{10}\text{Mg}_{90}\text{O}$ observe a change in their volume development across the 40-60 GPa interval, which is more distinct within their slower 5 s compression runs with longer exposures, whilst the run performed on $\text{Fe}_{40}\text{Mg}_{60}\text{O}$ depicts a continues development up to 65-70 GPa before a slight variation in trend is observed. In accordance with the thermodynamic definition [Eq. 3.3], the bulk modulus development over the compression interval was extracted by a rolling linear fit to the data sets over the range of three consec-

utive diffraction images, $\sim 3\text{-}5$ GPa [Fig. 5.25]. Therefore, the uncertainty in Bulk modulus is based on the standard error of the slope in the fitting of $\frac{dP}{dV}$. Both fast $\text{Fe}_{10}\text{Mg}_{90}\text{O}$ runs show a defined softening of the bulk modulus above 40 GPa and below 60 GPa. Whereas, the slower runs start at about 50 GPa and record a narrow pressure interval and a drastic change, which matches the direct observation in the volume development. In contrast to those results, $\text{Fe}_{40}\text{Mg}_{60}\text{O}$ does not record the softening within this pressure range and Pt information is lost above 80 GPa, nevertheless above 65 - 70 GPa its general Bulk modulus increase seems to slow down.

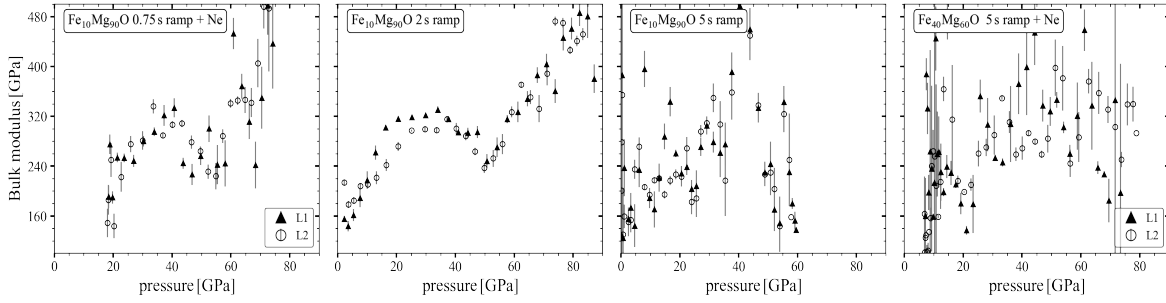


Figure 5.25: Bulk modulus evolution of $\text{Fe}_{10}\text{Mg}_{90}\text{O}$ and $\text{Fe}_{40}\text{Mg}_{60}\text{O}$ across the compression interval based on a rolling linear fit over three consecutive XRD images. The resulting uncertainty is based on the standard error of the slope in the fitting process of $\frac{dP}{dV}$

High iron content solid solutions are found to record the spin crossover transition at pressures above 100 GP [Fig. 4.1], however they should show the occurrence of the B1-rB1 and for wüstite even the rB1-B8 phase transitions. Experiments were performed on pure wüstite samples and on $\text{Fe}_{80}\text{Mg}_{20}\text{O}$ solid solutions. The c-axis and a-axis development over the course of the B1 - rB1 transition, respectively distortion of the cubic lattice cell, is present for the pure wüstite sample [Fig. 5.26].

The a-axis records a monotonous decreasing trend correlating to the collapse of the unit cell volume. In contrast the c-axis records an increase in the lattice parameter up to pressures of ~ 30 GPa, preceded by the similar trend observed in the a-axis parameter. Unfortunately, no data of the c and a parameter exist of the $\text{Fe}_{80}\text{Mg}_{20}\text{O}$ runs, where diamond culets and lower sample volume were probed across the phase boundary. The intensity of the Bragg reflections are weak, inconsistent and data refinement is still ongoing image by image.

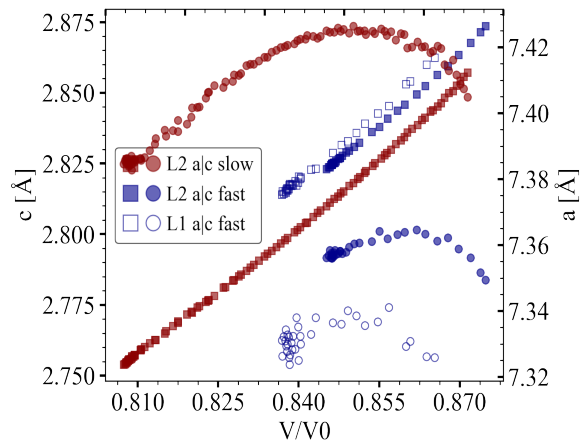


Figure 5.26: The c and a-axis evolution of FeO during the B1 to rB1 transition.

The phase diagram of wüstite (FeO) and ferroperricase ($[\text{Fe},\text{Mg}]\text{O}$) solid solutions observes

both electronic and phase transitions within the pressure range from ambient to 100 GPa. Hence, a Pt pressure calibrant was used to verify the pressure evolution during the runs and estimate the compression rates. The resulting pressure, micro-strain and compression rate evolution as a function of time is illustrated for $\text{Fe}_{10}\text{Mg}_{90}\text{O}$ and FeO runs in [Fig 5.27].

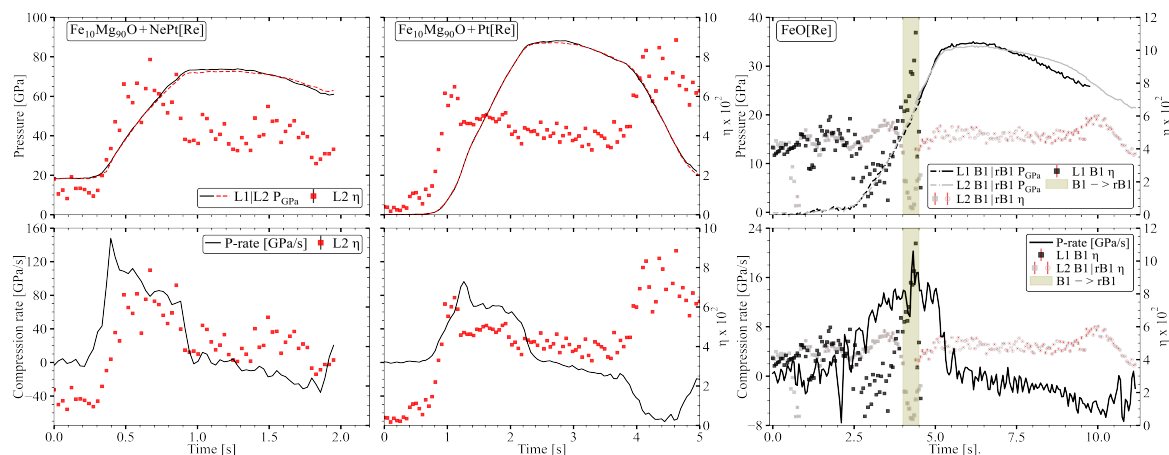


Figure 5.27: Pressure, micro-strain and compression rate evolution of $\text{Fe}_{10}\text{Mg}_{90}\text{O}$ and FeO as a function of time: From left to right: $\text{Fe}_{10}\text{Mg}_{90}\text{O}$ during 0.75 s, 2 s and FeO during 5 s compression intervals.

The $\text{Fe}_{10}\text{Mg}_{90}\text{O}$ and $\text{Fe}_{40}\text{Mg}_{60}\text{O}$ runs with compression rates < 50 GPa/s show a fast initial micro-strain increase at pressures < 10 GPa. This increase in micro-strain is preceding the observation of the maximum compression rate in the event, whereas the faster run, 76 GPa/s, reaches the micro-strain maximum at $\sim 2/3$ of the compression event and after the interval of maximum compression rates. In runs of the FeO endmember, the onset of the $\text{B1} \rightarrow \text{rB1}$ transition has been recorded at 14-15 GPa, showing a full developed splitting of the (111), (220) and (311) diffraction planes at 20-26 GPa. The micro-strain calculation is conducted for both LAMBDA detectors across the stability field of the B1 -phase. However, the onset of the rB1 transitions is accompanied by lower peak intensities and new faint reflections, which limits the line-width analysis to the observation of the LAMBDA 2 detector, showing four to five reflections of rB1 . Starting at almost ambient pressure FeO accumulates a marginal amount of micro-strain across the onset of compression and before the $\text{B1} \rightarrow \text{rB1}$ transition, but a drastic changes is observed during the distortion of the unit cell. The change is dependent in the azimuthal angle and the LAMBDA 2 observes a sudden increase, whilst LAMBDA 1 observes a sudden decrease. Nevertheless, those changes are ephemeral and are evened out during the progression of the distortion. This results in almost identical micro-strain conditions before and after the transition period. In addition, the interval of max. compression rate and max. micro-strain coincide as well as in this observations the phase transition interval falls into the time interval with max. compression rates.

5.2 [Fe,Mg]O LH-mDAC at the ECB P02.2

Table 5.9: Experimental run conditions of the laser heated [Fe,Mg]O at the ECB P02.2 beamline, PETRA III, DESY.

Run mDAC	Sample	Gasket	culet (mm)	P_{start} (GPa)	Exposure (s)	membrane $\frac{bar}{min}$	comp. rate \varnothing	T Kelvin
LH#1	Fe ₂₀ Mg ₈₀ O* ¹	Re	0.3	12	2	0.5	0.005 GPa/s	1400
LH#2	Fe ₂₀ Mg ₈₀ O* ¹	Re	0.2	16	5	0.5	0.015 GPa/s	1200
LH#3	Fe ₂₀ Mg ₈₀ O* ¹	Re	0.15	30	5	0.5	0.026 GPa/s	1700
LH#4	Fe ₂₀ Mg ₈₀ O* ¹	Re	0.15	25	5	0.5	0.023 GPa/s	1700
LH#5	Fe ₂₀ Mg ₈₀ Ot* ¹	Re	0.1	47	5	0.5	0.044 GPa/s	1900

*¹ sample + 20 wt% Pt

On-axis, double sided laser heated mDAC compression experiments were performed at the ECB P02.2 beamline, PETRA III, DESY using the large area Perkin Elmer XRD 1621 detector and a 200 W Yb-fiber laser with wavelength of 1072 nm. The X-ray beam of 42.7 keV was focused down by KB-mirrors to 2 (vertical) x 2 (horizontal) μm beam size and the sample was observed at the center of a defocused, 20-30 μm , laser heating spot, preventing a radial temperature gradient [217]. At the same time, the thermal radiation was observed by a Czerny-Turner spectrograph with an iCCD camera. A total of five successful runs were performed [Tab. 5.9] at different temperatures ranging from 1200 K to 1900 K [Supp.Fig. 3] and with a resolution of 4000 to 400 diffraction images.

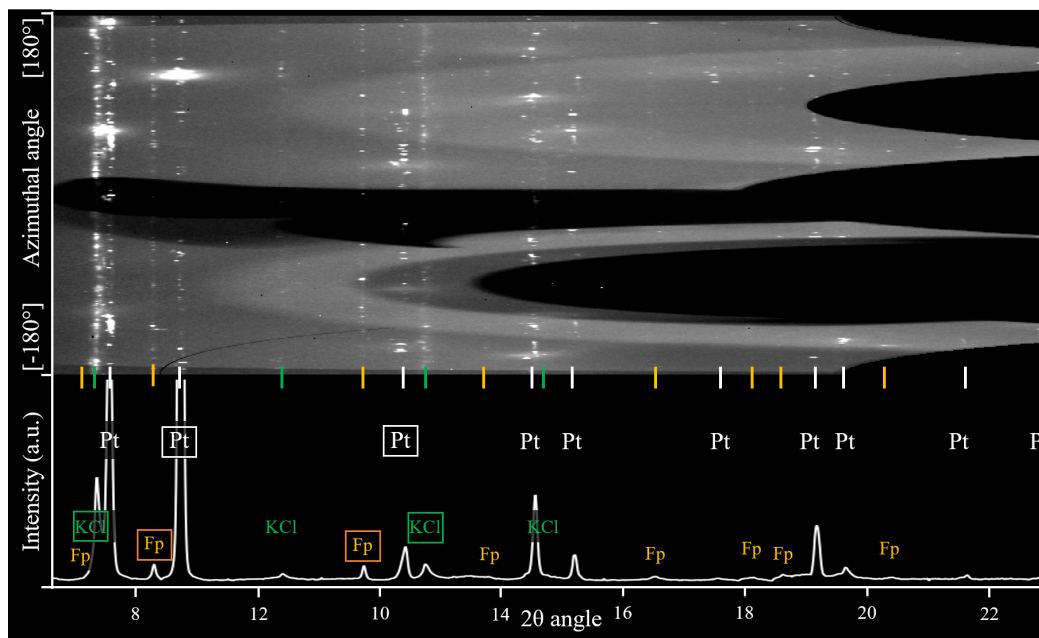


Figure 5.28: Representative enrolled raw X-ray diffraction image and azimuthal integration of Fe₂₀Mg₈₀O during the compression. Pt (white), KCl (green) and Fe₂₀Mg₈₀O (orange, here as Fp = ferropericlase) are assigned to recorded Bragg reflections and those usable in bunch pattern refinement across the whole compression event are highlighted [white, orange, green] boxes.

A raw unrolled diffraction image and its azimuthal integrated pattern is depicted [Fig.

5.28], showing the observable 2θ range and the common Bragg reflections of the sample ($[\text{Fe}_{20},\text{Mg}_{80}]\text{O}$), pressure calibrant (Pt) and thermal insulator (KCl). The unit cell volume of ferroperricite was obtained from both the (200) and (220) Bragg reflections, whilst the pressure information is derived from the position of the (200) and (220) of Pt, or the (110), respectively, (211) reflection of KCl using the EoS by [59, 203]. Furthermore, the thermal pressure component was obtained using the Mie-Grüneisen-Debye approach [Eq. 2.23] and the EoS parameters of [59, 210, 211] as well as the electronic thermal pressure component determined by [64].

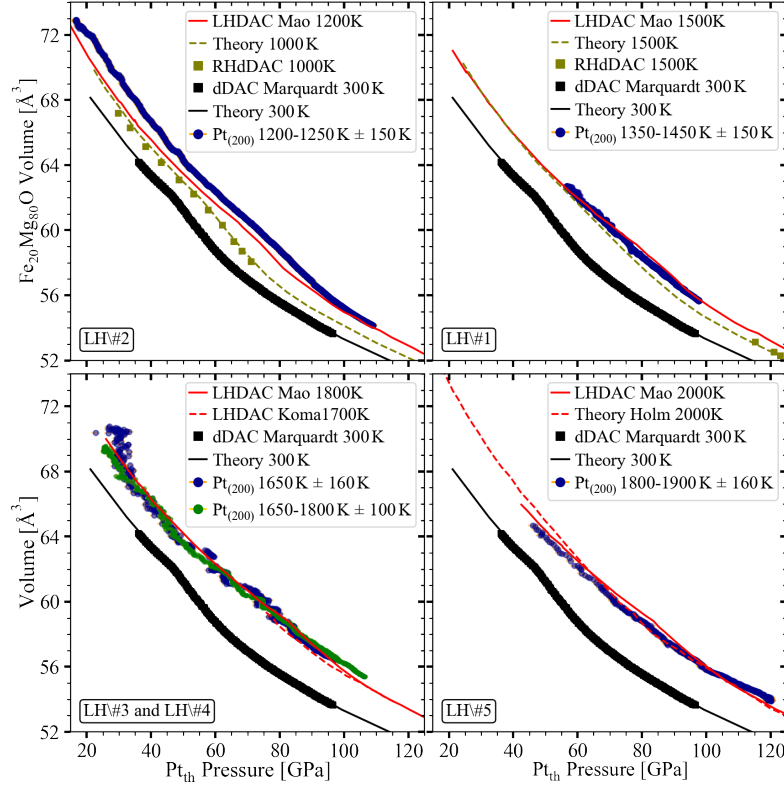


Figure 5.29: Volume evolution of $[\text{Fe}_{20}\text{Mg}_{80}]\text{O}$ as a function of pressure. P_{th} is obtained using the internal Pt pressure calibrant and the error (2 times the spectrograph average temperature variation) is mostly smaller than the marker. Blue and green (circles) represent the volume evolution obtained in this study and the data from the literature is based on [25, 175, 181, 218, 219].

An overview of the volume evolution of $[\text{Fe}_{20},\text{Mg}_{80}]\text{O}$ as a function of Pt $P_{(V,T)}$ during the five runs is illustrated [Fig. 5.29] and plotted against literature of laser heating (LH) and resistive heating (RH) experimental and theoretical results [25, 175, 181, 218, 219]. From LH#2 at 1200 K the volume collapse of $[\text{Fe}_{20},\text{Mg}_{80}]\text{O}$ is found between 70-75 GPa. Yet, large volumes of the sample material are observed compared to the literature data across the whole compression event and the spin crossover interval is broader. The reason for the volume variation is the uncertainty of the temperature measurement in this run, where only the upstream path was alignable to show continuous heating on the camera and no continuous signal could be observed on the downstream camera, due to the low temperatures. A general overview of the temperature development in the runs is shown in [Supp.Fig. 3] In the other runs temperature observation was possible with both the upstream and downstream

camera and the general volumes at 1400 K, 1700 K and 1900 K comply with literature of LH experiments and LH theory [181, 218, 219], but except the 1400 K run completely miss the observation of the volume collapse. In fact, at pressure above 90 GPa the volume evolution of LH#4 and LH#5 record higher unit cell volumes of $[\text{Fe}_{20},\text{Mg}_{80}]\text{O}$, which opposes the observations of a volume collapse during the spin crossover. Moreover, even at 1400 K (LH#1) the correlation within the spin crossover interval is faint and a possible account of the spin crossover onset is recorded, if at all, by the faint change at 75 GPa. Furthermore, not only the results of this study, but also from the previous LH experiments and theory diverge from recent observations in RHDAC experiments and their theoretical calculations [25, 175], where a stronger volume decrease across the spin crossover interval is observed.

The bulk modulus development over the compression events is obtained in accordance with the thermodynamic definition [Eq 3.3] by a rolling linear fit to the pressure vs volume development with 3 GPa intervals [Fig. 5.30]. Therefore, the uncertainty in Bulk modulus is based on the standard error of the slope in the fitting of $\frac{dP}{dV}$. Consistent with the observations in the volume development a distinct softening of the bulk modulus is found in LH#2 (1200 K) at pressures ~ 65 -95 GPa and possibly in LH#1 (1400 K) at pressure above 75 GPa. Furthermore, the absence of the spin crossover in the runs with higher temperature LH#3-LH#5 is supported by the general increasing trend of the bulk modulus without a distinct interval of lower values and even though a large spread of the data, hence low resolution of the exact bulk modulus value, is obtained.

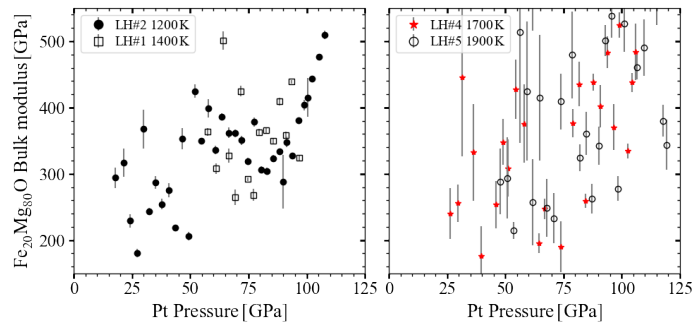


Figure 5.30: Bulk modulus development of $[\text{Fe}_{20},\text{Mg}_{80}]\text{O}$ as a function of Pt pressure. LH#3 is not shown, due to the large volume variation. LH#4 and LH#5 show a large uncertainty in the bulk modulus values, as a faster pressure increase with the diamonds of small culet size resulted in a much lower resolution. This leads to a much lower number of data points in the calculation of each 3 GPa interval.

5.3 Combining the diamond anvil cell and European XFEL,

First pulse to pulse resolved commissioning experiments were performed at the HED instrument, European XFEL, using the AGIPD detector at 4.5 and 2.25 MHz operation in a combined X-ray and laser heating DAC experiment. Thereby, the trigger of the laser-heating pulse was aligned to coincide with the X-ray timing and the streak camera observation. The initial runs were performed on LaB_6 , YAG, Pt, Fe, $\text{Mg}_{10}\text{Fe}_{90}\text{O}$ and FeCO_3 samples, where LaB_6 and YAG were used to calibrate the instrumental setup. An overview of LaB_6 [Fig. 5.31] illustrates the available 2θ range at ~ 379 mm SDD and 17.8 keV, as well as instrumental broadening of the peaks: average FWHM = 0.081° .

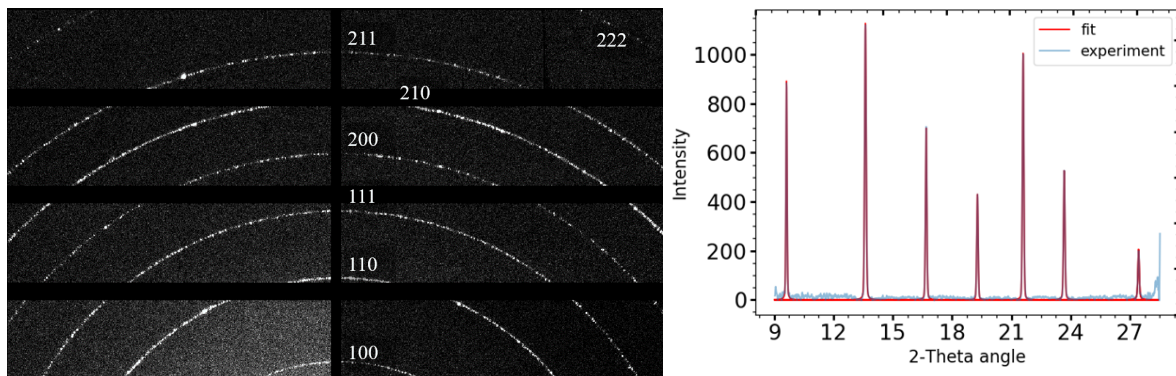


Figure 5.31: Raw XRD image of LaB_6 collected at 2.2 MHz with 1 pulse and 40 % X-ray transmission (left) and the fit of its azimuthal integration (right). The observable Bragg reflections, diffraction intensity and available 2θ space at ≈ 379 mm SDD is shown.

Several runs with a variety of pulses, 1-360, were performed during the commissioning of the AGIPD detector and this study concentrates on the runs of $\text{Mg}_{10}\text{Fe}_{90}\text{O} + 30$ wt% Pt and a pure Pt example that were performed at 2.2 MHz repetition and with 10 pulses. During the experiment different modes of transmission were chosen to adjust the amount of X-ray energy on the sample material and thus control X-ray heating. The resulting evolution of the $\text{Mg}_{10}\text{Fe}_{90}\text{O}$ unit cell volume as a function of the X-ray and LH energy is shown [Fig. 5.32], recording both the volume increase of Pt, $\text{Mg}_{10}\text{Fe}_{90}\text{O}$ and the rB1-B1 phase transition in $\text{Mg}_{10}\text{Fe}_{90}\text{O}$ as a result of increasing temperature. The resulting temperatures in the figure are obtained using the Mie-Grüneisen-Debye approach [Chapter 2.3] on the line-shift of the Pt pressure calibrant as well as refined starting conditions, Pt at 30 GPa and $\text{Mg}_{10}\text{Fe}_{90}\text{O}$ in the rB1 phase, obtained by prior screening at the ECB P02.2, PETRA III, DESY.

At the lowest transmission mode, 20 % X-ray energy on the sample, a slight temperature increase (300 K \rightarrow 450 K \rightarrow 600 K) is observable over the initial three pulses, whereas 50 % transmission initializes 650 K and a maximum of 950 K within the 5th pulse. Both runs observe rB1 not only in the initial cold probing pulse, but also within second pulse at elevated temperatures, whereas the other two runs, at full transmission, observe the rB1 phase only within the initial, cold probing, pulse. At full transmission 800 K are observed within the second pulse and a relative stable temperature plateau is reached at 900 ± 50 K across the consecutive pulse. In contrast to the plateau, full transmission in combination with the 80 W

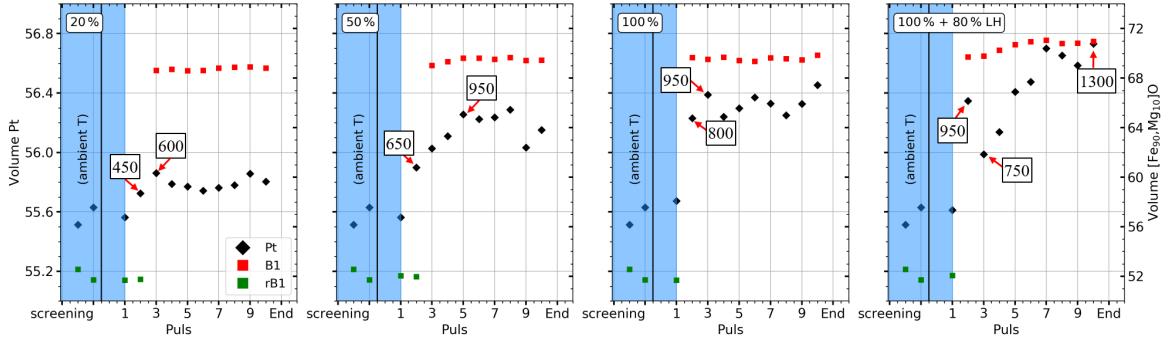


Figure 5.32: Volume development of Pt and $\text{Mg}_{10}\text{Fe}_{90}\text{O} + \text{Pt}$ at ~ 28 GPa. From left to right: Development at 20 %, at 50 %, at 100 % X-ray transmission and 100 % X-ray transmission + 80 % pulsed laser heating. Temperatur [K] is obtained by Debye approximation of the Pt volume shift observed in the XRD images. The (Black diamonds) depict Pt, whereas, $\text{Mg}_{10}\text{Fe}_{90}\text{O}$ is depicted as rB1 (green) and B1 (red) squares.

laser heating pulses records a continuous temperature increase from 750 K to 1300 K in the seventh pulse, where a larger variation can be observed between the initial hot (second pulse) and the third pulse. Here, Pt shows lower unit cell volumes in the third pulse compared to the second pulse, which would correlate to lower temperatures, while the $\text{Mg}_{10}\text{Fe}_{90}\text{O}$ sample records higher unit cell volumes consistent with the continuous heating development also observed in the subsequent pulses of Pt.

The commissioning time was further used to align the LH trigger with X-ray pulse and Shimadzu streak camera timing for *in-situ* temperature observation. The low temperatures, obtained by the Mie-Grüneisen-Debye approach (≤ 1000 K), within the first three runs, is supported by the absence of illumination of the streak camera. This camera records temperatures only during the combined X-ray and laser heating runs [Fig. 5.33. However, The streak camera observes higher temperatures, 7000 ± 500 K, within the second pulse compared to the observations of the volume change. Furthermore it shows decreasing

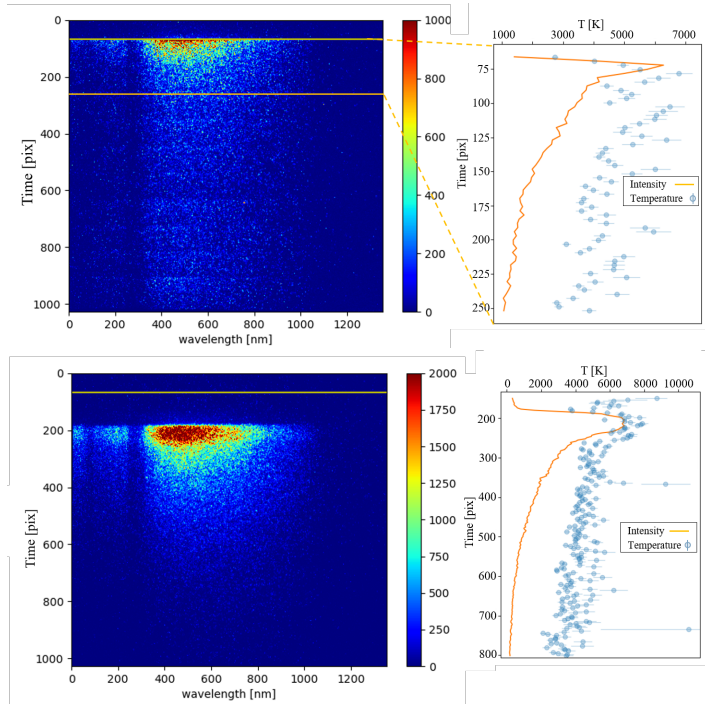


Figure 5.33: Streak camera observation of both Pt, 50 % X-ray + 100 % LH, (Top) and magnesiowüstite (100 % X-ray + 80 % LH (Bottom)). The images show the diminishing intensity and wavelength on the streak camera over the $4.45 \mu\text{s}$ duration of the 10 pulses.

temperatures across consecutive pulses whilst the volume change records increasing temperatures. A similar variance in the recorded temperature of the streak camera and the

volume change can be observed in Pt combining 50% X-ray transmission with 100 W laser heating. Here, the streak camera shows about 6500 ± 500 K [Fig. 5.33] within the initial hot pulse whilst the line-shift analysis estimates 2400 K [Fig. 5.34]. Moreover, the observable Pt peaks are doublets, with one shoulder recording almost ambient and the other shoulder hot states of the sample material.

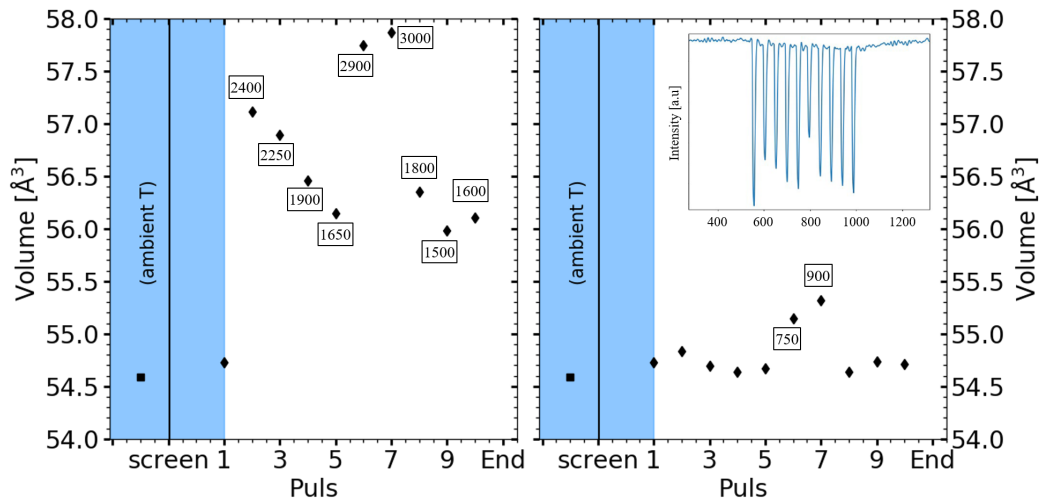


Figure 5.34: Pulse to pulse resolved volume development of Pt at ~ 36 GP (black diamonds) and correlating temperatures [K] obtained by Debye approximation [chapter 2.3]. Development of the hot (Left) and cold (Right) shoulder as well as the observed intensity of each pulse (inlet) across the experiment. The black square represents volume information obtained during initial, screening of the cell at ECB P02.2, PETRA III, DESY.

The raw X-ray diffraction images of those two runs further record an increasing background after the initial pulse [Fig. 5.35] and indicating the formation of melting. Nevertheless, a larger amount of the sample material is solid, which can be seen from the defined Bragg reflections, where $\text{Mg}_{10}\text{Fe}_{90}\text{O}$ is gradually heating up, whilst the overall temperature seems to be decreasing. In the platinum experiment the sixth pulse records 3000 K, a temperature close to the melting point of Pt at 35 GPa [220], yet it coincides with the lowest pulse energy.

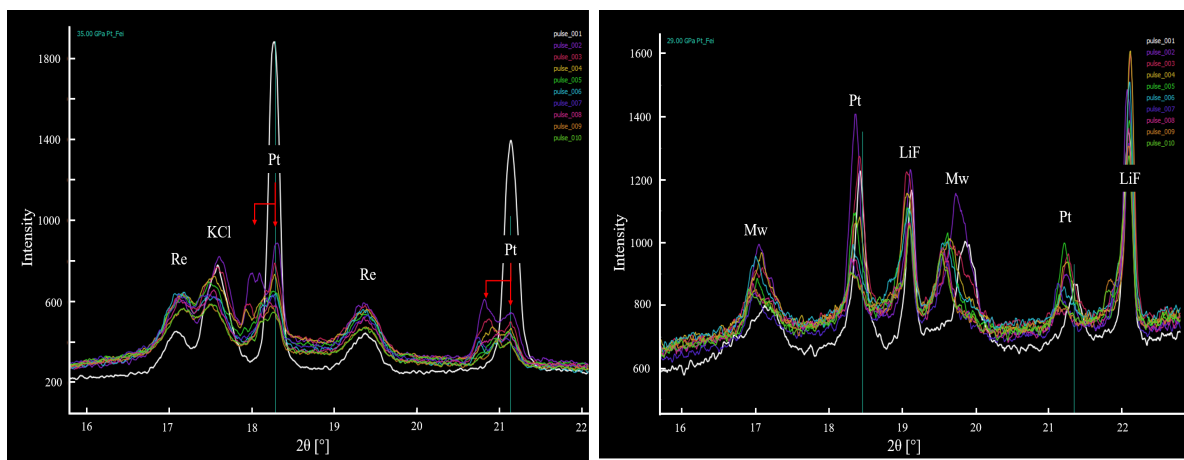


Figure 5.35: Observation of melting in both Pt (Left) and magnesiowüstite (Mw, Right) experiments using combined X-ray and Laser heating pulse. Stacked azimuthal integrated XRD record increased background after the first pulse (white) and temperature gradient, splitting of the Pt reflections (Left), or heating of LiF (Right).

Chapter 6

Discussion

In this work, the effects of different compression rates on a variety of cubic and hexagonal symmetric sample materials, Au, Pt, Re, Zn, Fe and [Mg,Fe]O solid solutions, were investigated using both mDAC and dDAC experiments on pure sample, or sample + PTM DAC loadings. A total of 47 loadings were prepared, enabling 75 compression experiments over the course of six beamtimes at the ECB P02.2, PETRA III, DESY. The variation observed in the micro-strain development of mDAC experiments based on the use of either Dioptas or the P02.2tool software is discussed in section [6.1]. Subsequently, the conditions, non-hydrostatic or quasi-hydrostatic, are dissected in both mDAC and dDAC experiments. The factors affecting them are the compression rates, gasket material and used detector setups. This study starts with the stress and strain evolution in comparison to the pressure development during the runs of cubic metals, Pt and Au [6.2], continues with the lattice parameter and strain evolution of used hcp phase [6.3] and ends with first results of [Mg,Fe]O at both high-P and high-T conditions, resulting from laser heated mDAC experiments. This ultimately leads to a summary of the results and to the discussion of the implications of first 2.2 MHz pulse to pulse resolved X-ray and laser heating experiments performed at HED, European XFEL.

6.1 P02.2tool vs. Dioptas

High resolution high-pressure experiments result in a large amount of diffraction images during a single ramping interval and require dedicated software tools to visualize and further process the raw data into usable 2D and azimuthal integrated diffraction images. During the performance of the mDAC experiments the "P02.2tool" by *Andre Rothkirch*, software developed in-house at the ECB P02.2 beamline, PETRA III, DESY, was available for bunch processing of both Tiff and nxs data formats. Furthermore, only recently Dioptas [221], a software based on the commonly used Fit2D application [222, 223], has been adapted to enable bunch processing of nxs data. The resulting pressure and micro-strain evolution obtained by both Dioptas and P02.2tool is shown in [Fig. 6.1], recording an identical pressure development and maximum pressures. However, the P02.2tool not only observes larger amounts of micro-strain, but also shows a different evolution across the compression and decompression

intervals.

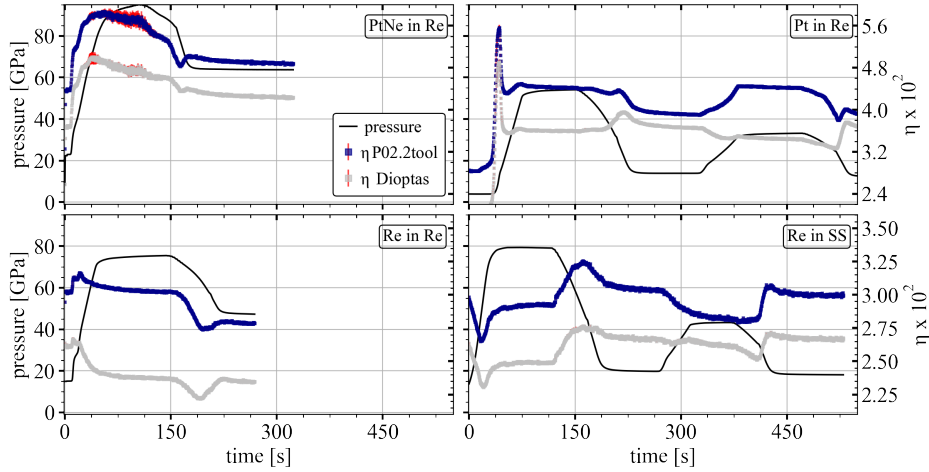


Figure 6.1: Pressure and micro-strain development of Pt and Re sample in Re or SS gaskets. From left to right: PtNe[Re] and Pt[Re] (Top) as well as Re[Re] and Re[SS] (Bottom). The solid black line shows the pressure evolution, while the micro-strain is depicted as silver (Dioplas) and blue (P02.2tool) squares.

The micro-strain calculation after [114] uses two parameters of the azimuthal integrated diffraction images, first the peak position and second the FWHM. Here, the peak position can be excluded from the list of suspects, given that the recorded pressure trend and pressure maximum of both programs coincides. This leaves the FWHM parameter as the source of the inconsistency and a representative evolution of the individual Bragg reflections obtained by Dioplas or P02.2tool, of the fast Re[SS] mDAC run, as illustrated in [6.2].

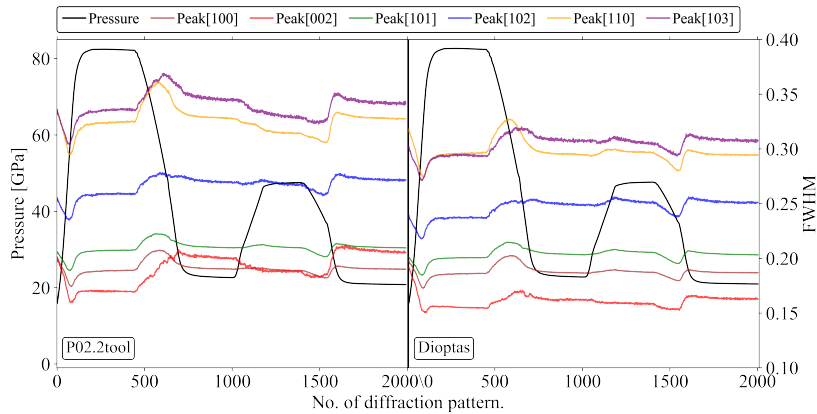


Figure 6.2: The FWHM evolution of the Re Bragg reflections during the 40 bar/min mDAC run of Re[SS]. Depicted are the results of azimuthal integrated images by the P02.2tool (left) and Dioplas (right)

Whilst the individual Bragg reflections obtained of the azimuthal integration with Dioplas display a common uniform trend, the P02.2tool integration results in variations based on the observed 2Θ angle and the reflections intensity and broadness. This integration results in larger FWHM values compared to the calculations with integrated data from Dioplas, too. A possible explanation of the origin of this variations is the source code of the P02.2tool. The P02.2tool uses the $2\Theta/Q$ positions of each (center of) pixels weighted by the accumulated intensity to perform the azimuthal integration, whereas Dioplas uses the open source pyFAI

library [224]. Within this code neighboring output bins are accounted to obtain contributions of the pixels next to its borders due to pixel splitting on the detector's sensors. This means that peaks at higher angles and with lower and broader intensity distribution are appointed lower intensities at their boundaries, due to splitting, whilst the P02.2tool appoints the full intensity to the bin. The assumption is further supported by the results of tests using only those Bragg reflections below $20^\circ 2\Theta$, as they display the same trend depicted by the integration with Dioptas. Dioptas and especially Fit2D are commonly used applications and staying true to their observations should allow comparability of this work with literature. Thus, all raw diffraction images have been integrated with Dioptas.

6.2 Stress and strain in cubic metals: Pt, Au

An apparent line-width in XRD diffraction images is often referred to as the result of the crystallites size, instrumental effects, instrumental background as well as the apparent tensile strain, micro-strain (η) and its distribution perpendicular to the Bragg reflections [121, 122, 225]. In this study micro-strain calculations have been performed on all experiments with at least 2 refinable lattice reflections, following the approach in chapter 3.4 [114], to identify effects of the gasket material, hydrostaticity and variation of compression rates. This study concentrates on the relative evolution of the stress as a function of pressure rather than the actual values, due to the limited number of available peaks and the suboptimal intensity of the reflections, which resulted from the used method and short exposure times during the runs.

In the line-width analysis, the micro-strain (η), is proportional to the aggregate Young's modulus (E) of the polycrystalline material and its compressive strength (p_{max}). The compressive strength and the differential stress (t) from the line-shift analysis are both independent measurements of the sample's strength and under identical stress conditions should be equal. For example, it was found that for MgO [212], Au [119], W [226], and Fe [114] the line-width is proportional to 2^*p_{max} , but Nb [227] was found to be in better agreement with p_{max} . In this study, the line-shift analysis is limited to the samples with cubic crystal symmetry [Eq. 3.8] due to the observation of the sample parallel to the compression axis, whereas lower symmetry samples would require either a radial diffraction geometry or angle dependent measurements in order to enable Q(hkl) determination [228].

Platinum

For the slow compression data on Pt [Fig. 6.3], at a strain rate of $4 \times 10^{-4} \text{ s}^{-1}$, the uniaxial stress or strength calculated from both the line-shift and line-width analysis are brought into a good agreement only under the assumption that the line-width corresponds to η^*E , and not $2\eta^*E$ [Fig. 5.8]. This agrees with the study on Nb [227], but a similar study on Pt, derived equal strength from the line-width analysis compared to the line-shift method assuming $t \cong 2p_{max}$ [206]. Therefore, a was adjusted between 0.5-1 and a best match was found at

$\alpha = 0.6$. In the current study, α is assumed to be smaller than 1, due to $2^*C_{44}/(C_{11}-C_{12}) > 1$ (Pt ≈ 1.55) [229] and the best match is found at $\alpha = 0.5$.

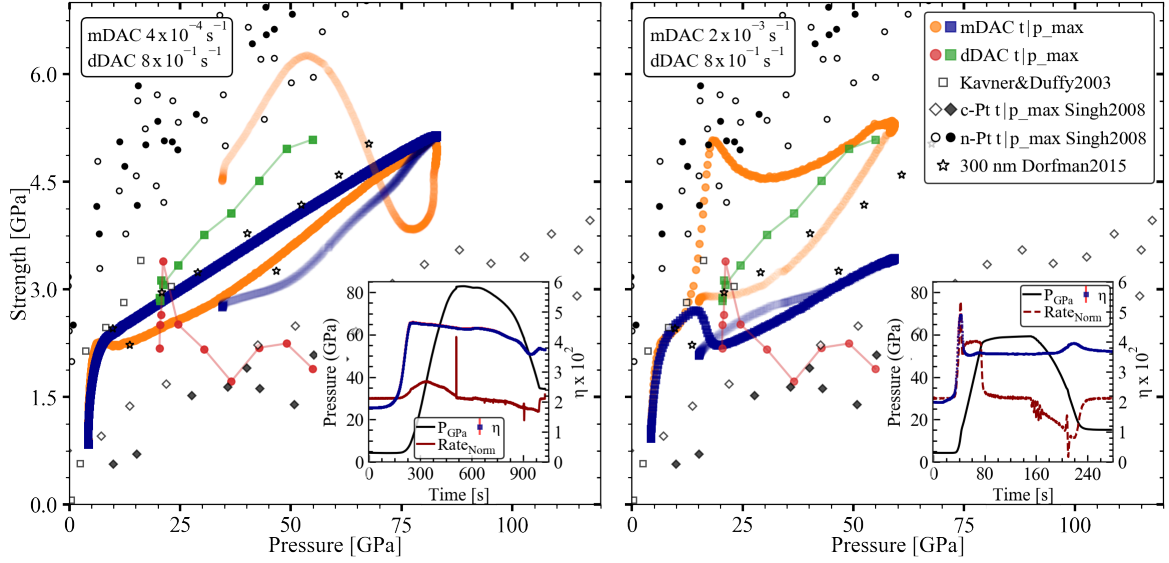


Figure 6.3: Strength of Pt during mDAC and dDAC compression, comparing (Left) mDAC ($4 \times 10^{-4} \text{ s}^{-1}$) with the dDAC and (Right) mDAC ($2 \times 10^{-3} \text{ s}^{-1}$) with dDAC. The results of current line-shift (solid colored circles), line-width analysis (solid colored squares) are given and prior results [206, 213, 230] as black open and solid symbols. The small inlets depict the micro-strain and compression rate evolution during the mDAC compression events.

The evolution of strength shows a sharp increase at pressures below 5 GPa, not recognized for neither coarse-grained nor nanocrystalline Pt in the study by [206]. However, a similar evolution of strength is consistent with reports from a variety of studies, i.e. bcc – Fe [164], hcp-Co [231], phase D [232], MgO [212, 233, 234], MgSiO₃ [235] and Nb [227]. Two factors might be the cause of the difference in stress obtained in this study and the one of *AK. Singh* [206]: 1. a time-dependent stress relaxation during the experiments [230] - Our study records a continuous pressure increase, whereas [206] allowed for 2-3 hour relaxation times before the image acquisition; 2. the high time resolution of the data makes it possible to detect large pressure derivatives. The initial large increase has been explained by elastic plastic self-consistent (EPSC) models [231] to be caused by sequential activation of plastic deformation mechanism (pyramidal $\langle c+a \rangle$ and prismatic slips or compressive twinning and prismatic slip) and the main deformation mechanism of the plastic response of fcc metals are stacking faults, twinning and full slip [236]. The primary of those is the $111\langle 110 \rangle$ slip system, albeit recent radial diffraction studies found the largest strain amplitude on the (200) plane instead of on the (111) plane, showing that the elastic anisotropy may play a role as significant as the anisotropy in strength [230]. At higher pressure, this initial increase changes, under the yield conditions, into a monotonous increase with lower rates, which is primarily the result of pressure-induced increase in the sample's elasticity and hardness.

The absolute strength of the material is shown to be grain size dependent [206, 213], where smaller grains, e.g nano-scale samples, support higher differential stresses compared to larger,

coarse grained material. The starting size of the Pt sample was 0.5 - 1.2 μm and the resulting absolute strength values of the slow, $4 \times 10^{-4} \text{s}^{-1}$, run in mDAC best match data of the 300 nm, particles from energy dispersive X-ray diffraction (EDXD) studies [213] [Fig. 6.3]. This particle size matches the observed starting crystallite sizes of Pt, 300 - 200 nm from the line-width analysis. It has to be noted that the analysis is limited by the occurrence of apparent negative intercepts after the subtraction of the instrumental broadening.

An order of magnitude higher strain rate $2 \times 10^{-3} \text{s}^{-1}$ is reached during faster compression, 0.85 GPa/s, [Fig. 6.3] and a departure from the evolution in the slow run can be observed at pressure above 12 GPa. The t values markedly increase to 5 GPa at 15 GPa, whilst p_{max} records a slight decrease. In the P-time curve, this is accompanied by the slight bend of the pressure evolution corresponding to halving of the compression rate and increasing diffraction intensity and narrowing of the Bragg reflections. The line-width analysis displays a sharp maximum at this pressure and the fact that it happens at pressures where most of the deformation should take place plastically hints that the variation may be caused due to higher strain rates and a change in the active deformation mechanism. In fact, a change in α from 0.5 to ~ 0.75 would allow for a maintenance of the correlation of t and p_{max} .

The highest compression rate run in a dDAC (390 GPa/s) records a strain rate of Pt of $8 \times 10^{-1} \text{1/s}$ and the data are available starting from higher pressures of 20 GPa only. Despite the different detector setup and diffraction coverage, the uniaxial stress data before the compression ramp matches the slow, $4 \times 10^{-4} \text{s}^{-1}$, mDAC compression data at 20 GPa. Thus, they can be considered as the strength from a static experiment after long relaxation times. However, across the compression the line-shift t appears to be relative pressure independent, or even decreasing. It has to be noted that a relative large pressure gradient is sampled (1 data point $\approx 5 \text{GPa}$), due to the insufficient diffraction intensities in sub-second exposures currently attainable at a synchrotron source. Further developments and higher resolution data requires these experiments to be performed at the hard X-ray free electron lasers. Nonetheless, the large deviation between line-shift and line-width analysis as a function of the strain rate is indicative of the importance of understanding the effects of the strain rate on the macroscopic deformation behaviour of sample in a DAC. Thereby, it needs to be taken into account the elastic response of the diamond anvils [231], the elasto-plastic deformation of different gasket materials [126] and not solely the intrinsic deformation mechanisms of the crystallographic planes.

Gold

dDAC experiments with gold reached strain of 10^{-1}s^{-1} to 10^0s^{-1} corresponding to compression rates between 2 - 350 GPa/s. The line-width analysis results in apparent crystallite sizes of 400 nm, decreasing to $240 \pm 40 \text{nm}$ over the compression events 5.17. As with Pt, the

literature *Singh et al 2006* [119] shows a close correlation between $2p_{max}$ and t as well as an overall dependence of the material strength on the grain size of the sample. whereas in this study a match of t with p_{max} is observed [Fig. 5.18]. Au shows a similar behaviour to the slow Pt, $4 \times 10^{-4} \text{ s}^{-1}$, runs as it shows a distinctly stronger increase at the start of compression replaced by a slower increase across higher pressures [Fig. 6.4].

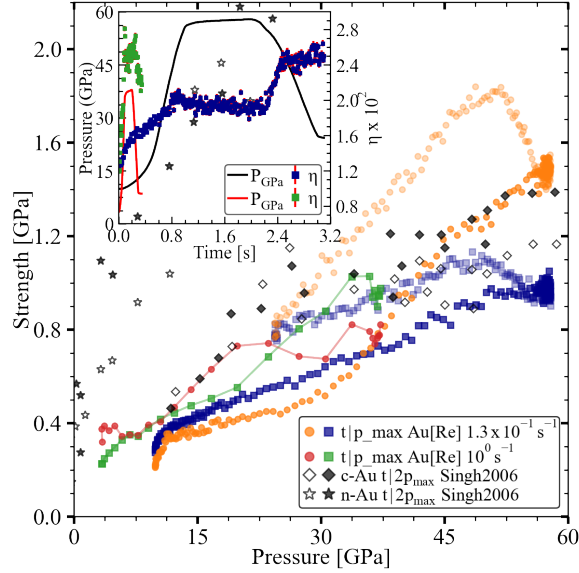


Figure 6.4: Strength of Au[Re] during dDAC compression, showing both the results of line-width, line-shift analysis and prior results [119]. The small inlet depicts the micro-strain and compression rate evolution during the compression events.

During the run, 10^{-1} s^{-1} , p_{max} shows an almost linear trend, whilst t records lower starting values but a change in the evolution at $>35 \text{ GPa}$, where it ends up with ≈ 1.5 times the value of p_{max} . As with Pt, the $2^*C_{44}/(C_{11}-C_{12})$ is > 1 in Au (≈ 2.85) [229]. A best match of the starting conditions is found with $\alpha = 0.5$ and at pressures $> 35 \text{ GPa}$ with $\alpha = 0.75$. The faster run, 10^0 s^{-1} , requires t with $\alpha = 0.75$ to overlap with p_{max} , whereas $\alpha = 0.5$ result in higher t values. Those higher t values in fact show a close correlation with 2^*p_{max} , nevertheless the closest correlation is found with $\alpha = 0.75$ [Fig. 6.4]. Alpha contains the effects of plastic deformation in cubic systems, where $\alpha = 1$ represents the lower bound of strength [229]. This means the difference of alpha shows a change in the deformation mechanism due to the applied strain rates.

Gold and Platinum in Neon

Further runs of Pt and Au were performed at hydrostatic conditions using Ne PTM [Fig. 6.5]. Thereby, the slow mDAC run ($2 \times 10^{-3} \text{ s}^{-1}$), records a linear correlation of both the micro-stress and differential stress evolution during compression, without the initial fast increase that would show the sequential activation of the plastic deformation mechanism. In the comparison the closest correlation of both parameters is recorded for p_{max} and $\alpha = 0.5$. With it, come slight variations in the differential stress development in the range of 25 - 50 GPa, where it first shows slightly higher and then lower strength compared to the micro-stress evolution.

In contrast, the sequential activation of the plastic deformation mechanism can be observed during the fast dDAC run ($9 \times 10^{-2} \text{ s}^{-1}$) at the initiation of the compression event followed by a linear increase with pressure above 5 GPa. Again, p_{max} is required to match both parameters and here α had to be adjusted to 0.6. Interestingly, in this run the decompression seems to be balanced out the differential stress and one can observe conditions with no variation between the the compression and radial axis component ($t \approx 0$).

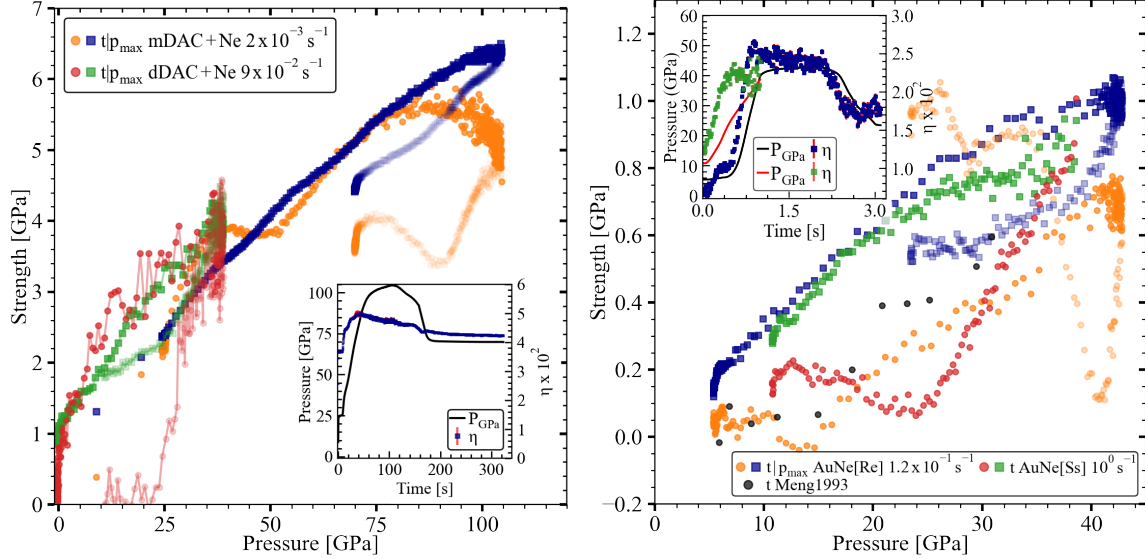


Figure 6.5: Strength of both Pt and Au sample in Ne PTM, *s* showing Pt[Re] (Left) and Au once in Re and once in Ss gasket (Right). The results of line-shift (solid colored circles), line-width analysis (solid colored squares) during hydrostatic compression are given. The small inlets depict the development of the compression rate during the compression events.

Au, like Pt, shows a linear correlation between p_{max} and the pressure increase independent of the used gasket material and despite the use of Ne PTM the resulting trend and absolute strength is in corresponds to non-hydrostatic observations by [119, 206]. Moreover, the results obtained by the line-shift analysis match well with the hydrostatic observations of [216]. In the run with Re gasket ($1.2 \times 10^{-1} \text{ s}^{-1}$) the differential stress remains quasi-constant to pressures of > 10 GPa, which is preceded by slight decrease within the pressure interval up to 16 GPa. A linear increase is observable subsequent to the slight decrease and comparable with the general trend of p_{max} , albeit with lower absolute values. In contrast, the run with Ss-gasket ($8 \times 10^{-2} \text{ s}^{-1}$) starts at 10 GPa and shows the slight initial increase that may be associated to the sequential activation of plastic deformation mechanism or the interaction of the softer gasket material with the sample material. The increase is preceded by a slow decrease during the pressure interval up to ≈ 25 GPa and > 25 GPa a fast increasing trend is recorded until diamond failure. Trying to balance out the difference in observed absolute strength would require to adjust $\alpha < 0.5$, but the difference is more likely due to the distribution of stress in the Ne PTM and the delayed onset of the differential stress increase would thus be the result of the solidification of Ne and the resulting interaction with the used gasket material.

An explanation for the changes in line-shift evolution may be found within the properties of neon. Neon is used as the PTM, homogeneously distributing the applied load onto the sample material. However, the onset of non-hydrostatic distribution has been found at pressure of ≈ 14 GPa [216], which can account for the almost constant pressure interval observed in AuNe[Re]. Additionally the gasket material has to be taken into account Ss cannot impede the radial flow of the sample as much as Re, as it is a much softer material [239]. Therefore, higher pressures are required to confine the sample and may give the explanation of the delayed onset of the line-shift increase at pressures of ≈ 25 GPa, compared to 16 GPa in Re gasket. Moreover a variation in the volume development of neon has been found at pressures of ≈ 23 -25 GPa [237, 238], which may affect this interaction and the pressure interval would match with the onset of the differential stress increase in the AuNe[Ss] run. Albeit, recent studies on the EoS of Ne [91] do not observe a change in volume, but the data coverage especially within the 25-50 GPa interval is very low and further investigation are required to solve this question.

6.3 The effect of high strain rates on hcp metals and [Fe,Mg]O

Hcp phases have been shown to be sensitive to changes in the compression environment, where they observe variations in their lattice parameter ratio [162, 163], or the short-lived presence of Bragg reflections of α -Fe in the stability field of ε -Fe in non-hydrostatic experiments [164]. The main active plastic deformation mechanisms, dislocation slip or twinning, were observed to vary depending on the implied compression rate [240]. In this study a variety of hcp materials (Zn, Re, Fe) and simple metallic oxides ([Fe,Mg]O solid solutions and the FeO endmember) have been investigated at high pressure and at high strain rates of 10^{-4} s $^{-1}$ - 10^2 s $^{-1}$.

6.3.1 Zinc

The c/a axis ratio of Zn as a function of the relative volume (V/V_0), obtained from the initial compression events are shown in [Fig. 6.6], covering strain rates of 10^{-2} s $^{-1}$ to 10^2 s $^{-1}$. As envisioned they comply with either the evolution described in [162] or [163].

K. Takemura [162, 163] investigated the pressure dependence of the lattice axes based on previous controversial results [199, 241, 242], predicting the presence of an anomaly at high pressures. Moreover, based on a recent Mössbauer study, which showed the occurrence of an electronic topological transition (ETT) of the Fermi surface, which affects the shielding of the ionic cores. It thus predicted a drastic change in the lattice dynamics at ~ 6.6 GPa and 4.2 K [243]. Within his research *K. Takemura* observed a singularity at $c/a = \sqrt{3}$ [162], which was later revoked in studies with He [163]. The supposed singularity turned out to be the results of the onset of solidification, at ~ 10 GPa, of the used methanol-ethanol-water mixture (MEW) PTM. Thus, the singularity, respectively the divergent trends in the lattice

axis development can be explained by the quantity of deviatoric stress and most probably the development of lattice preferred orientation (LPO) in the sample material.

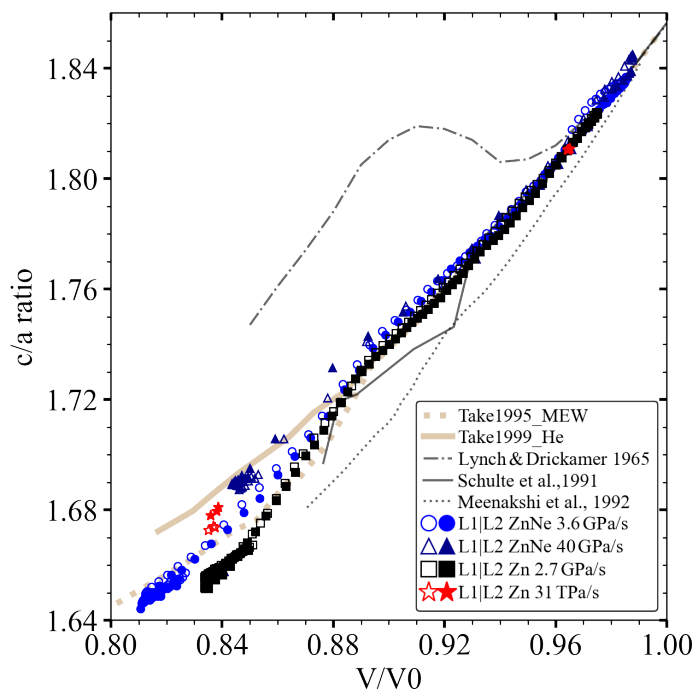


Figure 6.6: The c/a ratio of Zn across the compression intervals. Solid and open symbols represent L1 and L2 data of the different loadings. Previous data by Takemura [162, 163] is shown as a dotted and solid taint line, whilst prior results observed by Drickamer apparatus [241], DAC [199] and first principle calculations [242], are plotted as a dash-dotted, solid, and dotted black line.

Four DAC loadings were prepared in this study, two with Ne PTM and two pure Zn samples. Here, only one initial gas-loaded run, load10 ($3 \times 10^{-2} \text{ s}^{-1}$), fits in with the quasi-hydrostatic trend [163], whilst the other run, load3 ($3 \times 10^{-1} \text{ s}^{-1}$), shows correspondence with the observations in MEW PTM [162]. A simple explanation for this variation is found not to be related to the strain rate, but to the collapse of the gasket hole during gas loading and compression. The sample material came into contact with the gasket and load3 involuntarily reproduced the onset of deviatoric stress distribution. The deviatoric stress distribution is driven from the contact zone of the Zn sample with the Re gasket. In contrast, load7, the slow 6 s pure Zn compression event at strain rates of $2 \times 10^{-2} \text{ s}^{-1}$, records again the onset of variation at $c/a = \sqrt{3}$, yet with an even stronger c/a axis ratio decrease. This stronger decrease is reasonable, because no PTM is used and LPO development should be imminent with the start of compression and it further implies that even though load3 or [162] record the accumulation of deviatoric stress, some amount of the stress is still balanced out by the soft PTM.

Using fast compression rates requires short exposure times to reach a good resolution of the compression interval. However, short exposures limit the available diffraction intensity on the detectors and a compromise has to be made. As a compromise a run on pure Zn sample was performed using a fast 0.5 ms compression interval, loading 16 and 1 s exposures. Those exposures were used to observe the c/a ratios before and after the event. The long

exposures and the variation in type of compression ramp hinder the determination of the axial trend during the compression interval and prevent the onset determination for possible changes in the c/a evolution. However, any variations compared to the slow run with pure Zn sample, requires an explanation and is expected to be a change of deformation behaviour and/or mechanism. Across the 0.5 ms compression ramp a compression rate of 31 TPa/s was reached with a strain rate of $2.7 \times 10^2 \text{ s}^{-1}$. The resulting c/a ratios plot between the quasi-hydrostatic [163] and non-hydrostatic [162] conditions, but show a strong deviation from the observations in the slower run, $2 \times 10^{-2} \text{ s}^{-1}$. This means that the lattice parameter in the run resemble the development in hydrostatic compression experiments despite the absence of a PTM and despite non-hydrostatic stress distribution. Nevertheless, the resemblance could be even higher as the long 1 s exposures may allow for the onset of texture (LPO) due to relaxation over time. However, the compression environment in the run is non-hydrostatic and recently it has been shown that much faster strain rates are required to change the axial stress distribution behaviour as a result of changes in the dislocation density [244]. It has to be noted that the study intended to build a model for the deformation of single crystals so it is not entirely clear whether those rates are equally accurate for multi grain or powder samples. Compared to the idea of the observation of hydrostatic condition it is much more reasonable to assume that the main plastic deformation mechanism is alternating. This alternation is in accordance with literature on hcp metals, where dislocation slip has been determined as the main deformation mechanism during low strain rates [245] and twinning at higher strain rates of 10^3 s^{-1} [240]. Therefore, twinning accounts for fast changes (μs) and results in hardening of the sample, whilst dislocation slip would require longer timescales (ms) to distribute stress and start relaxation [246]. Beryllium is also a hcp phase and *Sisneros et al., 2010* [240] compares different compression rates and compression environments, yet it is missing strain rates of 10^1 s^{-1} to 10^2 s^{-1} and Zn compared to Be has a lower shear resistivity. It is thus, assumable that the main deformation mechanism in Zn at strain rates of 10^2 s^{-1} is twinning and the higher c/a ratios are due to hardening of the sample material and the different effect it has on the lattice axes.

6.3.2 Rhenium

Both mDAC and dDAC runs have been performed with Re applying strain rates of 10^{-4} s^{-1} to 10^0 s^{-1} and a study of the c/a axial ratio during the initial compression ramps of Re is illustrated [Fig. 6.7]. Our results from the mDAC and dDAC are shown along with the data obtained by radial diffraction DAC [205], DAC + NaCl [247] and DAC + He [214].

A compression rate independent evolution of the micro-stress is found within the range of 0.2 GPa/s to 1.3 TPa/s for Re[Re] samples and only one exception of the rule in Re[Ss] samples. Re is much less compressible than Zn and shows a maximum variation of ~ 0.01 in c/a axial ratio compared to ~ 0.2 in Zn. This is most likely due to its higher shear strength

$G = 178 \text{ GPa}$ [248] compared to $G = 40 \text{ GPa}$ [249] and results in strain rates of 10^{-4} s^{-1} - 10^0 s^{-1} .

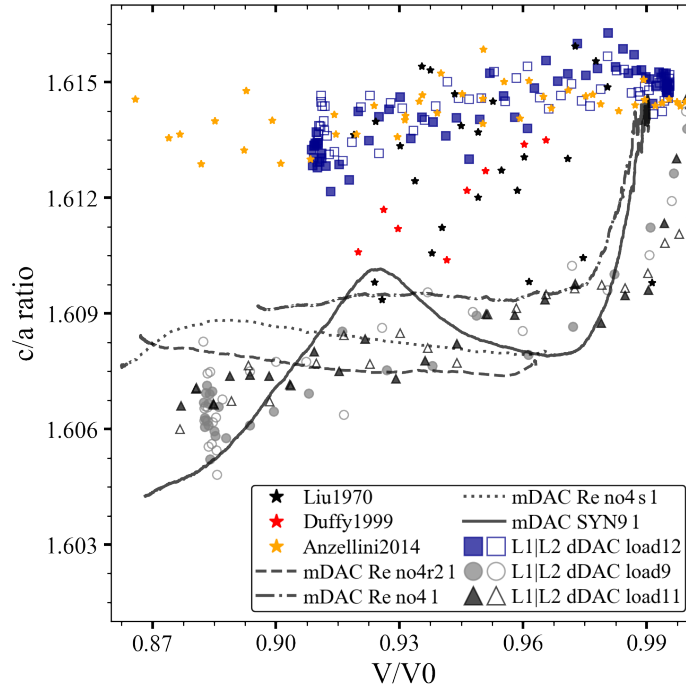


Figure 6.7: Development of the c/a axial ratio of the initial Re compression events performed with $mDAC$ (lines) and $dDAC$ (open and solid squares, circles and triangles). Literature data (colored stars) depicts either conditions observed during radial diffraction, collected at 54.7° , the "magic angle", [205], $DAC + NaCl$ [247], or $DAC + He$ [214].

Two general trends can be observed: 1. An abrupt decrease, from 1.615 to ~ 1.609 , followed by a fairly consistent plateau ($mDAC$), or monotonous slow decreasing trend ($dDAC$); 2. A homogeneous compression of the lattice cell without, or with only the slightest change, ~ 1.615 to ~ 1.613 , in the axial ratio. The first trend can be observed in all runs without a PTM and starting at pressure below 10 GPa. Furthermore, precompressed loadings and consecutive compression cycles [Supp Fig. 4] show starting c/a ratios < 1.61 and their trends record a monotonous decrease or plateau during further compression, too. The second trend can be observed only within the run using Ne as the pressure transmitting medium and the axial ratio development is consistent with the records of [214], which were used to determine the EoS of Re up to 144 GPa. The only exception from those trends is recorded during the $mDAC$ run of $Re[SS]$ (10^{-4} s^{-1}) where the initial decrease is instead replaced by the observation of increasing c/a axial ratios up to pressures of 45-50 GPa. At this point the increase of the c/a ratios stops and turns into the decreasing trend matching the observations in all $Re[Re]$ runs. The other studies $NaCl$ PTM [247] and radial DAC [205] at 54.7° deg, the "magic angle" observe c/a ratios between the trends of hydrostatic and non-hydrostatic runs found in this current study. Their trend has a close correlation with the observations by [162] or the fast ($2.7 \times 10^2 \text{ s}^{-1}$) Zn run [Chapter 6.3.1]. It seems that either the observed angle in the radial diffraction or the soft $NaCl$ PTM in the DAC experiment limits the deviatoric stresses, but can not compensate all of it. Therefore, the absence of representative c/a ratio paths correlating with these results of [247] or [205] shows that the achieved strain rates were

not fast enough to alternate the main deformation mechanism in Re. This observation is consistent with [240], where some amount of twinning can be found at strain rates of 10^0 s^{-1} , yet the main mechanism remains dislocation slip and progresses over longer time scales (ms).

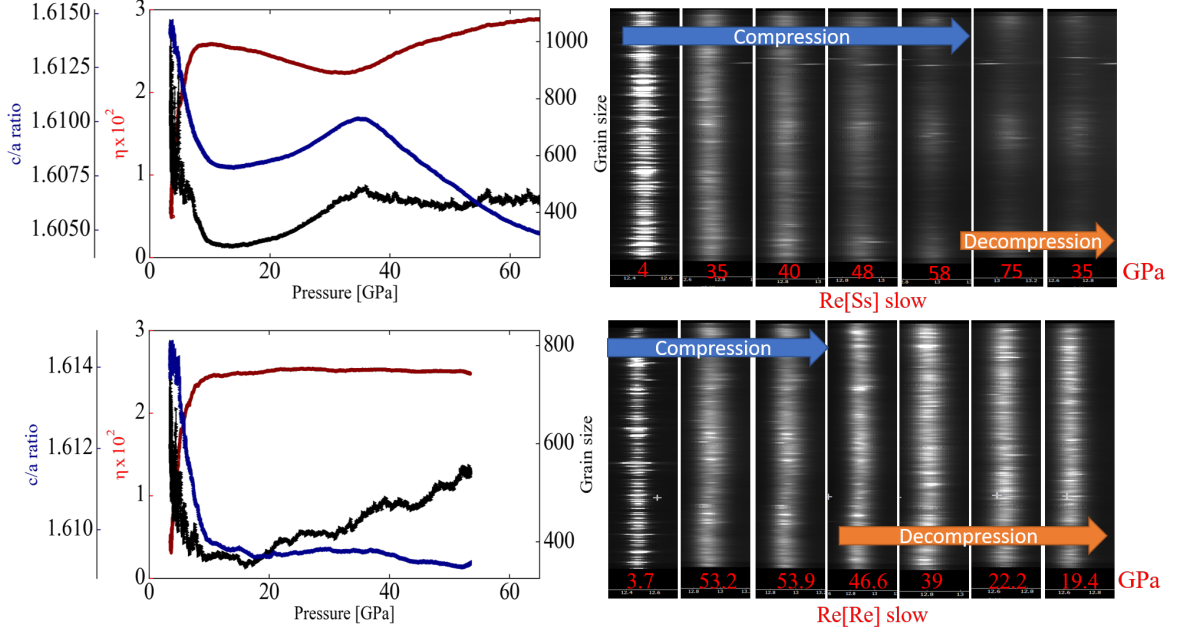


Figure 6.8: Comparison of the micro-strain, grain size and c/a ratio development of both slow, $2 \times 10^{-4} \text{ s}^{-1}$ mDAC runs in Ss (Top), Re (Bottom) gasket and the resulting (002) Bragg reflection intensity during the run.

Nevertheless, the c/a ratio observes a dependence on the gasket material and the micro-strain evolution [Fig. 5.10] in both Re[Ss] runs and diverges from the observations in Re[Re]. A comparison of the micro-strain, grain size and c/a ratio evolution as well as the development of the (002) Bragg reflection in the slow (10^{-4} s^{-1}) Re[Ss] and Re[Re] run is presented [Fig. 6.8].

Upon compression both runs observe a decrease in the effective grain size, which transfers directly to the observations of a less spotty and homogeneous intensity of the diffraction lines. Further compression of Re[Re] shows a continuous increase in grain size whilst both micro-strain and c/a ratio observe quasi-steady states. In contrast, Re[Ss] observes an increase of the grain size only up to 35 GPa, which is accompanied by an increase in the c/a ratio and a decrease of the micro-strain. At 35 GPa the grain size reaches a plateau, whilst the micro-strain starts to increase and the c/a ratio starts to decrease. At the same pressure, 35 GPa the consistent evolution of the Re[Re] and Re[Ss] XRD images diverges. The Re[Re] run shows a consistent evolution of the diffraction lines, whereas Re[Ss] observes the development of texture (LPO), showing the variation in reflection intensity dependent on the azimuthal angle and on the observed diffraction peak. The onset of LPO is observed at ~ 35 -37 GPa, becomes clearly distinguishable at pressure > 40 GPa and continues to develop until peak pressures are achieved. Here, Not only the (002) plane is affected, but at pressures > 40 GPa LPO can be observed in the (102) and (103) lattice plane as well.

A similar development of LPO in the (002), (102) and (103) lattice planes, can be observed within the fast mDAC run on Re[Ss] ($2.5 \times 10^{-3} \text{ s}^{-1}$) albeit only with the onset of decompression [Fig 5.13]. The run observes an increase of micro-strain during the decompression event and a slow decline during the initial compression event [5.10].

The first explanation of the variation could be the grain size, because of the slow Re[Ss] run that shows the development of a plateau at 35 GPa, coinciding with the onset of a micro-strain increase, LPO development and the variation in the c/a ratio. However, the grain size development of both the fast Re[Re] and Re[Ss] mDAC runs ($2.5 \times 10^{-3} \text{ s}^{-1}$) is equivalent and matches not only during compression but also decompression [Fig. 5.12]. During decompression both runs show an increase in effective grain size, whereas increasing micro-strain is associated with smaller grain-size [206]. Furthermore, the development of a quasi-steady state of the grain size can also be observed in Re[Re] runs and it onsets at a variety of pressures and with a variety of recorded grain sizes, $500 \text{ nm} \pm 100 \text{ nm}$.

Another possibility is the interaction of Re with the soft Ss gasket compared to the interaction of Re with the Re gasket. In DAC experiments the gaskets provides support for the diamond anvils, impedes the direct contact of the diamonds and most importantly limits the perpendicular flow of the sample material to the compression axis [239]. It becomes evident, from the results of the XRD images that the soft Ss gasket is not able to impede the flow of Re, as we observe strong developments of LPO only in these runs. Further evidence for the sample flow is the development of the increasing c/a ratio during the compression events. With the soft gasket the Re sample is fully confined only by the diamond anvils parallel to the compression axis, whilst the perpendicular force can partially even out by the freedom of Re to flow in the periphery. In addition, the flow of the sample can explain the stronger relaxation of strain in both Re[Ss] runs compared to the slight decrease in the Re[Re] runs, which is observed after the initial fast accumulation of micro-strain associated to the activation of a plastic deformation mechanism [231]. The two trends of micro-strain and c/a ratio are overturned with the onset of LPO, where the difference in confining force along and perpendicular to the compression axis reaches a limit and the whole sample and the individual grains start to rotate into the direction of the lowest stress [111]. Here, the study shows that the compression rate can strongly affect the development of LPO and can support the confinement of stronger sample material in soft gaskets. The slow Re[Ss] mDAC run (10^{-4} s^{-1}) reaches the limit at 35 GPa during the compression and the LPO development progresses along side further pressure increase, whereas the fast Re[Ss] mDAC run ($2.5 \times 10^{-3} \text{ s}^{-1}$) shows LPO only with the onset of decompression. Therefore, the higher strain rate in combination with the Ss gasket is able to restrain the sample flow during compression and the maximum pressure in the run is high enough, to support the restraintment of Re after the compression event. However, with the onset of decompression the load of the diamonds on the sample and gasket decreases, which leads to a collapse of the restraining force and the onset of LPO.

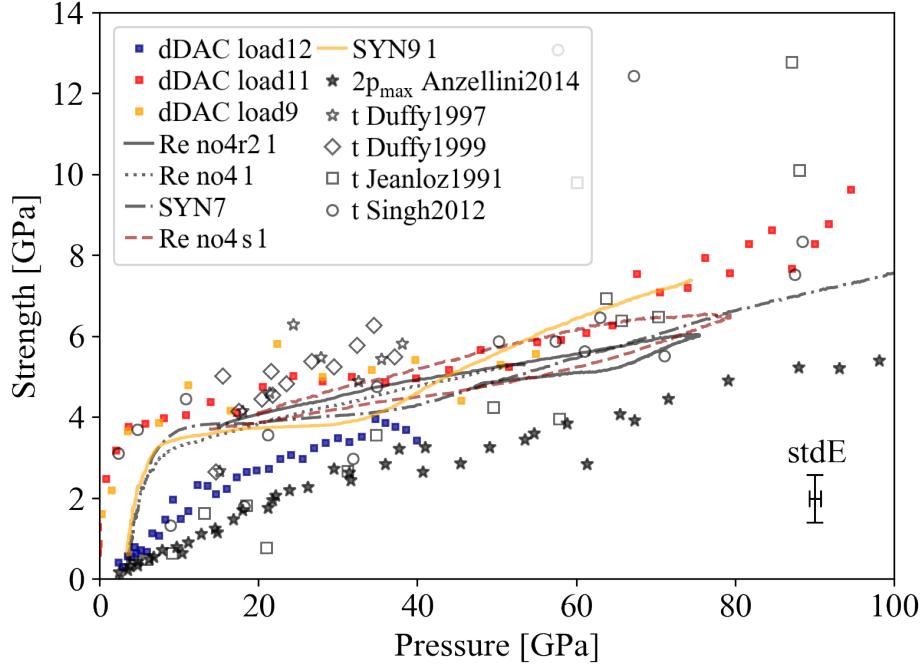


Figure 6.9: Differential stress of Re across the compression event in mDAC (lines), dDAC (colored squares) runs and as a function of p_{max} (line-width analysis). Further markers record literature data obtained by line-shift (open symbols) or line-width (full symbols) analysis [205, 214, 250, 251]

Despite the grain size variation during the compression event [Fig. 5.12] and the development of strong texture (LPO) in the runs with Ss gasket [Fig. 6.8] both the micro-strain as well as the proportional dependent micro-stress [Fig.6.9] (2^*p_{max} ; p_{max}) show only two general trends as a function of pressure: 1. A sharp increase at pressure below 10 GPa, followed by an either more or less pressure independent evolution (micro-strain) or a monotonous slow increase (micro-stress); 2. A consistent linear increase across the compression event. The first trend is observed in all runs without Ne PTM and is consistent with the observations in the slow (10^{-4} s^{-1}) mDAC run of Pt and the slow (10^{-1} s^{-1}) dDAC run of Au. As with the cubic samples and in [227], p_{max} is required to observe a correlation with literature [205, 214, 250, 251, 252]. Nevertheless, by doing a very good match is achieved. After the initial fast increase of strength [231] the mDAC results match closely with the observations of [250], whilst dDAC results match with [205, 252] up to ~ 50 GPa, at which point they comply with [250] and the mDAC results. The second trend is observed only within the run with Ne PTM and depicts the absence of the initial fast increase and a close correlation with the pressure increase, due to quasi-hydrostatic distribution of the diamond load. The resulting trend is in close agreement with observations by [214], who used He as the PTM in their studies. Despite the match in evolution, this study observes higher strength compared to the results in He, yet this variation can be explained by the properties of He. He solidifies at higher pressure compared to Ne and it shows a higher onset pressure and a slower increase of deviatoric stresses [124]. In conclusion: 1. micro-stress development and 2. the c/a ratio across the initial compression events in Re do not indicate a change of the main plastic and elastic deformation mechanism within the strain rate interval of 10^{-4} s^{-1} to 10^{-0} s^{-1} .

6.3.3 Iron

At compression rates of 10 GPa/s-1 TPa/s and strain rates of 10^{-2} s^{-1} - $4 \times 10^0 \text{ s}^{-1}$ iron is found to display the onset of a bcc \rightarrow hcp phase transition at pressures of 12-16 GPa. This transition progresses sluggishly over a pressure range of 5-11 GPa and shows a hysteresis during decompression to 9 GPa [Fig. 6.10]. The onset at 12 GPa, the sluggish transition progress and a defined hysteresis are in accordance to literature [164, 253, 254].

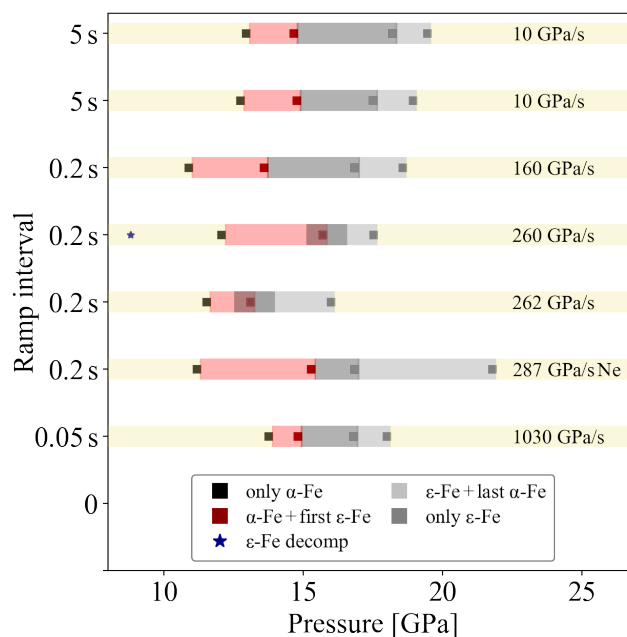


Figure 6.10: Development of the iron bcc-hcp phase transition. The color coding represents a guide for the eye, pastel-colored region only one phase, onset of transitions red, dark gray coexistence of bcc + hcp and gray end of transition, based on the results (squares), which record the observation of the phases Bragg reflections during the experiments. Hcp - bcc hysteresis across the decompression is recorded (blue star) within one experiment down to ~ 9 GPa

The recorded compression events can not resolve a strain rate dependent change in the onset pressure or pressure interval of the transition, because of the pressure resolution of consecutive X-ray diffraction images and independent of a pure sample or sample + Ne PTM. Here, it has to be noted that load2, FePt[Re] + Ne PTM seems to record the broadest transition interval. But in fact, it only records the lowest resolution of both pressure intervals: 1. only bcc \rightarrow first hcp Bragg reflections and 2. last bcc \rightarrow only hcp Bragg reflections, whilst the pressure interval of bcc and hcp coexistence complies with the other runs. After the transition the c/a axial ratio as a function of the relative volume has been obtained [Fig. 6.11].

Again, two general trends dependent on the usage of a PTM or pure sample material can be observed and fit with literature [164, 254]. The FePt[Re] + Ne load observes a very consistent c/a ratio during further pressure increase, whilst pure Fe[Re] samples runs record a monotonous slow decrease. Therefore, Fe[Re] runs at compression rates of 10 GPa/s to 260 GPa/s display closely correlating axial ratios, whilst Fe[Re] at 1 TPa/s and FePt[Re] record a slightly steeper decline till pressures of 38-35 GPa, respectively relative volumes of 0.865-0.87. This

means that either the compression rate starts to effect the general trend at strain rates of $4 \times 10^0 \text{ s}^{-1}$, the short exposures start to affect the results of the analysis or, in case of the FePt[Re], the Pt pressure calibrant affects the lattice parameter development in runs without a PTM.

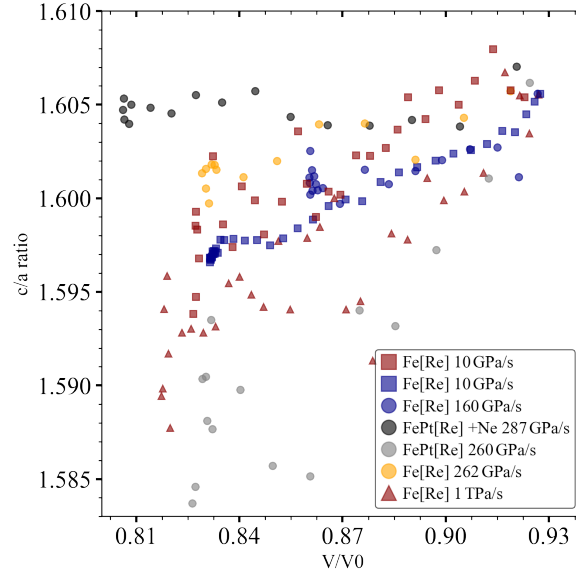


Figure 6.11: Development of the c/a axial ratio of all Fe compression runs performed in the dDAC. Showing current data across 50 ms (triangles), 200 ms (circles) and 5 s (squares) compression intervals.

Another reason to investigate the compression behaviour of iron was the report of reappearing 100 and 211 bcc reflections following the completion of the phase transition in non-hydrostatic mDAC experiments [164]. This reappearance would further confirm the complexity of the α - ϵ iron transition as well as its sensibility and dependence to the stress state and compression rate conditions [254, 255]. However, no evidence was found neither in slow nor in fast compression events, where only the hcp phase is recorded after the transition interval [e.g. Fig. 6.12]. This study is focused on fast compression rates, but the recorded X-ray diffraction image intensity is weak and furthermore varies in fast or slow experiments. Thus, low intensity reappearing reflections could be missed due to the absorption limit, sample to noise ratio of the detectors or due to the source brilliance.

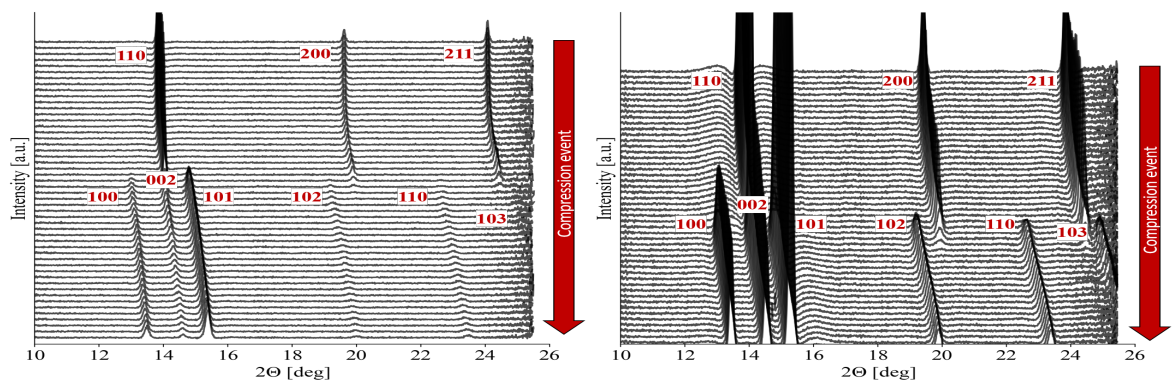


Figure 6.12: Diffraction image evolution of fast, 1.03 TPa/s, (Left) and slow, 10 GPa/s, (Right) experiments on Fe across the compression interval, showing the bcc-hcp transition. The indices of the diffraction lines are given.

6.3.4 Wüstite, Periclase solid solutions

The volume development of both $\text{Fe}_{10}\text{Mg}_{90}\text{O}$ and $\text{Fe}_{40}\text{Mg}_{60}\text{O}$ during fast compression experiments is summarized [Fig. 6.13] and compared to experimental data on ferropericlase solid solutions from literature [25, 181, 218]. The refined volume trends, obtained in this work, are in excellent agreement with the literature, showing a defined change in the recorded volume evolution associated with the iron spin crossover. Furthermore, the observations are consistent with the results of [59], in which the onset of the spin crossover is dependent on the amount of iron in the solid solution. The $\text{Fe}_{10}\text{Mg}_{90}\text{O}$ runs record an onset of the spin crossover at pressures as low as ~ 40 GPa, whereas $\text{Fe}_{40}\text{Mg}_{60}\text{O}$ records a first slight variation above ~ 50 GPa and a general decrease at ~ 70 GPa. This study observes a variation in the onset pressure of the $\text{Fe}_{10}\text{Mg}_{90}\text{O}$ runs dependent on the enforced compression rate. The fast compression events (0.75 and 2 s), with strain rates of $2 \times 10^{-1} \text{ s}^{-1}$ to $1.5 \times 10^{-1} \text{ s}^{-1}$, record the onset at ~ 40 GPa, whilst both slower (5 s) compression events, strain rates $6 \times 10^{-2} \text{ s}^{-1}$ to $5 \times 10^{-2} \text{ s}^{-1}$, record the onset at ~ 50 GPa but with a stronger volume decrease.

In accordance with the thermodynamic definition [Eq 3.3] the bulk modulus evolution has been derived from a comparison with previous studies is shown [Fig. 6.14], based on first dDAC experiments [24], direct acoustic wave velocity measurements on single crystals [256, 257, 258] and computational results [259, 260]. The significant decrease of the bulk modulus can be observed in all performed runs and during the iron spin change, consistent with most previous studies. Only the inelastic X-ray scattering (IXS) study on single crystals [258] at terahertz frequencies, does not observe a softening of the bulk modulus. A possible explanation of the absence in this specific study is the required timescale of transition. The actual electronic change is expected to be very fast, but the associated lattice distortion, due to the decrease in ionic size, may proceed at slower frequencies [24, 261]. The fast compression events [Fig. 6.13] record a match with the single crystal data by [256] and show a spin crossover interval from 38-73 GPa. Again and in combination with the observation in the volume evolution [Fig. 6.13] a delayed spin crossover onset can be observed during the slow compression events and despite a larger scatter of the data. Here the spin crossover onset is recorded from 44 GPa and supposedly occurs over a much narrower interval. However, it is not clear if it is really a narrow interval, due to the peak pressures (60 GPa) reached during

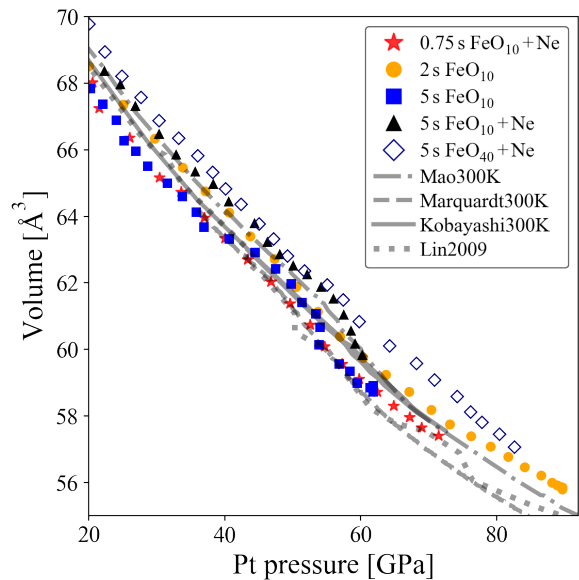


Figure 6.13: Volume development of $\text{Fe}_{10}\text{Mg}_{90}\text{O}$ and $\text{Fe}_{40}\text{Mg}_{60}\text{O}$ during compression.

compression events [Fig. 6.13] record a match with the single crystal data by [256] and show a spin crossover interval from 38-73 GPa. Again and in combination with the observation in the volume evolution [Fig. 6.13] a delayed spin crossover onset can be observed during the slow compression events and despite a larger scatter of the data. Here the spin crossover onset is recorded from 44 GPa and supposedly occurs over a much narrower interval. However, it is not clear if it is really a narrow interval, due to the peak pressures (60 GPa) reached during

the runs and the lack of possibility to extrapolate. The larger scatter in the runs $\text{Fe}_{10} + \text{Ne}$ and $\text{Fe}_{40} + \text{Ne}$ can most likely be associated to a smaller sample volume in the DAC loadings that used smaller diamond culets [Tab. 5.8]. Nevertheless, the scatter is compensated by the observable volume decrease in [Fig. 6.13].

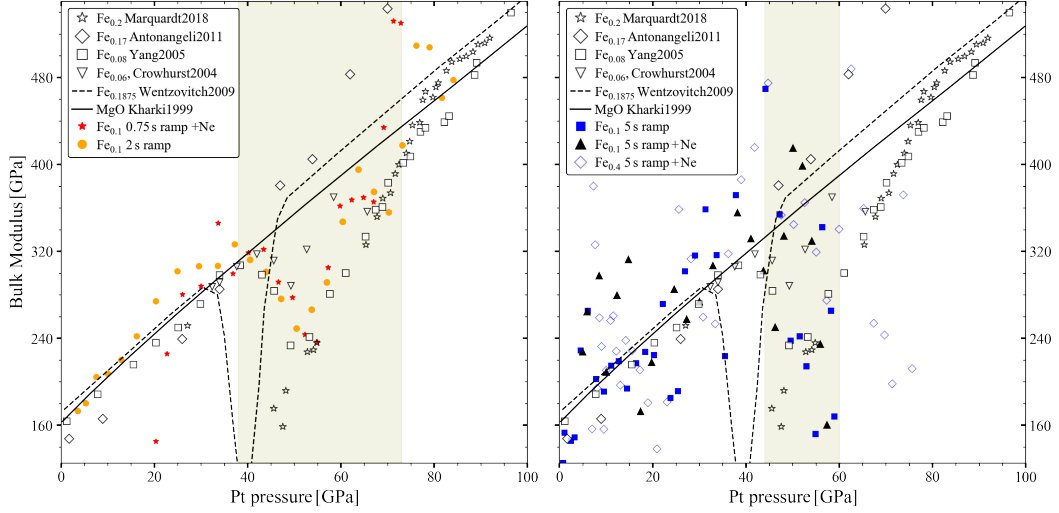


Figure 6.14: Bulk modulus of $\text{Fe}_{10}\text{Mg}_{90}\text{O}$ and $\text{Fe}_{40}\text{Mg}_{60}\text{O}$ as a function of pressure measured during 0.75–2 s (Left) and 5 s (Right) compression events with strain rates of $2 \times 10^{-1} \text{ s}^{-1}$ to $1.5 \times 10^{-1} \text{ s}^{-1}$, respectively $6 \times 10^{-2} \text{ s}^{-1}$ to $5 \times 10^{-2} \text{ s}^{-1}$. Previous determinations by single crystal and dDAC studies are given by the various black open symbols [24, 256, 257, 258] and computational results [259, 260] are given by the solid and dashed lines. The shaded area depicts the approximate region where this study finds the spin crossover. For the reason of a better illustration, the errors are not shown here, but can be found in the results section.

Further experiments on ferroperriclinite were conducted, but in contrast to the prior experiments high iron content solid solutions and wüstite are not expected to show the spin crossover at pressures below $\sim 90 \text{ GPa}$ [262]. Instead they are expected to record the B1-rB1 phase transition, respectively the rhombohedral distortion of the fcc lattice parameter due to compression [165, 169, 172]. The onset (13.8 or 14.4 GPa) of the B1 \rightarrow rB1 distortion is found to be in close agreement with the lower limit predictions in literature [165] [Fig. 6.15] and its progress can be observed *in-situ* from the lattice parameter development [Fig. 5.26], showing an increasing c-axis parameter across a wider pressure interval. Therefore, the pace of the distortion seems to be affected by the applied strain rate ($2 \times 10^{-2} \text{ s}^{-1}$ and $1 \times 10^{-2} \text{ s}^{-1}$), showing a narrower pressure interval during the experiment with faster compression rate, 14–23 GPa compared to 14–25 GPa. Here, it has to be noted that only two runs with relative similar compression rates are analyzed and the supposed strain dependence could be described by the non defined pressure range of a sluggish transition, respectively distortion. However and despite the large uncertainty, this results would match well with the compression rate dependence of the spin crossover in low iron solid solutions.

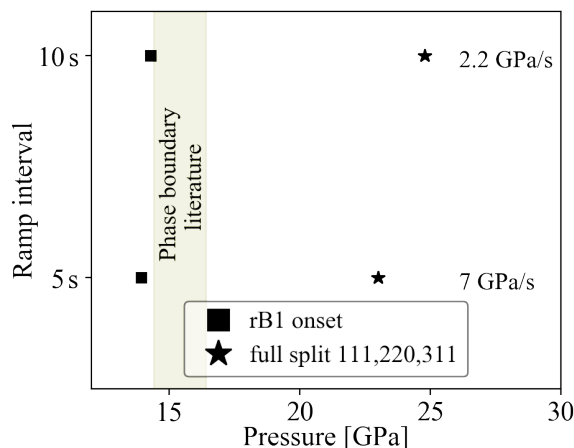


Figure 6.15: Onset of the rhombohedral distortion in wüstite. The $B1 \rightarrow rB1$ transition.

6.4 Laser heating

High pressure experiments independent of the compression rate enable only a first approximation of the material behaviour in the Earth's or planetary interior, because they take no account of the correlating temperature increase associated with the pressure increase [Fig. 1.1]. Nevertheless, they allow the development, refinement and falsification of theoretical or numerical calculations and models. In this work, the spin crossover and the $B1 \rightarrow rB1$ transition of ferropicriase are found to be compression rate dependent. Nonetheless as of now the experiments missed out to take into account the second main parameter of the environmental conditions: The temperature.

Previous theoretical and experimental studies of ferropicriase at high temperature predict and observe a positive Clapeyron slope of the spin crossover and most phase transitions, except for the $rB1$ -inverse $B8$ or normal $B8$ - $B2$ transition [165, 169, 181, 218, 263, 264]. Higher temperatures are found to result in a broadening of the transition interval [181, 183, 265, 266, 267]. The onset pressure or the existence of a spin crossover and/or phase transitions is dependent on the iron content in the solid solution [59]. Here, first continuous mDAC compression and laser heating (LH) experiments were performed to enable meticulous tracking of the volume development of ferropicriase ($\text{Fe}_{20}\text{Mg}_{80}\text{O}$) and in the course of it investigate *in-situ* the evolution of the spin crossover.

The volume collapse associated with the spin crossover in the iron component [25, 175, 181, 218, 219] is observed only in the runs at lower temperatures (<1400 K), while in the runs at 1700K and 1900K the volume collapse is not obvious [Fig. 5.29]. There are several explanations for the absence of the volume collapse and the higher volume parameter: 1. The required PT conditions were not reached; 2. The thermal pressure of Pt is wrong/ affected by the sample environment or 3. The decomposition of $[\text{Mg,Fe}]\text{O}$ into Mg- and Fe-rich oxides.

The first explanation is not likely, as previous LH- and RHDAC studies show the spin crossover associated volume collapse of $\text{Fe}_{20}\text{Mg}_{80}\text{O}$ within the achieved pressure range and in accordance to the generated temperatures. Moreover, at low pressures the volume evolution as a function of P_{th} complies with the previous LH results [181, 218, 219] and the variation develops only during the compression event.

The second explanation is supported by recent studies [25, 175], which observe a variation in the degree of the volume collapse, comparing results of LHDAC or RHDAC experiments [Fig. 5.29]. In the current study, the thermal pressure contribution was obtained using the Mie-Grüneisen-Debye (MGD) approach and showed an almost constant thermal pressure evolution. The largest variation in thermal pressure at 1900 K was +1 GPa between 45 GPa and 120 GPa. However, the MGD approach calculates P_{th} as a function of the pressure calibrant only. This calculations might be reasonable for RHDAC experiments, where the whole DAC assembly is heated up and only the sample material and pressure calibrant are enclosed by the gasket. However, in LHDAC experiments it misses out on the properties of the thermal insulator which encloses the sample and pressure calibrant. The thermal insulator (KCl) is a soft medium compared to the gasket and during the spin crossover, where the samples volume collapses [25, 218], the pressure calibrant might be able to expand/ relax more. This would result in a thermal pressure decreases, whereas the calculations still assumes the large contribution.

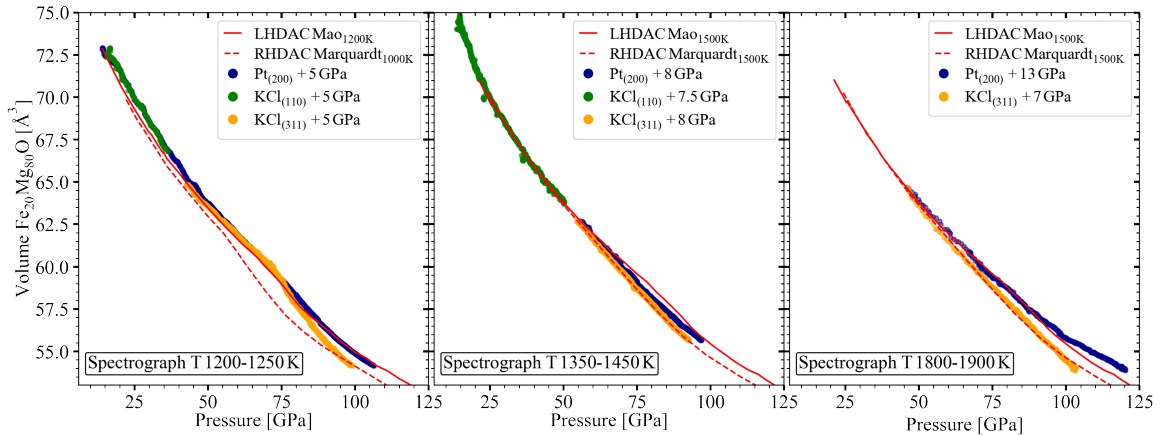


Figure 6.16: $\text{Fe}_{20}\text{Mg}_{80}\text{O}$ volume evolution as a function of pressure using KCl and Pt EoS. The pressure evolution of Pt (blue circles) and KCl (green and orange circles) is shown assuming a constant thermal pressure contribution. The thermal pressure is adjusted to match with the previous LHDAC [218] and RHDAC theory [25] observations at low pressure.

Furthermore, this cause is supported by the pressure development observed in KCl. In contrast to Pt, the KCl is in direct contact with the diamond anvils, thus it can be assumed to measure the cold isotherm of the pressure development. A comparison of the pressure development in KCl and Pt is given in [Fig. 6.16], assuming a constant thermal pressure - in accordance with the quasi-constant observations of the MGD approach - to match with the conditions of the previous studies.

The figure [Fig. 6.16] shows a close correlation of the Pt and KCl pressure evolution at 1200 K and 1400 K until the onset of the spin crossover in iron, where the volume decrease of Pt is much less pronounced compared to the observation in KCl. With the onset of the spin crossover, Pt matches with the previous observations in the LHDAC [218] at 1200 K, but lies between LHDAC and RHDAC at 1400 K. Whereas, at both temperatures KCl complies closer with the observations in the RHDAC [25]. At higher temperatures this deviation becomes even more pronounced and it becomes evident that KCl has a much lower-thermal expansivity compared to Pt [211], because a correlation of the trends requires a stronger adjustment of the Pt pressure (+ 13 GPa) compared to KCl (+ 7 GPa). Furthermore, the onset of the deviation seems to be temperature dependent, as higher temperatures shift the onset pressure to lower pressures. KCl again matches with the observations in the LHDAC study [218] and Pt complies with the observations in the RHDAC study [25]. However, only up to ~ 90 GPa, at this pressure the RHDAC study records a change in the volume development, which is associated to the spin crossover and interestingly Pt complies with this change and starts to record higher sample volumes compared to prior LHDAC observations.

Both, the difference in the RHDAC and LHDAC observations and the change in pressure development in KCl and Pt, during the predicted spin crossover interval, hint at a change in the EoS of Pt. It can be assumed that this change is caused by the sample environment in LHDAC experiments and to modulate this effect theoretical calculations are planned. The calculations will use a combination for the thermoelastic module of the steady-state heat transfer equation and the stress-strain relation. First preliminary results [Supp.Fig 5] show that the thermal pressure development is heavily dependent on the bulk modulus of the environment and the thermal expansion coefficient of the sample, thermal insulator and the pressure calibrant. However, calculations have started only recently and are ongoing.

The third and last explanation, includes the ongoing debate about the stability field of ferropericlase and its reported decomposition into Fe-rich and Mg-rich oxides at high pressure (> 80 GPa) and high temperatures [268, 269, 270]. With higher iron content the spin crossover would shift to higher onset pressures [59]. However, no splitting of the diffraction lines of ferropericlase is observed in this study, whereas those studies reporting a decomposition [268, 269, 270] observe the coexistence of two cubic phases. This aside, diffraction images were collected in this study during much shorter timescales (max 5 s) and continuous compression, hence the diffraction intensity might be too low to observe the peak shoulder of the decomposed phases. Therefore, a post-mortem analysis of LH#5 (1900 K) is currently in progress, using scanning and transmission electron microscopes (SEM and TEM) to have a closer look at possible reactions or changes of the sample composition. Their results are pending.

Chapter 7

Summary and implications

This thesis aims at investigating the effect of the compression rate on the kinetic response of diamond anvil cell experiments. It begins with a look into the high-pressure as a dynamic system and continues with the properties of the materials, the diamond anvil cell and the X-ray diffraction. In the course of it, benchmark experiments with the dynamic diamond anvil cell technique were performed on six different sample materials: gold; platinum; rhenium; iron; zinc and the ferroperricite solid solutions, offering a scientific discussion of the results. Both mDAC and dDAC drivers were used and compression rates of 0.1 GPa/s - 38 TPa/s were achieved in *in-situ* X-ray diffraction experiments at the synchrotron radiation source PETRA III, DESY, Germany. These compression rates relate to strain rates in the range of seven orders of magnitudes 10^{-4} s^{-1} - 10^2 s^{-1} and to conditions with few other comparable campaigns, 10^{-2} s^{-1} - 10^2 s^{-1} , due to the novelty of the dDAC technique [10].

The stress and strain evolution of **Au** and **Pt** at pressures up to 100 GPa was determined in this study. With the novel technique a compression rate dependence of the differential stress development can be observed at strain rates of 10^{-4} s^{-1} - 10^0 s^{-1} , where the micro-stress development is found to be compression rate independent. Furthermore, this finding shows that a correlation of both parameters requires the exact knowledge of the development of plastic deformation mechanism. Much higher micro-stress values are obtained here compared to the literature [119, 206, 213], requiring the comparison of p_{max} with differential stress instead of $2p_{max}$ (micro-stress). However, this comparison is consistent with the findings in Nb [227]. At slow compression rates (10^{-4} s^{-1}) of pure Pt a consistent correlation of micro-stress and differential stress is given using $\alpha = 0.5$. Whereas, at fast compression in Au (10^0 s^{-1}) this correlation requires usage of $\alpha = 0.75$. Consistent with this variation are the runs performed at strain rates between those two conditions (10^{-4} s^{-1} - 10^0 s^{-1}) for Pt and Au. They show a diverting trend of p_{max} and differential stress during the compression event. The changing trend requires a steady shift of α from 0.5 - 0.75 in the analysis and in Pt it is accompanied by a change of the effective grain size. Alpha (α) contains all the effects of plastic deformation in a cubic system [229], hence the variation depicts a change in these

deformation mechanism. Furthermore, in accordance with the expectation that a pressure transmission medium (PTM) effects the distribution of stress, different trends are observed for runs using Ne PTM [216]. In Pt the effect of the used PTM is independent of the strain rate $4 \times 10^{-4} \text{ s}^{-1} - 8 \times 10^{-2} \text{ s}^{-1}$, whereas in Au the onset of differential stress increase is delayed to 16 GPa or 25 GPa and dependent on the used gasket material Re, or Ss.

In **Rhenium** the lattice parameter response and the micro-stress development have been investigated at strain rates of $10^{-4} \text{ s}^{-1} - 10^0 \text{ s}^{-1}$ and at peak pressures of up to 80 GPa. Consistent with the observations by [240, 245], no change in the main deformation mechanism can be observed within this range of strain rates neither in the micro-stress, nor in the lattice parameter response. Thus, the homogeneous distribution of soft pressure calibrants stress becomes clearly visible, drastically altering the response in both micro-stress and lattice parameter development. Nevertheless, it becomes evident in this study that the compression rate has a major impact on the development of texture (LPO). At strain rates of 10^{-4} s^{-1} within a soft Ss gasket strong LPO development is observed during the compression interval as a result of the difference in constraining forces along and perpendicular to the compression axis. Whereas, the Ss gasket at strain rates of 10^{-3} s^{-1} is effectively able to prevent the development of LPO during compression and to delay onset until decompression.

The lattice response of **Zinc** was investigated at strain rates of $10^{-2} \text{ s}^{-1} - 10^2 \text{ s}^{-1}$ and at pressure from ambient to 36 GPa. In runs with and without Ne PTM and at strain rates of $10^{-2} \text{ s}^{-1} - 10^0 \text{ s}^{-1}$ a variation in the c/a ratio at pressures >9 GPa is found based on the hydrostaticity conditions and regardless of the strain rate, which complies with the observations in [163]. In contrast, the results of the jump compression run (0.5 μs ramp and image collection before and after the event) at strain rates of 10^2 s^{-1} show a more complex development of the deformation mechanism. The run was performed without Ne PTM and despite that c/a ratios fit with quasi-hydrostatic conditions. It was demonstrated before, that the main deformation mechanism of hcp metals at low strain rates is dislocation slip [245], requiring ms to allow sample relaxation and stress distribution. At a higher strain rate dislocation slip is replaced by an increase of twin formation [240], which results in changes at μs and results in hardening of the sample [246]. The jump compression run is non-hydrostatically compressed, hence one can assume that the variation of the lattice parameter development is due to the transition from a dislocation slip to a twin formation preferred deformation. Therefore, this study reports that the onset conditions required for the change in the deformation mechanism of Zn are within the range of $10^0 \text{ s}^{-1} - 10^2 \text{ s}^{-1}$.

A phase transition onset from $\alpha \rightarrow \varepsilon$ -**Fe** was observed in this work at 12-16 GPa which progresses sluggishly over a pressure range of 5-11 GPa consistent with [164, 253, 254, 255]. This transition is uniform and no remnant reflections of α -Fe are found within the stability field of ε -Fe. This stands in contrast to some findings of a possibility of time dependent

remnant α -Fe domains shielded by a fully transformed ε -Fe matrix [164]. Furthermore, no effect on the transition onset or the pressure range could be observed in neither the lattice parameter nor the micro-strain evolution at strain rates of 10^{-2} s^{-1} - 10^0 s^{-1} . However, the use of a PTM stabilizes the c/a ratio during compression and seems to broaden the pressure interval of the phase transition, whilst high compression rate runs have a more defined and narrow transition interval.

From this work, a clear variation in the volume development of **ferropericlase** ($\text{Fe}_{10}\text{Mg}_{90}\text{O}$ and $\text{Fe}_{40}\text{Mg}_{60}\text{O}$) is observed during compression up to 90 GPa, which correlates with the softening of the bulk modulus. These two developments illustrate the high to low spin transition in iron [24, 256] and the spin crossover is found to be compression rate dependent. Higher strain rates, 10^{-1} s^{-1} , show lower onset pressures and a broad transition intervals, 38-73 GPa, whilst slower strain rates, 10^{-2} s^{-1} show a narrow transition interval at higher pressures $\sim 50 \text{ GPa}$ -60 GPa and with a significantly greater change in the volume as well as the bulk modulus. Moreover, the runs support the theory that the spin crossover interval depends on the iron content, showing an onset of volume and bulk modulus decrease of $\text{Fe}_{40}\text{Mg}_{60}\text{O}$ at 65-70 GPa. Instead of the spin crossover, **wüstite** and **magnesiowüstite** have been found to undergo a B1 \rightarrow rB1 distortion of the unit cell [165, 180]. This transition shifts to higher pressures with lower iron content in the solid solution. In this work, the evolution of the c and a -axis in wüstite was meticulously tracked and onset of the rB1 distortion is found (as early as) at 13.8-14.4 GPa which progresses until 25 GPa. This transition/distortion seems to be affected by the compression rate, showing a slightly earlier start and narrower distortion interval, yet more dedicated studies with larger compression rate variations are required to support this assumption with experimental data.

Finally, the volume development of **ferropericlase**, $\text{Fe}_{20}\text{Mg}_{80}\text{O}$ was investigated in continuous mDAC and laser heating compression experiments, enhancing the correlation to conditions in the Earth's and planetary interiors. Five runs were performed in the range of 1200-1900 K and $\sim 100 \text{ GPa}$ to quantify the temperature dependence of the spin crossover. However, the volume collapse associated with the spin crossover was found only at temperatures below 1400 K, whilst higher temperatures showed larger volume parameters compared to [25, 181, 218, 219]. Furthermore, a significant deviation in the pressure evolution from either the Pt pressure calibrant or the KCl thermal insulator was recorded. This deviation cannot simply be explained by the temperature difference in the insulator and sample, because equating the starting conditions observes a temperature dependent onset of the variation, while increasing the temperatures results in deviating Pt and KCl pressure trends at lower pressures.

In summary, it becomes evident that the development of stress, strain, lattice parameter, phase- and spin transition can be influenced by the compression rate and are specific to the

properties of both sample material and the sample environment (PTM, Gasket). However, major limitations impacted this work at fast compression rates. The most evident is a predicament of the technique itself, as it needs short exposure times to maintain a high time resolution of the event. Likewise the sample volume, at high pressure experiments requires small anvils. Short exposures and a small sample volume decreased the available intensity of the diffraction image and lacked the resolution to perform an extensive analysis [Fig. 5.15, 5.23], or just show the conditions before and after the event [Fig. 5.19]. Thus, fast compression rate experiments are strongly dependent on the brilliance of the X-ray source and the availability of fast and sensitive detectors. Furthermore, the dDAC does not allow the direct adjustment of the compression/ strain rate, but only the adjustment of the applied voltage and time of extension, hence compression and strain rates will depend on the individual loading, the sample and the DAC and therefore are not easily reproducible. In addition, the observation of the strain and stress development parallel to the compression axis, results in the incapability to perform certain analysis with samples aside from the highest (cubic) unit cell symmetry.

Nonetheless, the results show that investigating the compression rates with the dDAC is an important step to enable intermediate compression rates and also opens a good way of looking for answers and help scientists to understand extreme and dynamic processes, which is invaluable not only for planetology, but our scientific understanding of static and common dynamic (shock, ramp) processes in general.

Chapter 8

Outlook

The present study is a first step towards mDAC and dDAC experiments at the European XFEL and to resolve the gap of unavailable strain rates ($10^{-3} - 10^5 \text{ s}^{-1}$) with common shock and static techniques. The new hard X-ray free electron laser facilities, like European XFEL, play a major role in resolving the main limitation of the current third generation synchrotron facilities: limited diffraction intensity at short exposures. They provide a much higher source brilliance of the X-ray beam [152, 271], hence the possibility to probe shorter timescales which makes them perfect for compression rate dependent experiments. In this study, encouraging results [5.3] of the first commissioning experiment with the AGIPD detector [161] of the HED instrument, European XFEL, are presented. The experiment enabled pulse-to-pulse resolved XRD-image collection at 2.25-4.5 MHz repetition, combined with laser as well as X-ray heating and in-situ temperature observation capabilities. The performed runs are isobaric and only a small amount of data can be compared. Nevertheless, a time dependence of the [Mg,Fe]O rB1 \rightarrow B1 transition is found [Fig. 8.1].

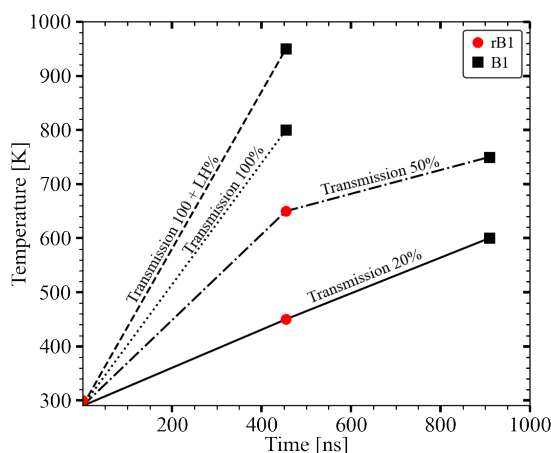


Figure 8.1: Time dependence of the rB1 and B1 phase transition during the X-ray and laser heating experiments at HED, European XFEL.

The Low transmission mode (20%) results in a slow temperature increase from 300 \rightarrow 600 K over 900 ns and shows the stability field of rB1 at temperatures between 300-450 K but not at 600 K. A higher transmission mode (50%) records a faster temperature increase from

300 → 650 K over 450 ns and the extension of the rB1 stability field to temperatures of at least 650 K.

Along with the new XFEL capabilities, which are planned to be used in the course of the upcoming fast compression experiments, further improvements for the investigation of high compression rates appear now and in the near future, as important synchrotron sources [e.g. ESRF, PETRA III] are upgrading their accelerators [272, 273]. The upgrade will increase the flux, thus brilliance of the facilities and enable shorter exposures or higher intensity at the conditions investigated during this study. Furthermore, ECB P02.2, Petra III, is about to obtain a larger version of the LAMBDA GaAs 2M detectors that will enable a wider 2Θ space and full 360° azimuthal range. In the course of future investigations, taking advantage of those improvements, thoughts should also be given to use metallic glass inserts with the gaskets [274, 275], as they does not show parasitic reflections of the gasket material when smaller diamond culets are used.

Nevertheless, the experimental setup of fast compression rates needs to be further optimized to allow for extensive texture, strain and stress as well as for anisotropy studies. Usually, these analyses is performed in static DAC and mDAC studies using radial diffraction to probe the sample perpendicular to the compression axis and take advantage of the azimuthal dependence of the resulting XRD images [138, 276, 277, 278]. In contrast, the current dDAC design is limited to observations parallel to the compression axis. Such a device (radial dDAC) is being developed at the ECB P02.2, PETRA III DESY and in collaboration with the Los Alamos National Laboratory (LANL), while the dDAC design of the Lawrence Livermore National Laboratory (LLNL) [145] is already compatible with radial diffraction, but not available for general usage. As soon as these DACs become generally accessible, they could be very useful to for quantifying and explaining the variations in observations parallel to the compression axis. Wherever possible and the source brilliance allows it the radial diffraction approach should replace, or go along with the parallel observation.

Finally, this study is a work in progress and there are technical and methodical aspects we are planing and currently using to further investigate and explain the variation in the results. 1. Post-mortem analysis of the laser heated $[\text{Fe}_{20}, \text{Mg}_{80}]\text{O}$ runs, by means of scanning and transmission electron microscopes (SEM and TEM) to investigate the possibility of decomposition [268, 269, 270]; 2. A thermoelastic module of the steady-state heat transfer equation and the stress-strain relation to calculate the stress and temperature distribution, hence to identify changes in the thermal pressure evolution of Pt as a function of the matrix and sample properties and last but not least 3. Dislocation density analysis of the sample materials, as it is also dependent on the FWHM evolution of the diffraction peaks [279, 280, 281] and may unravel an explanation for the difference of micro-stress and differential stress development.

Bibliography

- [1] I. Jackson, ed., *The Earth's Mantle: Composition, Structure and Evolution* (Cambridge University Press, Cambridge, 1998), ISBN 9780511573101, URL <https://www.cambridge.org/core/product/identifier/9780511573101/type/book>.
- [2] P. Faupl, *Historische Geologie* (Facultas Verlag- und Buchhandels AG, Wien, 2003), 2nd ed., ISBN 978382522149.
- [3] *Die Erde, accessed (04.2021)*, URL eclipse.gsfc.nasa.gov.
- [4] A. Wolszczan and D. A. Frail, *Nature* **355**, 145 (1992), ISSN 0028-0836, URL <http://www.nature.com/articles/355145a0>.
- [5] M. Lopez-Morales, R. D. Haywood, J. L. Coughlin, L. Zeng, L. A. Buchhave, H. A. C. Giles, L. Affer, A. S. Bonomo, D. Charbonneau, A. C. Cameron, et al., *The Astronomical Journal* **152**, 1 (2016), ISSN 1538-3881, 1609.07617, URL <http://arxiv.org/abs/1609.07617> <http://dx.doi.org/10.3847/0004-6256/152/6/204>.
- [6] H.-k. Mao and R. J. Hemley, in *Ultra-high Pressure Mineralogy*, edited by R. J. Hemley (De Gruyter, Berlin, Boston, 1998), pp. 1–32, ISBN 9781501509179, URL <https://www.degruyter.com/document/doi/10.1515/9781501509179/html>.
- [7] M. Yabashi and H. Tanaka, *Nature Photonics* **11**, 12 (2017), ISSN 17494893.
- [8] C. B. Agee, in *Ultra-high Pressure Mineralogy*, edited by R. J. Hemley (De Gruyter, Berlin, Boston, 1998), pp. 165–204, URL <https://www.degruyter.com/document/doi/10.1515/9781501509179-007/html>.
- [9] K. T. Ramesh, *Handbook of Experimental Solid Mechanics* p. 874 (2008).
- [10] W. J. Evans, C. S. Yoo, G. W. Lee, H. Cynn, M. J. Lipp, and K. Visbeck, *Review of Scientific Instruments* **78**, 0 (2007), ISSN 00346748.
- [11] N. Velisavljevic, S. Sinogeikin, R. Saavedra, R. S. Chellappa, A. Rothkirch, D. M. Dattelbaum, Z. Konopkova, H. P. Liermann, M. Bishop, G. M. Tsoi, et al., *Journal of Physics: Conference Series* **500** (2014), ISSN 17426596.
- [12] G. W. Lee, W. J. Evans, and C.-S. Yoo, *Proceedings of the National Academy of Sciences* **104**, 9178 (2007), ISSN 0027-8424.

- [13] J.-Y. Chen and C.-S. Yoo, Proceedings of the National Academy of Sciences **108**, 7685 (2011), ISSN 0027-8424.
- [14] B. Chen, J. M. Jackson, W. Sturhahn, D. Zhang, J. Zhao, J. K. Wicks, and C. A. Murphy, Journal of Geophysical Research: Solid Earth **117**, 1 (2012), ISSN 21699356.
- [15] D. Pennicard, S. Smoljanin, F. Pithan, M. Sarajlic, A. Rothkirch, Y. Yu, H. Liermann, W. Morgenroth, B. Winkler, Z. Jenei, et al., Journal of Instrumentation **13**, C01026 (2018), ISSN 1748-0221, URL <https://iopscience.iop.org/article/10.1088/1748-0221/13/01/C01026>.
- [16] C. Lin, J. S. Smith, S. V. Sinogeikin, C. Park, Y. Kono, C. Kenney-Benson, E. Rod, and G. Shen, Journal of Applied Physics **119** (2016), ISSN 10897550.
- [17] M. Sims, S. J. Jaret, E.-R. Carl, B. Rhymer, N. Schrodt, V. Mohrholz, J. Smith, Z. Konopkova, H.-P. Liermann, T. D. Glotch, et al., Earth and Planetary Science Letters **507**, 166 (2019), ISSN 0012821X, URL <https://linkinghub.elsevier.com/retrieve/pii/S0012821X18306976>.
- [18] G. W. Lee, W. J. Evans, and C. S. Yoo, Physical Review B - Condensed Matter and Materials Physics **74**, 1 (2006), ISSN 10980121.
- [19] M. Fisch, A. Lanza, E. Boldyreva, P. Macchi, and N. Casati, Journal of Physical Chemistry C **119**, 18611 (2015), ISSN 19327455.
- [20] J. Y. Chen, C. S. Yoo, W. J. Evans, H. P. Liermann, H. Cynn, M. Kim, and Z. Jenei, Physical Review B - Condensed Matter and Materials Physics **90** (2014), ISSN 1550235X.
- [21] R. J. Husband, E. F. O'Bannon, H.-P. Liermann, M. J. Lipp, A. S. Mendez, Z. Konopkova, E. E. McBride, W. J. Evans, and Z. Jenei, submitted and under review (2021).
- [22] E. R. Carl, U. Mansfeld, H. P. Liermann, A. Danilewsky, F. Langenhorst, L. Ehm, G. Trullenque, and T. Kenkmann, Meteoritics and Planetary Science **52**, 1465 (2017), ISSN 10869379.
- [23] M. O. Schoelmerich, T. Tschentscher, S. Bhat, C. A. Bolme, E. Cunningham, R. Farla, E. Galtier, A. E. Gleason, M. Harmand, Y. Inubushi, et al., Scientific Reports **10**, 1 (2020), ISSN 20452322, URL <http://dx.doi.org/10.1038/s41598-020-66340-y>.
- [24] H. Marquardt, J. Buchen, A. S. Mendez, A. Kurnosov, M. Wendt, A. Rothkirch, D. Pennicard, and H. P. Liermann, Geophysical Research Letters **45**, 6862 (2018), ISSN 19448007.
- [25] H. Marquardt (17th International Symposium on Experimental Mineralogy, Petrology and Geochemistry, Potsdam, 2021).

-
- [26] A. S. Méndez, F. Trybel, R. J. Husband, G. Steinle-Neumann, H. P. Liermann, and H. Marquardt, *Physical Review B* **103**, 1 (2021), ISSN 24699969.
- [27] U. Zastrau, K. Appel, C. Baehtz, O. Baehr, L. Batchelor, A. Berghäuser, M. Banjafar, E. Brambrink, V. Cerantola, T. E. Cowan, et al., in peer review (2021).
- [28] F. Birch, *Journal of Geophysical Research* **57**, 227 (1952), ISSN 01480227, URL <http://doi.wiley.com/10.1029/JZ057i002p00227>.
- [29] N. Ashcroft and N. Mermin, *Solid State Physics* (Brooks Cole, Belmont, CA., 1976), ISBN 9780030839931, URL <https://b-ok.cc/book/1224378/1d6073>.
- [30] P. Ravindran, L. Fast, P. A. Korzhavyi, B. Johansson, J. Wills, and O. Eriksson, *Journal of Applied Physics* **84**, 4891 (1998), ISSN 00218979.
- [31] A. Lavakumar, *Concepts in Physical Metallurgy: Concise lecture notes* (IOP Concise Physics, Bristol, 2017).
- [32] M. Drury and J. Fitz Gerald, in *The Earth's mantle: Composition, Structure and Evolution*, edited by I. Jackson (Cambridge University Press, Cambridge, 1998), pp. 503–549, 2nd ed.
- [33] D. J. Frost and M. Ashby, *Deformation-mechanism Maps: The Plasticity and Creep of Metals and Ceramics* (Pergamon Press, Oxford, 1982).
- [34] J. P. Poirier, *Creep of Crystals: High-Temperature Deformation Processes in Metals, Ceramics and Minerals* (Cambridge University Press, Cambridge, 1985).
- [35] B. Evans and D. Kohlstedt, in *Rock Physics and Phase Relations - A Handbook of Physical Constants*, edited by T. Ahrens (American Geophysical Union, Washington, DC, 1995), pp. 148–165.
- [36] C. Clauser, *Einführung in die Geophysik: Globale physikalische Felder und Prozesse in der Erde*. (Springer Berlin Heidelberg, Heidelberg, 2014).
- [37] R. Newnham, *Properties of Materials: Anisotropy, Symmetry, Structure*. (Oxford University Press, Oxford, 2005).
- [38] J. Nye, *Physical Properties of Crystals: Their Representation by Tensors and Matrices* (Clarendon Press, Oxford, 1985).
- [39] R. Yu, J. Zhu, and H. Q. Ye, *Computer Physics Communications* **181**, 671 (2010), ISSN 00104655, URL <http://dx.doi.org/10.1016/j.cpc.2009.11.017>.
- [40] W. Kleber, *Einführung in die Kristallographie* (VEB Verlag Technik, Berlin, 1977).
- [41] R. Hill, *Proceedings of the Physical Society. Section A* **65**, 349 (1952), ISSN 03701298.
-

- [42] A. Reuss, ZAMM - Zeitschrift für Angewandte Mathematik und Mechanik **9**, 49 (1929), ISSN 00442267, URL <http://doi.wiley.com/10.1002/zamm.19290090104>.
- [43] W. Voigt, in *Sammlung von Lehrbüchern auf dem Gebiet der mathematischen Wissenschaften, mit Einschluss ihrer Anwendungen*, edited by B. Teubner (Berlin, Leipzig, 1928), p. 962.
- [44] F. R. N. Nabarro, The Physical Society, London p. 75 (1948).
- [45] R. L. Coble, Journal of Applied Physics **34**, 1679 (1963), ISSN 0021-8979, URL <http://aip.scitation.org/doi/10.1063/1.1702656>.
- [46] J. P. Poirier, *Introduction to the Physics of the Earth's Interior* (Cambridge University Press, Cambridge, 2000).
- [47] P. Cordier, Reviews in Mineralogy and Geochemistry **51**, 137 (2002).
- [48] C. M. Hu, C. M. Lai, P. W. Kao, N. J. Ho, and J. C. Huang, Materials Characterization **61**, 1043 (2010), ISSN 10445803.
- [49] J. W. Christian and S. Mahajan, Progress in Materials Science **39**, 1 (1995), ISSN 00796425.
- [50] R. E. Cohen, O. Gülseren, and R. J. Hemley, American Mineralogist **85**, 338 (2000), ISSN 0003004X, 9905389.
- [51] N. C. Holmes, J. A. Moriarty, G. R. Gathers, and W. J. Nellis, Journal of Applied Physics **66**, 2962 (1989), ISSN 00218979.
- [52] F. Birch, Journal of Geophysical Research **83**, 1257 (1978), ISSN 0148-0227, URL <http://doi.wiley.com/10.1029/JB083iB03p01257>.
- [53] P. Vinet, J. Ferrantef, J. R. Smith, and J. H. Rose, Journal of Physics C: Solid State Physics **19**, L467 (1986), ISSN 00223719.
- [54] P. Vinet, J. H. Rose, J. Ferrante, and J. R. Smith, Journal of Physics: Condensed Matter **1**, 1941 (1989), ISSN 09538984.
- [55] W. B. Holzapfel, Reports on Progress in Physics **59**, 29 (1996), ISSN 00344885.
- [56] Y. Fei, H.-k. Mao, J. Sbu, and J. Hu, Phys Chem Minerals **18**, 416 (1992).
- [57] I. Jackson and S. M. Rigden, Physics of the Earth and Planetary Interiors **96**, 85 (1996), ISSN 00319201.
- [58] T. S. Duffy and Y. Wang, in *Ultrahigh Pressure Mineralogy*, edited by R. J. Hemley (De Gruyter, Berlin, Boston, 1998), pp. 425–458, URL <https://www.degruyter.com/document/doi/10.1515/9781501509179-016/html>.

-
- [59] Y. Fei, A. Ricolleau, M. Frank, K. Mibe, G. Shen, and V. Prakapenka, Proceedings of the National Academy of Sciences of the United States of America **104**, 9182 (2007), ISSN 00278424.
- [60] C. S. Zha, K. Mibe, W. A. Bassett, O. Tschauner, H. K. Mao, and R. J. Hemley, Journal of Applied Physics **103** (2008), ISSN 00218979.
- [61] S. Speziale, C.-S. Zha, T. S. Duffy, R. J. Hemley, and H.-k. Mao, Journal of Geophysical Research: Solid Earth **106**, 515 (2001), ISSN 01480227, URL <http://doi.wiley.com/10.1029/2000JB900318>.
- [62] J. Swegle, Tech. Rep., Sandia report, SAN89-1443 UC-404 (1989).
- [63] D. A. Boness, J. M. Brown, and A. K. McMahan, Physics of the Earth and Planetary Interiors **42**, 227 (1986), ISSN 00319201.
- [64] T. Tsuchiya and K. Kawamura, Journal of Chemical Physics **116**, 2121 (2002), ISSN 00219606.
- [65] L. Ma, J. Nie, and J. Yang, Latin-American Journal of Physics Education **3**, 566 (2009), ISSN 1870-9095.
- [66] R. S. McWilliams, D. K. Spaulding, J. H. Eggert, P. M. Celliers, D. G. Hicks, R. F. Smith, G. W. Collins, and R. Jeanloz, Science **338**, 1330 (2012), URL <https://www.sciencemag.org/lookup/doi/10.1126/science.1229450>.
- [67] K. Miyanishi, Y. Tange, N. Ozaki, T. Kimura, T. Sano, Y. Sakawa, T. Tsuchiya, and R. Kodama, Physical Review E - Statistical, Nonlinear, and Soft Matter Physics **92**, 1 (2015), ISSN 15502376.
- [68] Q. B. Zhang, C. H. Braithwaite, and J. Zhao, Philosophical Transactions of the Royal Society A: Mathematical, Physical and Engineering Sciences **375** (2017), ISSN 1364503X.
- [69] M. A. Meyers, *Dynamic Behavior of Materials* (John Wiley & Sons, Inc., 1994), ISBN 9780471582625, URL <https://onlinelibrary.wiley.com/doi/book/10.1002/9780470172278>.
- [70] N. Dubrovinskaia, L. Dubrovinsky, N. A. Solopova, A. Abakumov, S. Turner, M. Hanfland, E. Bykova, M. Bykov, C. Prescher, V. B. Prakapenka, et al., Science Advances **2** (2016), ISSN 23752548.
- [71] E. F. O'Bannon, Z. Jenei, H. Cynn, M. J. Lipp, and J. R. Jeffries, Review of Scientific Instruments **89** (2018), ISSN 10897623.
- [72] F. P. Bundy and K. J. Dunn, Review of Scientific Instruments **51**, 753 (1980), ISSN 00346748.
-

- [73] A. Palmer, D. M. Silevitch, Y. Feng, Y. Wang, R. Jaramillo, A. Banerjee, Y. Ren, and T. F. Rosenbaum, *Review of Scientific Instruments* **86** (2015), ISSN 10897623, URL <http://dx.doi.org/10.1063/1.4929861>.
- [74] G. Spiekermann, I. Kupenko, S. Petitgirard, M. Harder, A. Nyrow, C. Weis, C. Albers, N. Biedermann, L. Libon, C. J. Sahle, et al., *Journal of Synchrotron Radiation* **27**, 414 (2020), ISSN 16005775.
- [75] W. A. Bassett, *High Pressure Research* **29**, 163 (2009), ISSN 08957959.
- [76] K. Shimizu, *Physica C: Superconductivity and its Applications* **552**, 30 (2018), ISSN 09214534, URL <https://linkinghub.elsevier.com/retrieve/pii/S0921453418302119>.
- [77] G. J. Ackland, M. Dunuwille, M. Martinez-Canales, I. Loa, R. Zhang, S. Sinogeikin, W. Cai, and S. Deemyad, *Science* **356**, 1254 (2017), ISSN 10959203.
- [78] C. M. Brown, E. Beer, C. Bellavia, L. Cristofolini, R. González, M. Hanfland, D. Häusermann, M. Keshavarz-K, K. Kordatos, K. Prassides, et al., *Journal of the American Chemical Society* **118**, 8715 (1996), ISSN 00027863.
- [79] P. M. Oger, I. Daniel, and A. Picard, *Annals of the New York Academy of Sciences* **1189**, 113 (2010), ISSN 17496632.
- [80] H.-K. Mao and P. Bell, in *Carnegie Institute Washington Year Book 74* (Carnegie Institute Washington, 1975), pp. 402–405.
- [81] L. Merrill and W. A. Bassett, *Review of Scientific Instruments* **45**, 290 (1974), ISSN 0034-6748.
- [82] R. Boehler and K. De Hantsetters, *High Pressure Research* **24**, 391 (2004), ISSN 0895-7959, URL <http://www.tandfonline.com/doi/abs/10.1080/08957950412331323924>.
- [83] G. Shen and H. K. Mao, *Reports on Progress in Physics* **80**, 16101 (2016), ISSN 00344885, URL <http://dx.doi.org/10.1088/1361-6633/80/1/016101>.
- [84] D. A. Nelson and A. L. Ruoff, *Journal of Applied Physics* **50**, 2763 (1979), ISSN 00218979.
- [85] J. J. Zhao, S. Scandolo, J. Kohanoff, G. L. Chiarotti, and E. Tosatti, *Applied Physics Letters* **75**, 487 (1999), ISSN 00036951.
- [86] H. Chacham and L. Kleinman, *Physical Review Letters* **85**, 4904 (2000), ISSN 00319007.
- [87] R. H. Telling, C. J. Pickard, M. C. Payne, and J. E. Field, *Physical Review Letters* **84**, 5160 (2000), ISSN 10797114.

-
- [88] D. Roundy and M. L. Cohen, *Physical Review B - Condensed Matter and Materials Physics* **64**, 2 (2001), ISSN 1550235X.
- [89] H. K. Mao, J. Xu, and P. M. Bell, *Journal of Geophysical Research* **91**, 4673 (1986), ISSN 0148-0227, URL <http://doi.wiley.com/10.1029/JB091iB05p04673>.
- [90] I. Kantor, Ph.D. thesis, Universität Bayreuth (2007).
- [91] A. Dewaele, F. Datchi, P. Loubeyre, and M. Mezouar, *Physical Review B - Condensed Matter and Materials Physics* **77**, 1 (2008), ISSN 10980121.
- [92] P. I. Dorogokupets and A. R. Oganov, *Physical Review B - Condensed Matter and Materials Physics* **75**, 1 (2007), ISSN 10980121.
- [93] W. B. Holzapfel, *Journal of Applied Physics* **93**, 1813 (2003), ISSN 00218979.
- [94] M. Rivers, V. B. Prakapenka, A. Kubo, C. Pullins, C. M. Holl, and S. D. Jacobsen, *High Pressure Research* **28**, 273 (2008), ISSN 08957959.
- [95] S. Ono, K. Mibe, and Y. Ohishi, *Journal of Applied Physics* **116** (2014), ISSN 10897550.
- [96] Y. Akahama and H. Kawamura, *Journal of Applied Physics* **96**, 3748 (2004), ISSN 00218979.
- [97] Y. Akahama and H. Kawamura, *Journal of Applied Physics* **100** (2006), ISSN 00218979.
- [98] M. Hanfland and K. Syassen, *Journal of Applied Physics* **57**, 2752 (1985), ISSN 00218979.
- [99] N. Dubrovinskaia, L. Dubrovinsky, R. Caracas, and M. Hanfland, *Applied Physics Letters* **97**, 2008 (2010), ISSN 00036951.
- [100] A. Lacam and C. Chateau, *Journal of Applied Physics* **66**, 366 (1989), ISSN 00218979.
- [101] D. D. Ragan, R. Gustavsen, and D. Schiferl, *Journal of Applied Physics* **72**, 5539 (1992), ISSN 00218979.
- [102] F. Datchi, R. LeToullec, and P. Loubeyre, *Journal of Applied Physics* **81**, 3333 (1997), ISSN 00218979.
- [103] S. Sundberg and P. Lazor, *Journal of Physics Condensed Matter* **16** (2004), ISSN 09538984.
- [104] F. Datchi, A. Dewaele, P. Loubeyre, R. Letoullec, Y. Le Godec, and B. Canny, *High Pressure Research* **27**, 447 (2007), ISSN 0895-7959, URL <http://www.tandfonline.com/doi/abs/10.1080/08957950701659593>.
- [105] Q. Wei, N. Dubrovinskaia, and L. Dubrovinsky, *Journal of Applied Physics* **110**, 0 (2011), ISSN 00218979.
-

- [106] A. F. Goncharov, J. M. Zaug, J. C. Crowhurst, and E. Gregoryanz, *Journal of Applied Physics* **97** (2005), ISSN 00218979.
- [107] N. J. Hess and D. Schiferl, *Journal of Applied Physics* **71**, 2082 (1992), ISSN 00218979.
- [108] Z. Q. Wu and F. Lin, *Science China Earth Sciences* **60**, 114 (2017), ISSN 16747313.
- [109] C. R. Bina, in *Ultrahigh Pressure Mineralogy*, edited by R. J. Hemley (De Gruyter, Berlin, Boston, 1998), pp. 205–240, URL <https://www.degruyter.com/document/doi/10.1515/9781501509179-010/html>.
- [110] A. L. Ruoff, *Journal of Applied Physics* **46**, 1389 (1975), ISSN 00218979.
- [111] H.-R. Wenk, *Reviews in Mineralogy and Geochemistry* **51**, 291 (2002), ISSN 1529-6466, URL <https://pubs.geoscienceworld.org/ring/article/51/1/291-329/87447>.
- [112] D. Mainprice and A. Nicolas, *Journal of Structural Geology* **11**, 175 (1989), ISSN 01918141.
- [113] C. Naumann, *Lehrbuch der Geognosie* (Engelmann, Leipzig, 1850).
- [114] A. K. Singh, A. Jain, H. P. Liermann, and S. K. Saxena, *Journal of Physics and Chemistry of Solids* **67**, 2197 (2006), ISSN 00223697.
- [115] S. Merkel, in *High-Pressure Crystallography*, edited by E. Boldyreva and P. Dera (Springer Netherlands, Dordrecht, 2010), NATO Science for Peace and Security Series B: Physics and Biophysics, pp. 111–122, ISBN 978-90-481-9257-1, URL <http://link.springer.com/10.1007/978-90-481-9258-8>.
- [116] A. K. Singh and K. Takemura, *Journal of Applied Physics* **90**, 3269 (2001), ISSN 00218979, URL <https://doi.org/10.1063/1.1397283>.
- [117] A. K. Singh, H. K. Mao, J. Shu, and R. J. Hemley, *Physical Review Letters* **80**, 2157 (1998), ISSN 10797114.
- [118] A. K. Singh, *Journal of Physics and Chemistry of Solids* **65**, 1589 (2004), ISSN 00223697.
- [119] A. K. Singh, H. P. Liermann, S. K. Saxena, H. K. Mao, and S. U. Devi, *Journal of Physics: Condensed Matter* **18**, S969 (2006), ISSN 0953-8984, URL <http://stacks.iop.org/0953-8984/18/i=25/a=S05?key=crossref.055e7e939b4d68babecaa29d187e5031>.
- [120] J. I. Langford, *Journal of Applied Crystallography* **4**, 164 (1971), ISSN 0021-8898.
- [121] P. Scherrer, *Nachrichten von der Gesellschaft der Wissenschaften zu Göttingen, Mathematisch-Physikalische Klasse* pp. 98–100 (1918).

-
- [122] A. R. Stokes and A. J. Wilson, *Proceedings of the Physical Society* **56**, 174 (1944), ISSN 09595309.
- [123] J. E. Graebner, in *Diamond: Electronic Properties and Applications* (Springer US, Boston, MA, 1995), pp. 285–318, URL http://link.springer.com/10.1007/978-1-4615-2257-7_{_}7.
- [124] S. Klotz, J. C. Chervin, P. Munsch, and G. Le Marchand, *Journal of Physics D: Applied Physics* **42** (2009), ISSN 00223727.
- [125] R. L. Mills, D. H. Liebenberg, J. C. Bronson, and L. C. Schmidt, *Review of Scientific Instruments* **51**, 891 (1980), ISSN 00346748.
- [126] B. Li, C. Ji, W. Yang, J. Wang, K. Yang, R. Xu, W. Liu, Z. Cai, J. Chen, and H.-k. Mao, *Proceedings of the National Academy of Sciences* **115**, 1713 (2018), ISSN 0027-8424.
- [127] H. MAO and W. MAO, *Theory and Practice – Diamond-Anvil Cells and Probes for High P–T Mineral Physics Studies* (Carnegie Institute Washington, 2007), ISBN 9780444527486.
- [128] W. C. Moss and K. A. Goettel, *Applied Physics Letters* **50**, 25 (1987), ISSN 00036951.
- [129] W. Bassett and T. Takahashi, *Adv. High Press. Res.* **4**, 165-247 (1974).
- [130] W. A. Bassett, *Annual Review of Earth and Planetary Sciences* **7**, 357 (1979), ISSN 0084-6597, URL <http://www.annualreviews.org/doi/10.1146/annurev.ea.07.050179.002041>.
- [131] S. Merkel, R. J. Hemley, and H. K. Mao, *Applied Physics Letters* **74**, 656 (1999), ISSN 00036951.
- [132] W. C. Moss, J. O. Hallquist, R. Reichlin, K. A. Goettel, and S. Martin, *Applied Physics Letters* **48**, 1258 (1986), ISSN 00036951.
- [133] I. L. Spain and D. J. Dunstan, *Journal of Physics E: Scientific Instruments* **22**, 923 (1989), ISSN 00223735.
- [134] R. J. Hemley, H. K. Mao, G. Shen, J. Badro, P. Gillet, M. Hanfland, and D. Häusermann, *Science* **276**, 1242 (1997), ISSN 00368075.
- [135] Z. Jenei, E. F. O’Bannon, S. T. Weir, H. Cynn, M. J. Lipp, and W. J. Evans, *Nature Communications* **9**, 1 (2018), ISSN 20411723, URL <http://dx.doi.org/10.1038/s41467-018-06071-x>.
- [136] S. S. Lobanov, V. B. Prakapenka, C. Prescher, Z. Konôpková, H. P. Liermann, K. L. Crispin, C. Zhang, and A. F. Goncharov, *Journal of Applied Physics* **118** (2015), ISSN 10897550, URL <http://dx.doi.org/10.1063/1.4927213>.
-

- [137] Y. Meng, R. Hrubciak, E. Rod, R. Boehler, and G. Shen, *Review of Scientific Instruments* **86** (2015), ISSN 10897623.
- [138] H.-P. Liermann, Z. Konôpková, W. Morgenroth, K. Glazyrin, J. Bednarčík, E. E. McBride, S. Petitgirard, J. T. Delitz, M. Wendt, Y. Bican, et al., *Journal of Synchrotron Radiation* **22**, 908 (2015).
- [139] I. Kantor, C. Marini, O. Mathon, and S. Pascarelli, *Review of Scientific Instruments* **89** (2018), ISSN 10897623.
- [140] I. Kupenko, L. Dubrovinsky, N. Dubrovinskaia, C. McCammon, K. Glazyrin, E. Bykova, T. B. Ballaran, R. Sinmyo, A. I. Chumakov, V. Potapkin, et al., *Review of Scientific Instruments* **83** (2012), ISSN 00346748.
- [141] R. Letoullec, J. P. Pinceaux, and P. Loubeyre, *High Pressure Research* **1**, 77 (1988), ISSN 0895-7959, URL <http://www.tandfonline.com/doi/abs/10.1080/08957958808202482>.
- [142] E. R. Carl, H. P. Liermann, L. Ehm, A. Danilewsky, and T. Kenkmann, *Meteoritics and Planetary Science* **53**, 1687 (2018), ISSN 10869379.
- [143] J. Y. Chen and C. S. Yoo, *Journal of Chemical Physics* **136** (2012), ISSN 00219606.
- [144] Y. J. Kim, Y. H. Lee, S. Lee, H. Nada, and G. W. Lee, *Proceedings of the National Academy of Sciences of the United States of America* **116**, 8679 (2019), ISSN 10916490.
- [145] Z. Jenei, H. P. Liermann, R. Husband, A. S. Méndez, D. Pennicard, H. Marquardt, E. F. O'Bannon, A. Pakhomova, Z. Konopkova, K. Glazyrin, et al., *Review of Scientific Instruments* **90** (2019), ISSN 10897623, URL <http://dx.doi.org/10.1063/1.5098993>.
- [146] J. S. Smith, S. V. Sinogeikin, C. Lin, E. Rod, L. Bai, and G. Shen, *Review of Scientific Instruments* **86** (2015), ISSN 10897623, URL <http://dx.doi.org/10.1063/1.4926887>.
- [147] S. V. Sinogeikin, J. S. Smith, E. Rod, C. Lin, C. Kenney-Benson, and G. Shen, *Review of Scientific Instruments* **86** (2015), ISSN 10897623.
- [148] W. H. Bragg and W. L. Bragg, *Proceedings of the Royal Society of London. Series A, Containing Papers of a Mathematical and Physical Character* **88**, 428 (1913), ISSN 09501207, URL <http://www.jstor.org/stable/93501>.
- [149] H. Winick, G. Brown, K. Halbach, and J. Harris, *Physics Today* **34**, 50 (1981), ISSN 0031-9228, URL <http://physicstoday.scitation.org/doi/10.1063/1.2914568>.
- [150] W. Morgenroth, Z. Konopkova, H.-P. Liermann, and B. Winkler, *Laser heating at P02.2 at PETRA III, capabilities and planning* (2014).

-
- [151] W. Freund, L. Fröhlich, S. Karabekyan, A. Koch, J. Liu, D. Nölle, J. Wilgen, and J. Grünert, *Journal of Synchrotron Radiation* **26**, 1037 (2019), ISSN 16005775.
- [152] W. Decking, S. Abeghyan, P. Abramian, A. Abramsky, A. Aguirre, C. Albrecht, P. Alou, M. Altarelli, P. Altmann, K. Amyan, et al., *Nature Photonics* **14**, 391 (2020), ISSN 17494893.
- [153] European XFEL, *European XFEL Overview* (2020), URL <https://www.xfel.eu/facility/overview/index{ }eng.html>.
- [154] J. Grünert, M. P. Carbonell, F. Dietrich, T. Falk, W. Freund, A. Koch, N. Kujala, J. Laksman, J. Liu, T. Maltezopoulos, et al., *Journal of Synchrotron Radiation* **26**, 1422 (2019), ISSN 16005775.
- [155] H. J. Kirkwood, R. Letrun, T. Tanikawa, J. Liu, M. Nakatsutsumi, M. Emons, T. Jezynski, G. Palmer, M. Lederer, R. Bean, et al., *Optics Letters* **44**, 1650 (2019), ISSN 0146-9592.
- [156] N. Kujala, M. Makita, J. Liu, A. Zozulya, M. Sprung, C. David, and J. Grünert, *Journal of Synchrotron Radiation* **26**, 708 (2019), ISSN 16005775.
- [157] J. Laksman, J. Buck, L. Glaser, M. Planas, F. Dietrich, J. Liu, T. Maltezopoulos, F. Scholz, J. Seltmann, G. Hartmann, et al., *Journal of Synchrotron Radiation* **26**, 1010 (2019), ISSN 16005775.
- [158] T. Maltezopoulos, F. Dietrich, W. Freund, U. F. Jastrow, A. Koch, J. Laksman, J. Liu, M. Planas, A. A. Sorokin, K. Tiedtke, et al., *Journal of Synchrotron Radiation* **26**, 1045 (2019), ISSN 16005775.
- [159] E. Syresin, A. Grebentsov, O. Brovko, M. Yurkov, W. Freund, and J. Grünert, *Journal of Synchrotron Radiation* **26**, 1400 (2019), ISSN 16005775.
- [160] H. P. Liermann, H. Damker, K. Appel, A. Schropp, and C. Baetz, pp. 1–48 (2016).
- [161] B. Henrich, J. Becker, R. Dinapoli, P. Goettlicher, H. Graafsma, H. Hirsemann, R. Klanner, H. Krueger, R. Mazzocco, A. Mozzanica, et al., *Nuclear Instruments and Methods in Physics Research, Section A: Accelerators, Spectrometers, Detectors and Associated Equipment* **633**, S11 (2011), ISSN 01689002, URL <http://dx.doi.org/10.1016/j.nima.2010.06.107>.
- [162] K. Takemura, *Physical Review Letters* **74**, 252 (1995).
- [163] K. Takemura, *Physical Review B - Condensed Matter and Materials Physics* **60**, 6171 (1999), ISSN 1550235X.
- [164] Z. Konôpková, A. Rothkirch, A. K. Singh, S. Speziale, and H. P. Liermann, *Physical Review B - Condensed Matter and Materials Physics* **91**, 1 (2015), ISSN 1550235X.
-

- [165] Y. Fei and H.-k. Mao, *Science* **266**, 1992 (1994).
- [166] H. Ozawa, K. Hirose, S. Tateno, N. Sata, and Y. Ohishi, *Physics of the Earth and Planetary Interiors* **179**, 157 (2010), ISSN 00319201, URL <http://dx.doi.org/10.1016/j.pepi.2009.11.005>.
- [167] H. Ozawa, K. Hirose, K. Ohta, H. Ishii, N. Hiraoka, Y. Ohishi, and Y. Seto, *Physical Review B - Condensed Matter and Materials Physics* **84** (2011), ISSN 10980121.
- [168] T. Kondo, E. Ohtani, N. Hirao, T. Yagi, and T. Kikegawa, *Physics of the Earth and Planetary Interiors* **143**, 201 (2004), ISSN 00319201.
- [169] R. A. Fischer, A. J. Campbell, O. T. Lord, G. A. Shofner, P. Dera, and V. B. Prakapenka, *Geophysical Research Letters* **38**, 2 (2011), ISSN 00948276.
- [170] R. Boehler, *Earth and Planetary Science Letters* **111**, 217 (1992), ISSN 0012821X.
- [171] K. Ohta, R. E. Cohen, K. Hirose, K. Haule, K. Shimizu, and Y. Ohishi, *Physical Review Letters* **108**, 1 (2012), ISSN 00319007.
- [172] K. Ohta, K. Hirose, K. Shimizu, and Y. Ohishi, *Physical Review B - Condensed Matter and Materials Physics* **82**, 16 (2010), ISSN 10980121.
- [173] M. Murakami, K. Hirose, S. Ono, T. Tsuchiya, M. Isshiki, and T. Watanuki, *Physics of the Earth and Planetary Interiors* **146**, 273 (2004), ISSN 00319201.
- [174] E. Knittle, R. Jeanloz, A. C. Mitchell, and W. J. Nellis, *Solid State Communications* **59**, 513 (1986), ISSN 00381098.
- [175] H. Marquardt, S. Speziale, H. J. Reichmann, D. J. Frost, and F. R. Schilling, *Earth and Planetary Science Letters* **287**, 345 (2009), ISSN 0012821X, URL <http://dx.doi.org/10.1016/j.epsl.2009.08.017>.
- [176] S. Speziale, A. Milner, V. E. Lee, S. M. Clark, M. P. Pasternak, and R. Jeanloz, *Proceedings of the National Academy of Sciences* **102**, 17918 (2005), ISSN 0027-8424.
- [177] J.-F. Lin, D. L. Heinz, H.-k. Mao, R. J. Hemley, J. M. Devine, J. Li, and G. Shen, *Proceedings of the National Academy of Sciences* **100**, 4405 (2003), ISSN 0027-8424.
- [178] K. Glazyrin, R. Sinmyo, E. Bykova, M. Bykov, V. Cerantola, M. Longo, C. McCammon, V. B. Prakapenka, and L. Dubrovinsky, *Physical Review B* **95** (2017), ISSN 24699969.
- [179] N. V. Solomatova, J. M. Jackson, W. Sturhahn, J. K. Wicks, J. Zhao, T. S. Toellner, B. Kalkan, and W. M. Steinhardt, *American Mineralogist* **101**, 1084 (2016), ISSN 19453027.

-
- [180] J. K. Wicks, J. M. Jackson, W. Sturhahn, K. K. Zhuravlev, S. N. Tkachev, and V. B. Prakapenka, *Physics of the Earth and Planetary Interiors* **249**, 28 (2015), ISSN 00319201, URL <http://dx.doi.org/10.1016/j.pepi.2015.09.003>.
- [181] T. Komabayashi, K. Hirose, Y. Nagaya, E. Sugimura, and Y. Ohishi, *Earth and Planetary Science Letters* **297**, 691 (2010), ISSN 0012821X, URL <http://dx.doi.org/10.1016/j.epsl.2010.07.025>.
- [182] R. Sinmyo, K. Glazyrin, C. McCammon, I. Kuppenko, A. Kantor, V. Potapkin, A. I. Chumakov, R. Rüffer, and L. Dubrovinsky, *Physics of the Earth and Planetary Interiors* **229**, 16 (2014), ISSN 00319201, URL <http://dx.doi.org/10.1016/j.pepi.2013.12.002>.
- [183] S. Fu, J. Yang, Y. Zhang, J. Liu, E. Greenberg, V. B. Prakapenka, T. Okuchi, and J. F. Lin, *Earth and Planetary Science Letters* **503**, 1 (2018), ISSN 0012821X, URL <https://doi.org/10.1016/j.epsl.2018.09.014>.
- [184] M. Longo, C. A. McCammon, and S. D. Jacobsen, *Contributions to Mineralogy and Petrology* **162**, 1249 (2011), ISSN 00107999.
- [185] R. Dohmen and R. Milke, *Reviews in Mineralogy and Geochemistry* **72**, 921 (2010), ISSN 1529-6466.
- [186] Y. Zhang, *Reviews in Mineralogy and Geochemistry* **72**, 5 (2010), ISSN 1529-6466, URL <https://pubs.geoscienceworld.org/rimg/article/72/1/1-4/140869>.
- [187] J. A. Van Orman and K. L. Crispin, *Reviews in Mineralogy and Geochemistry* **72**, 757 (2010), ISSN 1529-6466, URL <https://pubs.geoscienceworld.org/rimg/article/72/1/757-825/140902>.
- [188] A. C. Lasaga, *Kinetic Theory in the Earth Sciences* (Princeton University Press, 2016, Princeton, NJ, 1998), ISBN 9780691636245, URL <https://books.google.de/books?id=TJKDjwEACAAJ>.
- [189] Y. Zhang, E. M. Stolper, and G. J. Wasserburg, *Earth and Planetary Science Letters* **103**, 228 (1991), ISSN 0012821X.
- [190] J. N. Lalena and D. A. Cleary, *Principles of Inorganic Materials Design* (John Wiley & Sons, Inc., Hoboken, NJ, USA, 2005), ISBN 9780471714897, URL <http://doi.wiley.com/10.1002/0471714895>.
- [191] S. Chakraborty, *Reviews in Mineralogy and Geochemistry* **72**, 603 (2010), ISSN 1529-6466, URL <https://pubs.geoscienceworld.org/rimg/article/72/1/603-639/140897>.
-

- [192] E. B. Watson and E. F. Baxter, *Earth and Planetary Science Letters* **253**, 307 (2007), ISSN 0012821X.
- [193] S. D. Jacobsen, *Journal of Geophysical Research* **107** (2002), ISSN 0148-0227.
- [194] R. L. Mössbauer, *Zeitschrift für Physik* **151**, 124 (1958), ISSN 14346001.
- [195] R. L. Mössbauer, *Hyperfine Interactions* **126**, 1 (2000).
- [196] M. D. Dyar, D. G. Agresti, M. W. Schaefer, C. A. Grant, and E. C. Sklute, *Annual Review of Earth and Planetary Sciences* **34**, 83 (2006), ISSN 00846597.
- [197] C. S. Zha, W. A. Bassett, and S. H. Shim, *Review of Scientific Instruments* **75**, 2409 (2004), ISSN 00346748.
- [198] O. L. Anderson, D. G. Isaak, and S. Yamamoto, *Journal of Applied Physics* **65**, 1534 (1989), ISSN 00218979.
- [199] O. Schulte, A. Nikolaenko, and W. B. Holzapfel, *High Pressure Research* **6**, 169 (1991), ISSN 0895-7959, URL <http://www.tandfonline.com/doi/abs/10.1080/08957959108203207>.
- [200] H. K. Mao, Y. Wu, L. C. Chen, J. F. Shu, and A. P. Jephcoat, *Journal of Geophysical Research* **95**, 21737 (1990), ISSN 0148-0227, URL <http://doi.wiley.com/10.1029/JB095iB13p21737>.
- [201] R. A. Fischer, A. J. Campbell, G. A. Shofner, O. T. Lord, P. Dera, and V. B. Prakapenka, *Earth and Planetary Science Letters* **304**, 496 (2011), ISSN 0012821X, URL <http://dx.doi.org/10.1016/j.epsl.2011.02.025>.
- [202] Z. Wu, R. M. Wentzcovitch, K. Umemoto, B. Li, K. Hirose, and J. C. Zheng, *Journal of Geophysical Research: Solid Earth* **113**, 1 (2008), ISSN 21699356.
- [203] D. Walker, L. M. Cranswick, P. K. Verma, S. M. Clark, and S. Buhre, *American Mineralogist* **87**, 805 (2002), ISSN 0003004X.
- [204] M. L. Shepard and J. F. Smith, *Journal of Applied Physics* **36**, 1447 (1965), ISSN 0021-8979, URL <http://aip.scitation.org/doi/10.1063/1.1714327>.
- [205] T. S. Duffy, G. Shen, D. L. Heinz, J. Shu, Y. Ma, H.-K. Mao, R. J. Hemley, and A. K. Singh, *Physical Review B* **60**, 15063 (1999), ISSN 0163-1829, URL <https://link.aps.org/doi/10.1103/PhysRevB.60.15063>.
- [206] A. K. Singh, H. P. Liermann, Y. Akahama, S. K. Saxena, and E. Méndez-Proupin, *Journal of Applied Physics* **103** (2008), ISSN 00218979.
- [207] A. Yoneda, H. Fukui, H. Gomi, S. Kamada, L. Xie, N. Hirao, H. Uchiyama, S. Tsutsui, and A. Q. Baron, *Japanese Journal of Applied Physics* **56**, 1 (2017), ISSN 13474065.

-
- [208] S. Biswas, P. Van 't Klooster, and N. Trappeniers, *Physica B+C* **103**, 235 (1981), ISSN 03784363, URL <https://linkinghub.elsevier.com/retrieve/pii/0378436381901273>.
- [209] E. R. Jette and F. Foote, *The Journal of Chemical Physics* **3**, 605 (1935), ISSN 00219606.
- [210] D. Gray McGraw Hill, *American Institute of Physics Handbook* (New York, 1963), 3rd ed., ISBN 978-0070014855.
- [211] S. Tateno, T. Komabayashi, K. Hirose, N. Hirao, and Y. Ohishi, *American Mineralogist* **104**, 718 (2019), ISSN 19453027.
- [212] A. K. Singh, H. P. Liermann, and S. K. Saxena, *Solid State Communications* **132**, 795 (2004), ISSN 00381098.
- [213] S. M. Dorfman, S. R. Shieh, and T. S. Duffy, *Journal of Applied Physics* **117**, 1 (2015), ISSN 10897550.
- [214] S. Anzellini, A. Dewaele, F. Occelli, P. Loubeyre, and M. Mezouar, *Journal of Applied Physics* **115** (2014), ISSN 10897550.
- [215] A. K. Singh, D. Andrault, and P. Bouvier, *Physics of the Earth and Planetary Interiors* **208-209**, 1 (2012).
- [216] Y. Meng, D. J. Weidner, and Y. Fei, *Geophysical Research Letters* **20**, 1147 (1993), ISSN 00948276, URL <http://doi.wiley.com/10.1029/93GL01400>.
- [217] R. Boehler, *Reviews of Geophysics* pp. 221–245 (2000).
- [218] Z. Mao, J. F. Lin, J. Liu, and V. B. Prakapenka, *Geophysical Research Letters* **38**, 2 (2011), ISSN 00948276.
- [219] E. Holmström and L. Stixrude, *Physical Review Letters* **114**, 1 (2015), ISSN 10797114.
- [220] S. Anzellini, V. Monteseguro, E. Bandiello, A. Dewaele, L. Burakovsky, and D. Errandonea, *Scientific Reports* **9**, 1 (2019), ISSN 20452322.
- [221] C. Prescher and V. B. Prakapenka, *High Pressure Research* **35**, 223 (2015), ISSN 0895-7959, URL <http://www.tandfonline.com/doi/full/10.1080/08957959.2015.1059835>.
- [222] A. P. Hammersley, S. O. Svensson, M. Hanfland, A. N. Fitch, and D. Hausermann, *High Pressure Research* **14**, 235 (1996), ISSN 0895-7959, URL <http://www.tandfonline.com/doi/abs/10.1080/08957959608201408>.
- [223] A. P. Hammersley, Tech. Rep., ESRF Internal Report, ESRF97HA02T (1997).
-

- [224] Jerome Kieffer, Valentin Valls, deschila, Thomas VINCENT, picca, payno... fpwg , *silx-kit/pyFAI* (2021), URL <http://doi.org/10.5281/zenodo.4457185>.
- [225] J. I. Langford and A. J. C. Wilson, *Journal of Applied Crystallography* **11**, 102 (1978), ISSN 0021-8898, arXiv:1011.1669v3, URL <http://scripts.iucr.org/cgi-bin/paper?S0021889878012844>.
- [226] D. He and T. S. Duffy, *Physical Review B - Condensed Matter and Materials Physics* **73**, 4 (2006), ISSN 10980121.
- [227] A. K. Singh and H. P. Liermann, *Journal of Applied Physics* **118** (2015), ISSN 10897550, URL <http://dx.doi.org/10.1063/1.4927727>.
- [228] A. K. Singh, C. Balasingh, H. K. Mao, R. J. Hemley, and J. Shu, *Journal of Applied Physics* **83**, 7567 (1998), ISSN 00218979.
- [229] A. K. Singh, *Journal of Applied Physics* **106**, 0 (2009), ISSN 00218979.
- [230] A. Kavner and T. S. Duffy, *Physical Review B - Condensed Matter and Materials Physics* **68**, 1 (2003), ISSN 1550235X.
- [231] S. Merkel, C. Tomé, and H. R. Wenk, *Physical Review B - Condensed Matter and Materials Physics* **79**, 1 (2009), ISSN 1550235X.
- [232] A. D. Rosa, C. Sanchez-Valle, C. Nisr, S. R. Evans, R. Debord, and S. Merkel, *Earth and Planetary Science Letters* **377-378**, 13 (2013), ISSN 0012821X, URL <http://dx.doi.org/10.1016/j.epsl.2013.06.036>.
- [233] G. L. Kinsland and W. A. Bassett, *Journal of Applied Physics* **48**, 978 (1977), ISSN 00218979.
- [234] S. Merkel, H. R. Wenk, J. Shu, G. Shen, P. Gillet, H.-k. Mao, and R. J. Hemley, *Journal of Geophysical Research: Solid Earth* **107**, ECV 3 (2002), ISSN 0148-0227.
- [235] S. Merkel, H. R. Wenk, J. Badro, G. Montagnac, P. Gillet, H. K. Mao, and R. J. Hemley, *Earth and Planetary Science Letters* **209**, 351 (2003), ISSN 0012821X.
- [236] M. Jo, Y. M. Koo, B. J. Lee, B. Johansson, L. Vitos, and S. K. Kwon, *Proceedings of the National Academy of Sciences of the United States of America* **111**, 6560 (2014), ISSN 10916490.
- [237] H. K. Mao, R. J. Hemley, Y. Wu, A. P. Jephcoat, L. W. Finger, C. S. Zha, and W. A. Bassett, *Physical Review Letters* **60**, 25 (1988).
- [238] R. J. Hemley, C. S. Zha, A. P. Jephcoat, H. K. Mao, L. W. Finger, and D. E. Cox, *Physical Review B* **39**, 11820 (1989), ISSN 01631829.
- [239] B. Feng and V. I. Levitas, *Journal of Applied Physics* **119** (2016), ISSN 10897550.

-
- [240] T. A. Sisneros, D. W. Brown, B. Clausen, D. C. Donati, S. Kabra, W. R. Blumenthal, and S. C. Vogel, *Materials Science and Engineering A* **527**, 5181 (2010), ISSN 09215093, URL <http://dx.doi.org/10.1016/j.msea.2010.04.035>.
- [241] R. Lynch and H. Drickamer, *Journal of Physics and Chemistry of Solids* **26**, 63 (1965), ISSN 00223697, URL <https://linkinghub.elsevier.com/retrieve/pii/0022369765900739>.
- [242] S. Meenakshi, V. Vijayakumar, B. K. Godwal, and S. K. Sikka, *Physical Review B* **46**, 14359 (1992), ISSN 0163-1829, URL <https://link.aps.org/doi/10.1103/PhysRevB.46.14359>.
- [243] W. Potzel, M. Steiner, H. Karzel, W. Schiessl, M. Köfferlein, G. M. Kalvius, and P. Blaha, *Physical Review Letters* **74**, 1139 (1995), ISSN 00319007.
- [244] B. L. Hansen, I. J. Beyerlein, C. A. Bronkhorst, E. K. Cerreta, and D. Dennis-Koller, *International Journal of Plasticity* **44**, 129 (2013), ISSN 07496419, URL <http://dx.doi.org/10.1016/j.ijplas.2012.12.006>.
- [245] W. Kanitpanyacharoen, S. Merkel, L. Miyagi, P. Kaercher, C. N. Tomé, Y. Wang, and H. R. Wenk, *Acta Materialia* **60**, 430 (2012), ISSN 13596454.
- [246] N. V. Kamyshanchenko, I. S. Nikulin, E. S. Kungurtsev, and M. S. Kungurtsev, *Technical Physics Letters* **39**, 469 (2013), ISSN 10637850.
- [247] L. G. Liu, T. Takahashi, and W. A. Bassett, *Journal of Physics and Chemistry of Solids* **31**, 1345 (1970), ISSN 00223697.
- [248] M. H. Manghnani, K. Katahara, and E. S. Fisher, *Physical Review B* **9**, 1421 (1974), ISSN 01631829.
- [249] H. M. Ledbetter, *Elastic properties of zinc: A compilation and a review* (1977).
- [250] A. K. Singh, J. Hu, J. Shu, H. K. Mao, and R. J. Hemley, *Journal of Physics: Conference Series* **377** (2012), ISSN 17426596.
- [251] R. Jeanloz, B. K. Godwal, and C. Meade, *Nature* **349**, 687 (1991), ISSN 0028-0836, URL <http://www.nature.com/articles/349687a0>.
- [252] T. S. Duffy, G. Shen, D. L. Heinz, Y. Ma, R. J. Hemley, H. K. Mao, and A. K. Singh, *MRS Proceedings* **499**, 145 (1997), ISSN 0272-9172, URL <http://link.springer.com/10.1557/PROC-499-145>.
- [253] D. Bancroft, E. L. Peterson, and S. Minshall, *Journal of Applied Physics* **27**, 291 (1956), ISSN 00218979.
-

- [254] F. M. Wang and R. Ingalls, *Physical Review B* **57**, 5647 (1998), ISSN 0163-1829, URL <https://link.aps.org/doi/10.1103/PhysRevB.57.5647>.
- [255] L. Miyagi, M. Kunz, J. Knight, J. Nasiatka, M. Voltolini, and H. R. Wenk, *Journal of Applied Physics* **104** (2008), ISSN 00218979.
- [256] J. Yang, X. Tong, J. F. Lin, T. Okuchi, and N. Tomioka, *Scientific Reports* **5**, 1 (2015), ISSN 20452322, URL <http://dx.doi.org/10.1038/srep17188>.
- [257] J. C. Crowhurst, J. M. Brown, A. F. Goncharov, and S. D. Jacobsen, *Science* **319**, 451 (2008), ISSN 0036-8075, URL <https://www.sciencemag.org/lookup/doi/10.1126/science.1149606>.
- [258] D. Antonangeli, J. Siebert, C. M. Aracne, D. L. Farber, A. Bosak, M. Hoesch, M. Krisch, F. J. Ryerson, G. Fiquet, and J. Badro, *Science* **331**, 64 (2011), ISSN 00368075.
- [259] B. B. Karki, R. M. Wentzcovitch, S. De Gironcoli, and S. Baroni, *Science* **286**, 1705 (1999), ISSN 00368075.
- [260] R. M. Wentzcovitch, J. F. Justo, Z. Wu, C. R. Da Silva, D. A. Yuen, and D. Kohlstedt, *Proceedings of the National Academy of Sciences of the United States of America* **106**, 8447 (2009), ISSN 00278424.
- [261] H. Fukui, T. Tsuchiya, and A. Q. Baron, *Journal of Geophysical Research B: Solid Earth* **117**, 1 (2012), ISSN 21699356.
- [262] M. Hamada, S. Kamada, E. Ohtani, T. Mitsui, R. Masuda, T. Sakamaki, N. Suzuki, F. Maeda, and M. Akasaka, *Physical Review B* **93**, 1 (2016), ISSN 24699969.
- [263] T. Tsuchiya, R. M. Wentzcovitch, C. R. Da Silva, and S. De Gironcoli, *Physical Review Letters* **96**, 1 (2006), ISSN 00319007.
- [264] H. Ozawa, F. Takahashi, K. Hirose, Y. Ohishi, and N. Hirao, *Science* **334**, 792 (2011), ISSN 10959203.
- [265] J. F. Lin and T. Tsuchiya, *Physics of the Earth and Planetary Interiors* **170**, 248 (2008), ISSN 00319201.
- [266] D. B. Ghosh and B. B. Karki, *Scientific Reports* **6**, 1 (2016), ISSN 20452322.
- [267] E. Holmström and L. Stixrude, *Physical Review B* **93**, 1 (2016), ISSN 24699969.
- [268] L. S. Dubrovinsky, N. A. Dubrovinskaia, S. K. Saxena, H. Annersten, E. Halenius, H. Harryson, F. Tutti, S. Rekhi, and T. Le Bihan, *Science* **289**, 430 (2000), ISSN 00368075.
- [269] L. Dubrovinsky, N. Dubrovinskaia, H. Annersten, E. Hålenius, and H. Harryson, *European Journal of Mineralogy* **13**, 857 (2001), ISSN 0935-1221.

-
- [270] L. Dubrovinsky, N. Dubrovinskaia, I. Kantor, C. McCammon, W. Crichton, and V. Urusov, *Journal of Alloys and Compounds* **390**, 41 (2005), ISSN 09258388.
- [271] V. Cerantola, A. D. Rosa, Z. Konôpková, R. Torchio, E. Brambrink, A. Rack, U. Zastrau, and S. Pascarelli, *Journal of Physics: Condensed Matter* **33**, 274003 (2021), ISSN 0953-8984.
- [272] R. Dimper, H. Reichert, P. Raimondi, L. S. Ortiz, F. Sette, and J. Susini, pp. 1–194 (2015), URL http://www.esrf.eu/Apache_files/Upgrade/ESRF-orange-book.pdf%5Cnpapers3://publication/uuid/15E113D0-D98A-4676-BEEA-DECOA05ACBE5.
- [273] C. G. Schroer, I. Agapov, W. Brefeld, R. Brinkmann, Y. C. Chae, H. C. Chao, M. Eriksson, J. Keil, X. Nuel Gavaldà, R. Röhlberger, et al., *Journal of Synchrotron Radiation* **25**, 1277 (2018), ISSN 16005775.
- [274] D. He, Y. Zhao, T. D. Sheng, R. B. Schwarz, J. Qian, K. A. Lokshin, S. Bobev, L. L. Daemen, H. K. Mao, J. Z. Hu, et al., *Review of Scientific Instruments* **74**, 3012 (2003), ISSN 00346748.
- [275] A. S. Méndez, H. Marquardt, R. J. Husband, I. Schwark, J. Mainberger, K. Glazyrin, A. Kurnosov, C. Otzen, N. Satta, J. Bednarcik, et al., *Review of Scientific Instruments* **91** (2020), ISSN 10897623, URL <https://doi.org/10.1063/5.0007557>.
- [276] S. Merkel, J. Shu, P. Gillet, H. K. Mao, and R. J. Hemley, *Journal of Geophysical Research: Solid Earth* **110**, 1 (2005), ISSN 21699356.
- [277] H. R. Wenk, I. Lonardelli, S. Merkel, L. Miyagi, J. Pehl, S. Speziale, and C. E. Tommaseo, *Journal of Physics Condensed Matter* **18** (2006), ISSN 09538984.
- [278] S. Merkel, H. P. Liermann, L. Miyagi, and H. R. Wenk, *Acta Materialia* **61**, 5144 (2013), ISSN 13596454, URL <http://dx.doi.org/10.1016/j.actamat.2013.04.068>.
- [279] M. Wilkens, *Physica Status Solidi (a)* **2**, 359 (1970), ISSN 1521396X.
- [280] G. Ribárik and T. Ungár, *Materials Science and Engineering A* **528**, 112 (2010), ISSN 09215093.
- [281] T. H. Simm, *Crystals* **8** (2018), ISSN 20734352.

Appendix

Table 1: Summary of all the gas-mixing runs performed at BGI.

Sample No.	Solid Solution	Flow rate	Temp [°C]	Log _{O₂}	CO ₂ / CO (ccm)	Holder depth (cm)	Time in the furnace (h)	Mössbauer	XRD
11	Mg ₅₀ Fe ₅₀ O	200	1300	-9.5	113 / 87	34 - 35	21:00	C7894	sample11
21* ¹	Mg ₉₀ Fe ₁₀ O + ⁵⁷ Iron	200	1300	-9.4	120 / 80	34 - 35	20:00		
12	Mg ₆₀ Fe ₄₀ O	200	1300	-9.5	113 / 87	34 - 35	22:00	C7896	sample12
FeO from Fe ₂ O ₃	FeO	200	1300	-9.7 / -9.8	100 / 100	34 - 35	22:00	C7905	FeOFe ₂ O ₃
16	Mg ₁₀ Fe ₉₀ O	200	1300	-9.8 / -9.9	9.4 / 106	34 - 35	20:15		sample16
FeO from Fe ₂ O ₃	FeO	200	1300	-9.8 / -9.9	94 / 106	34 - 35	20:00		
21* ¹	Mg ₉₀ Fe ₁₀ O + ⁵⁷ Iron	200	1300	-9.4	120 / 80	34 - 35	22:40		
19	Mg ₂₅ Fe ₇₅ O	200	1300	-9.5 / -9.6	104 / 96	34 - 35	24:00		
21* ¹	Mg ₉₀ Fe ₁₀ O + ⁵⁷ Iron	200	1300	9.4 / -9.5	115 / 85	34 - 35	23:20	C7909	sample21
12	Mg ₆₀ Fe ₄₀ O	200	1300	-9.6	108 / 92	34 - 35	23:20	C7910	
19	Mg ₂₅ Fe ₇₅ O	200	1300	-9.4 / -9.5	104 / 96	34 - 35	23:55	C7913	
II	Mg ₁₀ Fe ₉₀ O	200	1300	-9.8 / -9.9	94 / 106	34 - 35	23:35	C7912	sampleII
11	Mg ₅₀ Fe ₅₀ O	200	1300	-9.6	108 / 92	34 - 35	24:00	C7948	
21* ¹	Mg ₉₀ Fe ₁₀ O + ⁵⁷ Iron	200	1300	-9.6	108 / 92	34 - 35	24:00		
15	Mg ₂₀ Fe ₈₀ O	200	1300	-9.8 / -9.9	98 / 102	34 - 35	24:00		
15	Mg ₂₀ Fe ₈₀ O	200	1300	-9.8 / -9.9	98 / 102	34 - 35	24:00	C7945	
13	Mg ₄₀ Fe ₆₀ O	200	1300	-9.7	102 / 98	34 - 35	48:00	C7967	

*¹ = ⁵⁷Iron as 10% of all iron

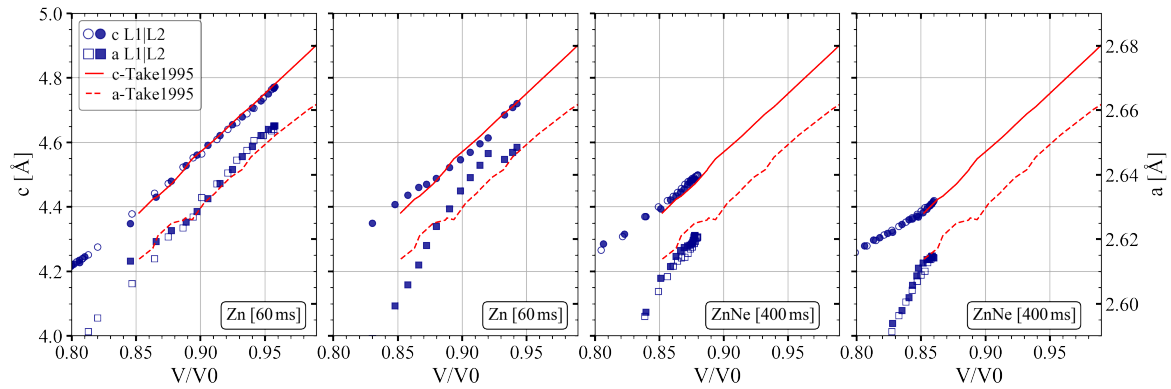


Figure 2: The lattice parameter evolution of all consecutive ramps of Zn as a function of relative volume. The current results of either LAMBDA 1 or LAMBDA 2 are represented by open and solid squares and circles. The open and solid triangles show previous data by Takemura [162, 163]. Notice the scaling difference between c axis and a axis.

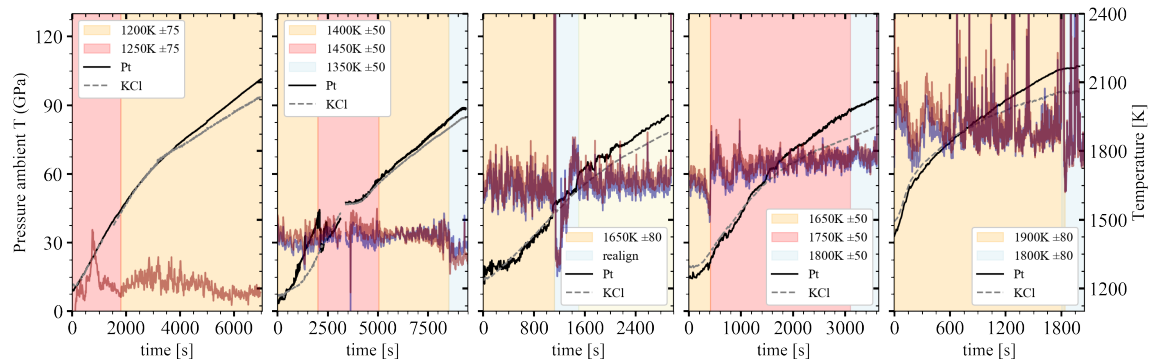


Figure 3: Temperature development observed by the Czerny-Turner spectrograph across all five runs and obtained KCl and Pt pressure from ambient T EoS. The colored background represents the average temperature observed within the time interval.

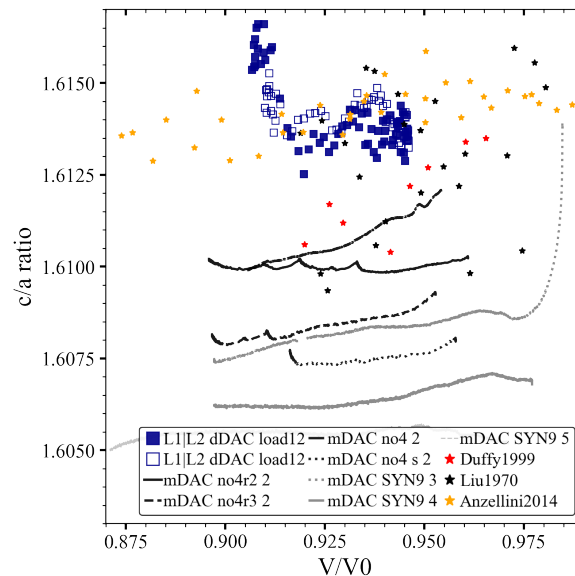


Figure 4: Development of the c/a axial ratio of all consecutive Re compression events performed with mDAC (lines) and dDAC (blue squares). Literature data (colored stars) depicts either conditions observed during radial diffraction, collected at 54.7° , the "magic angle", [205], DAC + NaCl [247], or DAC + He [214].

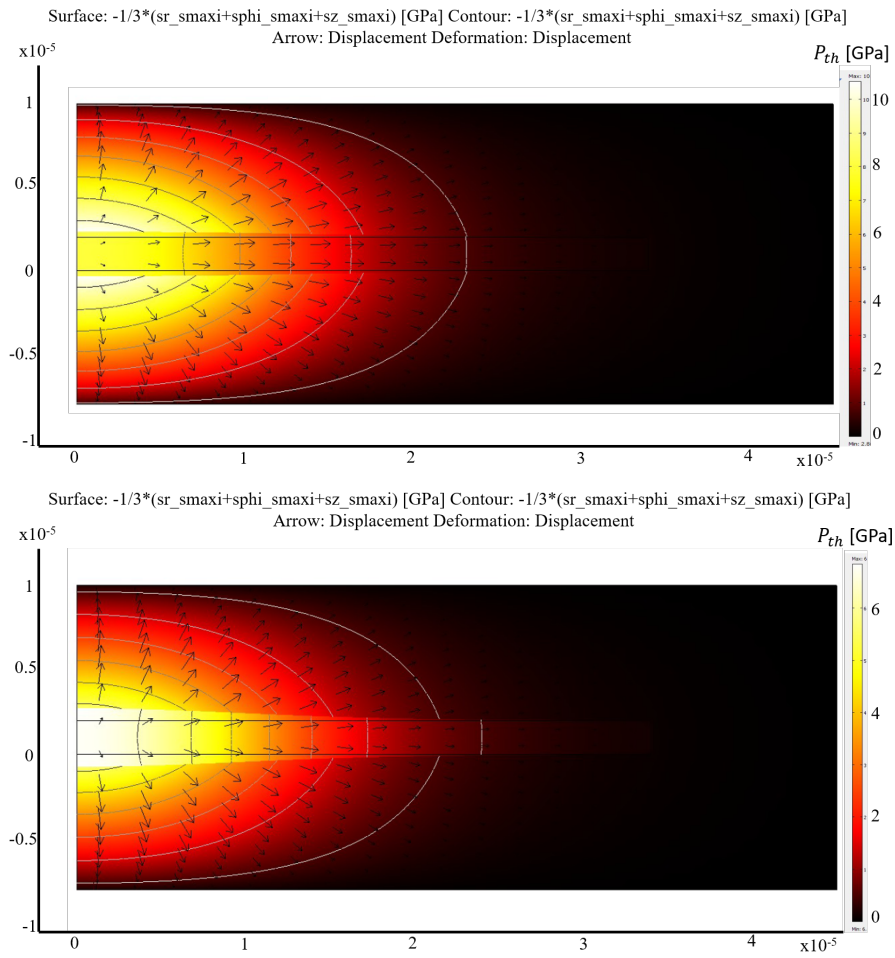


Figure 5: Thermal stress distribution and displacement-induced deformation of Pt for the case of a direct contact with a soft medium and assuming a change in the Bulk modulus parameter: (Top) $K=40$ GPa and (Bottom) $K=20$ GPa. The surface color and contours show P_{th} . Arrows and deformation shows the displacement and it is purposely exaggerated in the plots to visualize the changes (courtesy Konopkova, Z).

Register of abbreviation

(hkl) = Miller indices	E = Young's modulus
2θ = diffraction angle	ECB = Extreme Conditions Beamline
$a_m(hkl)$ = measured lattice parameter a	EDM = Electron-discharge Machine
a_p = lattice parameter compound under hydrostatic conditions	EDS = Energy dispersive spectroscopy
ADX = Angle dispersive X-ray diffraction	EDXD = Energy dispersive X-ray diffraction
α = constant determining the relative weight of isostrain and isostress	EoS = Equation of state
α -Ol = olivine (A,B) ₂ SiO ₄	ε = Strain
APS = Advanced Photon Source	$\dot{\varepsilon}$ = Accumulated strain
β -Ol = Wadsleyite (A,B) ₂ SiO ₄	η = Micro-strain
\vec{b} = Burgers vector	European XFEL = European X-ray Free-Electron Laser Facility GmbH
BGI = Bavarian Research Institute, Bayreuth	f_E = Eulerian strain
c, c_{ij} = Elastic stiffness, Single-crystal elastic constants	f_{O_2} = Oxygen fugacity
C_0 = Constant related to bulk wave speed	fcc = Face centred cubic
ΔC = Concentration difference	$f(x)$ = function of x
CPO = Crystallographic preferred orientation	$F_{V,T}$ = Total free Helmholtz energy
Cpx = Clinopyroxene (A)Si ₂ O ₆	FEL = Free Electron Laser
CRL = Compound reflective lenses	FWHM = Full width at half maximum
d = Lattice spacing	G_R, G_V = Shear modulus after Reuss, respectively, Voigt
$d_m(hkl)$ = measured lattice spacing at deviatoric stresses	GaAs = Gallium arsenide
d_p = lattice spacing under hydrostatic conditions	γ = Grüneisen parameter, thermodynamic property
d = grain size	$\Gamma(hkl)$ = lattice plane dependent value in range 0-1
δ = azimuthal angle	γ -Ol = Ringwoodite (A,B) ₂ SiO ₄
D = Diffusion coefficient	GFZ Potsdam = German Research Centre for Geoscience, Potsdam
DAC = Diamond anvil cell	Grt = Garnet (X ₃ Y ₂ (ZO ₄) ₃)
(mDAC = Membrane diamond anvil Cell)	h = Planck's constant (6.62607015*10 ⁻³⁴ J*s)
(dDAC = piezo-driven dynamic diamond anvil cell)	hcp = hexagonal close packed
(dsDAC = double stage diamond anvil cell)	HED = High Energy Density Scientific Instrument
DESY = Deutsches Elektronen-Synchrotron	HE-OL = High-energy optical laser
e = Energy	HPCAT = High Pressure Collaborative Access Team
E^* = Activation energy	IC1 = Interaction chamber 1 of the HED in-

strument	Q = Activation enthalpy
IC2 = Interaction chamber 2 of the HED instrument	$Q(hkl)$ = strain on individual lattice planes
IW = Iron-Wüstite oxygen fugacity Buffer	R = Ideal gas constant
J = Diffusion mass flux	ρ = Density
K_R, K_V = Bulk modouls after Reuss, respectively, Voigt	$\rho_p U_S$ = Shock impedance
K_0, K_S, K_T = Bulk modulus (K_S = isothermal resp. K_T = adiabatic)	s, s_{ij} = Elastic compliance, Elastic compliance constant
λ = Wavelength	$std(a_m)$ = standard deviation of average lattice constant
LAMBDA = Large Area Medipix-Based Detector Array	$std(a_p)$ = standard deviation of the hydrostatic compound of the lattice constant
LANL = Los Alamos National Laboratory	std_D = standard deviation independent of the differential stress trend
LLNL = Lawrence Livermore National Laboratory	S = Entropy
LPO = Lattice preferred orientation	S_i = Microstructural parameter (grain size, density of defects etc.)
LVP = Large volume press	SASE = Self-amplifying spontaneous emission
M_0 = differential stress dependent intercept of the gamma plot	Ss = Stainless steel
M_1 = differential stress dependent slope of the gamma plot	SEM = Scanning electron microscope
M_j = Material properties (lattice parameter, bond strength, activation etc.)	σ, σ_{ij} = Stress, stress component
MGD = Mie-Grüneisen-Debye approach	σ_{33} = Uniaxial stress component
n = Integral number, or number of atoms in a unit cell	SPO = Shape preferred orientation
ν = high-frequency edge shift of the Raman band	SDD = Sample detector distance
NIST = National Institute for Standards and Technology	t = Differential stress / uniaxial stress component
Ol = olivine (A,B) ₂ SiO ₄	T = Temperature
p = Linear momentum	TEM = Transmission electron microscopy
P = Pressure	θ = angle between impinging X-ray and lattice plane
Fe-Per = Ferropericlase (Fe,Mg)O	u_p = Particle velocity
p_{max} = maximum stress state	U_S = Shock velocity
Prv = Perovskite (Fe,Mg,Ca)SiO ₃	UHI-OL = Ultrahigh-intensity optical laser
ψ = angle between diffraction plane normal and load direction	V = Volume
PTM = Pressure transmitting medium	XRD = X-ray diffraction
	Z = Atomic number (respectively, Proton number)
	$zeta$ = lattice diffraction plane - load direction angle dependent parameter

Curriculum vitae

Education

- Feb. 2018 - Dec. 2021: European XFEL, Germany
Ph.D. student of the HED group, European XFEL and in the Statistical Physics Group, Rostock. Supervisors: Prof. Dr. Ronald Redmer, Dr. Zuzana Konopkova
- Oct. 2015 - Jan. 2018: University of Münster (WWU), Germany
Master of Science (M.Sc.) : Earth Science
Anisotropy in textured Ca-Mg carbonates in subducting slabs
Final Grade (1.7)
- Oct. 2012 - Sep. 2015: University of Münster (WWU), Germany:
Bachelor of Science (B.Sc.): Earth Science
Experimental constraints on the redox state of subduction zone fluids
Final Grade (2.2)
- Jun. 2010: Viktoria-Gymnasium Essen, Germany
University entrance diploma (Abitur)
Final Grade (3.0)

Employment History

- Feb. 2018 - Dec. 2021: Doctorate candidate, scientific assistant, European XFEL, Schenefeld, Germany
- Interne, Feb. 2015 - - Apr. 2015: Atlas Copco, Essen, Germany
- Jul. 2014 - Sep. 2015: Research Assistant, University of Münster (WWU), Germany:
- Jul. 2010 - May 2012: Radio Operator, Wehrdienst (Navy, frigate Rheinland-Pfalz), Germany

List of Publications during the Ph.D

1. Descamps, A., Ofori-Okai, B.K., Appel, K., Cerantola, V., Comley, A., Eggert, J.H., Fletcher, L.B., Gericke, D.O., Göde, S., Humphries, O., Karnbach, O., Lazicki, A., Loetzsch, R., McGonegle, D., Palmer, C.A.J., **Plueckthun, C.**, Preston, T.R., Redmer, R., Senesky, D.G., Strohm, C., Uschmann, I., White, T.G., Wollenweber, L., Monaco, G., Wark, J.S., Hastings, J.B., Zastrau, U., Gregori, G., Glenzer S.H., and McBride, E.E. *An approach for the measurement of the bulk temperature of single crystal diamond using an X-ray free electron laser*. Scientific Reports 10, 14564, (2020).
2. Wollenweber, L., Preston, T.R., Descamps, A., Cerantola, V., Comley, A., Eggert, J.H., Fletcher, L.B., Geloni, G., Gericke, D.O., Glenzer, S.H., Göde, S., Hastings, J.B., Humphries, O., Jenei, A., Karnbach, O., Konopkova, Z., Loetzsch, R., Marx-Glowna, B., McBride, E.E., McGonegle, D., Monaco, G., Ofori-Okai, B.K., Palmer, C.A.J., **Plückthun, C.**, Redmer, R., Strohm, C., Thorpe, I., Tschentscher, T., Uschmann, I., Wark J.S., White, T.G., Appel, K., Gregori, G. and Zastrau, U. *High-resolution Inelastic X-ray Scattering at the High Energy Density Scientific Instrument at the European X-Ray Free-Electron Laser*. Review of Scientific Instruments 92, 013101, (2021).
3. Zastrau, U., Appel, K., Baehtz, C., Baehr, O., Batchelor, L., Berghäuser, A., Banjafar, M., Brambrink, E., Cerantola, V., Cowan, T.E., Damler, H., Dietrich, S., Di Dio Cafisio, S., Dreyer, J., Engel, H.-O., Feldmann, T., Findeisen, S., Foese, M., Dulla-Marsa, D., Göde, S., Hassan, M., Hauser, J., Hermannsdörfer, T., Höppner, H., Kaa, J., Kaefer, P., Konopkova, Z., Laso García, A., Liermann, H.-P., Mainberger, J., Makita, M., Martens, E.-C., McBride, E.E., Möller, D., Nakatsutsumi, M., Pelka, A., **Plueckthun, C.**, Prescher, C., Preston, T.R, Röper, M., Schmidt, A., Seidel, W., Schwinkendorf, J.-P., Schoelmerich, M.O., Schramm, U., Schropp, A., Strohm, C., Sukharnikov, K., Talkovski, P., Thorpe, I., Toncian, M., Toncian, T., Wollenweber, L., Yamamoto, S. and Tschentscher, T. *The High Energy Density Scientific Instrument at the European X-ray Free Electron Laser*. Journal of Synchrotron Radiation, in peer Review. (2021)

List of Conference Contributions during the Ph.D

Oral

- **Plückthun, C.**, Husband, R., Liermann, H.-P., Morard, G. and Konopkova, Z. *Towards studying kinetics of structural and electronic phase transitions at variable strain rates using diamond anvil cells*. GEOMÜNSTER 2019, 22–25. Sep. 2019.
 - **Plueckthun, Ch.**, Husband, R., Liermann, H.-P., Marquardt, H., Méndez, A.S.J., Morard, G. and Konopkova, Z. *Kinetics of Deformation at high Compression Rates using dynamic Diamond Anvil Cell*. DESY/European XFEL User Meeting, Jan. 2020.
-

- **Plueckthun, C.**, Audéat, A., Boffa-Ballaran, T., Giordano, N., Husband, R., Kaa, Kurnosov, A., J., Liermann, H.-P., Marquardt, H., McCammon, C., Méndez, A.S.J., Morard, G. and Konopkova, Z. *Investigating the effect of compression rates on the stress development in experiments using the dynamic diamond anvil cell (dDAC) technique*. 1st European XFEL student's day, 17-18. Nov. 2020.

Poster and flash talks

- **Plückthun, C.**, Bhat, S., Farla, R., Liermann, H.-P. and Konopkova, Z. *The dynamic diamond anvil cell (dDAC) at the HED instrument of the European XFEL*. 7th Joint Workshop on High Pressure, Planetary, and Plasma Physics (HP4), 10-12. Oct 2018
 - **Plückthun, C.**, Bhat, S., Farla, R., Liermann, H.-P. and Konopkova, Z. *The dynamic diamond anvil cell (dDAC) at the HED instrument of the European XFEL*. IUCr HP Workshop, 29. Jul - 02. Aug 2018.
 - **Plückthun, C.**, Husband, R., Liermann, H.-P., Marquardt, H., A.S.J., Méndez, Morard, G. and Konopkova, Z. *Constraining the kinetics of deformation at high compression rates using the dDAC on Au and Re and Pt and Fe/[Mg,Fe]O samples*. DESY/European XFEL User Meeting, Jan.2020.
 - Descamps, A., Ofori-Okai, B., Fletcher, L., Hastings, J.B., Karnbach, O., McGonegle, D., Palmer, C., Humphries, O., Wark, J., Gianluca, G., Zastrau, U., Appel, K., Wollenweber, L., Preston, T.R., Strohm, C., **Plueckthun, C.**, Comley, A., Jenei, A., Eggert, J., Loetzsch, R., Uschmann, I., Senesky, D.G., Glenzer, S.H. and McBride, E.E. *A direct temperature measurement of resistively heated diamond using inelastic X-ray scattering*. DESY/European XFEL User Meeting, Jan. 2020.
 - **Plueckthun, C.**, Giordano, N., Husband, R., Kaa, J., Liermann, H.-P., Marquardt, H., Méndez, A.S.J., Morard, G. and Konopková Z. *Investigating the effects of compression rates on the stress development in experiments using the dynamic diamond anvil (dDAC) technique*. WE-Heraeus-Seminar /Matter under Extreme Conditions, Sep.2020.
 - **Plueckthun, C.**, Marquardt, H., Giordano, N., Husband, R., Kaa, J., Kurnosov, A., Liermann, H.-P., Mendez, A.S.J., Morard, G. and Konopkova, Z. *Investigating the effect of compression rates on the stress development in experiments using the dynamic diamond anvil cell (dDAC) technique*. DESY/European XFEL User Meeting, Jan.2021.
 - Sun, Y., **Plueckthun, C.**, Konopkova, Z. and Brockhauser, S., *Cloud-based Data Analysis Services for Photon and Neutron Science: Machine Learning Based Spectra Classification*. DESY/European XFEL User Meeting, Jan 2021, (PaNOSC, ExPaNDS).
-

-
- Descampes, A., McBride, E.E., Fletcher, L.B., White, T.G., Witte, B., Appel, K., Cerantola, V., Gauthier, M., Gericke, D.O., Goede, S., Hastings, J., Humphries, O., Karnbach, O., Kim, J.B., Lazicki, A., Loetzsch, R., McGonegle, D., Monaco, G., Nagler, B., Ofori-Okai, B., Oliver, M., Palmer, C.A.J., **Plueckthun, C.**, Preston, T.R., Redmer, R., Rigby, A., Schoenwaelder, C., Senesky, D.G., Strohm, C., Sun, P., Tschentscher, T., Uschmann, I., Wark, J.S., Wollenweber, L., Zastrau, U., Gregori, G. and Glenzer, S.H. *Towards Direct Measurements of Temperature and Transport Properties in Warm Dense Matter: meV-IXS from single crystal diamond*. DESY/European XFEL User Meeting, Jan. 2021.

List of Proposals with granted beamtime/facility access during the PH.D

1. Schoelmerich, M.O., (PI) Appel, K., (Co-PI) Plueckthun, C., (Co-Proposer) et al., *Dynamic compression of cristobalite at in-situ conditions*. ECB P02.2, PETRA III, DESY (proposal I-20180745, 2019).
 2. Plueckthun, C., (PI). *Synthesis of ferropericlase: Establishing a consistent sample set to quantify the effect of Fe content on the onset of phase and spin transitions*. DFG Core Facility, Bayrisches Geoinstitut (BGI), High-Pressure Laboratories, accepted 29. Mar. 2019, (19-25.05 and 01.07-15.07.).
 3. Plueckthun, C., (PI) Konopkova, Z., (Co-PI) et al., *The effect of compression rate on the onset pressure of the phase transitions in ferropericlase: (Mg,Fe)O*. ECB P02.2, PETRA III, DESY (proposal I-20190025, 2019).
 4. Plueckthun, C., (PI) Konopkova, Z., (Co-PI) et al., *Kinetics of deformation at high compression rates using dynamic diamond anvil cells*. ECB P02.2, PETRA III, DESY (proposal I-20190818, 2020).
 5. Plueckthun, C., (PI) Konopkova, Z., (Co-PI) et al., *Direct measurement of (Mg,Fe)O bulk modulus softening across the iron spin transition at realistic mantle temperatures*. ECB P02.2, PETRA III, DESY (proposal I-20200529, 2020).
 6. HED commissioning *MHz diffraction from DAC on AGIPD minihalf*. HED instrument, European XFEL (Proposal 2731, 03.11-15.11.2020)
 7. Sternemann, C., (Main Proposer) Cerantola, V., (PI) Plueckthun, C., (Co-proposer) et al., *Spin states of FeS and FeHx at and beyond telluric core-mantle boundary conditions by simultaneous X-ray emission and X-ray diffraction*. HED instrument, European XFEL (Proposal 2624, 03.09-05.09.2021)
-

Acknowledgements

First of all, I want to express my deep gratitude to my supervisors at the European XFEL, **Dr. Zuzana Konopkova**, and at the University of Rostock, **Prof. Dr. Ronald Redmer**, who gave me the opportunity to work in the scientific field of HP/HT mineralogy and introduced me to a new scientific tool: The large X-ray Free-Electron Laser facilities. Furthermore, I want to thank them for their outstanding scientific support and encouragement during the years and despite changing circumstances, arising problems or new challenges with tools, tasks and even daily life.

This study was funded by the Deutsche Forschungsgemeinschaft (DFG) under project number KO-5262/1 and the European XFEL GmbH and I would like to thank these institutions for their financial support and help. Moreover, I want to thank PETRA III, DESY, Hamburg for the delivery of the synchrotron beam and I want to acknowledge the staff of the ECB P02.2 for their technical support. Also, I want to thank **Dr. Hans-Peter Liermann**, **Dr. Konstantin Glazyrin**, **Dr. Rachel Husband**, **Dr. Nico Giordano** for their useful comments and scientific expertise.

Furthermore, I like to thank **Prof. Dr. Ulf Zastrau**, the Group leader of HED as well as **Dr. Karen Appel** for their great support and interest in my research and enhancement. In general, I want to express my gratitude to the whole HED/HIBEF group at the European XFEL, which made me feel to be an equal and reliable part of the team. Here, I want to thank **Christiana Franke**, for reading through the whole of the thesis and in the process killing a lot of convoluted sentences.

The outcome of this thesis would not have been the same without my fellow PH.D students at HED, **Nicole Biedermann**, **Lennart Wollenweber**, **Markus Schölmerich**, **Johannes Kaa** and **Aanad Dwivedi**. They helped to settle at the facility, provided help throughout beamtimes as well as gave input once question arose. However, more importantly they were just incredible colleagues to find a relaxing evening or social activity even during stressful times.

Thank you to **Vasilii Bazenhov**, **James Moore** and **Robin Schubert**, who provided help during the initial steps and tests of the sample synthesis of ferropericlase at the European

XFEL, to **Dr. Shrikant Bhat** and **Dr. Robert Farla** for their vivid help at the Large Volume Press as well as **Dr. Guillaume Morard** for the subsequent SEM analysis.

Furthermore, many thanks to **Prof. Dr. Hans Keppler** and to the Bavarian Research Institute (BGI) for access to their high-pressure laboratories as part of the DFG Core facility program and the opportunity to with progress and finish the synthesis and characterize of various ferropericlase solid solutions. In particular, I want to thank **PD. Dr. Catherine McCammon**, **Dr. Tiziana Boffa-Ballaran**, **Dr. Andreas Audéat**, **Serena Domini-janni** and **Caterina Melai** for their hospitality and help in this synthesis during my stay in Bayreuth (May and July 2019).

I also would like to seize the opportunity to thank fellow researchers and some collaborators: 1. **Apl. Dr. Hauke Marquardt** for his help with thermal pressure calculations and ideas for the experiments on ferropericlase. In particular, for his understanding that we do not try to compete with his own work on ferropericlase; 2. **Prof. Dr. Sébastien Merkel** for his insights in micro-stress and differential stress analysis, LPO as well as in general the effects of a diamond anvil setup on the sample; 3. **Dr. Alexander Kurnosov** for his support during the laser heating experiment, whilst the Corona pandemic; 4. **Dr. Earl O'bannon** for his help with the dynamic DAC and gamma plot analysis 5. **Biao Wang** for the exchange and work on the peak fitting routine with python and 6. **Dr. Sergio Speziale** for his help with EoS and single crystal elastic constants.

In addition, I want to acknowledge **Dr. Georg Spiekermann**, **Dr. Christian Sterne-mann**, **Lélia Libon**, **Christian Albers**, **Robin Sakrowski**, for their help and ideas during the preparation of the first DAC experiments using XES and XRD at the European XFEL. In this course, especially Christian Albers and Robin Sakrowski for making the complicated setup of the diamond anvil cell even more complex by flipping of the gasket and the require-ment to flatten the gasket walls after the indentation O-O.

I further would like to thank all of the above to put up with my habits and idiosyncrasies, especially when things got stressful. I hope that in the near future we will often run into each other and maintain a close working relationship.

Last and most importantly, my biggest gratitude goes to my **family**: my little **mother** ;-), little **sister** and the only real grandparents (**Willi** und **Christa**) I have and who have had to deal with me and my crazy and changing plans for the future. Also, to my closest friends **Yassine** and **Manuel**, who are always there when I need to talk and sometimes listen, or stop listening when I talk to much :-). Thank you for keeping me in track and making everything that did go wrong seem half as bad and over time become right! Without you, I would not be where I am today.

Eidesstattliche Erklärung

Doktorandinnen/Doktoranden-Erklärung gemäß § 4 Absatz 1 Buchstaben g und h der Promotionsordnung der Mathematisch-Naturwissenschaftlichen Fakultät der Universität Rostock

Ich gebe folgende Erklärung ab:

1. I hereby declare that I am the sole author of this thesis and that I have not used any sources other than those listed in the bibliography and identified as references. I further declare that I have not submitted this thesis at any other institution in this or another form.
2. Ich versichere hiermit an Eides statt, dass ich die vorliegende Arbeit selbstständig angefertigt und ohne fremde Hilfe verfasst habe. Dazu habe ich keine außer den von mir angegebenen Hilfsmitteln und Quellen verwendet und die den benutzten Werken inhaltlich und wörtlich entnommenen Stellen habe ich als solche kenntlich gemacht.
3. Die Gelegenheit zum vorliegendem Promotionsvorhaben ist mir nicht kommerziell vermittelt worden. Insbesondere habe ich keine Organisation eingeschaltet, die gegen Entgelt Betreuerinnen/Betreuer für die Anfertigung von Dissertationen sucht oder die mir obliegenden Pflichten hinsichtlich der Prüfungsleistungen für mich ganz oder teilweise erledigt.

Rostock, den 18/07/2021

.....

(Unterschrift)
